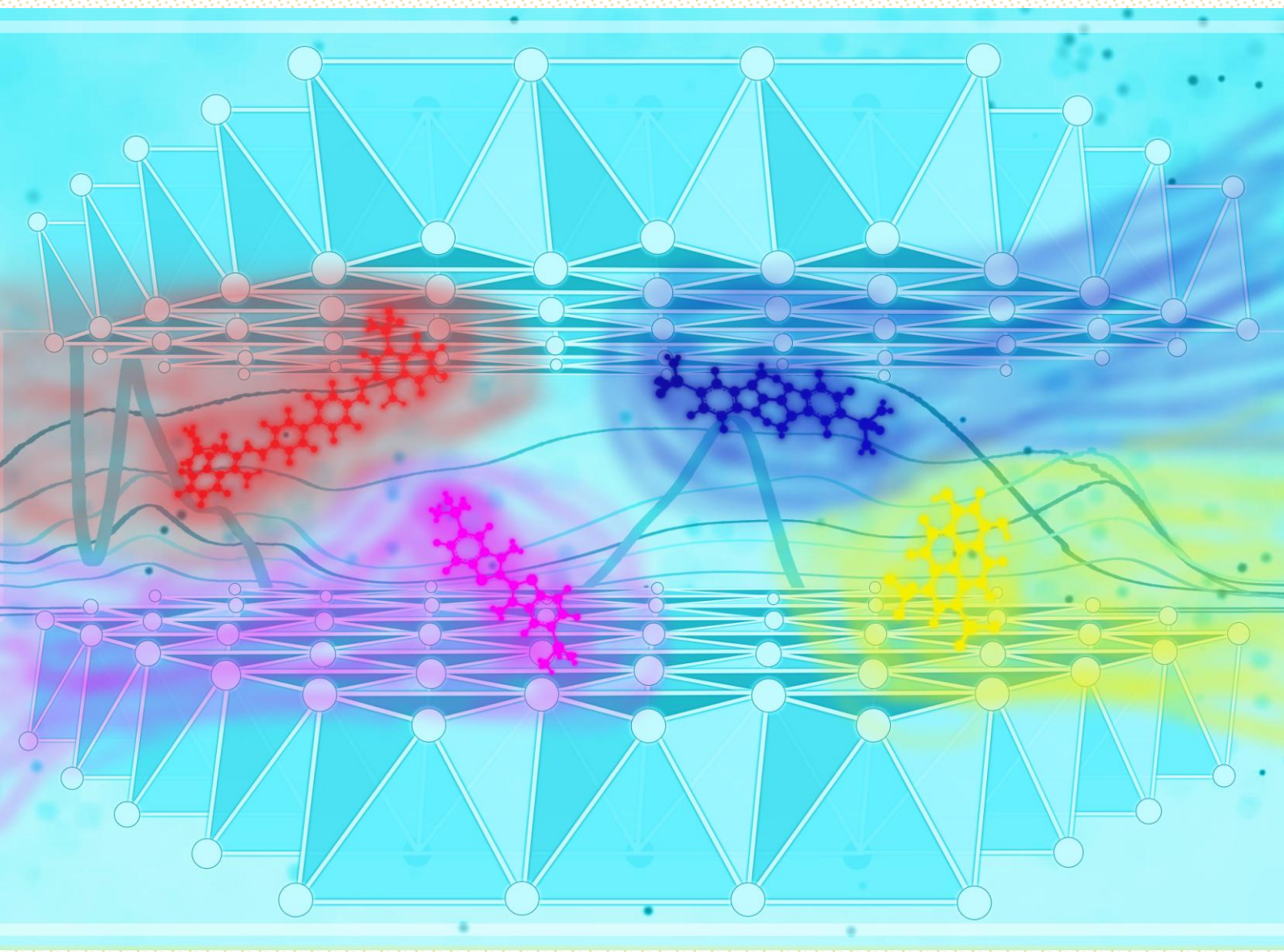

Ana Luísa Silva da Costa

SYNTHESIS AND PHOTOPHYSICAL STUDIES OF NEW HOST-GUEST HYBRID ORGANIC-INORGANIC SYSTEMS

Tese de doutoramento em Química, ramo de especialização em Fotoquímica, orientada por Professor Doutor João Sérgio Seixas de Melo e Professora Doutora Isabel Maria de Sousa Gonçalves e apresentada ao Departamento de Química da Faculdade de Ciências e Tecnologia da Universidade de Coimbra

Agosto 2017

· U C ·

UNIVERSIDADE DE COIMBRA

SYNTHESIS AND PHOTOPHYSICAL STUDIES OF NEW HOST-GUEST HYBRID ORGANIC-INORGANIC SYSTEMS

Ana Luísa Silva da Costa

Tese de doutoramento em Química, ramo de especialização em Fotoquímica, orientada por Professor Doutor João Sérgio Seixas de Melo e Professora Doutora Isabel Maria de Sousa Gonçalves e apresentada ao Departamento de Química da Faculdade de Ciências e Tecnologia da Universidade de Coimbra

UNIVERSIDADE DE COIMBRA

Agosto 2017

"Without data you are just another person with an opinion"

W. Edwards Deming

Aknowledgements

"Coimbra tem mais encanto na hora da despedida" já cantava Fernando Machado Soares na Balada da Despedida. Nunca tinha entendido o significado destas palavras até agora. A ambiguidade de sentimentos, alegria e orgulho pelo término de um ciclo académico, mas por outro lado, a nostalgia e melancolia de tudo o que foi vivenciado numa cidade como Coimbra, imbuída de saudade e simbolismo! Ao longo deste percurso, muitas foram as pessoas que se foram cruzando no meu caminho e que, de alguma forma contribuíram para o meu desenvolvimento pessoal e profissional. A essas pessoas tenho muito a agradecer!

Ao meu orientador, Prof. Dr. João Sérgio Seixas de Melo, pelo espírito crítico, pela exigência e rigor incutidos, características necessárias à investigação nomeadamente na área da fotoquímica. Por ser visionário e sempre com novas ideias (que dariam para mais 2 ou 3 teses de doutoramento) e pelo seu lado humano! Por me permitir fazer um projecto que englobasse áreas diferentes e por ter acreditado que eu era capaz!

À minha co-orientadora, Profª Dra. Isabel Gonçalves, por ter sido das melhores pessoas com quem trabalhei até hoje. Pela sua sensibilidade, carinho, dedicação e gentileza! Por ver sempre a luz ao fundo do túnel quando o cenário parecia negro, por nunca me fazer sentir que o meu trabalho foi em vão, pela motivação e pelo seu lado humano e capacidade de se colocar no lugar do outro.

Ao Dr. João Pina, por ser um pilar no grupo de Fotoquímica e que infelizmente nem sempre tem o reconhecimento merecido! Tenho muito a agradecer-lhe porque foi com ele que aprendi muito de Fotoquímica e foi sempre um apoio. O João faz das nossas angústias as dele e faz por encontrar uma solução, é preocupado e dá sempre a sua opinião sincera.

À Dra. Ana Gomes, por ter sido um pilar no grupo do CICECO em Aveiro. Quando conheci a Ana, tive a sensação que a conhecia desde sempre! Juntas conseguimos muitas conquistas, algumas delas muito suadas e difíceis.

Ao Dr. Martyn Pillinger pelos ensinamentos e pelas resoluções de todos os problemas.

À Celeste Azevedo pelas análises de TGA e DSC e à Manuela Marques pela análise elementar.

À Solange, uma amizade nascida em Coimbra e que eu espero que seja para toda a vida, pela paciência, pela cumplicidade e lealdade, por estar sempre presente, por ser frontal, verdadeira e autêntica.

À Raquel, outra amizade de Coimbra, por me incentivar e estar sempre presente.

Aos amigos do grupo de Fotoquímica, Dani S. pela serenidade e a sua forma pacífica de estar e de ver o mundo, à Catarina, a minha pequenina por quem eu tenho um carinho enorme, por ser genuína e trazer sempre alegria ao grupo, à Dani P. pela simpatia e ao Ricardo por ter sintetizado um dos compostos e por nos aturado a todas com muita paciência.

Ao meu amigo brasuca Fábio, por estar sempre alegre e de bem com a vida e por me ter tratado sempre tão bem.

Aos demais colegas do Departamento de Química, que embora não citados, deram também o seu contributo ao longo destes anos.

Às meninas do CICECO, Patrícia, Margarida, Sofia, Lucie, Diana e Clara por facilitarem a minha integração no grupo, pelos momentos sempre divertidos e por me ajudarem sempre que precisei. Foi muito bom estar por Aveiro!

À Eliana, pela sua tranquilidade e bons conselhos, à Catherine por me ter auxiliado em muitas questões fotoquímicas, pelos bons e caricatos momentos partilhados e à Diana, amiga de uma vida!

Aos meus pais, por me terem dado sempre liberdade nas minhas escolhas e por terem possibilitado todo o meu percurso até aqui.

À minha irmã, a quem eu devo muito do que sou hoje como pessoa. Por me apoiar sempre, por ser a minha melhor amiga e por nunca duvidar do meu valor. Para sempre lhe estarei grata! Ao meu cunhado pela amizade e carinho, por ter sempre uma palavra sábia e acolhedora. Ao meu sobrinho e afilhado Mateus, o amor incondicional da minha vida, por me ter distraído muitas vezes do processo de escrita.

À Fundação para a Ciência e Tecnologia (FCT) pelo financiamento do projecto de doutoramento (SFRH/BD/88806/2012).

OBRIGADA!!!

Table of Contents

1. General introduction:

Layered Double Hydroxides

2. A Congo Red-based LDH

3. An Indigo Carmine-based hybrid LDH with control of dye aggregation

4. Controlling the fluorescence behavior of a LDH-supported 1-pyrenesulfonate

5. Cointercalation of two indigo derivatives into LDH and LHS

6. Final Remarks and Future Perspectives

7. Experimental Section

Abstract

The present work consisted in the synthesis of new organic-inorganic host-guest systems and their photophysical characterization in the solid-state. Several organic molecules (guest species) were incorporated in layered double hydroxides (inorganic hosts) in order to study the interactions between host-guest hybrids with the aim to improve the stability of organic components and the fluorescence properties.

A detailed structural characterization of new materials was undertaken in solid-state using diverse techniques such as powder X-Ray diffraction (PXRD), Fourier Transform Infrared (FTIR) and Raman spectroscopies, ^{1}H and ^{13}C nuclear magnetic resonance, elemental analysis, scanning electron microscopy (SEM) and thermogravimetry analysis (TGA). Moreover, the study involved a photophysical and spectroscopic characterization, which encompasses absorption and fluorescence spectra, together with fluorescence quantum yields as well as excited lifetimes in solution and in solid-state (when possible).

With Congo Red (CR) in aqueous and DMSO solutions, it was found that internal conversion was the dominant deactivation route with more than 99.99% of the quanta loss (attributed to the energy gap law for radiationless transitions). Spectral data for more concentrated CR solutions indicated the presence of oblique or twisted J-type aggregates. These results were compared with spectra for CR in the solid-state (sodium salt) and intercalated in a layered double hydroxide (LDH) via a one-step coprecipitation route. Powder XRD and electronic spectral data for the nanohybrid indicate that the CR guest molecules were intercalated as a monolayer consisting of slipped cofacial J-type aggregates.

A Zn-Al layered double hydroxides containing solely indigo carmine (IC) or 1-hexanesulfonate (HS) anions, or a mixture of the two with different HS/IC molar ratios were prepared. Moreover, a comprehensive electronic spectral and photophysical study was undertaken for IC in solution and all materials in solid-state showing that incorporation of IC within the LDH decreases the level of aggregation, and that further addition of HS induces the appearance of isolated IC units within the LDH galleries. The incorporation of dye simultaneously with surfactant showed that is possible to perform a fine-tuning of color and spectral properties of the hybrid LDH by varying the amount of surfactant.

A similar approach was taken for sulfonated substituted derivative of pyrene, 1-pyrenesulfonate (PS), and a surfactant (heptanesulfonate, HpS) with the intercalation of each molecule individually or both with different loadings in a Zn-Al LDHs. Well-ordered intercalates were obtained with basal spacings of 18.8 Å for the LDH intercalated by PS and 19.2-19.4 Å for the other materials containing HpS. The fluorescent spectra of the solid samples display two bands at 376 nm and 495 nm. Depending on the HpS/PS ratios, the 375 to 520 nm band intensity ratio changes, reflecting different contributions from monomer and dimer species.

New inorganic-organic hybrid systems consisting on layered double hydroxides (LDHs) and layered hydroxy salts (LHSs) with the water-soluble forms of indigo (indigo carmine, IC) and thioindigo (thioindigo-5,5'-disulfonate, TIS) have been synthesised by coprecipitation route. For the cointercalated materials, it was observed that for LDH hybrids the basal spacing decreases with increasing TIS content while the opposite trend was observed for the LHS materials. A comprehensive spectral and photophysical study of these systems in the solid state has been performed. From the absorption and emission data (steady-state and time-resolved) the coexistence of monomer and aggregates is observed. The incorporation of both TIS and IC in the LDH and LHS layers leads to an almost complete quenching of the fluorescence, which is totally compatible with a very efficient energy transfer process, from (the fluorescent) TIS to (the non-fluorescent) IC.

Resumo

O presente trabalho consistiu na síntese de novos sistemas orgânicos-inorgânicos de hóspede-hospedeiro e a sua caracterização fotofísica em estado sólido. Várias moléculas orgânicas (espécies convidadas) foram incorporadas em hidróxidos duplos lamelares (hospedeiros inorgânicos), a fim de estudar as interacções entre o hóspede e hospedeiro com o objectivo de melhorar a estabilidade dos componentes orgânicos e as propriedades de fluorescência.

Foi efectuada uma caracterização estrutural detalhada dos novos materiais obtidos em estado sólido usando técnicas diversas, como difracção de raios-X de pó (PXRD), espectroscopias de infravermelho com transformada (FTIR) e de Raman, ressonância magnética nuclear ^{1}H e ^{13}C, análise elementar, microscopia electrónica de varrimento (SEM) e análise de termogravimetria (TGA). Além disso, o estudo envolve uma caracterização fotofísica e espectroscópica, que engloba espectros de absorção e fluorescência, juntamente com rendimentos quânticos de fluorescência, bem como medição de tempos de vida em solução e em estado sólido (quando possível).

Com o Congo Red (CR) em soluções aquosas e DMSO, verificou-se que a conversão interna foi a via de desativação dominante com mais de 99,99% da perda de energia (atribuída à diferença de energia para transições não radiativas). Os dados espectrais para soluções de CR mais concentradas indicaram a presença de agregados oblíquos ou torcidos de tipo J. Estes resultados foram comparados com os espectros para o CR no estado sólido (sal de sódio) e intercalados num hidróxido duplo lamelar através da síntese por coprecipitação. O DRX e os dados fotofísicos para o nano-hibrido indicaram que as moléculas de CR foram intercaladas como uma monocamada consistindo em agregados de tipo J orientados cofacialmente.

Foram preparados hidróxidos duplos lamelares de Zn e Al contendo aniões índigo carmim (IC) ou 1-hexanosulfonato (HS), ou uma mistura dos dois com diferentes razões molares HS/IC. Além disso, um estudo fotofísico abrangente foi realizado para o IC em solução e todos os materiais em estado sólido e mostrou-se que a incorporação do IC dentro do LDH diminui o nível de agregação e que a adição adicional de HS induz a aparência de unidades isoladas de IC dentro do espaço interlamelar do LDH. A incorporação de corante simultaneamente com surfactante mostrou que é possível realizar um ajuste da cor e propriedades espectrais do híbrido LDH, variando a quantidade de surfactante.

A mesma abordagem foi adoptada para o derivado substituído sulfonado de pireno, 1-pirenosulfonato (PS) e um surfactante (heptanosulfonato, HpS) com a intercalação de cada molécula individualmente ou ambas com diferentes loadings no LDH de Zn-Al. Foram obtidas intercalações bem ordenadas com espaçamentos basais de 18,8 Å para o LDH intercalado com PS e 19,2-19,4 Å para os outros materiais contendo HS. Os espectros de emissão das amostras sólidas exibem duas bandas a 376 nm e 495 nm. Dependendo das razões HS/PS, a relação de intensidade da banda de 375 a 520 nm muda, reflectindo diferentes contribuições de espécies de monómeros e dímeros.

Novos sistemas híbridos orgânicos-inorgânicos consistindo em hidróxidos duplos lamelares e em sais de hidróxido lamelares (LHSs) com as formas solúveis em água do índigo (índigo carmim, IC) e tioindigo (tioindigo-5,5'-dissulfonato, TIS) foram sintetizados pelo método de coprecipitação. Para os materiais cointercalados, observou-se que, para os híbridos de LDH, o espaçamento basal diminui com o aumento do conteúdo de TIS, enquanto a tendência inversa foi observada para os materiais de LHS. Foi realizado um estudo abrangente (electrónico e fotofísico) destes sistemas no estado sólido. A partir dos dados de absorção e emissão (estado estacionário e estado dinâmico) é observada a coexistência de monómeros e agregados. A incorporação de TIS e IC nas cavidades de LDH e LHS conduz a uma extinção quase completa da fluorescência, que é totalmente compatível com um processo de transferência de energia muito eficiente, do TIS (fluorescente) ao IC (não fluorescente).

Introductory Note

1. Comment to the nomenclature used

The dyes 3,3'-([1,1'-biphenyl]-4,4'-diyl)(4-aminonaphthalene-1-sulfonic acid) sodium salt, indigo-5,5'-disulfonate, thioindigo-5,5'-disulfonate and the probe 1-pyrenesulfonic acid sodium salt are usually named as Congo Red (CR), Indigo carmine (IC), Thioindigosulfonate (TIS) and 1-Pyrenesulfonate (PS), respectively. The surfactants sodium 1-hexanesulfonate monohydrate and 1-heptanesulfonic acid sodium salt are denoted as simply hexanesulfonate (HS) and heptanesulfonate (HpS).

2. Numbering of figures, schemes and tables

The numbering of figures, schemes and tables presented in each chapter is dependent of that numeration used in each chapter.

3. References system

Throughout this thesis the bibliographic references are indicated by numbers, in ascending order and indicated in the bibliography in the end of each chapter.

Abbreviations and Symbols

ν	Frequency
δ	Chemistry shift
λ_{abs}	Absorption wavelength
ν_{as}	Asymmetric frequency
μJ	MicroJoule
ν_{s}	Symmetric frequency
^{13}C NMR	Nuclear Magnetic Resonance of Carbon
^{1}H NMR	Nuclear Magnetic Resonance of Proton
2D	Two-dimensional
3D	Tri-dimensional
A	Absorbance
Å	Angström
a_{ij}	Preexponential factors
br	Broad
c	Concentration
ca.	*Circa*
cm^{-1}	Wavenumber
CP MAS	Cross-Polarization Magic Angle Spinning
CR	Congo red
d	Duplet
DAS	Decay associated spectra
dd	Double duplet
DD	Deionized and decarbonated
DFT	Density Functional Theory
DHS	Double Hydroxide Salt
DMF	*N,N*-dimethylformamide
DMSO	Dimethyl sulfoxide
DMSO-d_6	Dimethyl sulfoxide hexadeuterate
DNA	Deoxyribonucleic acid
DPT	Double Proton Transfer
DSC	Differential scanning calorimetry
EDS	Energy dispersive X-Ray spectrometry
ESA	Excited state absorption
ESIPT	Excited State Intramolecular Proton Transfer
ESPT	Excited State Proton Transfer
et al.	*et alia* (from Latin, reference to other people)
EtOH	Ethanol
fs-TA	Femtosecond Transient absorption
FTIR	Fourier Transform Infrared Spectroscopy
FWHM	Full-Width Half-Maximum

GSB	Ground state bleaching
HpS	Heptanesulfonate
HR-ESI	High-resolution electronspray ionization
HS	Hexanesulfonate
Hz	Hertz
IC	Indigo carmine
ICP-OES	Inductively coupled plasma optical emission spectroscopy
I_E	Intensity of excimer emission
I_M	Intensity of monomer emission
J	Coupling constant (in hertz)
K	Kelvin
k_F	Fluorescence rate constant
k_{IC}	Internal conversion rate constant
k_{ISC}	Intersystem crossing rate constant
k_{NR}	Non-radiative rate constant
l	Length of the cuvette (in cm)
LDH	Layered Double Hydroxide
LHS	Layered Hydroxy Salt
LUMO	Lowest Unoccupied Molecular Orbital
m	Medium
M	Molar (in mol/dm^3)
M^-	Molecular ion
m/z	Mass-to-charge ratio
MB	Maya Blue
MeOH	Methanol
MHz	Megahertz
mL	Milliliter
mmol	Milimole
mol	Mole
MPa	Megapascal
NIR	Near Infrared
nm	Nanometers
ns	Nanoseconds
O/I	Organic-inorganic
ºC	Celsius degree
OD	Optical density
ppm	Parts per million
PS	Pyrenesulfonate
r.t	Room temperature
s	Strong
S_0	Ground State
S_1	Lowest Singlet Excited State
S_2	Second Singlet Excited State
SEM	Scanning Electron Microscopy
sh	Sharp

SPT	Single Proton Transfer
SVD	Singular value decomposition
T_1	Lowest Triplet Excited State
T_2	Second Triplet Excited State
TGA	Thermogravimetry Analysis
TIS	Thioindigosulfonate
TMS	Tetramethylsilane
UV	Ultraviolet
VIS	Visible
vr	Vibrational relaxation
vs	Very strong
vs.	Versus
w	Weak
PXRD	Powder X-Ray Diffraction
ε	Molar absorption coeficient
ϵ	Dielectric constant
λ_{em}	Emission wavelength
λ_{exc}	Excitation wavelength
ϕ_F	Fluorescence Quantum Yield
ϕ_{IC}	Internal conversion Quantum Yield
ϕ_{ISC}	Intersystem crossing Quantum Yield
ϕ_{Ph}	Phosphorescence Quantum Yield
τ_F	Fluorescence lifetime
τ_{Ph}	Phosphorescence lifetime

1. General Introduction

Layered Double Hydroxides

1.1 Nature as a teacher and the concept of hybrid materials

Mother Nature is wised and for more than five hundred million years has left us with elements and raw materials charged of magnificent. These natural raw materials are fascinating due to high degree of sophistication and detail displayed, combining areas as chemistry, biology, physics or engineering.[1-2] Where there is life, there is diversity! There are several examples of this diversity in natural organic-inorganic materials such as the complex and carved morphology in the skeleton of radiolaria (a protozoa of 0.1-0.2 nm in diameter that produces mineral skeletons) or diatoms, in crustacean carapaces or mollusk shells, bones and teeth tissues in vertebrates.[1, 3-4] The ability of Nature to combine (bio) organic and inorganic components to provide significant smart materials with diverse properties and/or functions is fascinating. Man with no intentional will to imitate Nature, has apparently followed this line of action. The development of organic-inorganic (O/I) hybrids goes back to ancient civilizations with the mixing of organic and inorganic components that leads to the production of bright and colorful paints as the ones found in Maya archeological sites.[5-6] However, and very interestingly these hybrids are not simple physical mixtures and the organic and inorganic components are intimately mixed; thus the properties of these type of systems are seen together and not just the contribution of the individual parts.

Nowadays with the huge growth of era of technology, the term *hybrid* has become very fashionable and is used to cover a variety of systems with great properties and innumerous potential applications. The name “hybrid” O/I material appeared around the 1990’s with the triggering of molecular chemistry which led to an astonishing rapid development in nanomaterials science. Geppi and co-authors[7] proposed a definition for organic-inorganic material: “*it is a material constituted by both organic and inorganic components, where the average domain sizes of either one or both components range from nano- to micrometers (…) both components exhibit a functional role in determining the final properties of the material*.” These materials can be divided into two classes taking in consideration the possible interactions between the organic and inorganic parts. Class I comprises the hybrid materials that show weak interactions such as Van der Waals, hydrogen and electrostatic bonds; Class II refers to materials where the established bonds between the two parts are stronger such as covalent and iono-covalent bonds.[8-9] Figure 1.1 shows schematically the differences between these two classes of hybrids.

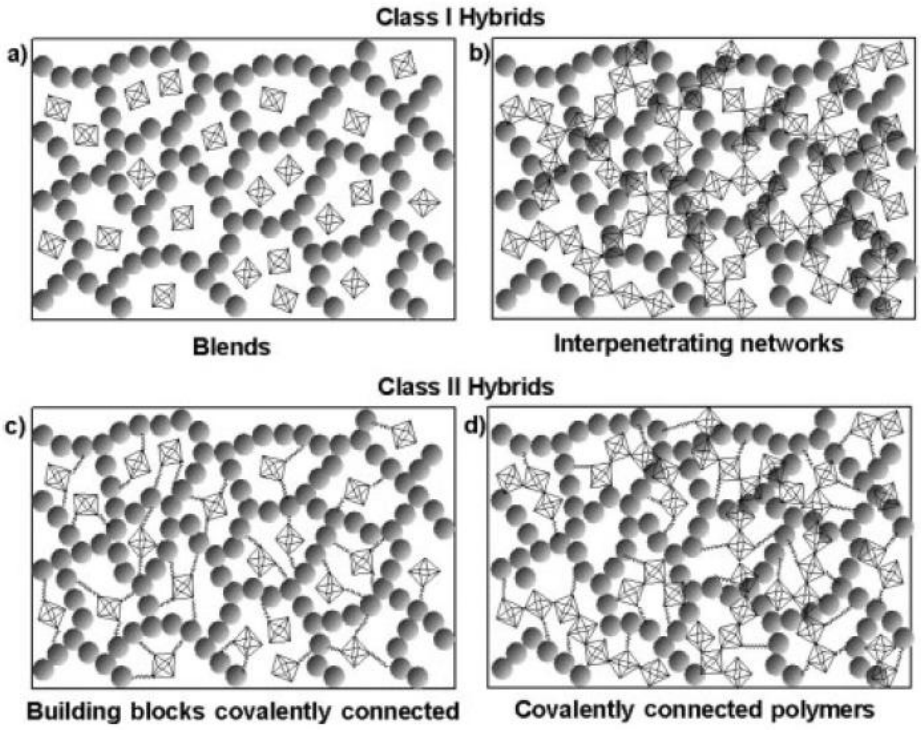

Figure 1.1 – The possible type of interactions of hybrid materials.[9]

The main advantages of hybrid materials are (i) in just one material, it is possible to combine the individual properties of organic and inorganic parts; (ii) these combination leads to multifunctional materials and (iii) the new hybrid material shows an increase in stability and performance, in most cases, when in comparison with the individual components.[9]

1.2 Learning the "savoir faire" that leads to the concept of host-guest chemistry

Among others, chemists, biologists, physicists and engineers are motivated by the desire to create new and more efficient materials. It could be possible the design of challenging and sophisticated hybrid compounds by learning the "savoir faire" of hybrid living systems.[3] The O/I hybrid materials came to revolutionize the materials science because the possibility to combine a wide variety of organic components with innumerous and different inorganic constituents brought a generation of "intelligent" materials for academic research, but they also open the door in many areas with promising applications: optics, electronics, mechanic, energy, environment, biology, medicine, etc.[10] Applications comprises smart membranes, photocatalysts and sensors, photovoltaic and fuel cells, smart microelectronic, micro-optical and photonic

components and systems, smart therapeutic devices,[3] nanoceramic-polymer composites for the automobile and packaging industries and so on.[10]

In the last years, the interest in the incorporation of organic molecules into inorganic hosts with well-defined cavities has been increasing mainly to their different properties.[11-12] Two approaches can occur for the modification of layered nanomaterials: host-guest reactions (intercalation technique or formation of inclusion compounds) and surface adsorption.[13] Intercalation reaction consists on the exchange of the interlayer components by functional molecules that are named “guest molecules”.

1.3 Lamellar/Layered materials

Layered compounds are obtained by packing of two-dimensional layers along the basal crystallographic axis.[14] Based on the primary forms present in Nature, the formation of layered materials is spontaneous with specific compositions.[15] There are a large number of layered hosts which can undergo intercalation reaction by guest molecules, such as graphene-based structures, carbon and metal oxides,[16] silicate clays (smectites, sepiolite, palygorskite and kaolinite),[17] metal chalcogenides [$(PbS)_{1.8}(TiS_2)_2$, MoS_2], metal phosphates and phosphonates, and layered double hydroxides.[18]

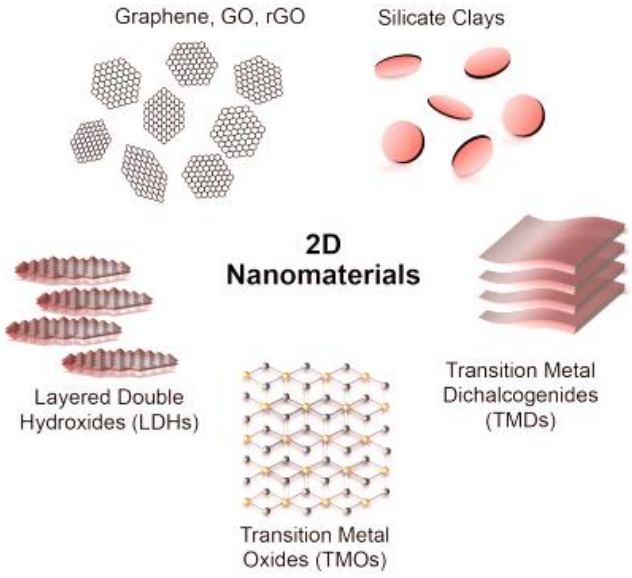

Figure 1.2 – Some examples of 2D nanomaterials (adapted from ref[19]).

Taking in account the charge of the host layer, layered compounds may be classified into three categories: neutral, negatively and positively charged (see Figure 1.3). The materials falling into the first category are graphite, hexagonal boron nitride, metal dichalcogenides and

indigo-palygorskite materials;[20-23] the negatively charged nanomaterials are the oxides and in the latter category are hydroxides. The negatively charged layered materials are the most common and shows cation exchange reactivity (such as smectite clays, metal phosphates and phosphonates, metal oxides, and others), thus, for that reason there are few examples of anion-exchangeable materials reported.[24-25] In the case of positively layered materials, the anionic species in the host should have appropriate charge and size to fill the metal coordination sphere. Moreover, besides the electrostatic interactions between the host and anions in the gallery, hydrogen bonds are also established in order to stabilize the system. For these reasons, materials with anion-exchange capacity are available mainly in the form of hydroxides.[26] Layered double hydroxides are an example and will be described below.

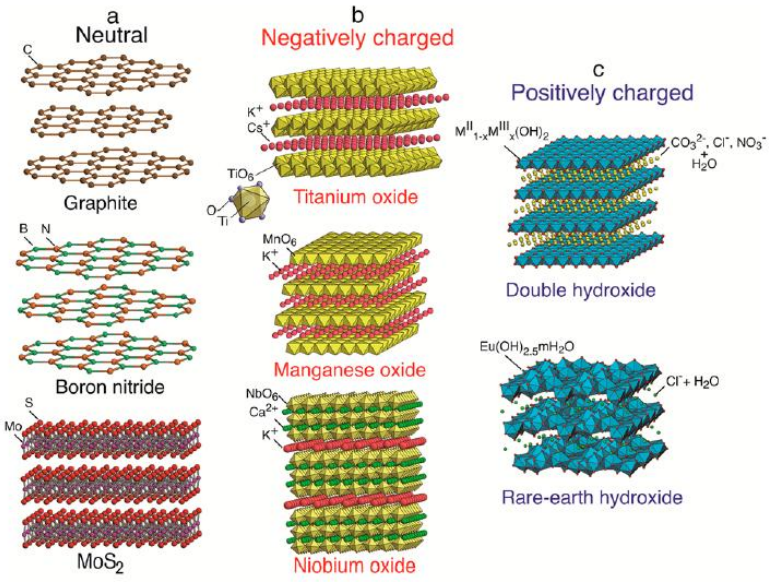

Figure 1.3 – Examples and structure of different types of layered materials: a) neutral, b) negatively charged and c) positively charged.[18]

1.4 Layered Double Hydroxides (LDHs)

The term of Layered Double Hydroxides (LDHs) is used to define synthetic or natural lamellar hydroxides with two type of metallic cations (divalent and trivalent ones) in the main layers, which generate a positively charged layer, and interlayer domains containing anionic species and water molecules in order to charge balance. This family of compounds is also denoted as *anionic clays*, *hydrotalcite-like* (HTl) or *hydrotalcite-type* (HTt) compounds,[27] since the discover of mineral called hydrotalcite, that was originally described by Hostetter in 1842,[28] in which he initially considered to be an aluminate. Later on, Dana[29] and Hermann[30] classified this mineral as being similar to brucite. Many other authors[31-34] supported the theory of the mineral being a mixture of other minerals. Although, only in 1915 the first studies on the stoichiometry of hydrotalcite were performed by Ernesto Manasse,[35] who proposed the general

formula $Mg_6Al_2(OH)_{16}CO_3.4H_2O$ showing that hydrotalcite was the aluminium analogue of pyroaurite (constituted by Fe instead of Al).[36] The interest on the chemistry of these type of lamellar materials only growth in 1930 with several studies carried out by Feitknecht.[37-38] The structure attributed to these materials consisted in a layer composed by a metallic hydroxide intercalated by layers of a second metallic hydroxide. It is only in the 1960's, that the structural features of LDHs were really understood with the determination of the single crystal X-Ray diffractogram (XRD) structure on pyroaurite and sjögrenite mineral samples by Allmann[39] and Taylor,[40-41] showing that both cations were in the same layer. Hitherto, 44 minerals have been described as natural examples of LDH phases (see Figure 1.4 for some examples) and they are usually known as "hydrotalcite group" of minerals. Different stackings arrangements of hydroxide layers can be observed – polytypism – and for that reason different names were attributed to distinct polytypes of the same compound.[42]

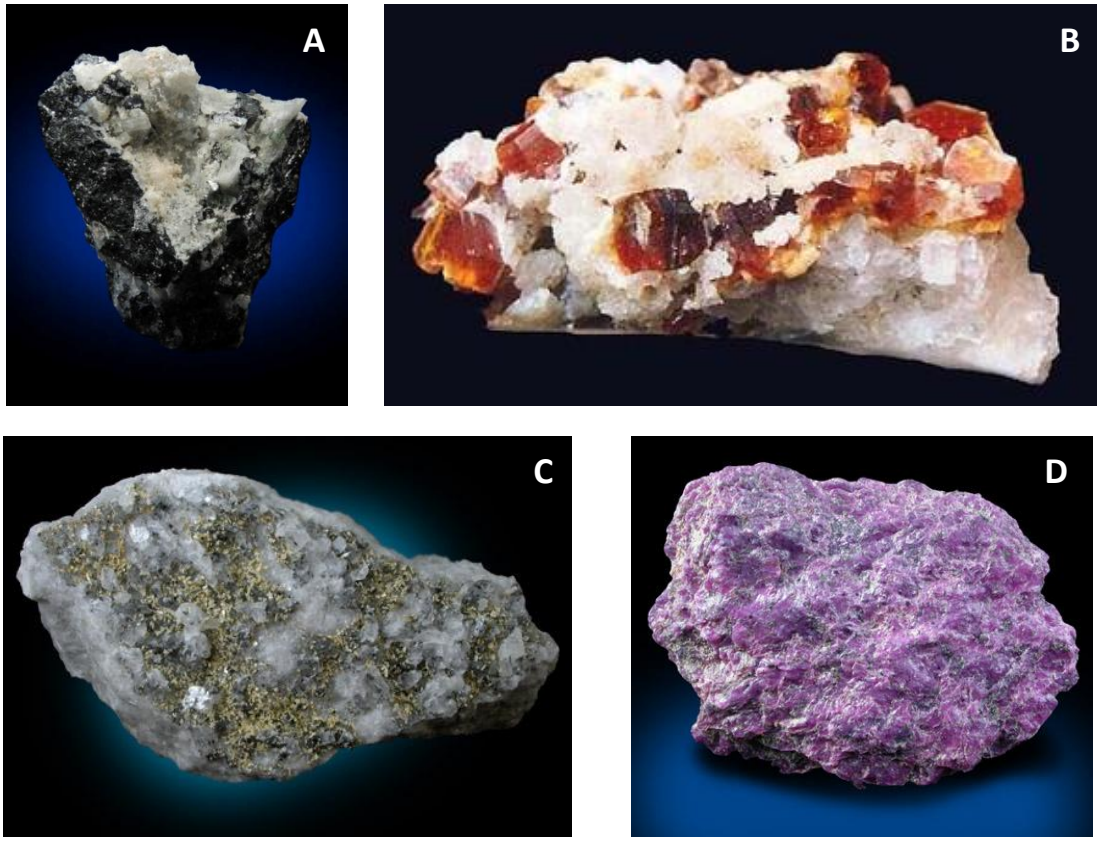

Figure 1.4 – Pictures of different types of natural minerals: (**A**) Hydrotalcite-2H *var* Manasseite from Brazil; (**B**) Hydrotalcite-2H from Russia; (**C**) Pyroaurite from Finland and (**D**) Stichite from Tasmania (ref. http://www.johnbetts-fineminerals.com).

1.4.1 Structural characteristics

The structure of LDHs is based on the structure of brucite, composed by $Mg(OH)_2$, and consists of Mg^{2+} ions coordinated octahedrally by hydroxyl groups. These octahedral units form infinite layers by edge-sharing with the OH ions being perpendicular to the plane of the layers. The 3D structure is formed by stacking the layers on top of one another along the *c*-axis to yield the characteristic plate like-solid (Figure 1.5).[42-45]

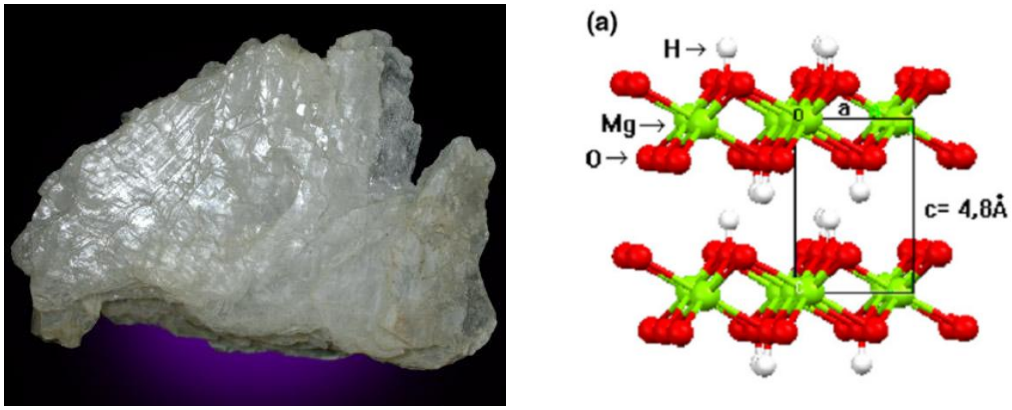

Figure 1.5 – a) Mineral brucite from Texas (ref. http://www.johnbetts-fineminerals.com) and b) structure of a brucite layer.[46]

Generally, the cell parameters are defined on the basis of a hexagonal unit cell. The lattice parameter *a* corresponds to the distance between the two metal cations in the layers and c_0 parameter is attributed to the distance from the center of one layer to that in the adjacent layer (basal spacing of an LDH). In brucite, the OH⋯OH distance is to 2.785 Å and the layer thickness (*h*) is 2.113 Å.[47] The octahedra is flattened which leads to the gradual loss of symmetry from O_h to D_{3d}, as ilustrated in Figure 1.6, which originate the increase in O⋯O and Mg⋯Mg distances parallel to the plane and a decrease in the thickness of the layers. This distortion does not affect the hexagonal symmetry of brucite layers.[42-43, 48]

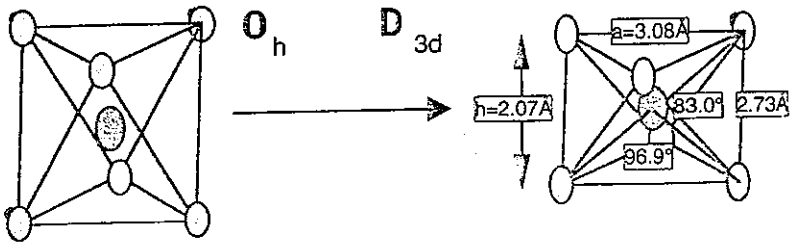

Figure 1.6 – Representation of the $M(OH)_6$ octahedra in a Zn,Al-LDH.[27]

The positive layers of an LDH are coordinated by six oxygen atoms forming $\{M(OH)_6\}$ octahedra, which is of CdI_2 type – hexagonal close packing of anions with total filling of octahedral holes by M^{2+} every two interlayers.[49] These octahedra share edges to form infinite charge-neutral sheets.

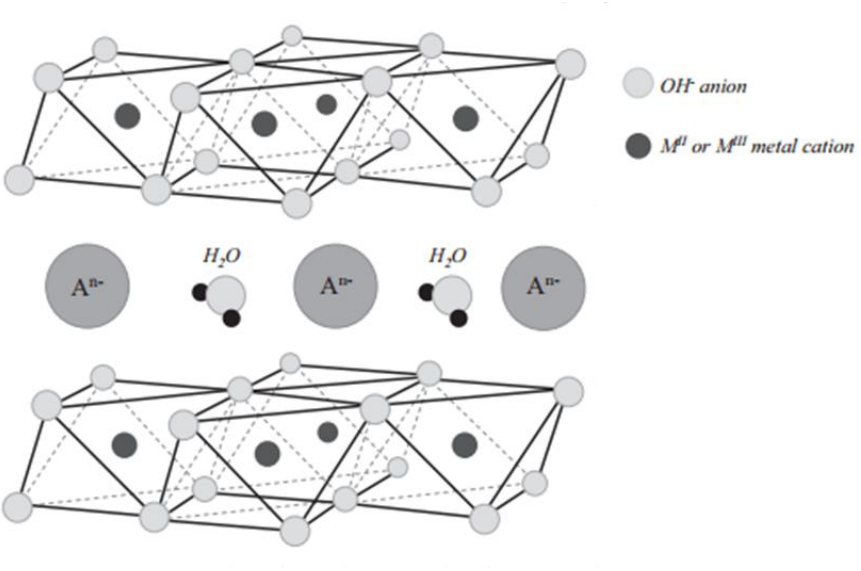

Figure 1.7 – Schematic representation of the structure of a typical LDH (adapted from ref[50]).

1.4.2 Chemical composition

The brucite layers are neutral and can undergo compositional changes in which the divalent cations are replaced isomorphously by trivalent cations, leading to a positively charged layer that needs the presence of interlayer anions. The general formula of LDHs can be written as the following[27, 43-44]

$$[M^{2+}_{1-x}M^{3+}_{x}(OH)_2]^{x+}(A^{m-})_{x/m}.nH_2O$$

where,

M^{2+} = divalent metal

M^{3+} = trivalent metal

A^{m-} = interlayer anion with charge m^-

$x = M^{3+}/(M^{2+} + M^{3+})$

n = number of mols of the co-intercalated water

However, Mills and co-workers[42, 51] proposed a new nomenclature system for hydrotalcite group of materials, considering that the one described above is not the most appropriate. This type of nomenclature is useful when it is possible to obtain a synthetic LDH polytype of the natural hydrotalcite. The main difference of this type of classification compared with the usual one is the identification of the simmetry. Their proposal uses the formula: **LDH *x*M^{2+} *y*M^{3+}. A[B]-C**, where x and y are the proportions of M^{2+} and M^{3+}; M^{2+} and M^{3+} are the divalent and trivalent metal cations, respectively; A is the intercalated anion, B is an interlayer cation (if one is present) and C is the polytype symbol. For instance, synthetic pyroaurite (Table 1.1) with this formula can be represented as LDH 6Mg2Fe.CO_3-3*R.* Although, nowadays the "old" nomenclature is still preferably used.

1.4.3 Metal cations in the layers

Approximately, half to one quarter of the divalent cations in LDHs can be replaced by trivalent cations of similar size.[52] The ionic radii of metals covers the range of 0.65-0.80 Å for divalent cations and 0.62-0.69 Å for trivalent ones, with the exception of Al cation – 0.50 Å. The most common divalent and trivalent cations on the structure of LDHs are the main group cations, such as Mg, Ca, Al, Ga, In, etc, or transition metal cations (e.g. Cu, Cd, Zn, Mn, Cr, Fe, Mn, Co, Ni, Cu, V),[27, 44, 53-54] although there are some reports about preparation of LDHs with monovalent[55-58] or tetravalent cations.[59-61] When the ionic radius of one of the metal cations has a higher value than the estimated, the octahedral coordination is lost due to the opening of one side of the octahedron on the interlamellar space originating the coordination with one interlamellar water molecule leading to a loss in symmetry which is now C_{3v} instead of D_{3d}.[27] The M^{2+}/M^{3+} ratio has a strong influence in charge density of LDHs (Figure 1.8). The LDH stability decreases in the order Mg < Mn < Co ≈ Ni < Zn for M^{2+} cations and Al < Fe for M^{3+}.[43] The cation-cation repulsion is minimized across the octahedra (cation avoidance rule, CAR) when the M^{2+}/M^{3+} ratio is ~ 2, meaning that there is order usually present in the system.[62] When there are a disordered distribution of cations, the unit cell equals the basic cell of the brucite-like layer (a_0 ~ 3 Å)*;* while, with an ordered arrangement of cations, $a = a_0\sqrt{3}$ ~ 5.2 Å.[63-64]

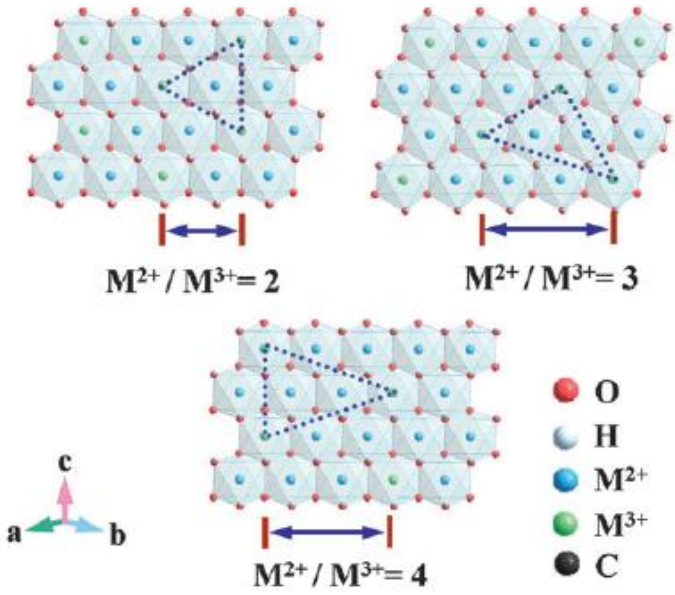

Figure 1.8 – Structure of LDHs layers with different M^{2+}/M^{3+} molar ratios.[65]

1.4.4 Trivalent metal ratio

The value of *x* represents the cation concentration of the trivalent metal, and affect the composition as well as the structure of the resulting LDHs.[66] In order to obtain true and crystalline LDH phases, this parameter should range between $0.2 \leq x \leq 0.33$ (which means M^{2+}/M^{3+} ratios ranging between 2 and 4). Although, it is possible to prepare LDHs outside this metal ratio range but the resulting material is not totally pure containing some impurities. The higher limit of *x* is attributed to the electrostatic repulsion between trivalent metals in the layers, the CAR[64, 67-68] and also the charge-balancing anions repulsion in the interlayer domains which occurs for $x > 0.33$. The lower limit corresponds to the increase of the distance between these anions (see below examples in the section 1.4.5) which could cause the collapse of interlamellar domain.

1.4.5 Interlayer anions

An important feature of LDHs is the lack of crosslinking between the cation layers thus allowing the interlayer spacing to expand or contract to accommodate a wide range of interlayer anions.[52] The dimension and functional groups of the anionic molecules are of great importance in determining the separation between the layers. In naturally LDH-based materials the more common anion found in the interlayer domain is carbonate. However, there are a huge diversity of molecules that can occupy the LDH galleries using a range of methods (will be discussed

later in Section 1.4.7) such as halides (Cl^-, F^-, etc),[56, 69-70] oxo-anions like CO_3^{2-}, OH^-, SO_4^{2-}, NO_3^-,[56, 69-70] organic molecules (carboxylates, phosphonates, alkyl sulphates), polyoxomethalates,[56, 71-78] anionic complexes (ferricyanide, $(PdCl_4)^{2-}$),[79-81] silicates[82-84] etc. One main characteristic of these layered materials is the weak interaction between the anions and the positive layers that occurs by electrostatic force.[85] Water molecules are also present in the interlayer domain establishing hydrogen bonds with the hydroxyl groups of the layers and with the intercalated anions. These bonds can constantly be broken and then reestablished as showed several studies of NMR and IR spectroscopies.[53, 86-87]

1.4.6 Symmetry/Polytypism

Naturally and synthetic occurring LDHs usually can be found in two polymorphic forms (see Figure 1.9), rhombohedral symmetry (denoted as 3R polytype) and hexagonal symmetry (denoted as 2H polytype).[27, 53, 88] In the rhombohedral form, $c = 3c_0$, while in the hexagonal form $c = 2c_0$ and the relation between cell parameters of both forms is $c_{hex} = (2/3)c_{rh}$ (hex = hexagonal and rh = rhombohedral). Although, it just possible to distinguish one form to another by powder X-Ray characterization because the two forms possess the same chemical composition and by thermogravimetry analysis they generate the same oxides.[89]

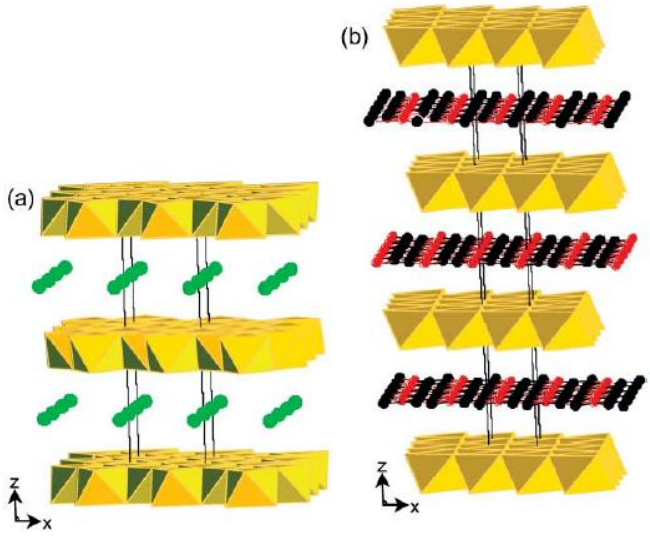

Figure 1.9 – Schematic representation of an LDH system showing the two polymorphic forms: a) hexagonal and b) rhombohedral.[53]

The polymorphic phases formed can be designated using a simple notation system. The single brucite layer can be represented as **AC** (OH groups occupy the **A** and **C** sites).[27, 43, 63] The arrangement of the brucite-like layers can be classified in two different ways, depending on how OH groups are oriented in the layers. A P-type arrangement is observed when the opposite

OH groups of neighboring layers lie above one another forming trigonal prisms while the O-type interlayer occurs when OH forms octahedra.[43, 63, 88, 90-91] The brucite can be represented as **AC**-**AC** or 1H, in which "1" corresponds to one-layer polytype and H to hexagonal symmetry. In the case of hexagonal form, each unit cell is constituted by two-layers of metal hydroxides represented by **BC**-**CB**-**BC** and for rhombohedral symmetry there are three-layers of metal hydroxides by unit per cell: **BC**-**CA**-**AB**-**BC**.[88] Thus, there are several possible stackings, either for hexagonal symmetry or rhombohedral one, depending if there is a P-type or an O-type arrangement in the brucite layers (see Figure 1.10). In the case of rhombohedral symmetry, as each unit cell has three-layers there are nine possible stackings that will not be discussed in detail.

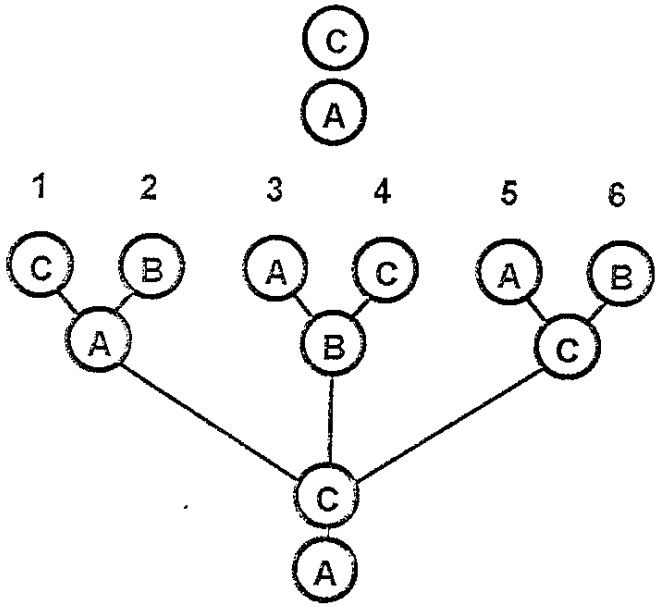

Figure 1.10 – Schematic representation of different stacking for hexagonal phase. The numbers indicate particular polytype.[27]

In Table 1.1 some examples of natural layered double hydroxides and their respective characterisitics are shown. Most naturally occurring LDHs are of rhombohedral symmetry; however, crystals containing both symmetry types have been discovered. Today a range of synthetic LDHs can be prepared as a single pure phase.[53]

Table 1.1 – List of chemical cmposition, symmetry, type of cations and anions of some natural layered double hydroxides.[27, 36, 39, 42, 92-96]

Mineral	M^{II}/M^{III}	Anion	Symmetry	Chemical composition
Natural Hydrotalcite	Mg/Al	CO_3^{2-}	Rhombohedral (3R)	$Mg_6Al_2(OH)_{16}(CO_3).4H_2O$
Manasseite			Hexagonal (2H)	
Pyroaurite	Mg/Fe	CO_3^{2-}	Rhombohedral (3R)	$Mg_6Fe_2(OH)_{16}(CO_3).4.5H_2O$
Sjögrenite			Hexagonal (2H)	
Stichtite	Mg/Cr	CO_3^{2-}	Rhombohedral (3R)	$Mg_6Cr_2(OH)_{16}(CO_3).4H_2O$
Barbertonite			Hexagonal (2H)	
Desaultesite	Mg/Mn	CO_3^{2-}	Rhombohedral (3R)	$Mg_6Mn_2(OH)_{16}(CO_3).4H_2O$
Takovite	Ni/Al	CO_3^{2-}	Rhombohedral (3R)	$Ni_6Al_2(OH)_{16}(CO_3,OH).4H_2O$
Reevesite	Ni/Fe	CO_3^{2-}	$3R_1$	$Ni_6Fe_2(OH)_{16}(CO_3).4H_2O$
Meixnerite	Mg/Al	OH^-	Rhombohedral (3R)	$[Mg_6Al_2(OH)_{16}](OH)_2.4H_2O$
Hydrocalumite	Ca/Al		Rhombohedral (3R)	$[Ca_8Al_4(OH)_{24}](CO_3)Cl_2(H_2O)_{1.6}.4H_2O$
Iowaite	Mg/Fe	Cl^-	Rhombohedral (3R)	$[Mg_6Fe_2(OH)_{16}](Cl_2).4H_2O$
Droninoite	Ni/Fe	Cl^-	(6R)	$[Ni_6Fe_2(OH)_{16}](Cl_2).4H_2O$
Woodallite	Mg/Cr	Cl^-	Rhombohedral (3R)	$[Mg_6Cr_2(OH)_{16}](Cl_2).4H_2O$
Jamborite*	Ni/Ni	S^{2-}	Hexagonal (2H)	$[Ni_6^{2+}Ni_2^{3+}(OH)_{16}](S^{2-}).4H_2O$
Quintinite	Mg/Al	CO_3^{2-}	2H/3R[a]	$[Mg_4Al_2(OH)_{12}](CO_3).3H_2O$
Woodwardite	Cu/Al	SO_4^{2-}	Rhombohedral (3R)	$[Cu_{1-x}Al_x(OH)_2](SO_4)_{x/2}.nH_2O$, x = 0.33-0.37 and n ≤ 0.5
Wermlandite	Mg/Al,Fe	SO_4^{2-}	Hexagonal (2H)	$[Mg_7Al_2(OH)_{18}][Ca(H_2O)_6](SO_4)_2.6H_2O$

* ideal formula because the coexistence of Ni^{3+} and S^{2-} is not usual

[a] Both polytypes exists in same mineral

1.4.7 Methods of synthesis

Layered double hydroxides can be synthesized by a wide range of compositions and a huge variety of different materials may be obtained due to several possible combinations of M^{2+} and M^{3+} cations, sometimes and more unusual M^{+} or M^{4+}, with different types of interlayer anions. The first LDH-like materials were prepared in the laboratory by Feitknecht, in 1942, a reaction of dilute aqueous metal salt solutions with a base.[37-38] There are several methods for the preparation of LDH materials taking in account the type of metals, the crystalline degree of the material, particle size and morphology of the crystals. The most common methods are the co-precipitation and anion exchange reaction.[27, 43-44] Although, there are different routes of preparation that are also suitable like the urea hydrolysis method, sol-gel technique,[97] recalcination-hydrothermal reaction, mechanochemical synthesis,[98] etc. The first requirement to obtain a pure LDH phase is to choose the appropriate cation to anion ratio in order to obey the final value $0.2 \leq x \leq 0.33$ and the anion to be intercalated should be in a higher concentration in the solution.[99] The selectivity of monovalent anions for LDHs varies in the order $OH^- > F^- > Cl^- > Br^- > NO_3^-$ while the divalent anions (SO_4^{2-} and CO_3^{2-}) have higher affinity than the former ones. Due to higher affinity of LDH for CO_3^{2-}, some care must be taken during the synthesis (no matter which is the preparation method) when the intercalated anion is different from carbonate, in order to avoid the contamination from CO_2. A way to solve or to minimize this is the use of decarbonated and deionized water during the synthesis and also keeping the mixture under nitrogen.[44]

1.4.7.1 Co-precipitation method

This method is the most used for the preparation of LDH and consists in the addition of aqueous solutions of divalent (or mixtures) and trivalent (or mixtures) metal salts containing the anion desired to be incorporated into the LDH. An alkaline solution is added, at the same time, in order to maintain the pH at a fixed value leading to the co-precipitation of the two metallic salts. In most cases, the metal salts are hydrated chloride or nitrate salts, for instance $MgCl_2.6H_2O$, $Mg(NO_3)_2.6H_2O$, $AlCl_3.6H_2O$, $Al(NO_3)_2.9H_2O$, etc.[52] The mechanism of the reaction consists in the condensation of hexa-aquo complexes in solution with the aim to form the brucite like-layers with a distribution of both metallic cations and with solvated interlamellar anions.[27]

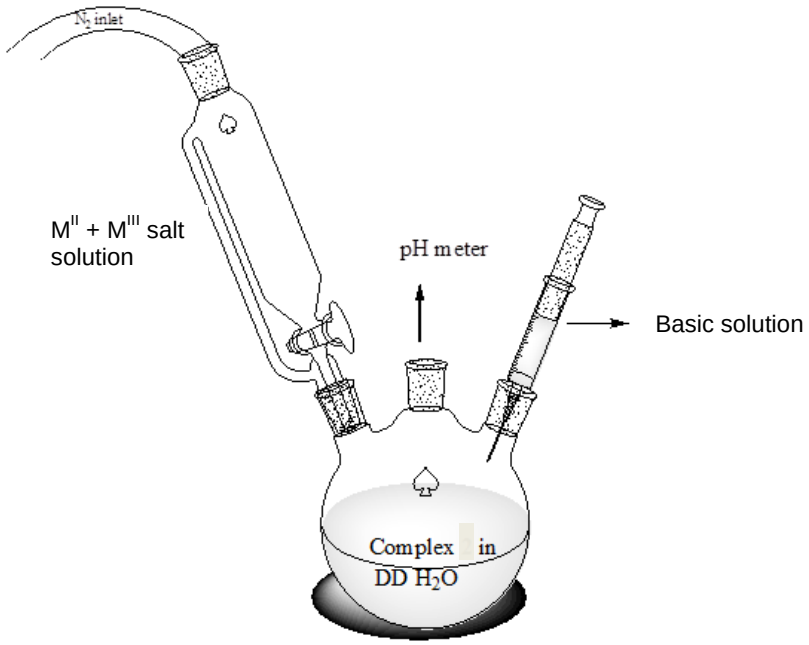

Figure 1.11 – Experimental setup for the preparation of LDHs by the co-precipitation low supersaturation method.

Several parameters such as temperature, pH of the reaction, concentration of metal salts solution, concentration of alkaline solution, flow rate of reactants and ageing of the precipitate can be controlled in an independent way during the synthesis and, depending on this, it is possible to obtain more or less well crystalized LDH phases.

In order to promote the precipitation of two or more cations, the synthesis has to be done in supersaturated environment. This can be achieved by physical (evaporation) or chemical (control of pH) methods.[99] The co-precipitation route can occur in a level of (i) low supersaturation or (ii) high supersaturation. The first one consists in the general procedure described above and the general experimental instrumentation is depicted in Figure 1.11. It is worth mentioning that the anions to be intercalated should be in excess otherwise it can exist competition with counter-anions of metal salts. The second method (ii) involves the addition of mixed divalent and trivalent metals solution to an alkaline solution with the desired interlayer anion but in this case without controlling the pH, which leads to a decrease in the crystallinity level of the materials formed. In conclusion, the method (i) presents more advantages because the possibility to control the pH allows the control of charge density of hydroxide layers and also the crystallinity of the obtained LDH materials.[43]

After the co-precipitation, and in order to obtain a higher degree of crystallinity of the amorphous and/or not so good crystallized materials, a thermal treatment is usually carried out and can be classified according to the temperature used. The traditional ageing method arises from heating the LDH suspension product at a temperature between 273-373 K for few hours or even several days. Hydrothermal treatment is the second possible method and consists on

heating the sample in a gold or silver capsule under high pressure (ranging between 10-150 MPa).[43, 100]

1.4.7.2 Ion exchange method

This method is useful when it is not possible to obtain LDH materials by the co-precipitation method due, for example, to the instability of divalent and trivalent cations or the anions in basic media. This synthetic route consists on the exchange of the guests with anions present in the interlayer regions of the LDHs precursors.[43] LDHs in nitrate form (i.e with NO_3^- as interlayer anion) are considered to be the most adequate precursors for the exchange and intercalation of a variety of anions, because of the less affinity of NO_3^- for the LDH galleries.[24, 97, 99] This technique is the best way to synthesize LDHs materials with anions other than carbonate, due to high affinity of carbonate anion for LDHs. There are several factors that should be considered to predict the capacity of ion exchange reaction such as (1) affinity for the desired intercalated anion, (2) exchange medium, (3) pH and (4) chemical composition of the layers. In (1) the exchange capacity increases with increasing charge and decreases with ionic radius; in (2) an aqueous medium favors the exchange of inorganic anions while organic solvents favors the substitution of organic anions;[44] in (3) a low pH value favors the release of the original anion as the conjugate acid of a less basic anion from solution and finally the point (4) influences the charge density of the layers and the hydration state which affect then the ion exchange process.

1.4.7.3 Calcination-rehydration method

This method consists on heating an LDH precursor at 300-500 ºC. Calcination of LDHs removes the interlayer water, the interlayer anions and the hydroxyl groups which results in a mixture of metal oxides. Then, the calcinated solid is able to regenerate the lamellar structure in water or in an aqueous solution of desired anions.[101-104] This method is also called “structural memory effect” or just “memory effect” and is usually used when the guests to be incorporated into LDH are too large. One advantage is that avoid the competitive intercalation of inorganic anions that come from metal salts. Although, this method is more complicated than previous ones described before and generally leads to the formation of amorphous materials.[43]

There are a wide variety of methods for the preparation of LDH-based materials. The method chosen will depend on the purpose for which LDH is to be used (Figure 1.12 for a summary of several methods). Here, it was described only the most common methods with specially focus on the co-precipitation because it was this one used for the synthesis of LDH compounds reported in this thesis.

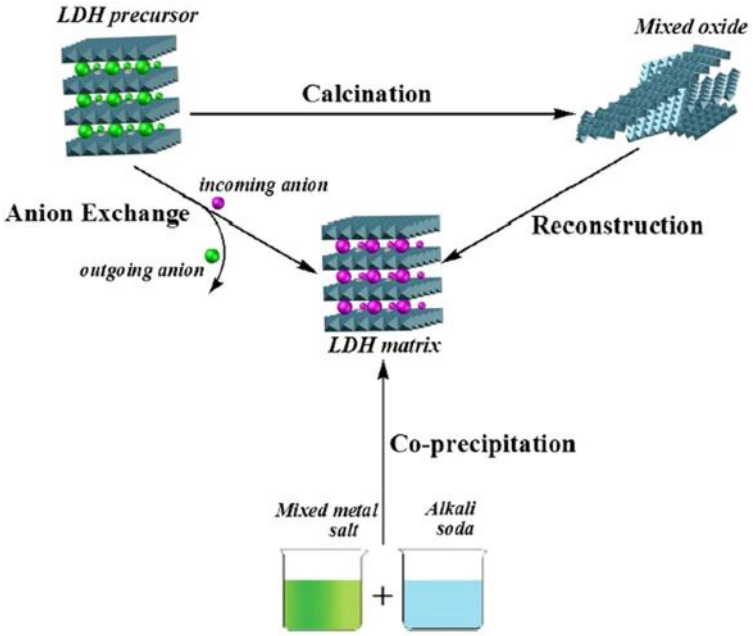

Figure 1.12 – Different methodologies for the preparation of LDHs materials.[11]

1.5 Layered Hydroxy Salts (LHSs)

Layered hydroxide salts or layered hydroxyl salts (LHS) are a subfamily of layered double hydroxides. LHS resemble LDH materials because they possess the same key structural characteristics. In this case, brucite layers can suffer other type of modifications – by isomorphic substitution of cations in the layers or by substitution of part of the hydroxide groups by appropriate anions or water molecules.[46] This kind of layered hosts have the general formula

$$[M^{2+}(OH)_{2-x}]^{x+}(A^{m-})_{x/m}.nH_2O$$

where M^{2+} is the divalent cation (e.g Zn^{2+}, Ni^{2+}, Ca^{2+}, Cd^{2+}, Mg^{2+}, Co^{2+} or Cu^{2+}) and A^{m-} is the interlayer anion (e.g NO_3^-, SO_4^{2-}, Cl^-, CO_3^{2-}, etc).[46, 105] LHSs could contain two types of divalent cations in the layers leading to the formation of the materials called “double hydroxide salts” (DHS). They can be described by the general formulation

$$[M^a_{1-y}M^b_y(OH)_{2-x}]^{x+}(A^{m-})_{x/m}.nH_2O$$

where M^a and M^b are the divalent cations.[46] Moreover, it is also possible to find LHS-based materials constituted by three different divalent metal cations.[106]

1.5.1 Structural features

LHS materials, like layered double hydroxides, are closely related anion-exchangeable materials with structure that can be derived from the brucite-type structure. The structure of LHS layers derives from the elimination of a quarter of M^{2+} cations in octahedral sites and their addition in tetrahedral sites at the bottom and top of each empty octahedron.[24, 46] Three vertices of each tetrahedron are occupied by hydroxide anions of the layer, while the fourth is occupied either by the interlayer anion or by water molecules, depending on the affinity of the interlayer anion for divalent cation.[107] This type of substitution introduces an additional divalent cation for each substitution without modifying the number of OH anions in the structure, being observed only small effects on the arrangement of hydroxide groups, which results in a positive charge for the layers.[108] The main type of interactions between the layers and interlayer anions are the electrostatic ones while in the case of the fourth vertices forming the base of tetrahedron, the anions are linked by a coordinate bond.[109] This depends on the synthesis conditions[110-111] and intercalated anion.[112] A schematic representation of an LHS structure is depicted in Figure 1.13.

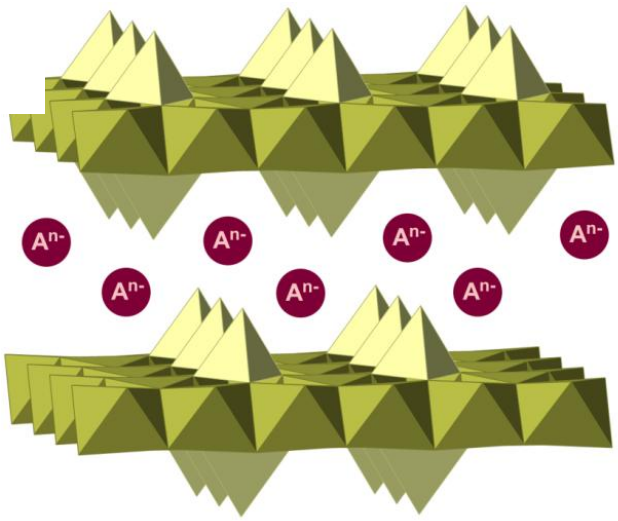

Figure 1.13 – Schematic representation of a LHS layer structure.

1.5.2 The Zinc Hydroxide Nitrate: $Zn_5(OH)_8(NO_3)_2{\cdot}2H_2O$

This material was first observed in 1970 by Stahlin *et al*.[113] where the authors reported for the first time the crystal structure of the material, in which one-fourth of the octahedral sites of brucite layers are vacant, generating a negative layer ($[Zn_3^{oct}(OH)_8]^{2-}$) and these empty octahedra are capped on either side by $\{Zn(OH)_3X\}$ tetrahedra. The apex (X) of the tetrahedra can be occupied either by water molecules, generating the formation of a positively charged layer ($[Zn_3^{oct}(OH)_8Zn_1^{tetr}(H_2O)_2]^{2+}$) as is the case with zinc hydroxide nitrate where unbound

charge-balancing nitrate ions occupy the interlayer (in which the symmetry D_{3h} is preserved), or by anions such as Cl^- as found for the mineral simonkolleite.

Another studies concerning LHS-based materials were also reported such as zinc hydroxide carbonate (hydrozincite)[114] and zinc hydroxide chloride monohydrate ($Zn_5(OH)_8Cl_2{\cdot}H_2O$, simonkolleite).[115-116] The former compound coordinates both to octahedral and tetrahedral sites while the latter chloride ion takes part in the tetrahedral coordination of zinc. Later on, Jones and his collaborators[24] synthesized several nitrate-LHS compounds with different divalent cation as Cu, Ni and La. Contrary to what was observed for zinc hydroxide nitrate, in the case of Cu and La hydroxide salts, the nitrate anion is directly coordinated to the matrix of cations, although they can also undergo anion exchange reaction.

1.5.3 Methods of preparation

There are many different ways to prepare layered hydroxide salts, depending on the type of material to be obtained. Coprecipitation route,[79, 99, 117-121] hydrolysis of salts and oxides,[113, 122-126] urea hydrolysis,[113, 127-128] are some of the methods that have been used.

1.5.3.1 Hydrolysis of salts of chosen metal

This method is also very common in the synthesis of LHS materials and is very similar to the coprecipitation one. In this procedure, the salt is used as starting material, which is dissolved in aqueous solution and the pH is controlled by the addition of a basic solution until precipitation occurs.[129]

1.5.3.2 Hydrolysis of metal oxide

In this case, metal oxide is dissolved in the solution of reaccional mixture containing the desired anions and pH is increased until precipitation occurs.[130-131] There are several reports concerning the intercalation of organic and inorganic anions using this methodology.[129, 131-133]

1.5.4 Comparison between LDH and LHS

There are more similarities between LDH and LHS materials, than differences. Both inorganic hosts can suffer modifications in the brucite-like sheets, although in the former is by isomorphic substitution of divalent cations by trivalent ones while in the latter, the brucite layers are composed only of divalent cations and a substitution of part of OH groups by appropriate anions or water molecules can occur. In LDH materials, electrostatic interactions are mainly present between the interlayer anions and the layers, while in LHS, the anions are linked through a coordinate bond. These aspects lead to different physicochemical properties.[109]

Both hosts can undergo exchange reactions but, due to different type of bonding, in the case of LHS is more appropriate to call ligand exchange reactions when the anions are attached through a coordinate bond, and not anion exchange reactions as in the case of LDHs.[134] LHS present a higher exchange sites density than LDH and the cation radii could be larger in comparison with LHS.[46] Due to the possibility to incorporate either organic or inorganic guests into the LDH or LHS galleries make of these materials useful for many applications such as in catalysis,[14, 66, 135-137] in environmental field,[138-141] energy applications,[142-143] in drug delivery,[11] cosmetics[3] and ophthalmics[8] and also in photochemistry area.[144-145]

The main purpose of this thesis was to obtain new novel organic-inorganic (OIH) hybrids with the interest on photochemical properties of organic dyes intercalated in the layer space of layered silicates. Some reports of photochemical applications will be given with some detail in Section 1.7.1 and 1.8. Although, before presenting several examples of applications of hybrid LDH and LHS in photochemistry, a few words are appropriate now concerning some theoretical aspects about photochemistry.

1.6 Light as a trigger of photochemical reactions

A photochemical reaction is a chemical reaction induced by light, resulting in the promotion of atoms or molecules from their ground state to excited state(s). With sun as main source of energy in the world we live in, there are several examples of photochemical light-driven processes such as photosynthesis, vision, biosynthesis of vitamin D, phototaxis (the ability of photosynthetic bacteria to swim selectively through illuminated areas avoiding the dark places), photoperiodism (physiological reaction of lived organisms to the length of day or night), etc. Photography, photopolymerization, photochromism (e.g photochromic sunglasses), electrophotography and laser technology are some examples of industrial applications of photochemical processes.[146-147] Photochemical and photophysical concepts have different meanings: the term photochemical is used when a chemical change (a breaking or making of chemical bond(s)) must occurs whereas photophysics is associated to the (physical) processes occurring during the excited state deactivation to the ground state.

The electromagnetic spectrum includes several types of radiation (X-rays, microwaves, radio waves, etc) besides the visible light, detectable by the human eye (see Figure 1.14). The range 200-400 nm is the ultraviolet (UV) radiation, 400-800 nm is the Visible (VIS) region and the near-infrared (NIR) is ca. 800-2000 nm.[148] The electronic spectra of most diatomic molecules are found in UV and/or Visible (Vis) region because the electronic energy levels are even more spaced than vibrational levels.

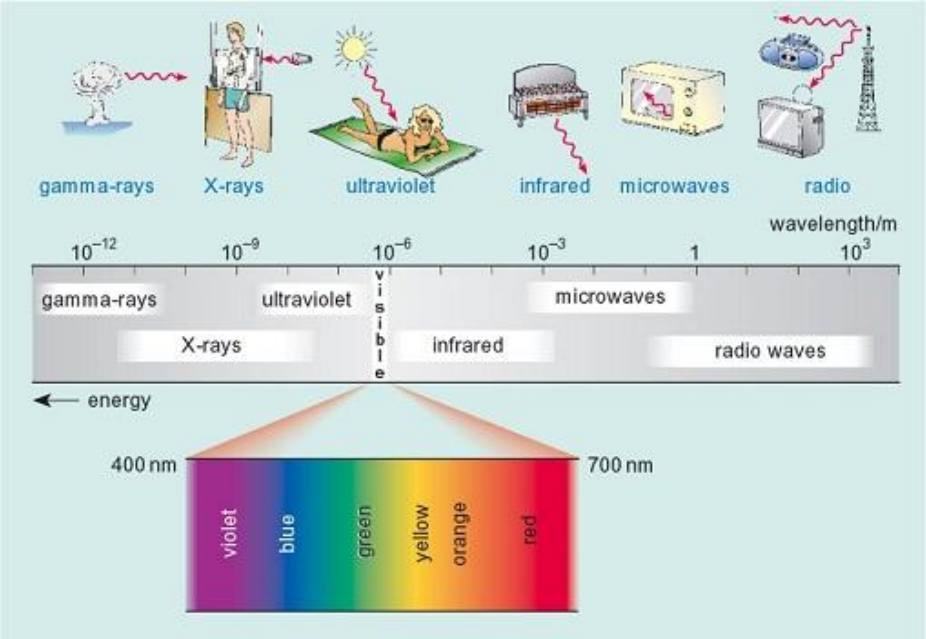

Figure 1.14 – Schematic representation of electromagnetic spectrum. Adapted from http://www.open.edu/openlearn/science-maths technology/science/healthsciences/forensicscience-and-fingerprints/content-section-1.3.2

Light and matter are intimately connected; several photochemical and photophysical processes occur when light interact with matter. When an incident beam ($\mathbf{I_0}$) of light reaches a material, some phenomenon does can occur: (**A**) Absorption; (**L**) Luminescence (emission of radiation in a form of fluorescence or phosphorescence); (**S**) Scattering (also known as diffuse reflection that consists in dispersion of light in different directions) and ($\mathbf{I_t}$) Transmission (Figure 1.15).

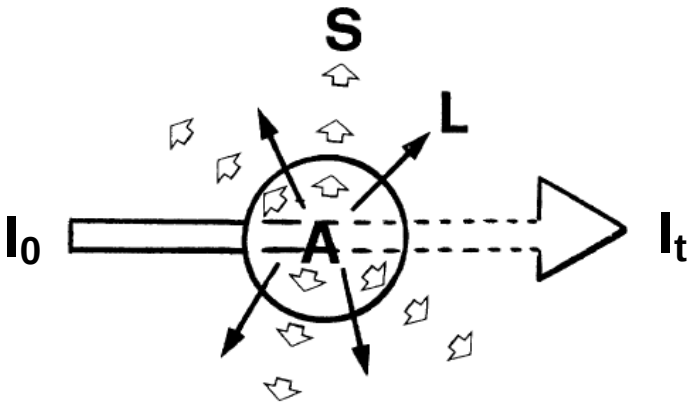

Figure 1.15 – Representation of different paths that light can take after reach a material. Adapted from ref[146].

1.6.1 The Jablonski-Périrrin Diagram

Chromophores are responsible for the absorption of light and are present in light-absorbing molecules.[149] The ability of a molecule to absorb more or less light can vary extensively from one molecule to another and the absorption can be measured by the molar absorption coefficient (ε), that is given by the Beer-Lambert law.

$$A = \varepsilon l c$$

The total energy of a molecule is the sum of the vibrational, rotational and electronic energies and, due to the large difference between them, it was stated that these can be treated separately as consider the Born-Oppenheimer approximation.[149] The Jablonski-Périrrin diagram is a typical diagram that is used to illustrate the photophysical processes that are associated to the decay upon absorption of light and is depicted in Figure 1.16.

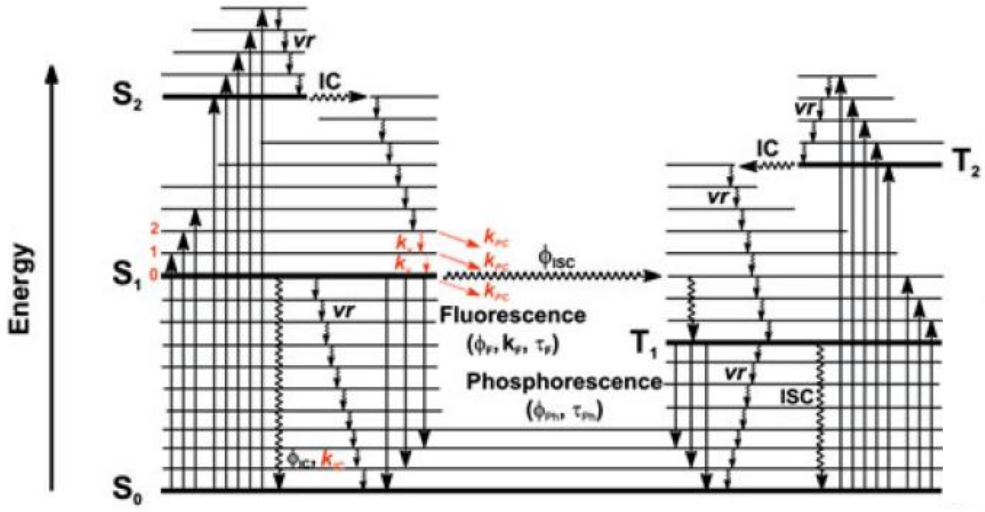

Figure 1.16 – A typical Jablonski-Périrrin diagram representing all the possible unimolecular photophysical processes upon excitation. Adapted from ref.[150]

A molecule with all electrons spin-paired possesses a total spin quantum number (S) equal to zero and a spin multiplicity (2S+1) equal to one and is in ground state, denoted as singlet, S_0. When this molecule is irradiated, electrons are promoted to the LUMO (Lowest Unoccupied Molecular Orbital) maintaining the same spin multiplicity and the excited state are now denoted as S_1, S_2, and so on. If the number of spin of the excited electron changes to one, an excited state with spin multiplicity value of 3 will be generated – triplet state denoted as T_1, T_2, etc. Each electronic state have associated several vibrational levels denoted as v = 0, v = 1, v = 2, and so on in order of increasing energy. This energy can be lost in the form of radiative

transitions (fluorescence or phosphorescence) or through non-radiative transitions (internal conversion, vibrational relaxation, intersystem crossing).

The fluorescence corresponds to the photon emission between states with the same multiplicity (is a spin-allowed transition) and generally occurs from the lowest vibrational level of lowest excited singlet state, S_1, according to Kasha's rule. The phosphorescence is the photon emission between states of different multiplicities, usually from the lowest vibrational level of the lowest excited triplet state, T_1 (is a spin-forbidden radiative transition, and therefore is much slower than spin-allowed transitions). Two important characteristics of the Jablonski-Pérrin diagram are (i) the spin-allowed transitions are represented as vertical lines whereas any spin-forbidden transition is shown as a horizontal line; (ii) the radiative transitions are represented by straight arrows while wavy arrows are used to represent the radiationless transitions.[146, 149] These transitions are the ones where no emission of electromagnetic radiation occurs during the deactivation process. Vibrational relaxation involves the deactivation of energy between vibrationally-excited state and the lowest vibrational level (v = 0) resulting from the collision of excited molecules with other species such as solvent molecules and the energy is dissipated as heat. The internal conversion involves the transition between isoenergetic vibrational excited states (levels with the same total energy) with the same spin multiplicity while intersystem crossing corresponds to the radiationless transitions between isoenergetic states with different multiplicity (is an intramolecular spin-forbidden transition).

1.6.1.1 Quenching

All the processes considered until now were unimolecular, which means that only one molecule is involved. Although, a bimolecular process consists in the collision between a molecule in the excited state S_1 and a quencher (Q). Any molecule that accelerate the rate of deactivation of an excited state is called a quencher and it's said that quench the excited-state, being this process known as quenching.[149]

1.6.1.2 Intermolecular electronic energy transfer

This process can be defined as being the transfer of energy of an excited state of a molecule (donor, D*) to another (acceptor, A) and can be described as

$$D^* + A \rightarrow D + A^*$$

If the energy transfer occur between molecules (i) with a spin multiplicity of 1, it's called a singlet-singlet energy transfer but if (ii) the spin multiplicity is equal to 3, it will be a triplet-triplet energy transfer and the equations proposed to defined the processes are

(i) $^1D^* + {}^1A \rightarrow {}^1D + {}^1A^*$

(ii) $^3D^* + {}^1A \rightarrow {}^1D + {}^3A^*$

The trivial mechanism is based in the absorption by A of the photon emitted by D*, so in terms of experimental conditions, the requirement is the overlap of the acceptor absorption spectrum with the donor emission spectrum.[149]

1.7 The photochemistry as a tool of prime importance in the characterization of O/I hybrids

Probably, the earliest problem that photochemists faced was the degradation of dyes induced by light.[146] Generally, organic molecules are “fragile” and by combining natural or synthetic dyes with the resistance of inorganic hosts, this can lead to the formation of hybrid materials with improved structural and chemical properties and higher stability. Maya blue (MB), an ancient pigment resulting from the interaction of indigo, a natural dye extracted from the leaves of añil (*Indigofera suffruticosa*), to a phyllosilicate clay, palygorskite, is generally considered to be the first man-made OIH nanocomposite.[21-23] It was widely used in mural paintings, pottery and sculptures by the ancient Mayas and other Mesoamerican cultures. This hybrid compound has a great stability and resistance towards several oxidizing and reducing agents, organic solvents, strong acids and alkalines and high temperatures.[23, 151-157] The extraordinary durability of MB[156] is due in part to the high intrinsic photostability of indigo which has been attributed to rapid and efficient internal conversion involving ultrafast intramolecular proton transfer.[158] In MB, the chemical and photochemical stability of indigo is enhanced even further by encapsulation of the dye molecules in the channels of the host. Investigations into the structure and properties of MB have inspired research on the synthesis of MB simulants and related organic-inorganic hybrid pigments.

There are several reports in literature concerning the intercalation of dyes in different hosts showing that dye-clays hybrids are more stable in terms of chemical,[159-160] photo[161] and thermal[162-163] properties when compared with dyes individually. The term intercalation is related with the reversible incorporation of guest molecules into layered hosts without changing the structural characteristics of the host.[164] The advantages of O/I hybrids are (i) the hosts provide a confined and stable environment for the guests; (ii) the establishment of host-guest interactions between the guest and host that can avoid dye aggregation and quenching phenomena; and (iii) the increase in the stability and performance of the guest species.[165] The photophysical and photochemical properties of the incorporated molecules can give information about the interlayer organization at a molecular level which make of these photoactive-based hybrids useful for solid-state dye laser application,[165] optical sensors, photo-induced switching and cell imaging.[166-167] Some examples of different studies in the last few years will be discussed briefly, focusing mainly on the intercalation of organic species into LDH and LHS inorganic matrices.

1.7.1 Photochemistry applications of LDH

Costantino and co-workers have shown in some reports that anionic dyes may be intercalated into the LDH galleries and/or adsorbed on the layer surface by a simple ion-exchange procedure,[168-171] where a in situ polymerization occurred into LDH[172] and also an evidence of photoinduced ionization process in the cavities of a Zn,Al LDH[173] together with a detailed photophysical characterization of the respective obtained hybrid materials. Moreover, they reported the co-intercalation of (i) a coumarin and anthracene derivatives and (ii) a naphthalene and benzoic acid derivatives compounds with donor-acceptor properties into Mg,Al LDH.[174] The results showed that (i) there was a strong dependence of fluorescence with the ratio of two guests and (ii) an energy transfer process seems to occur according to laser flash photolysis experiments. Another example with a more specific application was the storage of sunscreens in the interlayer region of LDHs in order to improve its photostability.[175] Some of the results are depicted in Figure 1.17 where is possible to conclude that the intercalation of solar screen in layered double hydroxides reduces the photodegradation process. The graphs on inset show that the free absorber has a faster decay when compared with the intercalated compounds.

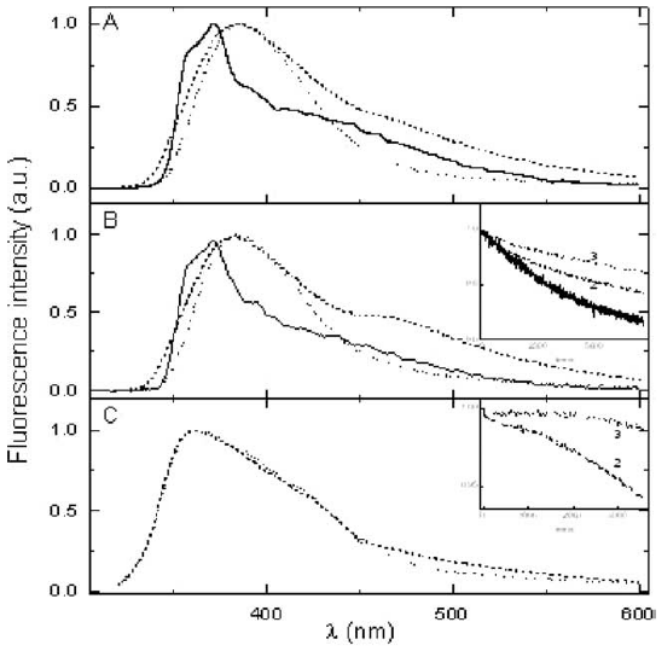

Figure 1.17 – Emission spectra of pure UV absorber (solid line), Mg,Al-absorber (dashed line) and Zn,Al-absorber (dotted line) before (A) and after (B) irradiation at 297 nm and in creams containing 10% of Mg,Al-absorber and Zn,Al-absorber (C); the inset shows the fluorescence kinetics of pure UV absorber (1), Mg,Al-absorber (2) and Zn,Al-absorber (3).[175]

Yan and his collaborators[176] published a report about the intercalation of a fluorescent anion, 2-[2-[4-[2-(4-carboxyphenyl)vinyl]phenyl]-vinyl]benzoate – abbreviated as CPBA, into the Zn,Al-NO_3 galleries by an anion-exchange method. The basal spacing for the new material Zn,Al-CPBA-LDH was ~ 29 Å indicating that occurred a successful substitution of NO_3 anions by the CPBA molecules and they were arranged in a perpendicular orientation relatively to LDH layers. The absorption results showed a blue shift when the CPBA was intercalated in the LDH due to the interactions between the guest and host layers (Figure 1.18). The steady-state fluorescence measurements showed that emission spectrum of Zn,Al-CPBA-LDH didn't changed when compared with pure CPBA while in excitation spectrum there was a shift from 364 (in CPBA) to 352 nm (in Zn,Al-CPBA-LDH) attributed to intermolecular interactions. Moreover, the fluorescence lifetime increased from 1.26 ns for CPBA to 4.83 ns in the intercalated material. These results showed that Zn,Al-CPBA-LDH, compared with pure CBPA, presented much better UV blocking properties with longer fluorescence lifetime and higher fluorescence quantum yield.

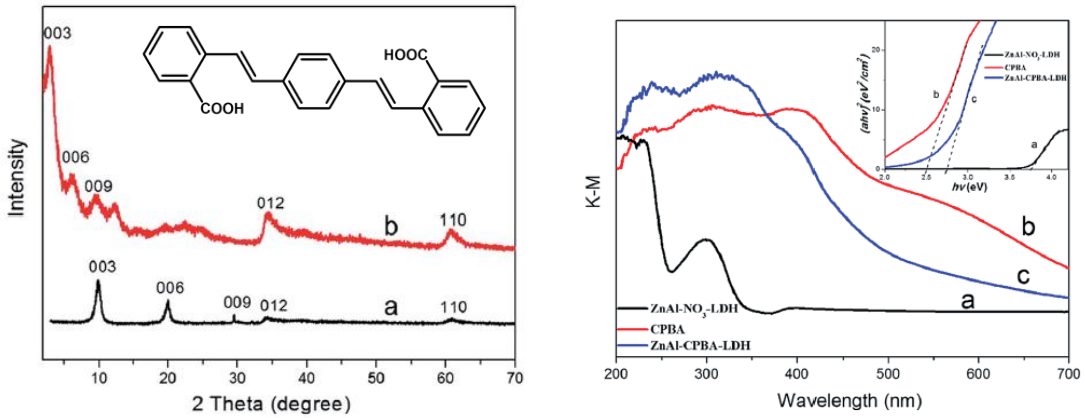

Figure 1.18 – XRD patterns (*left side*) of Zn,Al-NO_3-LDH (a) and Zn,Al-CPBA-LDH (b). UV-Vis diffuse reflectance (*right side*) spectra of Zn,Al-NO_3-LDH (a), CPBA (b) and Zn,Al-CPBA-LDH (c). Data from ref[176]

Another application of organic-inorganic hybrid assemblies is for sensor applications, in this case for the detection of nitroaromatic explosives as report the work of Ma *et al*.[177] The authors synthesized an organic-inorganic hybrid ultrathin film (UTF) material consisting on the incorporation of an optical brightener, a stilbene derivative abbreviated as BBU, into Mg,Al layered double hydroxide by the layer-by-layer (LBL) assembly technique. BBU molecule is constituted by four sulfonate and four hydroxyl groups, which make easier the assembly into LDH nanosheets. These researchers found that UTF's materials showed selective luminescence response to nitroaromatic compounds (nitrobenzene (NB), m-dinitrobenzene (*m*-DNB), 2,4-dinitrotoluene (DNT), trinitrotoluene (TNT), and picric acid (PA)) in methanol solutions with different concentrations. Particularly in the case of picric acid, the fluorescence emission

maximum suffered a red-shift (from 450 to 466 nm) together with a decrease in the fluorescence intensity with the PA concentration increase (see Figure 1.19e). It can be stated that the hybrid UTFs obtained can be applied as a polarized blue luminescent material and sensor film for the detection of nitroaromatic explosives.

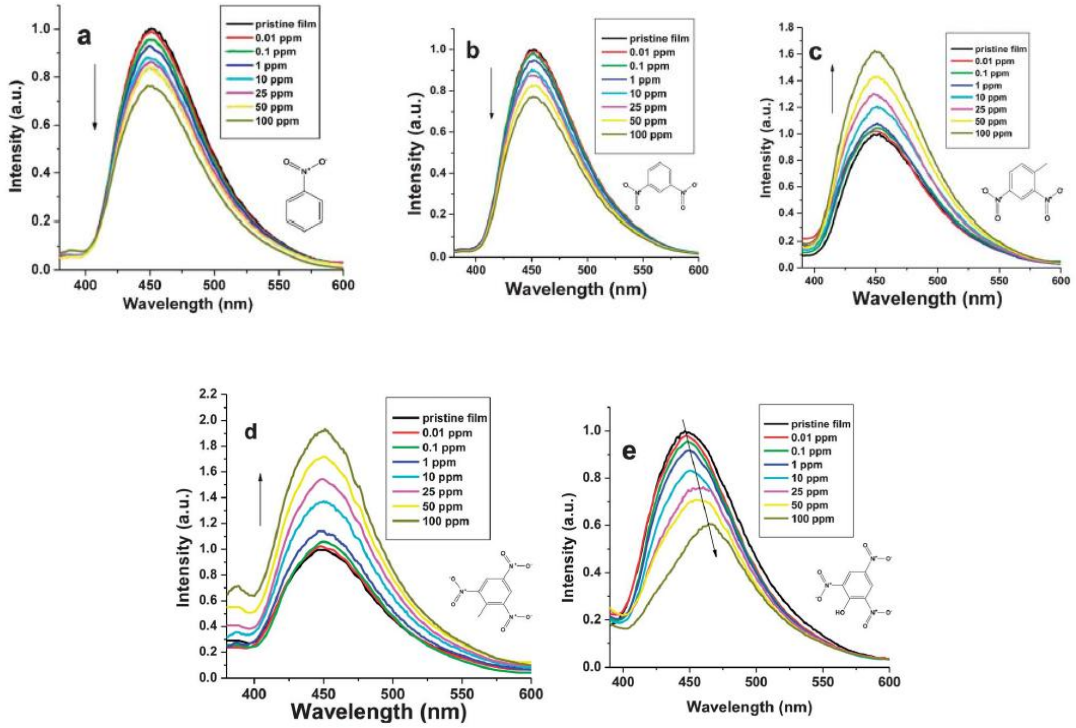

Figure 1.19 – Luminescent responses of the UTF to a) NB, b) *m*DNB, c) DNT, d) TNT and e) PA with different concentrations (adapted from ref[177])

From a luminescent efficiency point of view, the aggregates of luminescent molecules are usually instantaneously formed in the solid state, which can bring some problems as an emission shift, line broadening, and even luminescence quenching.[145] A way to solve or minimize this problem is the co-intercalation. The introduction of a surfactant leads to an enlarged interlayer spacing which facilitates the accommodation of the guest molecule; also, providing a more hydrophilic microenvironment which leads to an adjustment of the orientation of guest species depending on the loadings content of the surfactant, which further will have influence in the photophysical behavior.[178]

Li and co-workers[179] reported the successful co-intercalation of the luminescent tris(8-hydroxyquinoline-5-sulfonate)aluminum anions (AQS_3^-) and the surfactant dodecyl sulfonate (DDS^-) with different loadings into Mg-Al LDHs by the hydrothermal and co-precipitation routes. The as-prepared products were denominated as DDS-AQS(*x*%)/LDH and the structural and photophysical properties were investigated. The obtained XRD patterns of DDS-AQS(*x*%)/LDH samples confirmed the co-intercalation of surfactant and the luminescent probe. Moreover, a

thermal stability improvement of sodium tris(8-hydroxyquinoline-5-sulfonate)aluminum was observed when incorporated in the LDH galleries. The optical properties of these hybrids (Figure 1.20) showed that was possible to tune the photoluminescence intensity and lifetime by varying the guest content in which the optimal luminous intensity was found to the DDS-AQS(66.67%)/LDH hybrid material. A cyan to blue luminescence transition (from 450-470 nm, for Na_3AQS itself to 495 nm, when in LDH cavity) was observed due to the change of isomeric form meridianal to facial-AQS (*mer*- and *fac*-) driven by host-guest electrostatic interaction. These materials showed to have interesting properties for the fabrication of optoelectronic devices.

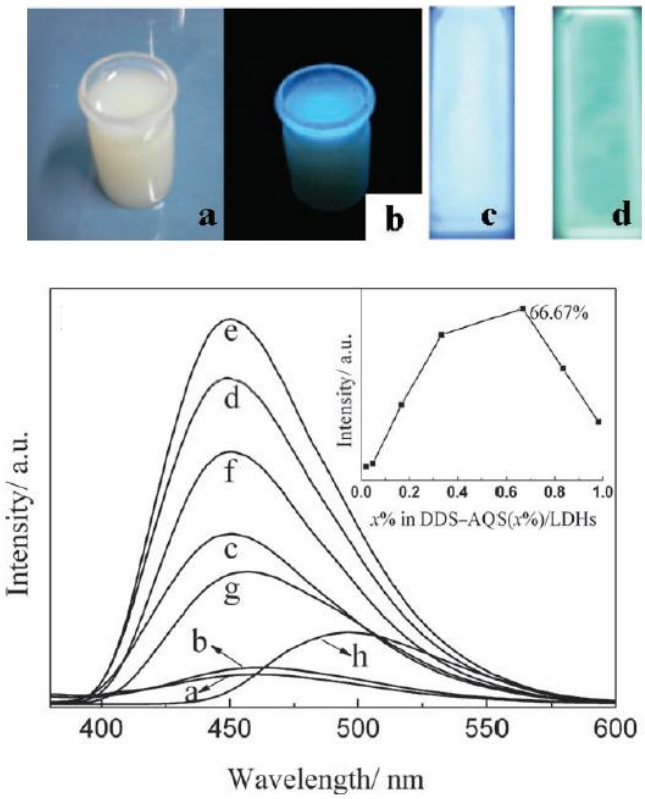

Figure 1.20 – (*Top panel*) Pictures of the material DDS-AQS(66.67%)/LDH suspension at a) daylight, b) under UV light, c) DDS-AQS(66.67%)/LDH and d) Na_3AQS film under UV light. (*Bottom panel*) Fluorescence emission spectra of DDS-AQS(*x*%)/LDH with *x*: a) 1.96, b) 4.76, c) 16.67, d) 33.33, e) 66.67, f) 83.33, g) 98.04 and h) Na_3AQS powder with λ_{exc} = 360 nm. The inset graph shows the intensity *vs.* content of AQS anions. From ref[179]

The introduction of two dyes in the same host can lead to materials with multicolor luminescence that have been considered great candidates for some applications related with light-emitting diodes (LEDs),[180] optoelectronic devices,[181] and so on. For this reason, some literature has reporting several studies concerning the co-intercalation of different chromophores simultaneously. Shi and collaborators[182] reported a multiple and configurable

optical systems based on layered double hydroxides. The work consisted on the incorporation of three chromophores (sulfonated poly(*p*-phenylene), APPP, fluorescein (FLU) and ethidium bromide (EB)) that were used as model chromophores due to their dual FRET property (Figure 1.21). In the case of EB cation, DNA was employed as the building unit for the assembly on LDHs and also as a support for the intercalation of EB. A multiple and configurable system of APPP/LDH-FLU/DNA-EB)$_n$ ultrathin films were achieved and a phenomenon of a dual FRET was observed in a two-step sequence: energy transfer from APPP to FLU, followed from another transfer process from FLU to EB. Based on fluorescence emissions of each chromophore - APPP, FLU and EB – it was possible to integrate, simultaneously, multiple logic responses in pararell. Moreover, these devices showed a great photo- and storage stability and also a good reproducibility.

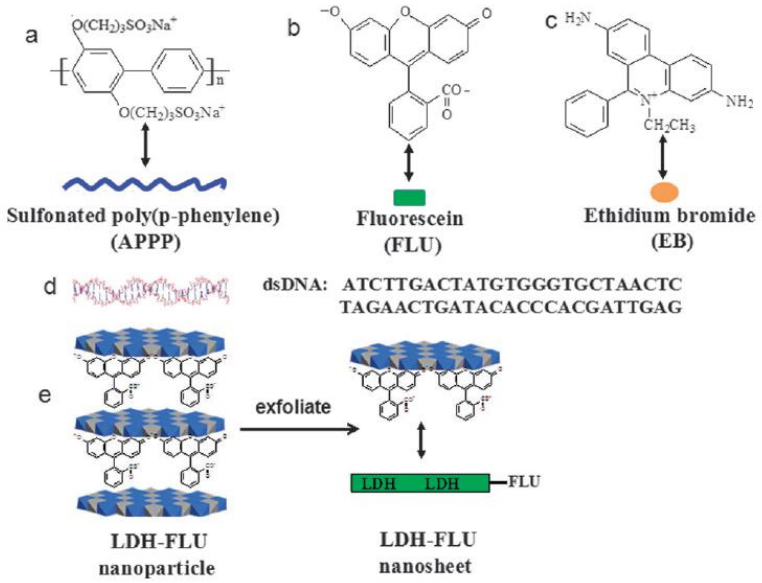

Figure 1.21 – Chemical structures of a) APPP, b) FLU, c) EB, d) DNA sequence of nucleotides and e) the chromophore FLU in the LDH layers. From ref[182]

1.8 The little-known studies of LHS as hosts for organic species

In comparison with LDHs, the analogue hydroxy salts are much fewer reported in the literature than the former ones. Due to the lack of scientific information in these type of inorganic hosts, Cursino *et al*.[183] published for the first time the intercalation of active UV absorbers into layered hydroxy salts cavities (contrary to found for LDHs) in order to evaluate the possibility to use them as matrixes for immobilization of negatively organic species with UV absorption capacity. These authors chose the organic UV-absorbents – 2-mercaptobenzoic acid, 2-aminobenzoic acid and 4-aminobenzoic acid - to incorporate between the layers by anion-exchange or coprecipitation methods. The new materials showed good UV absorption capacity, thermal stability and the UV properties improved when compared to the isolated organic

species. It is noteworthy to notice the case of 4-aminobenzoic acid, that usually degrades to nitrosamine, a product with potential carcinogenic effects; the intercalation in these inorganic matrixes bring a new alternative to avoid the degradation (see Figure 1.23).

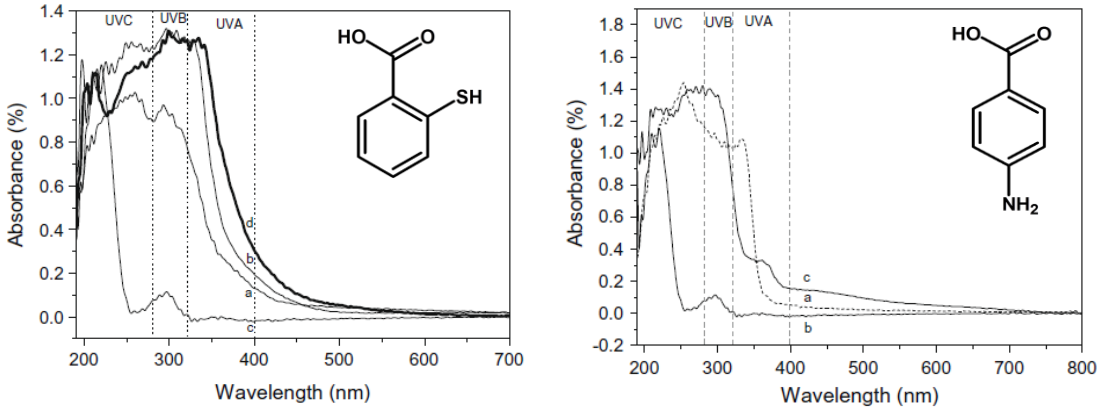

Figure 1.23 – Solid state UV-Vis absorbance spectra of (*Left side*) a) 2-mercaptobenzoic acid, b) sodium 2-mercaptobenzoate, c) Zn-NO_3 LHS and d) Zn-MB LHS; (*Right side*) a) 4-aminobenzoic acid, b) Zn-NO_3 LHS and c) Zn-4AB LHS. Adapted from ref[183]

Later on, the same authors reported a similar study concerning the intercalation of 2-aminobenzoate anion into layered hydroxyl salts doped with rare earth (RE) ions.[184] Zinc, europium (Eu^{3+}), yttrium (Y^{3+}) and terbium (Tb^{3+}) hydroxide nitrate were successfully prepared and after they were used to exchange the nitrate anion by 2-aminobenzoate anion which was also done successfully because the interlayer distances of all materials increased. It was shown that 2-aminobenzoate anion was linked to the layers through carboxylate bridge between the two metal ions of the layer.

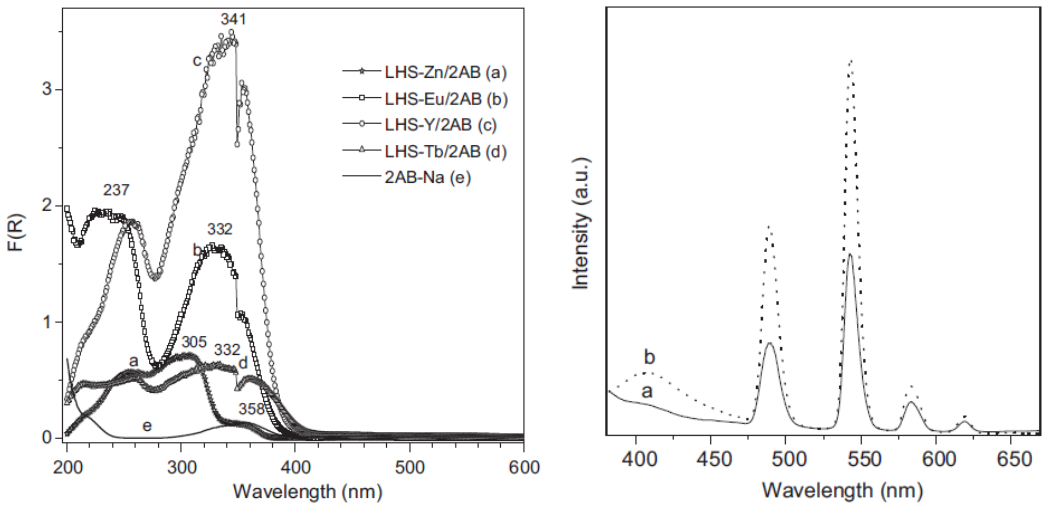

Figure 1.24 – (*Left side*) Diffuse reflectance UV-Vis spectra of intercalated LHS (*Right side*) Fluorescence emission spectra with λ_{exc} = 352 nm of a) LHS-Tb/NO_3 and b) LHS-Tb/2AB.[184]

The photophysical characterization (in Figure 1.24) showed that the 2-aminobenzoate anion enhanced the luminescence of terbium and decreased the emission intensity of Eu^{3+}. The photoluminescence measurements presented a strong blue and green luminescence under UV light excitation for the materials with Y and Tb, respectively. In conclusion, this strategy of doping the layered materials with lanthanide ions can be a good alternative for immobilization of organic species in order to obtain new photofunctional materials with luminescent characteristics.

1.9 References

1. Sanchez, C.; Arribart, H.; Giraud Guille, M. M., Biomimetism and bioinspiration as tools for the design of innovative materials and systems. *Nat Mater* **2005,** *4* (4), 277.
2. Bensaude-Vincent, B.; Arribart, H.; Bouligand, Y.; Sanchez, C., Chemists and the school of nature. *New Journal of Chemistry* **2002,** *26* (1), 1.
3. Sanchez, C.; Julian, B.; Belleville, P.; Popall, M., Applications of hybrid organic-inorganic nanocomposites. *Journal of Materials Chemistry* **2005,** *15* (35-36), 3559.
4. Mann, S., *Biomimetic Materials Chemistry*. Wiley-VCH: Weinheim, **1997**.
5. José-Yacamán, M.; Rendón, L.; Arenas, J.; Puche, M. C. S., Maya Blue Paint: An Ancient Nanostructured Material. *Science* **1996,** *273* (5272), 223.
6. Van Olphen, H., Maya Blue: A Clay-Organic Pigment? *Science* **1966,** *154* (3749), 645.
7. Geppi, M.; Borsacchi, S.; Mollica, G.; Veracini, C. A., Applications of Solid-State NMR to the Study of Organic/Inorganic Multicomponent Materials. *Applied Spectroscopy Reviews* **2008,** *44* (1), 1.
8. Sanchez, C.; Belleville, P.; Popall, M.; Nicole, L., Applications of advanced hybrid organic-inorganic nanomaterials: from laboratory to market. *Chemical Society Reviews* **2011,** *40* (2), 696.
9. Kickelbick, G., Introduction to Hybrid Materials. In *Hybrid Materials*, Wiley-VCH Verlag GmbH & Co. KGaA: 2007; pp 1-48.
10. Sanchez, C., State of the art developments in functional hybrid materials. *Journal of Materials Chemistry* **2005,** *15* (35-36), 3557.
11. Allou, N. g. B.; Saikia, P.; Borah, A.; Goswamee, R. L., Hybrid nanocomposites of layered double hydroxides: an update of their biological applications and future prospects. *Colloid and Polymer Science* **2017,** *295* (5), 725.
12. Song, N.; Yang, Y.-W., Molecular and supramolecular switches on mesoporous silica nanoparticles. *Chemical Society Reviews* **2015,** *44* (11), 3474.
13. Bhattacharyya, K. G.; Gupta, S. S., Adsorption of a few heavy metals on natural and modified kaolinite and montmorillonite: A review. *Advances in Colloid and Interface Science* **2008,** *140* (2), 114.

14. Nakagaki, S.; Mantovani, K.; Sippel Machado, G.; Dias de Freitas Castro, K.; Wypych, F., Recent Advances in Solid Catalysts Obtained by Metalloporphyrins Immobilization on Layered Anionic Exchangers: A Short Review and Some New Catalytic Results. *Molecules* **2016,** *21* (3), 291.

15. Roth, W. J.; Gil, B.; Makowski, W.; Marszalek, B.; Eliasova, P., Layer like porous materials with hierarchical structure. *Chemical Society Reviews* **2016,** *45* (12), 3400.

16. Kerativitayanan, P.; Carrow, J. K.; Gaharwar, A. K., Nanomaterials for Engineering Stem Cell Responses. *Advanced Healthcare Materials* **2015,** *4* (11), 1600.

17. Dawson, J. I.; Oreffo, R. O. C., Clay: New Opportunities for Tissue Regeneration and Biomaterial Design. *Advanced Materials* **2013,** *25* (30), 4069.

18. Ma, R.; Sasaki, T., Two-Dimensional Oxide and Hydroxide Nanosheets: Controllable High-Quality Exfoliation, Molecular Assembly, and Exploration of Functionality. *Accounts of Chemical Research* **2015,** *48* (1), 136.

19. Chimene, D.; Alge, D. L.; Gaharwar, A. K., Two-Dimensional Nanomaterials for Biomedical Applications: Emerging Trends and Future Prospects. *Advanced Materials* **2015,** *27* (45), 7261.

20. Bernardino, N. D.; Brown-Xu, S.; Gustafson, T. L.; de Faria, D. L. A., Time-Resolved Spectroscopy of Indigo and of a Maya Blue Simulant. *The Journal of Physical Chemistry C* **2016,** *120* (38), 21905.

21. Domenech-Carbo, A.; Teresa Domenech-Carbo, M.; Manuel Valle-Algarra, F.; Domine, M. E.; Osete-Cortina, L., On the dehydroindigo contribution to Maya Blue. *Journal of Materials Science* **2013,** *48* (20), 7171.

22. Lima, E.; Guzmán, A.; Vera, M.; Rivera, J. L.; Fraissard, J., Aged Natural and Synthetic Maya Blue-Like Pigments: What Difference Does It Make? *The Journal of Physical Chemistry C* **2012,** *116* (7), 4556.

23. Domenech, A.; Domenech-Carbo, M. T.; Sanchez del Rio, M.; Vazquez de Agredos Pascual, M. L.; Lima, E., Maya Blue as a nanostructured polyfunctional hybrid organic-inorganic material: the need to change paradigms. *New Journal of Chemistry* **2009,** *33* (12), 2371.

24. Newman, S. P.; Jones, W., Comparative Study of Some Layered Hydroxide Salts Containing Exchangeable Interlayer Anions. *Journal of Solid State Chemistry* **1999,** *148* (1), 26.

25. O'Hare, D., *Inorganic Materials*. John Wiley & Sons Ltd: West Sussex, England **1997**.

26. Geng, F.; Ma, R.; Sasaki, T., Anion-Exchangeable Layered Materials Based on Rare-Earth Phosphors: Unique Combination of Rare-Earth Host and Exchangeable Anions. *Accounts of Chemical Research* **2010,** *43* (9), 1177.

27. Rives, V., *Layered Double Hydroxides: Present and Future*. Nova Science Publishers, Inc: **2001**.

28. Hochstetter, C., Untersuchung über die Zusammensetzung einiger Mineralien. *Journal für Praktische Chemie* **1842,** *27* (1), 375.

29. Dana, J. D., *Am. Jour. Sci* **1851,** *12*.

30. Hermann, R., Untersuchungen russischer Mineralien. *Journal für Praktische Chemie* **1847,** *40* (1), 7.

31. Tschermak, G., *Lehrbuch der Mineralogie*. 2nd ed.; Vienna, **1905**.

32. Naumann, C. F., *Elemente der Mineralogie*. Leipzig, **1898**.

33. Bauer, M., *Lehrbuch der Mineralogie*. Berlin, **1904**.

34. Hintze, C., *Handbuch der Mineralogie*. Leipzig, **1910**.

35. Manasse, E., *Atti Soc. Toscana Sci. Nat* **1915,** *24*, 92.

36. Frondel, C., *American Mineralogist* **1941,** *26*, 295.

37. Feitknecht, W.; Gerber, M., Zur Kenntnis der Doppelhydroxyde und basischen Doppelsalze II. Über Mischfällungen aus Calcium-Aluminiumsalzlösungen. *Helvetica Chimica Acta* **1942,** *25* (1), 106.

38. Feitknecht, W.; Gerber, M., Zur Kenntnis der Doppelhydroxyde und basischen Doppelsalze III. Über Magnesium-Aluminiumdoppelhydroxyd. *Helvetica Chimica Acta* **1942,** *25* (1), 131.

39. Allmann, R., The crystal structure of pyroaurite. *Acta Crystallographica Section B* **1968,** *24* (7), 972.

40. Taylor, H. F. W., *Mineralogical magazine* **1969,** *37*, 287.

41. Taylor, H. F. W., *Mineralogical magazine,* **1973,** *39*, 304.

42. Mills, S. J.; Christy, A. G.; Génin, J.-M. R.; Kameda, T.; Colombo, F., Nomenclature of the hydrotalcite supergroup: natural layered double hydroxides. *Mineralogical Magazine* **2012,** *76* (5), 1289.

43. Duan, X.; Evans, D. G., *Layered Double Hydroxides*. Springer: **2006**.

44. P. Newman, S.; Jones, W., Synthesis, characterization and applications of layered double hydroxides containing organic guests. *New Journal of Chemistry* **1998,** *22* (2), 105.

45. Pesic, L.; Salipurovic, S.; Markovic, V.; Vucelic, D.; Kagunya, W.; Jones, W., Thermal characteristics of a synthetic hydrotalcite-like material. *Journal of Materials Chemistry* **1992,** *2* (10), 1069.

46. Arizaga, G. G. C.; Satyanarayana, K. G.; Wypych, F., Layered hydroxide salts: Synthesis, properties and potential applications. *Solid State Ionics* **2007,** *178* (15–18), 1143.

47. Greaves, C.; Thomas, M. A., Refinement of the structure of deuterated nickel hydroxide, Ni(OD)2, by powder neutron diffraction and evidence for structural disorder in samples with high surface area. *Acta Crystallographica Section B* **1986,** *42* (1), 51.

48. Zigan, F.; Rothbauer, R., *Neus Jahrb. Miner. Monatsh* **1967**, 137.

49. Rives, V.; Angeles Ulibarri, M. a., Layered double hydroxides (LDH) intercalated with metal coordination compounds and oxometalates. *Coordination Chemistry Reviews* **1999,** *181* (1), 61.

50. Salomão, R.; Milena, L. M.; Wakamatsu, M. H.; Pandolfelli, V. C., Hydrotalcite synthesis via co-precipitation reactions using MgO and Al(OH)3 precursors. *Ceramics International* **2011,** *37* (8), 3063.

51. Mills, S. J.; Hatert, F.; Nickel, E. H.; Ferraris, G., The standardisation of mineral group hierarchies: application to recent nomenclature proposals. *European Journal of Mineralogy* **2009,** *21* (5), 1073.

52. Theiss, F. L.; Ayoko, G. A.; Frost, R. L., Synthesis of layered double hydroxides containing Mg2+, Zn2+, Ca2+ and Al3+ layer cations by co-precipitation methods—A review. *Applied Surface Science* **2016,** *383*, 200.

53. Khan, A. I.; O'Hare, D., Intercalation chemistry of layered double hydroxides: recent developments and applications. *Journal of Materials Chemistry* **2002,** *12* (11), 3191.

54. Rives, V., Characterisation of layered double hydroxides and their decomposition products. *Materials Chemistry and Physics* **2002,** *75* (1–3), 19.

55. Serna, C. J.; Rendon, J. L.; Iglesias, J. E., Crystal-chemical study of layered [Al ₂ Li(OH) ₆] ^{PL} X (super -) .nH ₂ O. *Clays and Clay Minerals* **1982,** *30* (3), 180.

56. Chisem, I. C.; Jones, W., Ion-exchange properties of lithium aluminium layered double hydroxides. *Journal of Materials Chemistry* **1994,** *4* (11), 1737.

57. Besserguenev, A. V.; Fogg, A. M.; Francis, R. J.; Price, S. J.; O'Hare, D.; Isupov, V. P.; Tolochko, B. P., Synthesis and Structure of the Gibbsite Intercalation Compounds [LiAl2(OH)6]X {X = Cl, Br, NO3} and [LiAl2(OH)6]Cl·H2O Using Synchrotron X-ray and Neutron Powder Diffraction. *Chemistry of Materials* **1997,** *9* (1), 241.

58. Fogg, A. M.; Dunn, J. S.; O'Hare, D., Formation of Second-Stage Intermediates in Anion-Exchange Intercalation Reactions of the Layered Double Hydroxide [LiAl2(OH)6]Cl·H2O As Observed by Time-Resolved, in Situ X-ray Diffraction. *Chemistry of Materials* **1998,** *10* (1), 356.

59. Velu, S.; Suzuki, K.; Okazaki, M.; Osaki, T.; Tomura, S.; Ohashi, F., Synthesis of New Sn-Incorporated Layered Double Hydroxides and Their Thermal Evolution to Mixed Oxides. *Chemistry of Materials* **1999,** *11* (8), 2163.

60. Velu, S.; Suzuki, K., Synthesis and characterization of a new Sn-incorporated CoAl-layered double hydroxide (LDH) and catalytic performance of Co-spinel microcrystallites in the partial oxidation of methanol. In *Studies in Surface Science and Catalysis*, Abdelhamid, S.; Mietek, J., Eds. Elsevier: 2000; Vol. Volume 129, pp 451.

61. Velu, S.; Suzuki, K.; Kapoor, M. P.; Tomura, S.; Ohashi, F.; Osaki, T., Effect of Sn Incorporation on the Thermal Transformation and Reducibility of M(II)Al-Layered Double Hydroxides [M(II) = Ni or Co]. *Chemistry of Materials* **2000,** *12* (3), 719.

62. Radoslovich, E. W., *American Mineralogist* **1963,** *48*, 76.

63. Bookin, A. S.; Drits, V. A., Polytype diversity of the hydrotalcite-like minerals; I, Possible polytypes and their diffraction features. *Clays and Clay Minerals* **1993,** *41* (5), 551.

64. Vucelic, M.; Jones, W.; Moggridge, G. D., Cation ordering in synthetic layered double hydroxides. *Clays and Clay Minerals* **1997,** *45* (6), 803.

65. Fan, G.; Li, F.; Evans, D. G.; Duan, X., Catalytic applications of layered double hydroxides: recent advances and perspectives. *Chemical Society Reviews* **2014,** *43* (20), 7040.

66. Yan, K.; Wu, G.; Jin, W., Recent Advances in the Synthesis of Layered, Double-Hydroxide-Based Materials and Their Applications in Hydrogen and Oxygen Evolution. *Energy Technology* **2016,** *4* (3), 354.

67. Bellotto, M.; Rebours, B.; Clause, O.; Lynch, J.; Bazin, D.; Elkaïm, E., A Reexamination of Hydrotalcite Crystal Chemistry. *The Journal of Physical Chemistry* **1996,** *100* (20), 8527.

68. Bourrié, G.; Trolard, F.; Refait, P.; Feder, F., A solid-solution model for Fe(ii)-Fe(iii)-Mg(ii) green rusts and fougerite and estimation of their gibbs free energies of formation. *Clays and Clay Minerals* **2004,** *52* (3), 382.

69. Brindley, G. W.; Kikkawa, S., Thermal behavior of hydrotalcite and of anion-exchanged forms of hydrotalcite. *Clays and Clay Minerals* **1980,** *28* (2), 87.

70. Miyata, S., Anion-exchange properties of hydrotalcite-like compounds. *Clays and Clay Minerals* **1983,** *31* (4), 305.

71. Drezdzon, M. A., Synthesis of isopolymetalate-pillared hydrotalcite via organic-anion-pillared precursors. *Inorganic Chemistry* **1988,** *27* (25), 4628.

72. Chibwe, K.; Jones, W., Synthesis of polyoxometalate pillared layered double hydroxides via calcined precursors. *Chemistry of Materials* **1989,** *1* (5), 489.

73. Twu, J.; Dutta, P. K., Decavanadate ion-pillared hydrotalcite: spectroscopic studies of the thermal decomposition process. *Journal of Catalysis* **1990,** *124* (2), 503.

74. Narita, E.; Kaviratna, P. D.; Pinnavaia, T. J., Direct synthesis of a polyoxometallate-pillared layered double hydroxide by coprecipitation. *Journal of the Chemical Society, Chemical Communications* **1993,** (1), 60.

75. Ulibarri, M. A.; Labajos, F. M.; Rives, V.; Kagunya, W.; Jones, W.; Trujillano, R., Effect of Intermediates on the Nature of Polyvan-adate-Intercalated Layered Double Hydroxides. *Molecular Crystals and Liquid Crystals Science and Technology. Section A. Molecular Crystals and Liquid Crystals* **1994,** *244* (1), 167.

76. Wang, J. D.; Serrette, G.; Tian, Y.; Clearfield, A., Synthetic and catalytic studies of inorganically pillared and organically pillared layered double hydroxides. *Applied Clay Science* **1995,** *10* (1–2), 103.

77. Evans, J.; Pillinger, M.; Zhang, J., Structural studies of polyoxometalate-anion-pillared layered double hydroxides. *Journal of the Chemical Society, Dalton Transactions* **1996,** (14), 2963.

78. Weir, M. R.; Moore, J.; Kydd, R. A., Effects of pH and Mg:Ga Ratio on the Synthesis of Gallium-Containing Layered Double Hydroxides and Their Polyoxometalate Anion Exchanged Products. *Chemistry of Materials* **1997,** *9* (7), 1686.

79. Miyata, S.; Kumura, T., SYNTHESIS OF NEW HYDROTALCITE-LIKE COMPOUNDS AND THEIR PHYSICO-CHEMICAL PROPERTIES. *Chemistry Letters* **1973,** *2* (8), 843.

80. Chibwe, K.; Jones, W., Intercalation of organic and inorganic anions into layered double hydroxides. *Journal of the Chemical Society, Chemical Communications* **1989,** (14), 926.

81. Dutta, P. K.; Puri, M., Anion exchange in lithium aluminate hydroxides. *The Journal of Physical Chemistry* **1989,** *93* (1), 376.

82. Schutz, A.; Biloen, P., Interlamellar chemistry of hydrotalcites: I. Polymerization of silicate anions. *Journal of Solid State Chemistry* **1987,** *68* (2), 360.

83. Yun, S. K.; Costantino, V. R. L.; Pinnavaia, T. J., *Clays and Clay Minerals* **1995,** *43*, 503.

84. Depège, C.; El Metoui, F.-Z.; Forano, C.; de Roy, A.; Dupuis, J.; Besse, J.-P., Polymerization of Silicates in Layered Double Hydroxides. *Chemistry of Materials* **1996,** *8* (4), 952.

85. Omwoma, S.; Chen, W.; Tsunashima, R.; Song, Y.-F., Recent advances on polyoxometalates intercalated layered double hydroxides: From synthetic approaches to functional material applications. *Coordination Chemistry Reviews* **2014,** *258–259*, 58.

86. Marcelin, G.; Stockhausen, N. J.; Post, J. F. M.; Schutz, A., Dynamics and ordering of intercalated water in layered metal hydroxides. *The Journal of Physical Chemistry* **1989,** *93* (11), 4646.

87. Miyata, S., *Clays and Clay Minerals* **1975,** *23*, 369.

88. Thevenot, F.; Szymanski, R.; Chaumette, P., Preparation and characterization of Al-rich Zn-Al hydrotalcite-like compounds. *Clays and Clay Minerals* **1989,** *37* (5), 396.

89. Vaccari, A., Preparation and catalytic properties of cationic and anionic clays. *Catalysis Today* **1998,** *41* (1), 53.

90. Rives, V., *Layered double hydroxides: present and future. Nova Science Pub Incorporated*. Nova Science Publishers Inc: New York, **2001**.

91. Vucelic, M.; Moggridge, G. D.; Jones, W., Thermal Properties of Terephthalate- and Benzoate-Intercalated LDH. *The Journal of Physical Chemistry* **1995,** *99* (20), 8328.

92. Drits, V. A.; Sokolova, T. N.; Sokolova, G. V.; Cherkashin, V. I., New members of the hydrotalcite-manasseite group. *Clays and Clay Minerals* **1987,** *35* (6), 401.

93. Bish, D. L.; Livingstone, A., *Mineralogical Magazine* **1981,** *44*, 339.

94. Dunn, P. J.; Peacor, D. R.; Palmer, T. D., *American Mineralogist* **1979,** *64*, 127.

95. Bish, D. L.; Brindley, G. W., *American Mineralogist* **1977,** *62*, 458.

96. Taylor, H. F. W., *Mineralogical Magazine* **1973,** *39* (304), 377.

97. Costantino, U.; Costantino, F.; Elisei, F.; Latterini, L.; Nocchetti, M., Coupling physical chemical techniques with hydrotalcite-like compounds to exploit their structural features and new multifunctional hybrids with luminescent properties. *Physical Chemistry Chemical Physics* **2013,** *15* (32), 13254.

98. Qu, J.; Zhang, Q.; Li, X.; He, X.; Song, S., Mechanochemical approaches to synthesize layered double hydroxides: a review. *Applied Clay Science* **2016,** *119, Part 2*, 185.

99. Cavani, F.; Trifirò, F.; Vaccari, A., Hydrotalcite-type anionic clays: Preparation, properties and applications. *Catalysis Today* **1991,** *11* (2), 173.

100. Rabenau, A., The Role of Hydrothermal Synthesis in Preparative Chemistry. *Angewandte Chemie International Edition in English* **1985,** *24* (12), 1026.

101. Erickson, K. L.; Bostrom, T. E.; Frost, R. L., A study of structural memory effects in synthetic hydrotalcites using environmental SEM. *Materials Letters* **2005,** *59* (2–3), 226.

102. Stanimirova, T. S.; Kirov, G.; Dinolova, E., Mechanism of hydrotalcite regeneration. *Journal of Materials Science Letters* **2001,** *20* (5), 453.

103. Rocha, J.; del Arco, M.; Rives, V.; A. Ulibarri, M., Reconstruction of layered double hydroxides from calcined precursors: a powder XRD and 27Al MAS NMR study. *Journal of Materials Chemistry* **1999,** *9* (10), 2499.

104. Marchi, A. J.; Apesteguía, C. R., Impregnation-induced memory effect of thermally activated layered double hydroxides. *Applied Clay Science* **1998,** *13* (1), 35.

105. Wypych, F.; Satyanarayana, K. G., *Clays Surfaces: Fundamentals and Applications*. Elsevier: Oxford, UK, **2004**.

106. Rojas, R. M.; Kovacheva, D.; Petrov, K., Synthesis and Cation Distribution of the Spinel Cobaltites CuxMyCo3-(x+y)O4 (M = Ni, Zn) Obtained by Pyrolysis of Layered Hydroxide Nitrate Solid Solutions. *Chemistry of Materials* **1999,** *11* (11), 3263.

107. Rojas, R.; Giacomelli, C. E., Effect of structure and bonding on the interfacial properties and the reactivity of layered double hydroxides and Zn hydroxide salts. *Colloids and Surfaces A: Physicochemical and Engineering Aspects* **2013,** *419*, 166.

108. Forster, P. M.; Tafoya, M. M.; Cheetham, A. K., Synthesis and characterization of Co7(OH)12(C2H4S2O6)(H2O)2—a single crystal structural study of a ferrimagnetic layered cobalt hydroxide. *Journal of Physics and Chemistry of Solids* **2004,** *65* (1), 11.

109. Rojas, R.; Linck, Y. G.; Cuffini, S. L.; Monti, G. A.; Giacomelli, C. E., Structural and physicochemical aspects of drug release from layered double hydroxides and layered hydroxide salts. *Applied Clay Science* **2015,** *109–110*, 119.

110. Inoue, S.; Fujihara, S., Synthesis of Inorganic−Organic Layered Compounds Using Immiscible Liquid−Liquid Systems under the Distribution Law. *Langmuir* **2010,** *26* (20), 15938.

111. Miao, J.; Xue, M.; Itoh, H.; Feng, Q., Hydrothermal synthesis of layered hydroxide zinc benzoate compounds and their exfoliation reactions. *Journal of Materials Chemistry* **2006,** *16* (5), 474.

112. Kongshaug, K. O.; Fjellvåg, H., Organically pillared layered zinc hydroxides. *Journal of Solid State Chemistry* **2004,** *177* (6), 1852.

113. Stahlin, W.; Oswald, H. R., The crystal structure of zinc hydroxide nitrate, Zn5(OH)8(NO3)2.2H2O. *Acta Crystallographica Section B* **1970,** *26* (6), 860.

114. Ghose, S., The crystal structure of hydrozincite, Zn5(OH)6(CO3)2. *Acta Crystallographica* **1964,** *17* (8), 1051.

115. Allmann, R., Verfeinerung der Struktur des Zinkhydroxidchlorids II, Zn5(OH)8Cl2 · 1H2O. In *Zeitschrift für Kristallographie - Crystalline Materials*, **1968**; Vol. 126, p 417.

116. Nowacki, W.; Silverman Jeremiah, N., Die Kristallstruktur von Zinkhydroxychlorid II, Zn5(OH)8Cl2. 1 H2O. In *Zeitschrift für Kristallographie - Crystalline Materials*, **1961**; Vol. 115, p 21.

117. Xu, R.; Zeng, H. C., Dimensional Control of Cobalt-hydroxide-carbonate Nanorods and Their Thermal Conversion to One-Dimensional Arrays of Co3O4 Nanoparticles. *The Journal of Physical Chemistry B* **2003,** *107* (46), 12643.

118. Xu, R.; Zeng, H. C., Mechanistic Investigation on Salt-Mediated Formation of Free-Standing Co3O4 Nanocubes at 95 °C. *The Journal of Physical Chemistry B* **2003,** *107* (4), 926.

119. Hornick, C.; Rabu, P.; Drillon, M., Hybrid organic–inorganic multilayer materials: influence of π electrons as magnetic media in a series of bridged-layer compounds M2(OH)4−xAx/2 (M=Cu(II) or Co(II), A=dicarboxylate anion). *Polyhedron* **2000,** *19* (3), 259.

120. Fujita, W.; Awaga, K., Magnetic Properties of Cu2(OH)3(alkanecarboxylate) Compounds: Drastic Modification with Extension of the Alkyl Chain. *Inorganic Chemistry* **1996,** *35* (7), 1915.

121. Markov, L.; Petrov, K.; Lyubchova, A., Topotactic preparation of copper-cobalt oxide spinels by thermal decomposition of double-layered oxide hydroxide nitrate mixed crystals. *Solid State Ionics* **1990,** *39* (3–4), 187.

122. Xue, M.; Chitrakar, R.; Sakane, K.; Ooi, K.; Kobayashi, S.; Ohnishi, M.; Doi, A., Synthesis of ktenasite, a double hydroxide of zinc and copper, and its intercalation reaction. *Journal of Solid State Chemistry* **2004,** *177* (4–5), 1624.

123. Tagaya, H.; Sasaki, N.; Morioka, H.; Kadokawa, J., Preparation of New Inorganic—Organic Layered Compounds, Hydroxy Double Salts, and Preferential Intercalation of Organic Carboxylic Acids into Them. *Molecular Crystals and Liquid Crystals Science and Technology. Section A. Molecular Crystals and Liquid Crystals* **2000,** *341* (2), 413.

124. Rouba, S.; Rabu, P.; Drillon, M., Synthesis and Characterization of New Quasi-One-Dimensional Mn(II) Hydroxynitrates (MnxZn1-x)(OH)(NO3)H2O (x = 0.53, 1.00). *Journal of Solid State Chemistry* **1995,** *118* (1), 28.

125. Meyn, M.; Beneke, K.; Lagaly, G., Anion-exchange reactions of hydroxy double salts. *Inorganic Chemistry* **1993,** *32* (7), 1209.

126. Boehm, H.-P.; Steinle, J.; Vieweger, C., [Zn2Cr(Oh)6]X·2H2O, New Layer Compounds Capable of Anion Exchange and Intracrystalline Swelling. *Angewandte Chemie International Edition in English* **1977,** *16* (4), 265.

127. Henrist, C.; Traina, K.; Hubert, C.; Toussaint, G.; Rulmont, A.; Cloots, R., Study of the morphology of copper hydroxynitrate nanoplatelets obtained by controlled double jet precipitation and urea hydrolysis. *Journal of Crystal Growth* **2003,** *254* (1–2), 176.

128. Bénard-Rocherullé, P.; Rius, J.; Louër, D., Structural Analysis of Zirconium Hydroxide Nitrate Monohydrates by X-Ray Powder Diffraction. *Journal of Solid State Chemistry* **1997,** *128* (2), 295.

129. Biswick, T.; Jones, W.; Pacuła, A.; Serwicka, E., Synthesis, characterisation and anion exchange properties of copper, magnesium, zinc and nickel hydroxy nitrates. *Journal of Solid State Chemistry* **2006,** *179* (1), 49.

130. Saifullah, B.; Hussein, M. Z.; Hussein-Al-Ali, S. H.; Arulselvan, P.; Fakurazi, S., Sustained release formulation of an anti-tuberculosis drug based on para-amino salicylic acid-zinc layered hydroxide nanocomposite. *Chemistry Central Journal* **2013,** *7* (1), 72.

131. Al Ali, S. H. H.; Al-Qubaisi, M.; Hussein, M. Z.; Zainal, Z.; Hakim, M. N., Preparation of hippurate-zinc layered Hydroxide nanohybrid and its synergistic effect with tamoxifen on HepG2 cell lines. *Int J Nanomedicine* **2011,** *6*, 3099.

132. Mohsin, S. M. N.; Hussein, M. Z.; Sarijo, S. H.; Fakurazi, S.; Arulselvan, P.; Hin, T.-Y. Y., Synthesis of (cinnamate-zinc layered hydroxide) intercalation compound for sunscreen application. *Chemistry Central Journal* **2013,** *7* (1), 26.

133. Hussein, M. Z.; Al Ali, S. H.; Zainal, Z.; Hakim, M. N., Development of antiproliferative nanohybrid Compound with controlled release property using ellagic acid as the active agent. *Int J Nanomedicine* **2011,** *6*, 1373.

134. Williams, G. R.; Crowder, J.; Burley, J. C.; Fogg, A. M., The selective intercalation of organic carboxylates and sulfonates into hydroxy double salts. *Journal of Materials Chemistry* **2012,** *22* (27), 13600.

135. Mohapatra, L.; Parida, K., A review on the recent progress, challenges and perspective of layered double hydroxides as promising photocatalysts. *Journal of Materials Chemistry A* **2016,** *4* (28), 10744.

136. Zümreoglu-Karan, B.; Ay, A. N., Layered double hydroxides — multifunctional nanomaterials. *Chemical Papers* **2012,** *66* (1), 1.

137. Tang, C.; Wang, H.-F.; Zhu, X.-L.; Li, B.-Q.; Zhang, Q., Advances in Hybrid Electrocatalysts for Oxygen Evolution Reactions: Rational Integration of NiFe Layered Double Hydroxides and Nanocarbon. *Particle & Particle Systems Characterization* **2016,** *33* (8), 473.

138. Bhatta, L. K. G., Progress in hydrotalcite like compounds and metal-based oxides for CO2 capture: a review. *Journal of Cleaner Production* **2015,** *v. 103*, pp. 171.

139. Kuang, Y.; Zhao, L.; Zhang, S.; Zhang, F.; Dong, M.; Xu, S., Morphologies, Preparations and Applications of Layered Double Hydroxide Micro-/Nanostructures. *Materials* **2010,** *3* (12), 5220.

140. Zhao, Y.; He, S.; Wei, M.; Evans, D. G.; Duan, X., Hierarchical films of layered double hydroxides by using a sol-gel process and their high adaptability in water treatment. *Chemical Communications* **2010,** *46* (17), 3031.

141. Goh, K.-H.; Lim, T.-T.; Dong, Z., Application of layered double hydroxides for removal of oxyanions: A review. *Water Research* **2008,** *42* (6), 1343.

142. Varadwaj, G. B. B.; Nyamori, V. O., Layered double hydroxide- and graphene-based hierarchical nanocomposites: Synthetic strategies and promising applications in energy conversion and conservation. *Nano Research* **2016,** *9* (12), 3598.

143. Tan, H. T.; Sun, W.; Wang, L.; Yan, Q., 2D Transition Metal Oxides/Hydroxides for Energy-Storage Applications. *ChemNanoMat* **2016,** *2* (7), 562.

144. Zhong, J.; Yuan, Z.; Lu, C., Layered-nanomaterial-amplified chemiluminescence systems and their analytical applications. *Analytical and Bioanalytical Chemistry* **2016,** *408* (30), 8731.

145. Li, W.; Yan, D.; Gao, R.; Lu, J.; Wei, M.; Duan, X., Recent Advances in Stimuli-Responsive Photofunctional Materials Based on Accommodation of Chromophore into Layered Double Hydroxide Nanogallery. *Journal of Nanomaterials* **2013,** *2013*, 14.

146. Suppan, P., *Chemistry and Light*. Royal Society of Chemistry Cambridge, **1994**.

147. Rohatgi-Mukherjee, *Fundamentals of Photochemistry*. New Age International: New Deli, **1978**.

148. Douglas, P.; Burrows, H. D.; Evans, R. C., Foundations of Photochemistry: A Background on the Interaction Between Light and Molecules. In *Applied Photochemistry*, Evans, R. C.; Douglas, P.; Burrow, H. D., Eds. Springer Netherlands: Dordrecht, 2013; pp 1-88.

149. Wardle, B., *Principles and Applications of Photochemistry*. John Wiley & Sons, Ltd: United Kingdom, **2009**.

150. Seixas de Melo, J. S.; Pina, J.; Dias, F. B.; Maçanita, A. L., Experimental Techniques for Excited State Characterisation. In *Applied Photochemistry*, Evans, R. C.; Douglas, P.; Burrow, H. D., Eds. Springer Netherlands: Dordrecht, 2013; pp 533.

151. Arnold, Dean E.; Branden, Jason R.; Williams, Patrick R.; Feinman, Gary M.; Brown, J. P., The first direct evidence for the production of Maya Blue: rediscovery of a technology. *Antiquity* **2008,** *82* (315), 151.

152. Tilocca, A.; Fois, E., The Color and Stability of Maya Blue: TDDFT Calculations. *The Journal of Physical Chemistry C* **2009,** *113* (20), 8683.

153. Chiari, G.; Giustetto, R.; Druzik, J.; Doehne, E.; Ricchiardi, G., Pre-columbian nanotechnology: reconciling the mysteries of the maya blue pigment. *Applied Physics A* **2008,** *90* (1), 3.

154. Polette-Niewold, L. A.; Manciu, F. S.; Torres, B.; Alvarado Jr, M.; Chianelli, R. R., Organic/inorganic complex pigments: Ancient colors Maya Blue. *Journal of Inorganic Biochemistry* **2007,** *101* (11–12), 1958.

155. Manciu, F. S.; Reza, L.; Polette, L. A.; Torres, B.; Chianelli, R. R., Raman and infrared studies of synthetic Maya pigments as a function of heating time and dye concentration. *Journal of Raman Spectroscopy* **2007,** *38* (9), 1193.

156. Sánchez Del Río, M.; Martinetto, P.; Reyes-Valerio, C.; Dooryhée, E.; Suárez, M., Synthesis and acid resistance of Maya Blue pigment. *Archaeometry* **2006,** *48* (1), 115.

157. Sánchez del Río, M.; Martinetto, P.; Somogyi, A.; Reyes-Valerio, C.; Dooryhée, E.; Peltier, N.; Alianelli, L.; Moignard, B.; Pichon, L.; Calligaro, T.; Dran, J. C., Microanalysis study of archaeological mural samples containing Maya blue pigment. *Spectrochimica Acta Part B: Atomic Spectroscopy* **2004,** *59* (10–11), 1619.

158. Głowacki, E. D.; Voss, G.; Sariciftci, N. S., 25th Anniversary Article: Progress in Chemistry and Applications of Functional Indigos for Organic Electronics. *Advanced Materials* **2013,** *25* (47), 6783.

159. Kohno, Y.; Kinoshita, R.; Ikoma, S.; Yoda, K.; Shibata, M.; Matsushima, R.; Tomita, Y.; Maeda, Y.; Kobayashi, K., Stabilization of natural anthocyanin by intercalation into montmorillonite. *Applied Clay Science* **2009,** *42* (3), 519.

160. Bujdák, J.; Iyi, N.; Fujita, T., Aggregation and stability of 1,1′-diethyl-4,4′-cyanine dye on the surface of layered silicates with different charge densities. *Colloids and Surfaces A: Physicochemical and Engineering Aspects* **2002,** *207* (1), 207.

161. Saito, T.; Fukui, K.; Kodera, Y.; Matsushima, A.; Nishimura, H.; Inada, Y., Photostability of biliverdin bound to smectite, clay mineral. *Dyes and Pigments* **2005,** *65* (1), 21.

162. Riela, S.; Massaro, M.; Colletti, C. G.; Bommarito, A.; Giordano, C.; Milioto, S.; Noto, R.; Poma, P.; Lazzara, G., Development and characterization of co-loaded curcumin/triazole-halloysite systems and evaluation of their potential anticancer activity. *International Journal of Pharmaceutics* **2014,** *475* (1), 613.

163. López Arbeloa, F.; Martínez Martínez, V.; Arbeloa, T.; López Arbeloa, I., Photoresponse and anisotropy of rhodamine dye intercalated in ordered clay layered films. *Journal of Photochemistry and Photobiology C: Photochemistry Reviews* **2007,** *8* (2), 85.

164. Ogawa, M.; Kuroda, K., Photofunctions of Intercalation Compounds. *Chemical Reviews* **1995,** *95* (2), 399.

165. Yan, D.; Lu, J.; Wei, M.; Evans, D. G.; Duan, X., Sulforhodamine B Intercalated Layered Double Hydroxide Thin Film with Polarized Photoluminescence. *The Journal of Physical Chemistry B* **2009,** *113* (5), 1381.

166. Sun, L.; Liu, T.; Li, H.; Yang, L.; Meng, L.; Lu, Q.; Long, J., Fluorescent and Cross-linked Organic–Inorganic Hybrid Nanoshells for Monitoring Drug Delivery. *ACS Applied Materials & Interfaces* **2015,** *7* (8), 4990.

167. Cui, Y.; Chen, B.; Qian, G., Lanthanide metal-organic frameworks for luminescent sensing and light-emitting applications. *Coordination Chemistry Reviews* **2014,** *273*, 76.

168. Latterini, L.; Nocchetti, M.; Aloisi, G. G.; Costantino, U.; Elisei, F., Organized chromophores in layered inorganic matrices. *Inorganica Chimica Acta* **2007,** *360* (3), 728.

169. Latterini, L.; Elisei, F.; Aloisi, G. G.; Costantino, U.; Nocchetti, M., Space-resolved fluorescence properties of phenolphthalein-hydrotalcite nanocomposites. *Physical Chemistry Chemical Physics* **2002,** *4* (12), 2792.

170. Costantino, U.; Coletti, N.; Nocchetti, M.; Aloisi, G. G.; Elisei, F.; Latterini, L., Surface Uptake and Intercalation of Fluorescein Anions into Zn−Al−Hydrotalcite. Photophysical Characterization of Materials Obtained. *Langmuir* **2000,** *16* (26), 10351.

171. Costantino, U.; Coletti, N.; Nocchetti, M.; Aloisi, G. G.; Elisei, F., Anion Exchange of Methyl Orange into Zn−Al Synthetic Hydrotalcite and Photophysical Characterization of the Intercalates Obtained. *Langmuir* **1999,** *15* (13), 4454.

172. Aguzzi, A.; Ambrogi, V.; Costantino, U.; Marmottini, F., Intercalation of acrylate anions into the galleries of Zn–Al layered double hydroxide. *Journal of Physics and Chemistry of Solids* **2007,** *68* (5), 808.

173. Latterini, L.; Nocchetti, M.; Aloisi, G. G.; Costantino, U.; De Schryver, F. C.; Elisei, F., Structural, Photophysical, and Photochemical Characterization of 9-Anthracenecarboxylate−Hydrotalcite Nanocomposites: Evidence of a Reversible Light-Driven Reaction. *Langmuir* **2007,** *23* (24), 12337.

174. Aloisi, G. G.; Costantino, U.; Elisei, F.; Latterini, L.; Natali, C.; Nocchetti, M., Preparation and photo-physical characterisation of nanocomposites obtained by intercalation and co-intercalation of organic chromophores into hydrotalcite-like compounds. *Journal of Materials Chemistry* **2002,** *12* (11), 3316.

175. Perioli, L.; Ambrogi, V.; Rossi, C.; Latterini, L.; Nocchetti, M.; Costantino, U., Use of anionic clays for photoprotection and sunscreen photostability: Hydrotalcites and phenylbenzimidazole sulfonic acid. *Journal of Physics and Chemistry of Solids* **2006,** *67* (5), 1079.

176. Wang, G.; Xu, S.; Xia, C.; Yan, D.; Lin, Y.; Wei, M., Fabrication of host-guest UV-blocking materials by intercalation of fluorescent anions into layered double hydroxides. *RSC Advances* **2015,** *5* (30), 23708.

177. Ma, H.; Gao, R.; Yan, D.; Zhao, J.; Wei, M., Organic-inorganic hybrid fluorescent ultrathin films and their sensor application for nitroaromatic explosives. *Journal of Materials Chemistry C* **2013,** *1* (26), 4128.

178. Dongpeng, Y.; Wei, M., Photofunctional Layered Materials. *Structure and Bonding* **2015,** *166*.

179. Li, S.; Lu, J.; Wei, M.; Evans, D. G.; Duan, X., Tris(8-hydroxyquinoline-5-sulfonate)aluminum Intercalated Mg–Al Layered Double Hydroxide with Blue Luminescence by Hydrothermal Synthesis. *Advanced Functional Materials* **2010,** *20* (17), 2848.

180. Kim, S.; Kim, T.; Kang, M.; Kwak, S. K.; Yoo, T. W.; Park, L. S.; Yang, I.; Hwang, S.; Lee, J. E.; Kim, S. K.; Kim, S.-W., Highly Luminescent InP/GaP/ZnS Nanocrystals and Their Application to White Light-Emitting Diodes. *Journal of the American Chemical Society* **2012,** *134* (8), 3804.

181. Lee, M.; Yang, R.; Li, C.; Wang, Z. L., Nanowire−Quantum Dot Hybridized Cell for Harvesting Sound and Solar Energies. *The Journal of Physical Chemistry Letters* **2010,** *1* (19), 2929.

182. Shi, W.; Fu, Y.; Li, Z.; Wei, M., Multiple and configurable optical logic systems based on layered double hydroxides and chromophore assemblies. *Chemical Communications* **2015,** *51* (4), 711.

183. Cursino, A. C. T.; Gardolinski, J. E. F. C.; Wypych, F., Intercalation of anionic organic ultraviolet ray absorbers into layered zinc hydroxide nitrate. *J Colloid Interf Sci* **2010,** *347*.

184. Cursino, A. C. T.; Rives, V.; Arizaga, G. G. C.; Trujillano, R.; Wypych, F., Rare earth and zinc layered hydroxide salts intercalated with the 2-aminobenzoate anion as organic luminescent sensitizer. *Materials Research Bulletin* **2015,** *70*, 336.

2. A Congo Red-based LDH

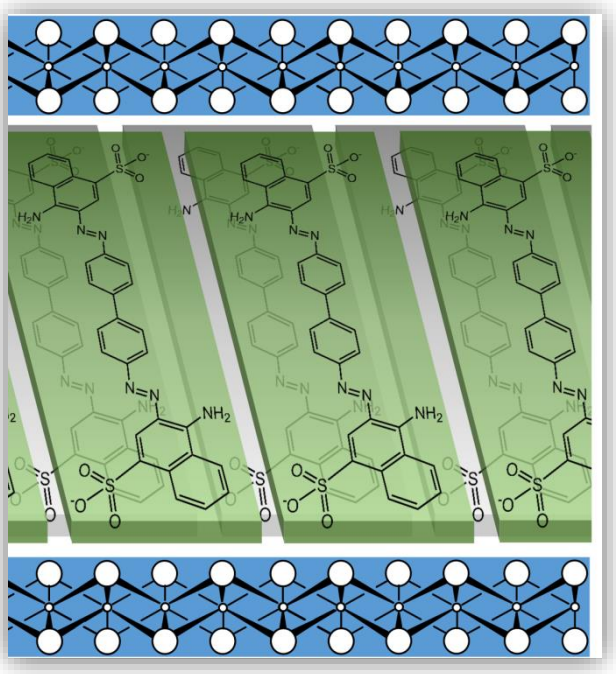

2.1 Introduction

The non-covalent self-association of organic dyes in solution and in the solid-state is a critically important phenomenon that leads to the formation of dimers and higher ordered aggregates.[1-4] Internal (dye structure related) factors that are involved in aggregate formation include electrostatic interactions, van der Waals forces, π-π stacking, and hydrogen bonding. Aggregation behavior is also strongly affected by external (dye environment related) factors such as temperature, pH, concentration of the dye, ionic strength, and solvent polarity. One of the main consequences of the self-assembly of dyes is that molecular aggregates have distinct photophysical properties compared to the individual monomer.[3-5] In many cases the strong intermolecular interactions that hold aggregates together are responsible for the weakening of emission ("aggregation-caused quenching") and this may severely limit the use of the dyes in real-world applications such as organic light-emitting diodes (OLEDs).[6] On the other hand, the fairly recent discovery of "aggregate-induced emission" (AIE), in which non-emissive luminogens are induced to emit by aggregate formation, has gone a long way to tempering the bad reputation of aggregation with respect to luminescence efficiencies.[1, 7] Therefore, studies on controlling dye aggregate formation and morphology, and the formation mechanism of these aggregates in, for example, thin films and dye-based nanohybrids,[8-12] are of great importance for practical applications as well as for fundamental research of assembled dye molecules.

The aggregation behavior of azobenzenes (ABs)[13] is of considerable interest with respect to applications in optics and photonics since these molecules exhibit attractive features such as vibrant, chemically tunable colors (especially red, orange and yellow),[14] good light fastness, an ability to undergo reversible *trans-cis* isomerization upon irradiation with UV or visible light,[15] and, in a few cases, AIE enhancement.[16]

2.2 The azo dye Congo Red (CR)

Congo Red (CR) is an anionic diazo dye with a high self-assembling tendency. In aqueous solution, CR is thought to form supramolecular structures of various sizes and shapes (ribbon or rod-like micelles) owing to the hydrophobic interactions between the aromatic rings of the dye.[17-21] These molecular assemblies may play a role in the remarkable ability of CR to bind to various Amyloid-β (Aβ) peptide species ranging from monomers to fibrils.[17, 22-23] In fact, the capacity of CR to inhibit Aβ aggregation has led to its study as a therapeutic agent for amyloid fibril-related diseases such as Alzheimer's disease.[22] Interestingly, CR exhibits enhanced fluorescence and/or induced optical activity (circular dichroism) when bound to amyloid fibrils,[24-25] synthetic peptides,[26] poly(L-lysine),[27] enzymes[28] and proteins.[29] CR readily forms complexes with other materials such as cellulose fibers,[30] the polysaccharide grifolan,[31] poly(vinyl alcohol) hydrogels,[32] graphite oxide,[33] and has been incorporated into polymer films and capsules.[34-36] Composite materials containing embedded CR molecules are potentially of interest as pH and

chemical sensors,[37-41] hybrid organic-semiconductor devices,[42] photoresponsive materials,[43] polymer-electrolyte fuel cells,[44] and nanotheranostics systems.[45]

In view of the fundamental and technological interest in organized assemblies of AB dyes like CR, and the desire for a "bottom-up" approach to the assembly of tailored molecular aggregates, it is vital to gain an in-depth knowledge of aggregation behavior and structure-property relationships for the dye molecules in different environments.

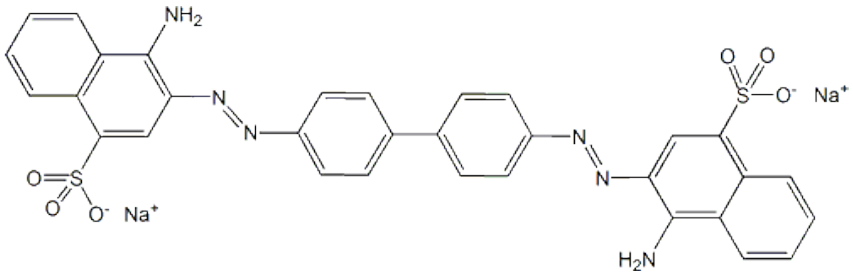

Scheme 2.1 – Chemical structure of Congo Red.

In this chapter, a comprehensive study of the electronic spectral and photophysical behavior of CR in solution and in the solid state as well as in the aggregated state in an organo-layered double hydroxide nanocomposite prepared by a direct coprecipitation route is described. In the latter case the photophysical characterization was complemented by several other solid-state measurements in order to determine more precisely the structural properties of the intercalated dye aggregates.

2.3 Photophysical characterization of CR in solution

2.3.1 Absorption, Fluorescence and Fluorescence Excitation Studies

The photophysical properties of CR were investigated in solution. UV-Vis absorption and steady-state fluorescence spectra of CR in aqueous solution were previously reported.[46] However, according to our results for as-received CR and recrystallized CR (Figure 2.1), the emission spectra (and photophysical parameters) reported by Iwunze[46] was originated from an impurity in the reagent-grade CR obtained from a commercial source (and used without further purification). Iwunze obtained a value of 0.011 for the fluorescence quantum yield (with excitation at 330 nm and observed fluorescence at 417 nm, in the $S_0 \rightarrow S_2$ transition) and determined the lifetime as 2.8 ns by using the Strickler-Berg equation.[47] As will be shown below the lifetime of the S_1 state is actually much shorter with a value of 7 ps. A similar excitation in the S_2 band (350 nm) for CR incorporated within a dendritic structure in ethanol, dichloromethane or pentane gave fluorescence emission spectra with maxima that ranged from 402 nm (polar solvent) to 632 (non-polar solvent), with this behavior being attributed mainly to aggregation induced by the nonpolar solvent.[48]

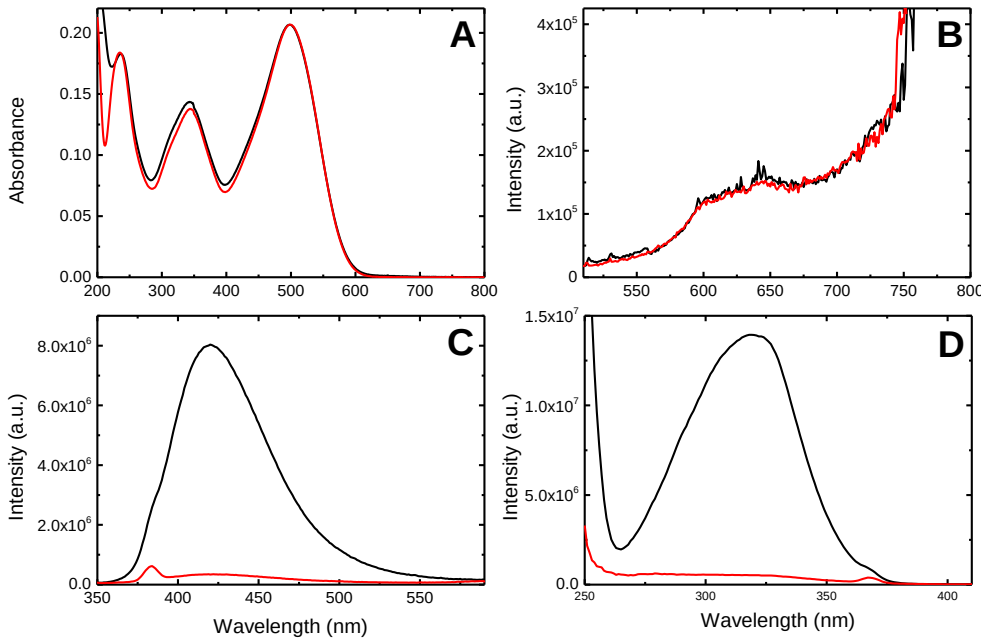

Figure 2.1 - Absorption (**A**), fluorescence emission with λ_{exc} = 497 nm (**B**) and λ_{exc} = 340 nm (**C**), and excitation spectra (**D**) with λ_{em} = 420 nm of as-received Na_2CR (black line) and recrystallized Na_2CR (red line).

The CR sample was purified by recrystallization and, although the absorption spectra recorded before and after purification were identical, the purification step led to a major change in the emission spectrum, namely the disappearance of the emission band at shorter wavelengths (Figure 2.1).

The absorption and fluorescence spectra of CR were measured in two solvents with different polarities, namely water, a polar protic solvent and a strong hydrogen-bond donor, and DMSO, a polar aprotic solvent with no ability to be a hydrogen-bond donor. The absorption spectra (Figure 2.2) display two broad bands with maxima at 340 and 497 nm in water (pH = 6.3), and at 340 and 532 nm in DMSO, assigned to π-π* transitions of the –NH and azo groups, respectively.[49] CR, with high absorptivity, can undergo solvatochromic shifts depending on the dye-solvent interactions.[49] The negative solvatochromism evident in Figure 2.2 is in agreement with the results previously published by Atvars and co-workers.[30]

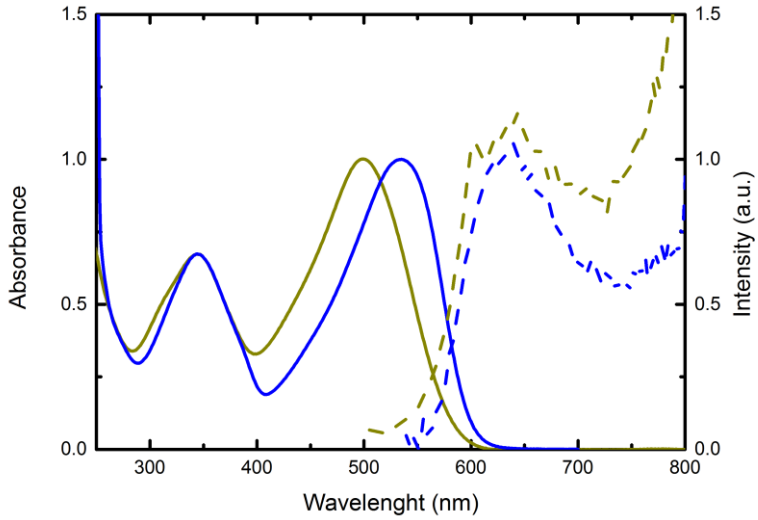

Figure 2.2 - Absorption spectra (unbroken lines) of Na_2CR in water (dark yellow) and in DMSO (blue), and fluorescence emission spectra (dashed lines) of Na_2CR in water with λ_{exc} = 497 nm (dark yellow) and in DMSO with λ_{exc} = 535 nm (blue).

At the concentrations used to acquire the spectra shown in Figure 2.2 the solution behavior is basically that of the isolated molecule, which has no parallel with the situation found with the CR-LDH hybrid (see below). In order to further support the type of aggregates formed by CR in CR-LDH we measured the absorption and emission excitation spectra of CR in DMSO and water from higher (2.64×10^{-4} M) to lower (2.64×10^{-6} M) concentrations (see Figure 2.3 for the absorption spectra at different concentrations and Figure 2.4 for the fluorescence excitation spectra). Typically, increasing dye concentration may induce molecular aggregation and cause spectral perturbation. Current interpretations of these effects have their historical roots in the exciton model introduced by Kasha[50-51] and have recently been (critically) reviewed.[3, 52] Nearest neighbor interactions have the most significant effects on the UV-Vis spectrum of the molecular aggregate. Head-to-tail stacking of dyes leads to a red-shift in the absorption spectrum (J-aggregates), while a parallel stacking arrangement leads to a blue shift (H-aggregates).[52-55]

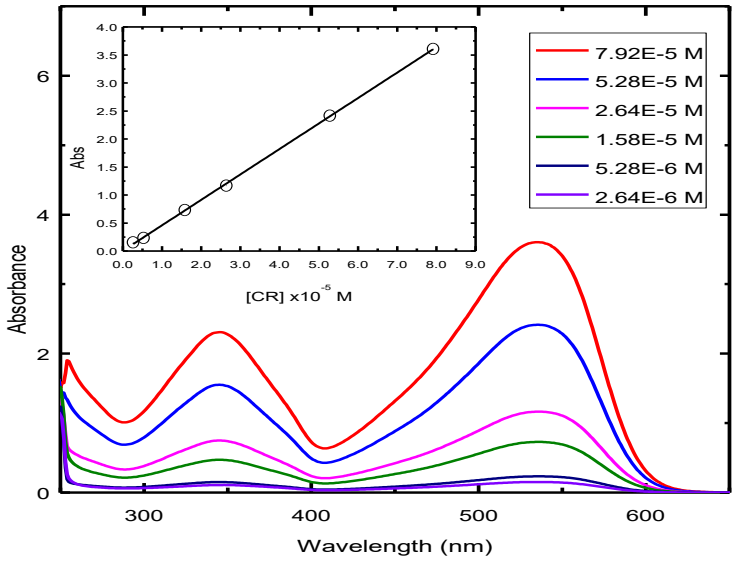

Figure 2.3 - Absorption spectra of CR in DMSO at different concentrations. Shown as inset is the linear dependence of the absorption (at the maximum wavelength of 532 nm).

For the absorption spectra of CR in DMSO, a linear dependence is observed within the concentration range studied (the saturation limit of the spectrophotometer is the limiting factor for this linear dependence). This means that the compound is very soluble (in DMSO and water). Nevertheless, the excitation spectra provide additional evidence for aggregation and the types of aggregates present in solution. Indeed, the fluorescence excitation spectra of CR in DMSO are different from the corresponding UV/Vis absorption spectra, particularly when the concentration is above 2.64×10^{-5} M.

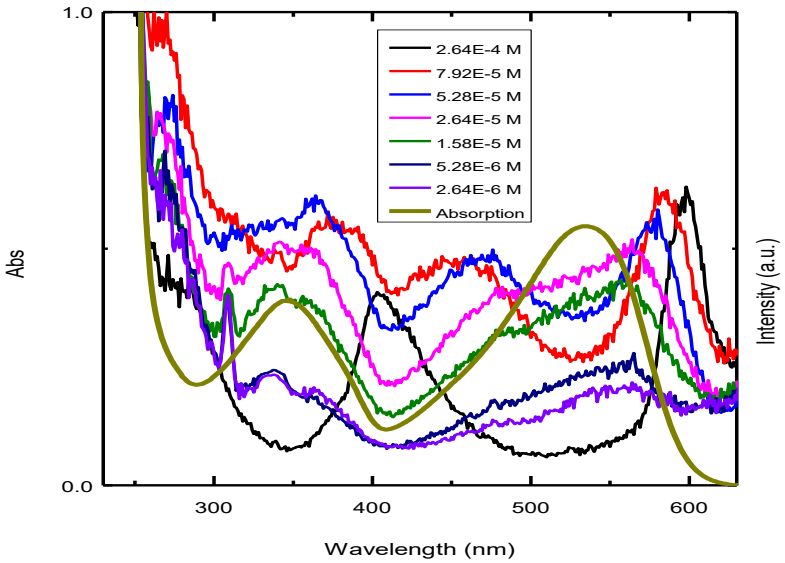

Figure 2.4 - UV-Vis Absorption and excitation spectra (obtained with λ_{em}= 680 nm) in the 230-630 nm wavelength range for CR in DMSO at different concentrations.

For concentrations in the range of 2.64×10^{-6} M to 1.58×10^{-5} M, the excitation spectra of CR can be considered identical to its absorption spectra (Figure 2.4). Within this concentration range the CR molecules can be considered as "isolated". When the concentration increases from 2.64×10^{-5} M to 7.92×10^{-5} M, a red-shift of the longest wavelength band, together with a significant change in the spectral shape (with a characteristically sharp absorption spectra) is observed, which indicates the presence of J-type aggregates. Moreover, at the final concentration of 2.64×10^{-4} M an additional, now blue-shifted band (at ~ 405 nm) is observed, which is consistent with the fact that with oblique-type aggregates there is an energetic split of the excited states leading to a splitting into two bands, which appear at low and high wavelengths in the absorption spectrum.[56-57] A similar situation is observed for the behavior in water as can be seen from the fluorescence excitation spectra obtained at different concentrations (Figure 2.5).

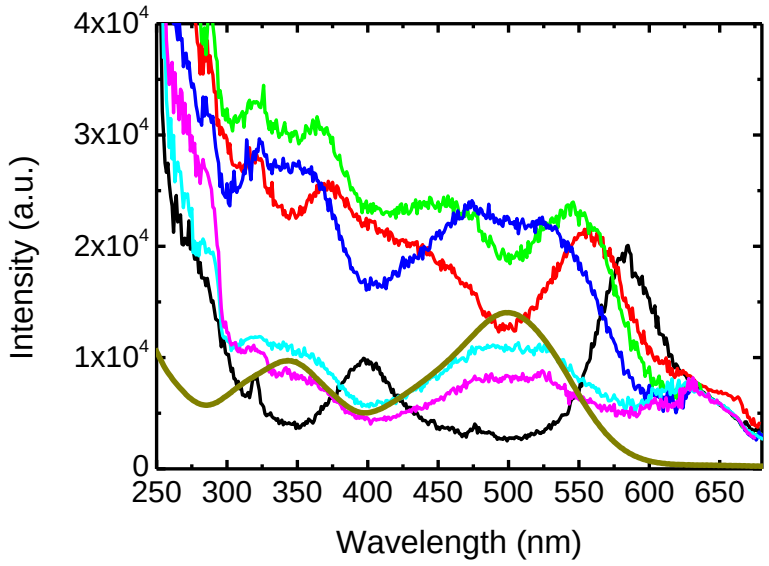

Figure 2.5 - Absorption and fluorescence excitation spectra of CR in water (pH=6.1) at different concentrations. Fluorescence excitation spectra (λ_{em} = 640 nm) of CR in water at pH = 6.1 with concentrations of 2.86×10^{-4} M (black line), 8.58×10^{-5} M (red), 5.72×10^{-5} M (green), 2.86×10^{-5} M (blue), 5.72×10^{-6} M (cyan) and 2.86×10^{-6} M (magenta) and absorption spectrum (dark yellow).

The fluorescence spectra present a broad band with maximum at 630 nm in water and 640 nm in DMSO (Figure 2.2). The fluorescence quantum yields were determined for both solvents and are presented in Table 2.1. From the very low fluorescence quantum yield values (ca. 10^{-4}) and the absence of a transient triplet-triplet signal (no signal was observed by nanosecond transient absorption flash-photolysis) it can be concluded that the main deactivation pathway in CR is the internal conversion radiationless channel. It is noteworthy that

the ϕ_F value is about two times lower in water than in DMSO. These low ϕ_F values, together with the fact that CR presents a pH dependent photophysical behavior (see below), suggest *a priori* that excited state proton transfer (ESPT) may be responsible for the domination of the radiationless deactivation channel. Indeed, in water the possibility of intermolecular ESPT in addition to intramolecular ESPT seems to suggest that it may open up an additional (and effective) deactivation channel for CR, thus decreasing the ϕ_F value. This will be further discussed in the section 2.3.2 in the light of the femtosecond time-resolved transient absorption data (fs-TA). Since the decay of the first excited singlet state basically occurs through radiationless internal conversion, the fluorescence decay time can be considered to be identical to the overall decay time of this state. Thus, based on the decay time value of the S_1 obtained from fs-TA experiments, the radiationless rate constant (k_{NR}) dominates relative to the radiative processes in the excited state deactivation of CR in solution (more than five thousand times for water), see Table 2.1. In DMSO this domination is reduced markedly (*ca*. 400 times difference).

Table 2.1 - Spectroscopic and photophysical properties of Congo Red, including absorption and emission wavelength maxima, in water (pH = 6.10) and DMSO, at room temperature.

Solvent	λ_{max}^{Abs} (nm)	$\varepsilon_{máx}$ (mol dm^{-3} cm^{-1})	λ_{max}^{Fluo} (nm)	ϕ_F[a]	τ_F (ns)[b]	k_F (ns^{-1})	k_{NR} (ns^{-1})
Water	340,497	37410	630	1.9×10^{-4}	0.0062	0.0306	161.26
DMSO	340,532	45500	640	3.8×10^{-4}	0.0075	0.0507	19.73

[a] Associated errors are ± 3.5×10^{-5} for water and ± 1.8×10^{-5} for DMSO. [b] Obtained from fs-TA experiments, considering that the dominating deactivation of the S_1 state does not involve the formation of a triplet state.

Others have reported a value of 2.3 ns for the fluorescence lifetime of CR in ethanol.[48] However, as mentioned above and as shown in the present work, we believe that this is likely related to an impurity present in CR. Indeed, it was also obtained a value of 8.11 ns (degassed solution) for the fluorescence decay time of CR in DMSO when excited at 339 nm (S_2) for the impure compound (Figure 2.6).

As mentioned in the introduction, cis-trans photoisomerization of azo-dyes is usually a dominant process in the excited state. However, in our case for CR in solution, only photodegradation was observed upon irradiation. This contrasts with previous observations for composite films of PDAC and CR where photoisomerization of CR was found together with degradation (with an Ar^+ laser with an intensity of 100 mW/cm^2 and excitation at 488 nm).[35]

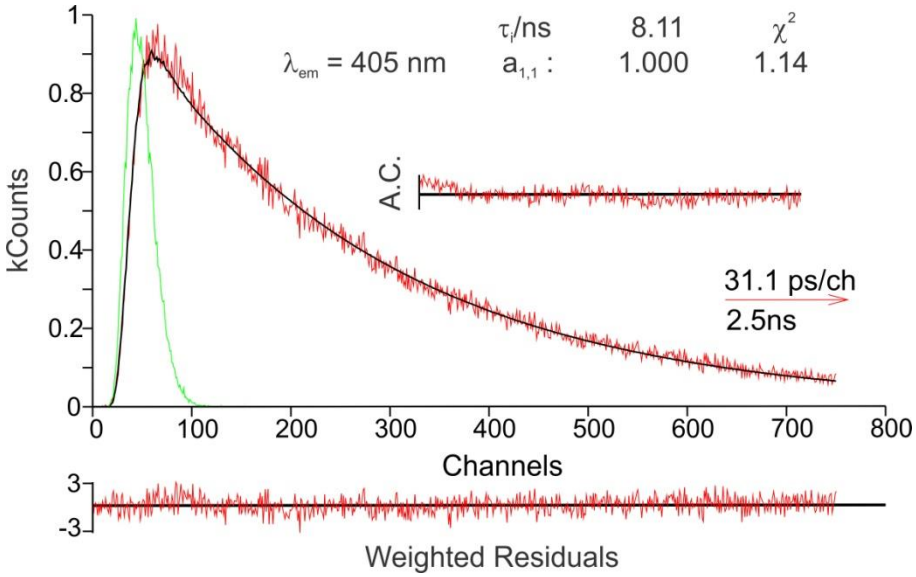

Figure 2.6 - Fluorescence decay for (impure) CR in methanol obtained with excitation at 339 nm and emission at 405 nm. The obtained decay time and pre-exponential factor are shown as insets. Also shown are the weighted residuals, autocorrelation functions (A.C.) and χ^2 values, for a better judgment of the quality of the fit.

Recently, a theoretical study on an azo-derivative (cyclopropyldiazo-2-naphthol) suggested an ESPT (wavelength-dependent) could be present.[58] Although it cannot be completely exclude the possibility of ESPT, the very low fluorescent quantum yields together with the high values (and dominance) of the radiationless rate constants (k_{NR}) seem to be better explained by the energy gap law for the radiationless transitions. In this case a small value in the S_1-S_0 energy gap, ΔE, as observed in the case of CR, favors the nonradiative *vs.* radiative decay pathway. This is limited by the degree of vibrational overlap (Franck-Condon factor, f_v) of the wavefunctions for the nonradiative modes of these two states. This is linked to the fact that the changes in the f_v factors of the nuclear wavefunctions become increasingly unfavorable with the increase in the energy separation between the two states.[59-60] Indeed if we consider that the rate constant for internal conversion $k_{IC} \sim 10^{13}\ f_v\ s^{-1}$ and $k_{IC} \sim 10^{13} \exp(-\alpha\Delta E)$, where α is a proportionality constant, the f_v value becomes largely unfavorable with the increase in ΔE.[60] In our case, considering that intersystem crossing ($S_1 \sim > T_1$) is a negligible excited state deactivation pathway, we can assume that $k_{NR} \sim k_{IC}$. Thus the values of $1.613 \times 10^{12}\ s^{-1}$ (water) and $1.97 \times 10^{12}\ s^{-1}$ (DMSO), see Table 2.1, are close to the limiting value for the rate of internal conversion ($10^{13}\ s^{-1}$).[60]

Figure 2.7 shows the evolution of the absorption spectra of an aqueous solution of Na_2CR as a function of pH. The color of the solution changes from blue for acidic solutions to red at higher pH values.[30, 49] It has been proposed that for pH values above 5.6 the disulfonate dianion of CR is present and gives rise to the band at 497 nm. Below a pH of 5.6, spectral changes are due to the protonation of CR and the existence of a tautomeric equilibrium mixture comprising an ammonium

form (λ_{max} = 520 nm) with the proton attached to the amino nitrogen and an azonium form (λ_{max} = 655 and 735 nm) with the proton attached to the α-azo nitrogen.[61] For pH values below 1.96, there is a tendency for CR to precipitate, which results in a decrease in the absorbance.

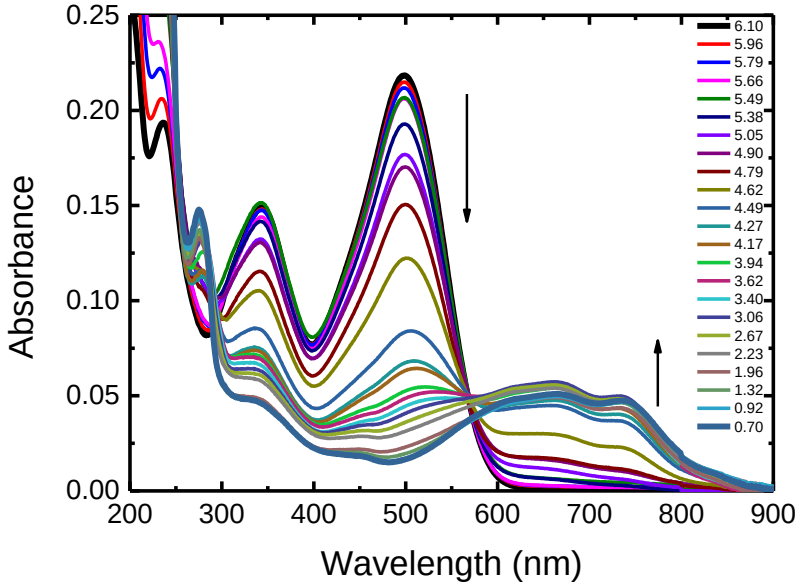

Figure 2.7 - Absorption spectra of an aqueous solution of Na_2CR (C = 5.83 × 10^{-6} M) as a function of pH.

2.3.2. Femtosecond transient absorption experiments

The transient absorption (TA) spectra for CR were obtained in aerated water and DMSO solutions at room temperature from pump-probe femtosecond time-resolved TA spectroscopy. The compounds were excited at 440 nm and 568 nm (pump light), thus promoting the population of the excited state, followed by an analysis/probing with light in the 450–800 nm range and recording the evolution of the TA spectra and decay kinetics up to a delay time of 50 ps.

Figure 2.8 depicts the ultrafast time-resolved TA spectra of CR in water at pH=10 and DMSO with excitation at 440 nm. In general in water and DMSO the spectra present a negative band ranging from ~ 400 nm to ~ 570 nm that is attributed to ground state bleaching (GSB), matching well the ground-state absorption peak, together with a positive excited state absorption (ESA) band in the 550-750 nm range. In water when excitation was made at 568 nm (0-0 transition band), similar TA spectra were obtained to that found with excitation at 440 nm, although in the latter case the ESA band appears more well defined, see Figures 2.8 and 2.9. In general, the ultrafast TA spectra do not display stimulated emission data, which may be explained by the very low fluorescence quantum yield found for CR (Table 2.1).

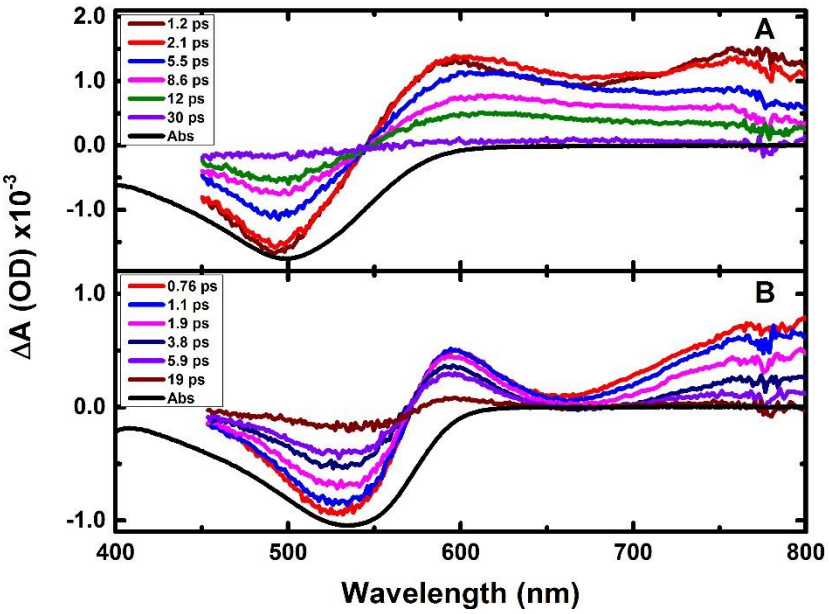

Figure 2.8 - Ultrafast time-resolved TA spectra for CR in (A) water at pH=10 and (B) DMSO collected with excitation at 440 nm. For comparison the absorption spectra ($S_0 \rightarrow S_1$) obtained from UV-Vis spectroscopy are also shown.

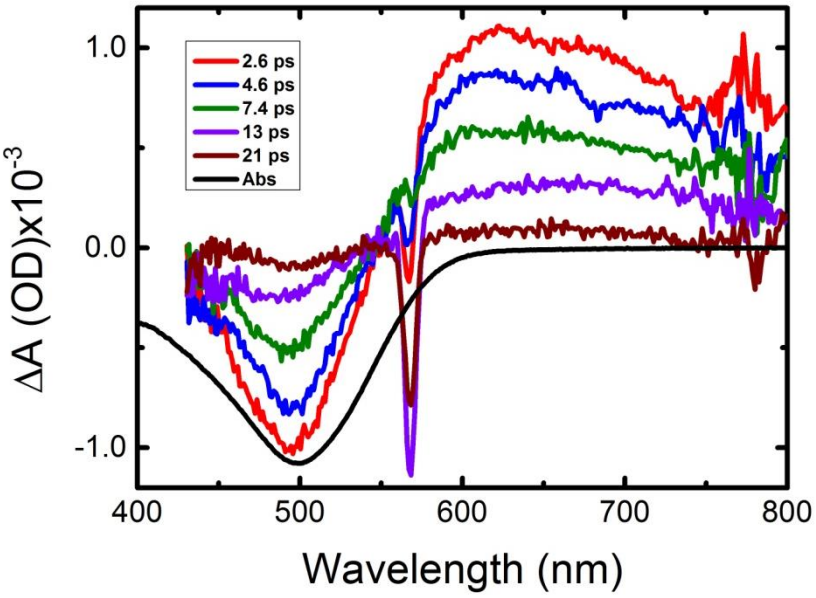

Figure 2.9 - Ultrafast time-resolved transient absorption spectra for CR in water at pH=10 collected with excitation at 568 nm. For comparison the absorption spectrum (S_0->S_1) obtained from UV-Vis spectroscopy is also shown.

At pH 10, and excitation at 440 nm and 568 nm, the individual analysis gives rise to a biexponential fit with decay times of 1.1-1.4 and 7.2-8.2 ps (data analysis not displayed). However, to describe properly the observed dynamics, global fit analysis of all of the kinetics at different wavelength regions was performed with singular value decomposition (SVD).[62] A sequential kinetic model was used in the global analysis of the time-resolved data. The resultant decay-associated spectra, DAS, for CR in water at pH= 10 and DMSO are shown in Figure 2.10. The best-fits to the kinetic traces together with the evaluation of the quality of the fits can be found in Table 2.2 and Figure 2.10 (C, D), respectively.

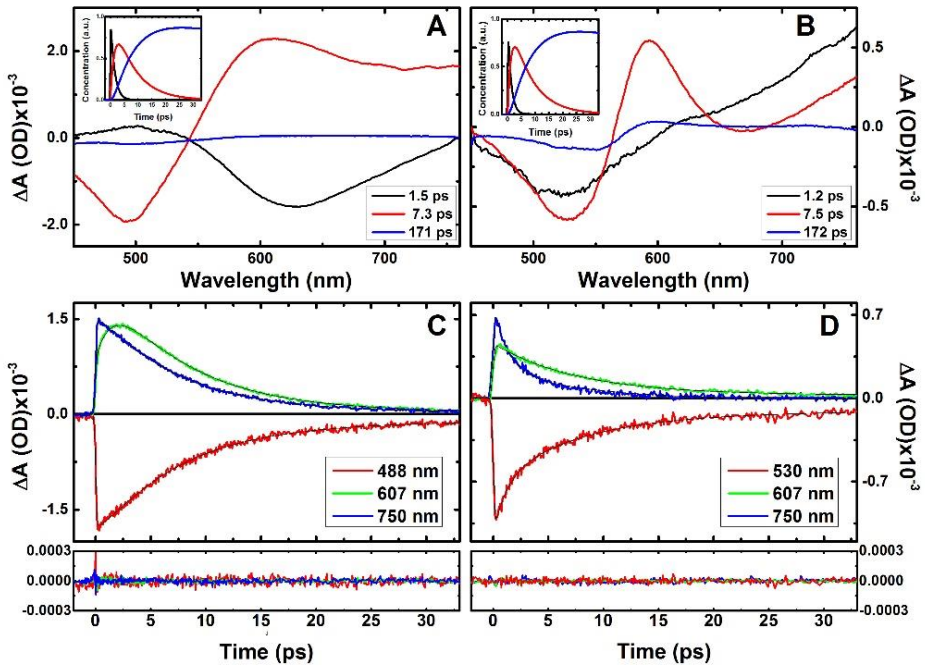

Figure 2.10 - Decay associated spectra (DAS) of the three time constants extracted from the TA data (λ_{exc}= 440 nm) after SVD/global analysis together with the concentration profiles of the time constants (inset) for CR in (A) water at pH=10 and (B) DMSO; Representative kinetic traces of the TA data for CR in (C) water at pH=10 and (D) DMSO together with the fits derived from global analysis over the full 450-760 nm spectral range. The residuals are also presented for a better judgment of the quality of the fits.

The results of the global analysis show that in general a better fit is obtained with a tri-exponential decay law. The two shorter components (1.2-1.5 ps and 7.3-7.5 ps) are basically identical to the values obtained with the individual analysis. However, the lifetime value of ~ 170 ps and the residual associated pre-exponential factors (see Table 2.2 and the DAS in Figure 2.10) suggest that this component may result from the formation of a photoproduct; nevertheless it constitutes a minor route of CR decay dynamics.

Regarding the nature of the shorter decay component the fact that similar lifetime values were observed when excitation is made at 440 nm and 568 nm (0-0), excludes the occurrence of fast vibrational relaxation processes (due to vibrational cooling to the lowest vibronic state of S_1); indeed this component is more likely to be associated with the solvation dynamics process of water molecules (or DMSO) around the excited CR.[62]

Table 2.2 - Results of the global fit analysis (lifetimes and normalized pre-exponential factors) for CR in water (pH = 10) and DMSO obtained from fs-TA experiments with λ_{exc} = 440 nm.

Solvent	λ (nm)	τ_1 (ps)	A_1	τ_2 (ps)	A_2	τ_3 (ps)	A_3
Water (pH = 10)	600	1.5	-0.59	7.3	0.98	171	0.02
	750		-0.10				
DMSO	600	1.2	-0.10	7.5	0.94	172	0.06
	750		0.66		0.34		-0.01

Overall the data is consistent with a sequential model where upon excitation with a short laser pulse (≤250 fs) the excited state (Franck-Condon) is formed instantaneously in the excited state which further gives rise (with 1-2 ps) to a relaxed species that decays with 7.3-7.5 ps (this range is dependent on the solvent and pH). In our case the short component should be considered to include both the initial, very rapid, relaxation (also known as inertial solvation of water molecules around the excited CR molecule), essentially complete within ~ 1 ps, and the subsequent longer (diffusional component of the solvation) relaxation.[63]

It is worth discussing in more detail the data obtained with λ_{exc}= 440 nm for CR in DMSO. Contrasting to the observation that at the band with maxima at ~ 596 nm and 750 nm (ESA) the kinetic trace completely decays, the decays in the GSB (530) do not completely recover. This is consistent with the formation of a long-lived (~ 170 ps) photoproduct (see Figure 2.10 (A and B)), which can be associated with a low degree of trans-cis photoisomerization.

2.4 CR in the solid-state

A Zn-Al LDH intercalated by Congo Red was prepared by coprecipitation of the Zn^{2+} and Al^{3+} hydroxides (initial Zn^{2+}/Al^{3+} molar ratio = 2) in the presence of an aqueous solution of the CR disodium salt at a constant pH of 7.5–8, followed by aging of the gel at 65 °C for 18 h.

It is always necessary to characterize the obtained materials in order to understand their structure and properties as well the guest-guest and host-guest interactions. Therefore, several

techniques were used to characterize the materials such as Powder X-Ray diffraction (PXRD), FT-IR and Raman spectroscopies, Scanning Electron Microscopy (SEM), ^{13}C {^{1}H} CP MAS NMR spectroscopy and elemental analysis. The instrumentation and some theoretical aspects of each technique will be described in Experimental Section (Chapter 7).

2.4.1 Powder X-Ray Diffraction

The PXRD pattern of the resultant dark red solid, denoted CR-LDH, exhibits several fairly broad, equally spaced peaks between 3 and 30º 2θ, which can be indexed as 00*l* reflections for an expanded hydrotalcite-type phase with a basal spacing (d_{003}) of 26.2 Å (Figure 2.11). This spacing is one of the largest yet reported for an LDH intercalated by an organic dye, surpassing that found for the azobenzenes methyl orange (24.2 Å),[64] (4-phenylazophenyl)acetate (25.6 Å),[65] and *trans*-azobenzene-4,4'-dicarboxylate (20.0 Å).[66] Relatively weak and asymmetric peaks above 30º 2θ are assigned as overlapping non-basal reflections. Subtraction of 4.8 Å (for the brucite-like layer thickness) from the basal spacing gives a gallery height of 21.4 Å. For comparison, Figure 2.11 shows the PXRD pattern of a nitrate-form Zn-Al LDH, which was prepared in a similar fashion to that for CR-LDH; as expected the basal spacing for NO_3-LDH (8.95 Å) is much lower than that for CR-LDH.

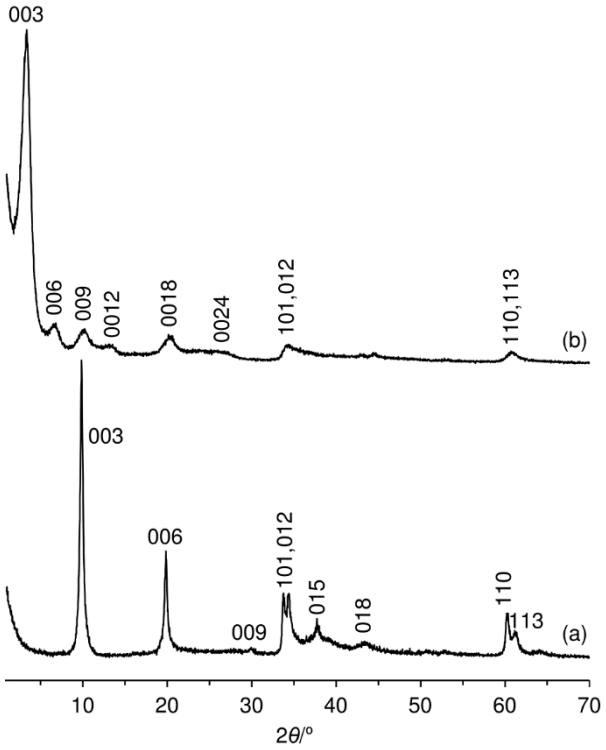

Figure 2.11 - PXRD patterns of (a) NO_3-LDH and (b) CR-LDH.

The crystal structure of the calcium salt of CR was described by Gleason et al. in 1995.[67] Based on the reported data, the minimum and maximum dimensions of the CR anion can be represented by a rectangle with dimensions of 9.9 × 28.2 Å (which include van der Waals radii of 1.5 Å for oxygen and 1.2 Å for hydrogen, respectively). Hence, a perpendicular orientation of guest molecules between the layers is not compatible with the observed gallery height. However, a tilted arrangement with the molecules inclined at an angle of ca. 50º with respect to the LDH layers could account for the observed interlayer spacing, as illustrated schematically in Figure 2.12. Two different families (or extremes) of stacking arrangements can be envisaged based on whether the planes of the aromatic rings are in a roughly perpendicular (Figure 2.12A) or flat/parallel (Figure 2.12B) orientation with respect to the LDH layer. CR is known to self-assemble and create supramolecular structures in water solutions.[17] At low concentrations (<10^{-5} M) and pH values higher than 5.5, CR possibly exists mainly as isolated molecules[26, 30, 34] and/or as small clusters composed of a few molecules.[20] At higher concentrations and/or lower pH values (where the amino groups are protonated, leading to a neutralization of electrostatic repulsive interactions between CR molecules) ribbon-shaped micellar species are created by the face-to-face stacking of CR molecules.[17-19, 21] A similar type of supramolecular arrangement may be present in the intercalated material CR-LDH, as represented in Figure 2.12A. This type of face-to-face arrangement can be classified as a H-type aggregate and has been proposed for a number of dye-intercalated materials such as LDHs containing Acid Red 27[68] and 9-fluorenone-2,7-dicarboxylate.[69] By rotating/twisting each CR molecule in this model by ca. 90º along the molecular axis we arrive at the alternative model represented in Figure 2.12B in which the CR molecules are stacked in a slipped coplanar inclined configuration. The slip angle α (as defined in Figure 2.12B) is ca. 50º in this model, which is in the range (0-54.7º) conventionally associated with J-type aggregates (as opposed to H-type aggregates with α > 54.7º).[3, 70] Examples of organic chromophores that have been proposed to adopt this type of guest packing when intercalated in LDHs include perylene derivatives,[71-73] 1,3,6,8-pyrenetetrasulfonate,[74] and indigo carmine.[75]

In the idealized representations shown in Figure 2.12 (A, B) all of the CR molecules are drawn such that they have the same relative orientation, i.e. they are translationally equivalent. The actual situation may be more complex and modifications of this scheme can be envisaged in which adjacent coplanar CR molecules are twisted with respect to one another to varying degrees (while maintaining coplanarity). In the extreme (successive 180º rotations) the molecules would adopt an antiparallel arrangement, which has been proposed to be the most stable/favorable configuration for the above-mentioned CR mesophases in water, probably because it avoids close contact between the sulfonate groups of neighboring molecules.[18]

The type(s) of guest packing (H- or J-aggregates, or possibly even a mixture of the two as reported previously for perylene tetracarboxylate intercalated in a LDH[72]) present in the material CR-LDH cannot be unambiguously determined from the powder XRD data alone. However, the absorption spectrum for CR-LDH points to the prevalence of J-type aggregates. This is further substantiated by the excitation spectra obtained for different concentrations of CR in DMSO

solution, where the progressive increase in concentration leads to the appearance of two bands (one sharp at λ>600 nm) at longer and shorter wavelengths, as will be discussed below.

Sun and co-workers studied the intercalation (by ion-exchange) of CR into arachidic acid/LDH hybrid films and concluded that the CR molecules formed head-to-tail J-type aggregates with a tilt angle of 31º with respect to the sheet surface (estimated from polarized UV-Vis absorption spectra and low-angle XRD).[76] This near-horizontal (parallel to the layers) arrangement is markedly different from the inclined (tilt angle of ca. 50º) orientation proposed here for the J-aggregate present in CR-LDH.

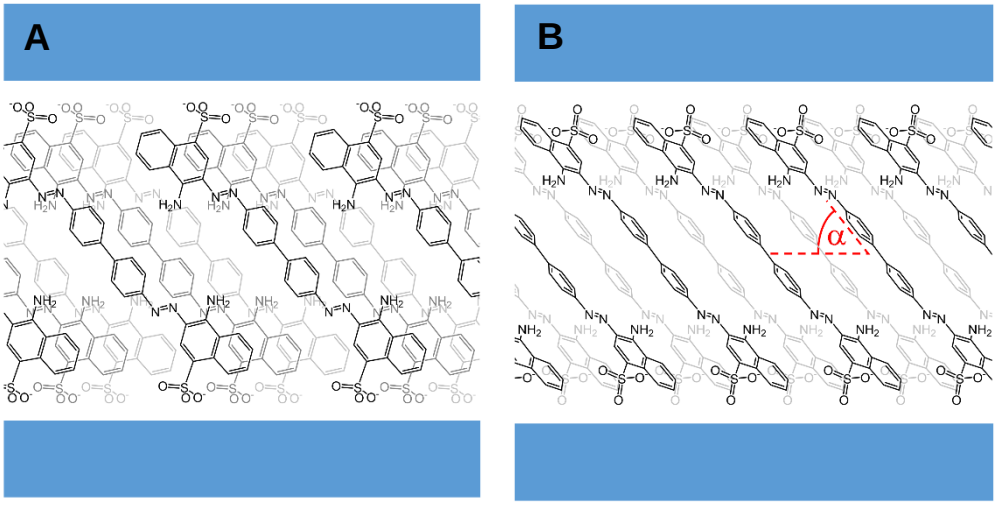

Figure 2.12 - Schematic representation of possible arrangements for CR anions between the brucite-like layers in the material CR-LDH: (**A**) Face-to-face alignment, which allows an optimum interaction between sulfonate groups and the host layers, (**B**) slipped coplanar inclined alignment.

2.4.2 Scanning Electron Microscopy (SEM)

Scanning electron microscopy (SEM) studies showed that the morphology of the sample CR-LDH consisted of irregular aggregates of plate-like particles (Figure 2.13).

2.4.3 Thermogravimetry

Thermogravimetric analysis (TGA) revealed a 10.2% mass loss from ambient temperature up to 200 ºC, attributed to removal of interlayer water molecules, followed by a further loss of 7.4% up to 350 ºC (DTG_{max} = 275 ºC), attributed to dehydroxylation of the hydroxide layers (Figure 14). Decomposition of intercalated CR anions takes place in the interval 350-670 ºC (44.8% mass loss in two overlapping steps with DTG_{max} = 510 and 560 ºC). The composition of CR-LDH as deduced

from elemental analysis (C, H, N and S) and thermogravimetry (water content) is $[Zn_4Al_2(OH)_{12}][(CR)_{0.86}(CO_3)_{0.14}(H_2O)_7]$. The CR content indicates that the anionic dye in effect balances about 86% of the positive charge of the hydroxide layers. In the proposed composition, carbonate anions counterbalance the remaining 14%.

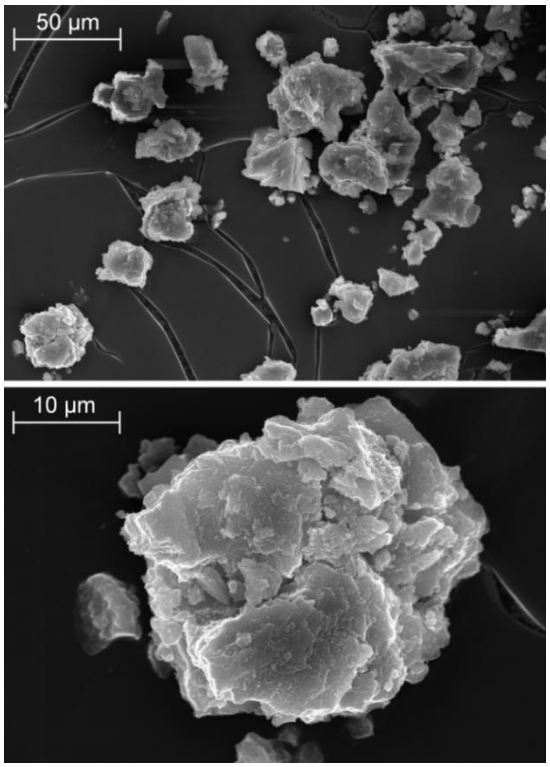

Figure 2.13 - Representative SEM image of CR-LDH at two different magnifications.

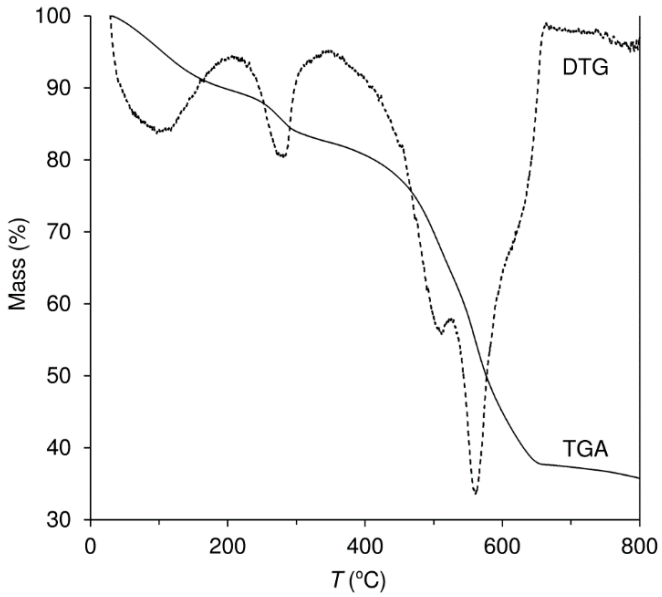

Figure 2.14 - TGA curve and corresponding DTG trace of CR-LDH.

However, as described below, the IR spectrum of CR-LDH does not support the presence of significant amounts of carbonate (or nitrate) ions. Hence, the carbonate content may be less than that represented by the above composition. As proposed previously for composites of perylene bisimide dyes and LDHs,[71] it is possible that part of the residual positive charge is counterbalanced by hydroxide anions, i.e., the sample may contain a minor amount of a Zn-Al-OH phase.

2.4.4 FTIR, Raman and $^{13}C\{^{1}H\}$ MAS NMR spectroscopies

The material CR-LDH was further characterized by spectroscopic techniques to confirm the presence of structurally intact CR anions. The $^{13}C\{^{1}H\}$ MAS NMR spectra of CR-LDH and the CR disodium salt (Figure 2.15) match very well and exhibit four broad peaks at about 115 (C^{6}), 125 ($C^{2,3,5,7\text{-}9,11\text{-}14}$), 138 ($C^{4,10}$) and 150 ($C^{1}$) ppm.

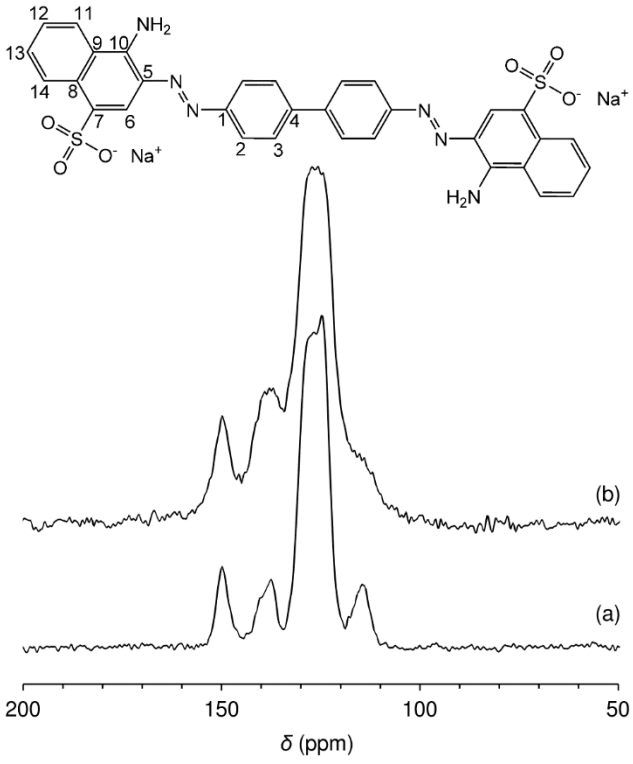

Figure 2.15 - $^{13}C\{^{1}H\}$ MAS NMR spectra of (a) the disodium salt of CR and (b) CR-LDH. Chemical structure of the Congo Red molecule, showing the numbering scheme for the ^{13}C NMR assignments.

As shown in Figures 2.16 and 2.17, the FT-IR and FT-Raman spectra of CR-LDH in the range 300-1800 cm^{-1} are dominated by bands due to the intercalated chromophore. In general, the bands are coincident with those displayed by the CR disodium salt, with only minor frequency shifts being observed. In the FT-IR spectrum of CR-LDH, the absorption bands for the asymmetric and symmetric stretching vibrations of the sulfonate group appear at 1174 and 1043 cm^{-1}, respectively, which are essentially unshifted when compared with those for Na_2CR (1176, 1045 cm^{-1}). Similarly, towards higher frequency, both Na_2CR and CR-LDH exhibit a broad band at 1612 cm^{-1} and a weak band at 1508 cm^{-1}, which are assigned to the aromatic ring C–C stretching vibrations.[35] Near-identical frequencies for these vibrations were reported by Tripathy and co-workers for a multilayer composite film of a polyelectrolyte, poly(dimethyl diallylammonium chloride) (PDAC), and CR.[35] As mentioned above, no bands characteristic of either carbonate [$\nu_3(CO_3^{2-})$ at 1365 cm^{-1}] or nitrate [$\nu_3(NO_3^-)$ at 1383 cm^{-1}] are present in the IR spectrum of CR-LDH. The Raman spectra of Na_2CR and CR-LDH are very similar in the range of 800-1800 cm^{-1} (Figure 2.17). Bands at 1156 (phenyl-N= stretching mode), 1376 (naphthyl ring C–C stretching mode), 1401, 1451 (–N=N– stretching), and 1592 cm^{-1} (phenyl ring C–C stretching mode) for the salt Na_2CR are all present for CR-LDH. Of these, only the phenyl-N= stretching mode shifts by more than 2 cm^{-1} (5 cm^{-1} to lower frequency) upon intercalation of the dye molecule. In summary, the vibrational spectra confirm the successful intercalation of structurally intact CR anions in the composite CR-LDH. The data do not reveal any configurational change of the azo group (trans-cis isomerization) upon formation of CR-LDH.[77]

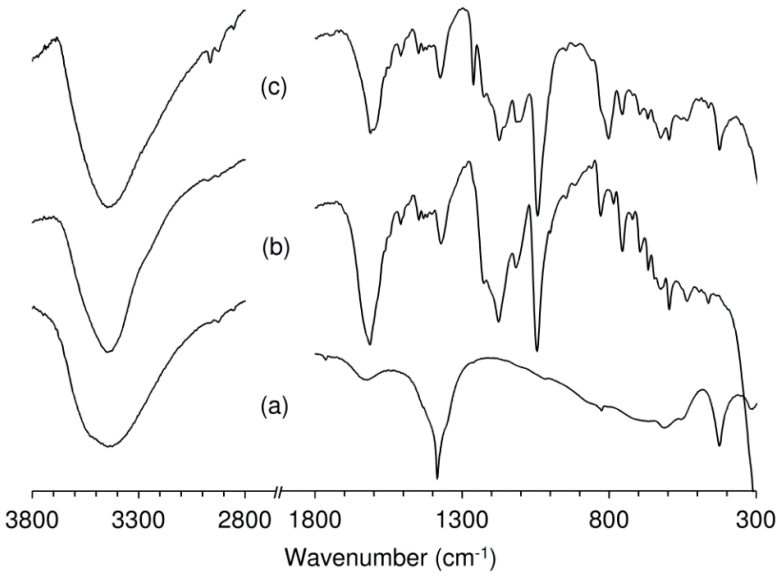

Figure 2.16 - Selected regions of the FT-IR spectra of (a) NO_3-LDH, (b) Na_2CR and (c) CR-LDH.

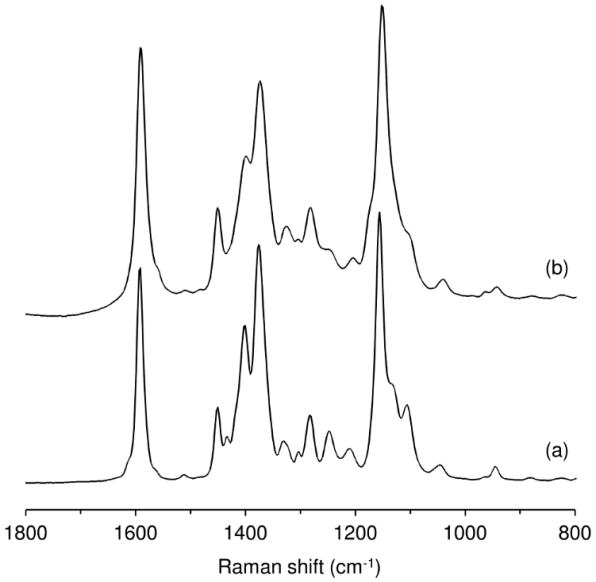

Figure 2.17 - FT-Raman spectra in the range of 800-1800 cm^{-1} for (a) the sodium salt of CR and (b) CR-LDH.

2.5 Photophysical characterization in the solid-state

A detailed photophysical characterization was performed (when it was possible) using for that different techniques like UV/Vis absorption, fluorescence emission and time-resolved measurements, in order to understand how the molecules are organized in the surrounded environment at a molecular level.

The absorption and fluorescence spectra recorded in the solid-state for CR-LDH and the CR disodium salt are compared in Figure 2.18 with the solution spectra obtained for Na_2CR in water and in DMSO. The spectrum for CR-LDH is red-shifted relative to both of the solution spectra, which is a direct consequence of the different electrostatic interactions present between the dye and the inorganic layers in the host-guest compound. Comparison of the solid-state spectra for Na_2CR and CR-LDH reveals the appearance of a shoulder at ~700 nm for the latter, which indicates the formation of J-type aggregates, according to exciton theory.[51, 78] The intermolecular π-π interaction involving the conjugated ring system of the azo dye CR is the driving force for the formation of slipped cofacial J-type aggregates of CR.[35]

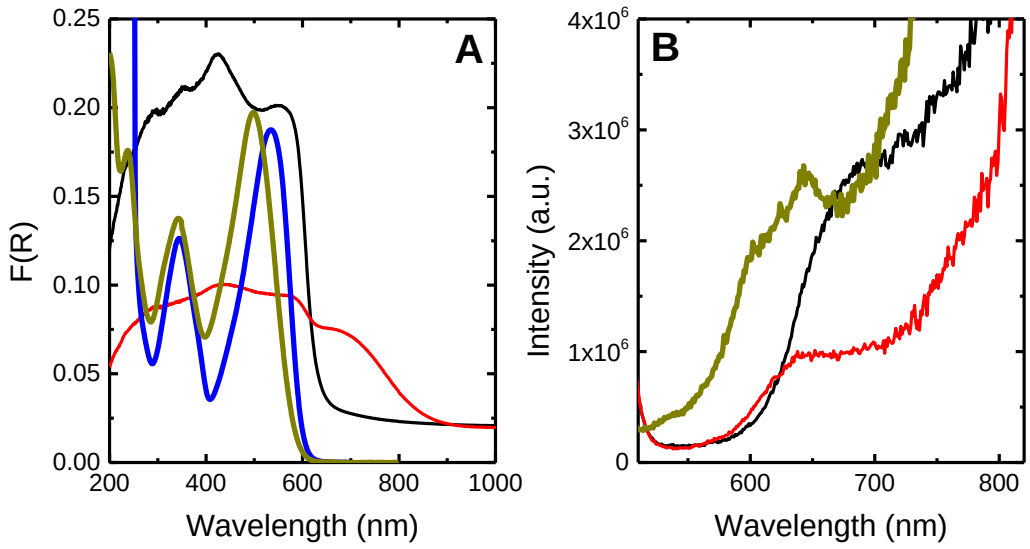

Figure 2.18 - (**A**) Diffuse reflectance spectra (Kubelka-Munk scale) in the range of 200-1000 nm for Na_2CR in the solid-state (black), CR-LDH (red), Na_2CR in DMSO with C = 4.12×10^{-6} M (blue) and Na_2CR in water with C = 5.27×10^{-6} M (dark yellow). (**B**) Fluorescence emission spectra (λ_{exc} = 497 nm) of Na_2CR in the solid-state (black), CR-LDH (red) and Na_2CR in water with C = 5.27×10^{-6} M (dark yellow).

The fluorescence emission spectrum of the CR disodium salt in the solid state shows a broad band at 685 nm. Upon incorporation of CR in the LDH to give the composite material CR-LDH, the band (although broad) blue-shifts to 640 nm (Fig. 2.18B). However, it is interesting to note that for both the CR disodium salt in the solid state and the LDH, the emission spectra are red-shifted relative to the solution spectra (more so in the case of CR in the solid state), which seems to be in line with the preferential formation of J-type aggregates. Due to the very low fluorescence of CR, it was not possible to measure reliable quantum yields and time-resolved parameters for Na_2CR and CR-LDH in the solid-state.

2.6 Conclusions

In this chapter a CR-LDH material was synthesized successfully by the direct coprecipitation method. The characterization data for the CR-LDH intercalation compound suggest that a similar type of slipped cofacial J-type aggregate of the dye is assembled within the interlayer region. From the photophysical characterization of CR in DMSO and for concentrations above ca. 3×10^{-5} M the fluorescence excitation spectra support the formation of oblique or twisted J-type aggregates of the dye.

2.7 References

1. Heyne, B., Self-Assembly Of Organic Dyes In Supramolecular Aggregates. *Photochemical & Photobiological Sciences* **2016,** *15* (9), 1103.

2. Chen, Z.; Lohr, A.; Saha-Moller, C. R.; Wurthner, F., Self-Assembled [Small Pi]-Stacks Of Functional Dyes In Solution: Structural And Thermodynamic Features. *Chemical Society Reviews* **2009,** *38* (2), 564.

3. Würthner, F.; Kaiser, T. E.; Saha-Möller, C. R., J-Aggregates: From Serendipitous Discovery to Supramolecular Engineering of Functional Dye Materials. *Angewandte Chemie International Edition* **2011,** *50* (15), 3376.

4. Möbius, D., Scheibe Aggregates. *Advanced Materials* **1995,** *7* (5), 437.

5. Rodríguez, H. B.; San Román, E., Effect of Concentration on the Photophysics of Dyes in Light-Scattering Materials. *Photochemistry and Photobiology* **2013,** *89* (6), 1273.

6. Chen, C.-T., Evolution of Red Organic Light-Emitting Diodes: Materials and Devices. *Chemistry of Materials* **2004,** *16* (23), 4389.

7. Mei, J.; Leung, N. L. C.; Kwok, R. T. K.; Lam, J. W. Y.; Tang, B. Z., Aggregation-Induced Emission: Together We Shine, United We Soar! *Chemical Reviews* **2015,** *115* (21), 11718.

8. Gsänger, M.; Bialas, D.; Huang, L.; Stolte, M.; Würthner, F., Organic Semiconductors based on Dyes and Color Pigments. *Advanced Materials* **2016,** *28* (19), 3615.

9. Pardo, R.; Zayat, M.; Levy, D., Photochromic Organic-Inorganic Hybrid Materials. *Chemical Society Reviews* **2011,** *40* (2), 672.

10. Lebeau, B.; Innocenzi, P., Hybrid Materials For Optics And Photonics. *Chemical Society Reviews* **2011,** *40* (2), 886.

11. Latterini, L.; Nocchetti, M.; Aloisi, G. G.; Costantino, U.; Elisei, F., Organized Chromophores In Layered Inorganic Matrices. *Inorganica Chimica Acta* **2007,** *360* (3), 728.

12. Yan, D.; Lu, J.; Wei, M.; Evans, D. G.; Duan, X., Recent Advances In Photofunctional Guest/Layered Double Hydroxide Host Composite Systems And Their Applications: Experimental And Theoretical Perspectives. *Journal of Materials Chemistry* **2011,** *21* (35), 13128.

13. Merino, E., Synthesis Of Azobenzenes: The Coloured Pieces Of Molecular Materials. *Chemical Society Reviews* **2011,** *40* (7), 3835.

14. Hunger, K., *Industrial Dyes: Chemistry, Properties, Applications*. Wiley-VCH: Germany, **2003**.

15. Bandara, H. M. D.; Burdette, S. C., Photoisomerization In Different Classes Of Azobenzene. *Chemical Society Reviews* **2012,** *41* (5), 1809.

16. Han, M.; Cho, S. J.; Norikane, Y.; Shimizu, M.; Kimura, A.; Tamagawa, T.; Seki, T., Multistimuli-Responsive Azobenzene Nanofibers With Aggregation-Induced Emission Enhancement Characteristics. *Chemical Communications* **2014,** *50* (99), 15815.

17. Spólnik, P.; Król, M.; Stopa, B.; Konieczny, L.; Piekarska, B.; Rybarska, J.; Zemanek, G.; Jagusiak, A.; Piwowar, P.; Szoniec, G.; Roterman, I., Influence Of The Electric Field On Supramolecular Structure And Properties Of Amyloid-Specific Reagent Congo Red. *European Biophysics Journal* **2011,** *40* (10), 1187.

18. Skowronek, M.; Stopa, B.; Konieczny, L.; Rybarska, J.; Piekarska, B.; Szneler, E.; Bakalarski, G.; Roterman, I., Self-Assembly Of Congo Red—A Theoretical And Experimental Approach To Identify Its Supramolecular Organization In Water And Salt Solutions. *Biopolymers* **1998,** *46* (5), 267.

19. Stopa, B.; Jagusiak, A.; Konieczny, L.; Piekarska, B.; Rybarska, J.; Zemanek, G.; Król, M.; Piwowar, P.; Roterman, I., The Use of Supramolecular Structures as Protein Ligands. *Journal of Molecular Modeling* **2013,** *19* (11), 4731.

20. Panczyk, T.; Wolski, P.; Jagusiak, A.; Drach, M., Molecular Dynamics Study of Congo Red Interaction with Carbon Nanotubes. *RSC Advances* **2014,** *4* (88), 47304.

21. Neumann, B.; Pollmann, P., Effect of pressure on the uv-vis spectra of acid red 266, benzopurpurine 4b and congo red in water and ethane-1,2-diol up to 2400 bar. *Physical Chemistry Chemical Physics* **2001,** *3* (20), 4508.

22. Frid, P.; Anisimov, S. V.; Popovic, N., Congo Red and protein aggregation In Neurodegenerative Diseases. *Brain Research Reviews* **2007,** *53* (1), 135.

23. Lendel, C.; Bolognesi, B.; Wahlström, A.; Dobson, C. M.; Gräslund, A., Detergent-like Interaction of Congo Red with the Amyloid β Peptide. *Biochemistry* **2010,** *49* (7), 1358.

24. Howie, A. J.; Brewer, D. B., Optical properties of amyloid stained by Congo red: History and mechanisms. *Micron* **2009,** *40* (3), 285.

25. Wu, C.; Scott, J.; Shea, J.-E., Binding of Congo Red to Amyloid Protofibrils of the Alzheimer Aβ9–40 Peptide Probed by Molecular Dynamics Simulations. *Biophysical Journal* **2012,** *103* (3), 550.

26. Cooper, T. M.; Stone, M. O., Investigation of Self-Assembly upon Formation of an Electrostatic Complex of Congo Red and a Helical Peptide. *Langmuir* **1998,** *14* (23), 6662.

27. Yamamoto, H.; Nakazawa, A.; Hayakawa, T., Induced optical activity in the complex of poly-l-lysine with azo dyes. *Journal of Polymer Science: Polymer Letters Edition* **1983,** *21* (2), 131.

28. Edwards, R. A.; Woody, R. W., Spectroscopic studies of Cibacron Blue and Congo Red bound to dehydrogenases and kinases. Evaluation of dyes as probes of the dinucleotide fold. *Biochemistry* **1979,** *18* (23), 5197.

29. Vasconcelos, D. N. d.; Ximenes, V. F., Albumin-induced circular dichroism in Congo red: Applications for studies of amyloid-like fibril aggregates and binding sites. *Spectrochimica Acta Part A: Molecular and Biomolecular Spectroscopy* **2015,** *150*, 321.

30. Yamaki, S. B.; Barros, D. S.; Garcia, C. M.; Socoloski, P.; Oliveira, O. N.; Atvars, T. D. Z., Spectroscopic studies of the intermolecular interactions of Congo red and tinopal CBS with modified cellulose fibers. *Langmuir* **2005,** *21* (12), 5414.

31. Mao, C.-F.; Hsu, M.-C.; Hwang, W.-H., Physicochemical characterization of grifolan: Thixotropic properties and complex formation with Congo Red. *Carbohydrate Polymers* **2007,** *68* (3), 502.

32. Katmiwati, E.; Nakanishi, T., Dye sorption and swelling of poly(vinyl alcohol) hydrogels in Congo red aqueous solution. *Macromolecular Research* **2014,** *22* (7), 731.

33. Barkauskas, J.; Dakševič, J.; Juškėnas, R.; Mažeikienė, R.; Niaura, G.; Račiukaitis, G.; Selskis, A.; Stankevičienė, I.; Trusovas, R., Nanocomposite films and coatings produced by interaction between graphite oxide and Congo red. *Journal of Materials Science* **2012,** *47* (15), 5852.

34. Ariga, K.; Lvov, Y.; Kunitake, T., Assembling Alternate Dye−Polyion Molecular Films by Electrostatic Layer-by-Layer Adsorption. *Journal of the American Chemical Society* **1997,** *119* (9), 2224.

35. He, J. A.; Bian, S. P.; Li, L.; Kumar, J.; Tripathy, S. K.; Samuelson, L. A., Photochemical behavior and formation of surface relief grating on self-assembled polyion/dye composite film. *Journal of Physical Chemistry B* **2000,** *104* (45), 10513.

36. Tao, X.; Li, J.; Möhwald, H., Self-assembly, optical behavior, and permeability of a novel Capsule based on an azo dye and polyelectrolytes. *Chemistry – A European Journal* **2004,** *10* (14), 3397.

37. Kurczewska, J.; Schroeder, G., The bifunctionality of silica gel modified with Congo red. *Central European Journal of Chemistry* **2011,** *9* (1), 41.

38. Onida, B.; Bonelli, B.; Flora, L.; Geobaldo, F.; Arean, C. O.; Garrone, E., Permeability of micelles in surfactant-containing MCM-41 silica as monitored by embedded dye molecules. *Chemical Communications* **2001,** (21), 2216.

39. Borello, L.; Onida, B.; Barolo, C.; Edler, K. J.; Arean, C. O.; Garrone, E., Accessibility of dye molecules embedded in surfactant-silica hybrid materials in both powder and film forms. *Sensors and Actuators B-Chemical* **2004,** *100* (1-2), 107.

40. Rivolo, P.; Pirasteh, P.; Chaillou, A.; Joubert, P.; Kloul, M.; Bardeau, J. F.; Geobaldo, F., Oxidised porous silicon impregnated with Congo Red for chemical sensoring applications. *Sensors and Actuators B: Chemical* **2004,** *100* (1), 99.

41. Pavan, F. A.; Schwingel Ribeiro, E.; Gushikem, Y., Congo Red immobilized on a silica/aniline xerogel: preparation and application as an amperometric sensor for ascorbic acid. *Electroanalysis* **2005,** *17* (7), 625.

42. Chouket, A.; Cherif, B.; Salah, N. B.; Khirouni, K., Optical and electrical properties of porous silicon impregnated with Congo Red dye. *Journal of Applied Physics* **2013,** *114* (24), 243105.

43. Wu, B.; Zhang, W. H.; Ren, Z. G.; Lang, J. P., A 1D anionic coordination polymer showing superior Congo Red sorption and its dye composite exhibiting remarkably enhanced photocurrent response. *Chemical Communications* **2015,** *51* (80), 14893.

44. Gültek, A.; Gökçen, Y.; Köytepe, S.; Seçkin, T., Synthesis and characterization of novel sulfonated hybrid Congo Red membranes from chlorofunctionalized silsesquioxanes for fuel cell application. *Macromolecular Symposia* **2010,** *296* (1), 92.

45. Hu, B.; Dai, F.; Fan, Z.; Ma, G.; Tang, Q.; Zhang, X., Nanotheranostics: Congo Red/Rutin-MNPs with enhanced magnetic resonance imaging and H2O2-responsive therapy of Alzheimer's disease in APPswe/PS1dE9 transgenic mice. *Advanced Materials* **2015,** *27* (37), 5499.

46. Iwunze, M. O., Aqueous Photophysical parameters of Congo Red. *Spectroscopy Letters* **2010,** *43* (1), 16.

47. Strickler, S. J.; Berg, R. A., Relationship between absorption intensity and fluorescence lifetime of molecules. *Journal of Chemical Physics* **1962,** *37* (4), 814.

48. Márquez, F.; Sabater, M. J., Emission frequency modulation by electronic confinement effect: Congo Red incorporated within a dendritic structure. *The Journal of Physical Chemistry B* **2005,** *109* (35), 16593.

49. Yokoyama, K.; Fisher, A.; Amori, A.; Welchons, D.; McKnight, R., Spectroscopic and calorimetric studies of Congo Red dye-amyloid peptide complexes. *J. Biophys. Chem* **2010,** *3*, 153.

50. Kasha, M., Energy transfer mechanisms and the molecular exciton model for molecular aggregates1, 2. *Radiation Research* **2012,** *178* (2), AV27.

51. Kasha, M.; Rawls, H.; El-Bayoumi, M., The Exciton Model in Molecular Spectroscopy. *Pure and Applied Chemistry* **1965,** *11* (3-4), 371.

52. Douglas, P.; Burrows, H. D.; Evans, R. C., Foundations of Photochemistry: A Background on the Interaction Between Light and Molecules. In *Applied Photochemistry*, Evans, R. C.; Douglas, P.; Burrow, H. D., Eds. Springer Netherlands: Dordrecht, **2013**; pp 1-88.

53. James, T., *The Theory of Photographic Process*. 3rd ed.; Macmillan: New York, **1966**.

54. Dean, J. C.; Oblinsky, D. G.; Rafiq, S.; Scholes, G. D., Methylene Blue Exciton States Steer Nonradiative Relaxation: Ultrafast Spectroscopy of Methylene Blue Dimer. *The Journal of Physical Chemistry B* **2016,** *120* (3), 440-454.

55. Deng, Y.; Yuan, W.; Jia, Z.; Liu, G., H- and J-Aggregation of Fluorene-Based Chromophores. *The Journal of Physical Chemistry B* **2014,** *118* (49), 14536.

56. Bujdák, J.; Iyi, N., Spectral properties and structure of the J-aggregates of pseudoisocyanine dye in layered silicate films. *Journal of Colloid and Interface Science* **2008,** *326* (2), 426.

57. Kobayashi, T., *J-Aggregates*. World Scientific Publishing Co. Pte. Ltd.: Singapore, **2012**.

58. Cui, G.; Guan, P.-J.; Fang, W.-H., Photoinduced Proton Transfer and Isomerization in a Hydrogen-Bonded Aromatic Azo Compound: A CASPT2//CASSCF Study. *The Journal of Physical Chemistry A* **2014,** *118* (26), 4732.

59. Becker, R. S., *Theory and Interpretation of Fluorescence and Phosphorescence*. Wiley-Interscience: New York, **1969**.

60. Turro, N., *Modern Molecular Photochemistry* University Science Books: California **1991**.

61. Pigorsch, E.; Elhaddaoui, A.; Turrell, S., Spectroscopic study of pH and solvent effects on the structure of Congo Red and its binding mechanism to amyloid-like proteins. *Spectrochimica Acta Part a-Molecular and Biomolecular Spectroscopy* **1994,** *50* (12), 2145.

62. Snellenburg, J. J.; Laptenok, S.; Seger, R.; Mullen, K. M.; van Stokkum, I. H. M., Glotaran: A Java-Based Graphical User Interface for the R Package TIMP. *2012* **2012,** *49* (3), 22.

63. Horng, M. L.; Gardecki, J. A.; Papazyan, A.; Maroncelli, M., Subpicosecond Measurements of Polar Solvation Dynamics: Coumarin 153 Revisited. *The Journal of Physical Chemistry* **1995,** *99* (48), 17311.

64. Stratt, R. M.; Maroncelli, M., Nonreactive Dynamics in Solution: The Emerging Molecular View of Solvation Dynamics and Vibrational Relaxation. *The Journal of Physical Chemistry* **1996,** *100* (31), 12981.

65. Costantino, U.; Coletti, N.; Nocchetti, M.; Aloisi, G. G.; Elisei, F., Anion Exchange of Methyl Orange into Zn−Al Synthetic Hydrotalcite and Photophysical Characterization of the Intercalates Obtained. *Langmuir* **1999,** *15* (13), 4454.

66. Iyi, N.; Kurashima, K.; Fujita, T., Orientation of an Organic Anion and Second-Staging Structure in Layered Double-Hydroxide Intercalates. *Chemistry of Materials* **2002,** *14* (2), 583.

67. Abellán, G.; Coronado, E.; Martí-Gastaldo, C.; Ribera, A.; Jordá, J. L.; García, H., Photo-Switching in a Hybrid Material Made of Magnetic Layered Double Hydroxides Intercalated with Azobenzene Molecules. *Advanced Materials* **2014,** *26* (24), 4156.

68. Ojala, W. H.; Ojala, C. R.; Gleason, W. B., The x-Ray crystal-structure of the sulfonated azo-dye Congo-Red, a nonpeptidic inhibitor of HIV-1 protease which also binds to reverse-transcriptase and amyloid proteins. *Antiviral Chemistry & Chemotherapy* **1995,** *6* (1), 25.

69. Rad, F. A.; Rezvani, Z.; Khodam, F., Molecular design confirmation for proposition of improved photophysical properties in a dye-intercalated layered double hydroxides. *RSC Advances* **2016,** *6* (14), 11193.

70. Yan, D.; Zhao, Y.; Wei, M.; Liang, R.; Lu, J.; Evans, D. G.; Duan, X., Regular assembly of 9-fluorenone-2,7-dicarboxylate within layered double hydroxide and its solid-state photoluminescence: a combined experiment and computational study. *RSC Advances* **2013,** *3* (13), 4303.

71. Adachi, K.; Watanabe, K.; Yamazaki, S., pH-Responsive Switchable Aggregation Phenomena of Xanthene Dyes Adsorbed on Tungsten(VI) Oxide Colloid Surface. *Industrial & Engineering Chemistry Research* **2014,** *53* (33), 13046.

72. Bauer, J.; Behrens, P.; Speckbacher, M.; Langhals, H., Composites of perylene chromophores and layered double hydroxides: Direct synthesis, characterization; and photo- and chemical stability. *Advanced Functional Materials* **2003,** *13* (3), 241.

73. Yan, D.; Lu, J.; Wei, M.; Ma, J.; Evans, D. G.; Duan, X., A combined study based on experiment and molecular dynamics: perylene tetracarboxylate intercalated in a layered double hydroxide matrix. *Physical Chemistry Chemical Physics* **2009,** *11* (40), 9200.

74. Gago, S.; Costa, T.; Seixas de Melo, J.; Goncalves, I. S.; Pillinger, M., Preparation and photophysical characterisation of Zn-Al layered double hydroxides intercalated by anionic pyrene derivatives. *Journal of Materials Chemistry* **2008,** *18* (8), 894.

75. Costa, A. L.; Gomes, A. C.; Pillinger, M.; Gonçalves, I. S.; de Melo, J. S. S., An Indigo Carmine-Based Hybrid Nanocomposite with Supramolecular Control of Dye Aggregation and Photobehavior. *Chemistry – A European Journal* **2015,** *21* (34), 12069.

76. Wang, J.; Ren, X. M.; Feng, X. S.; Liu, S. Y.; Sun, D. J., Study of assembly of arachidic acid/LDHs hybrid films containing photoactive dyes. *Journal of Colloid and Interface Science* **2008,** *318* (2), 337.

77. Miura, T.; Yamamiya, C.; Sasaki, M.; Suzuki, K.; Takeuchi, H., Binding mode of Congo Red to Alzheimer's amyloid beta-peptide studied by UV Raman spectroscopy. *Journal of Raman Spectroscopy* **2002,** *33* (7), 530.

78. McRae, E., *The Molecular exciton Model in Physical processes in Radiation Biology*. Academic Press: New York, **1964**.

3. AN INDIGO CARMINE-BASED LDH WITH CONTROL OF DYE AGGREGATION

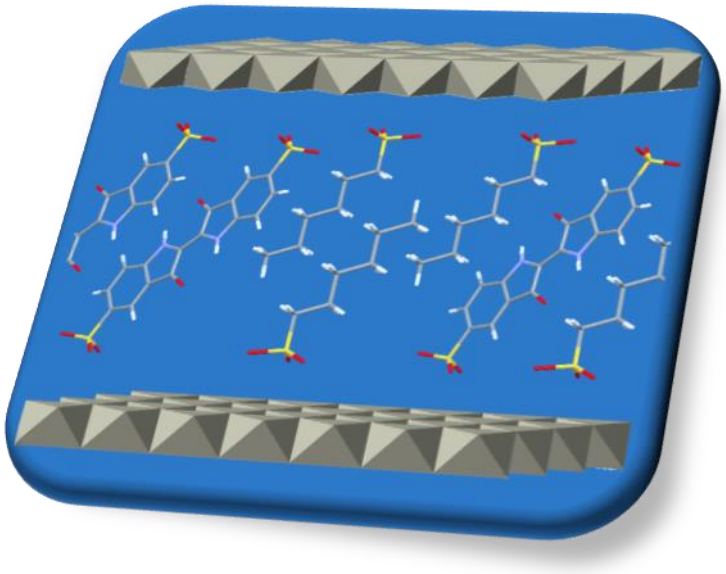

3.1 Introduction

The formation of dye aggregates within the LDH galleries can cause fluorescence quenching, as observed in the previous chapter with CR incorporated in a Zn,Al-LDH[1] and, for instance, for a perylene bisimide incorporated in a Zn-Al LDH.[2] One approach to decrease the local concentration of LDH-intercalated dyes consists in lowering the host layer charge density by increasing the M^{2+}/M^{3+} molar ratio. Wei and co-workers did, indeed, find that the separation of benzocarbazole anions intercalated into Mg-Al LDHs could be increased by raising the Mg/Al ratio, which suppressed the aggregation of the dye.[3] Another strategy to isolate incorporated molecules is to cointercalate the dye with an anionic surfactant.[4-14] In these composites the surfactant can modulate the fluorescence performance by providing the fluorophore with a homogeneous nonpolar environment that inhibits nonradiative processes (or at least decreases the contribution of this deactivation pathway) and prevents dye aggregation.

In this chapter, Zn-Al LDHs containing intercalated indigo carmine (IC-LDH) and the surfactant 1-hexanesulfonate (HS-LDH) have been prepared by a coprecipitation route. Four cointercalated hybrid materials consisting of IC and HS in different proportions have also been prepared. Here, is presented data on the chemical, thermal and structural characterization of the materials obtained, together with a comprehensive photophysical characterization including absorption, steady-state and time-resolved fluorescence of IC in solution or in the solid phase (pure disodium salt or intercalated in the Zn-Al LDH).

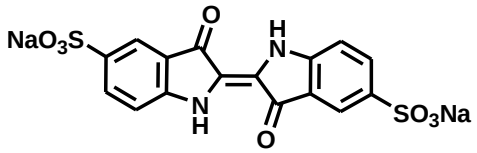

Indigo carmine (IC)

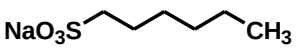

1-Hexanesulfonate (HS)

Scheme 3.1 – Structures and acronyms of Indigo carmine and the surfactant 1-hexaneesulfonate.

3.2 Synthesis of IC-LDH and cointercalated samples with different loadings of IC and HS

A Zn-Al LDH intercalated by indigo carmine dianions was prepared by coprecipitation of the Zn^{2+} and Al^{3+} hydroxides (initial Zn^{2+}/Al^{3+} molar ratio = 2) in the presence of an aqueous Na_2IC solution at a constant pH of 7.5–8, followed by aging of the gel at 65 °C for 18 h under inert atmosphere. Having prepared and characterized the LDH sample containing intercalated IC anions, cointercalated samples containing IC and an organosulfonate surfactant were prepared. Ideally, the arrangement and orientation of IC anions in the cointercalated samples should be, as far as possible, similar to that for the LDH containing solely the organic dye. Hence, the first step was to identify a surfactant molecule

that, when intercalated under the synthesis conditions used for IC-LDH, would give an LDH with a basal spacing close to IC. The best candidate was found to be 1-hexanesulfonate (HS).

Following the preparation of HS-LDH, the same method was used to prepare the cointercalated LDH samples IC(*x*%)/HS-LDH, where *x*% is the final molar percentage of IC present in the isolated solids (calculated *vs*. the total content of IC + HS). Four different samples were prepared by varying the molar percentage of Na_2IC in the starting solutions (2.51, 1.16, 0.53 and 0.25 mol%). As carried out for IC-LDH and HS-LDH, the reactions were performed using a 100% excess of organosulfonate anions over that theoretically required to balance the positive charge of the hydroxide layers in the final LDH. The obtained materials are shown in Figure 3.1.

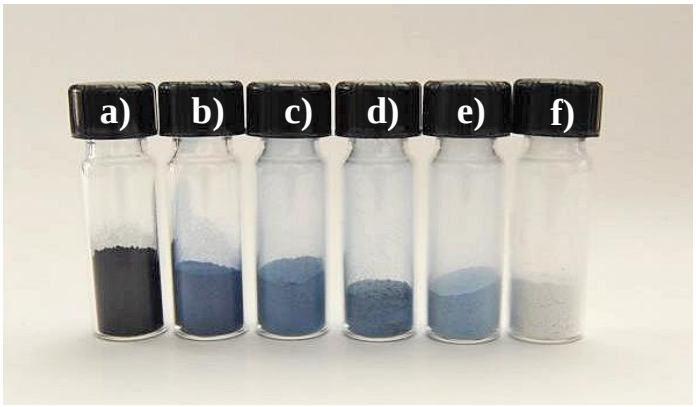

Figure 3.1 – Digital photos of a) IC-LDH, b) IC(3.9%)/HS-LDH, c) IC(2.2%)/HS-LDH, d) IC(1.1%)/HS-LDH, e) IC(0.6%)/HS-LDH and f) HS-LDH.

3.3 Structural characterization of the LDH materials

3.3.1 Powder X-Ray Diffraction (PXRD)

The powder X-ray diffraction pattern of the resultant deep blue solid, denoted IC-LDH, exhibits five fairly broad, equally spaced peaks between 3.5 and 30º 2θ, which can be indexed as 00*l* reflections for an expanded hydrotalcite-type phase with a basal spacing (d_{003}) of 17.6 Å (Figure 3.2). Relatively weak and asymmetric peaks above 30º 2θ are assigned as overlapping non-basal reflections. Subtraction of 4.8 Å (for the brucite-like layer thickness) from the basal spacing gives a gallery height of 12.8 Å. The crystal structure of a polymorphic form of Na_2IC was recently described.[5] Based on the reported data, the length of the indigo carmine anion, *i.e.*, the distance between two sulfonate groups, is 17.4-18.0 Å, when the van der Waals radius of oxygen is assumed to be 1.4 Å. Hence, a perpendicular orientation of guest molecules (17.4-18.0 Å) between the layers (12.8 Å) is not compatible with the observed gallery height.

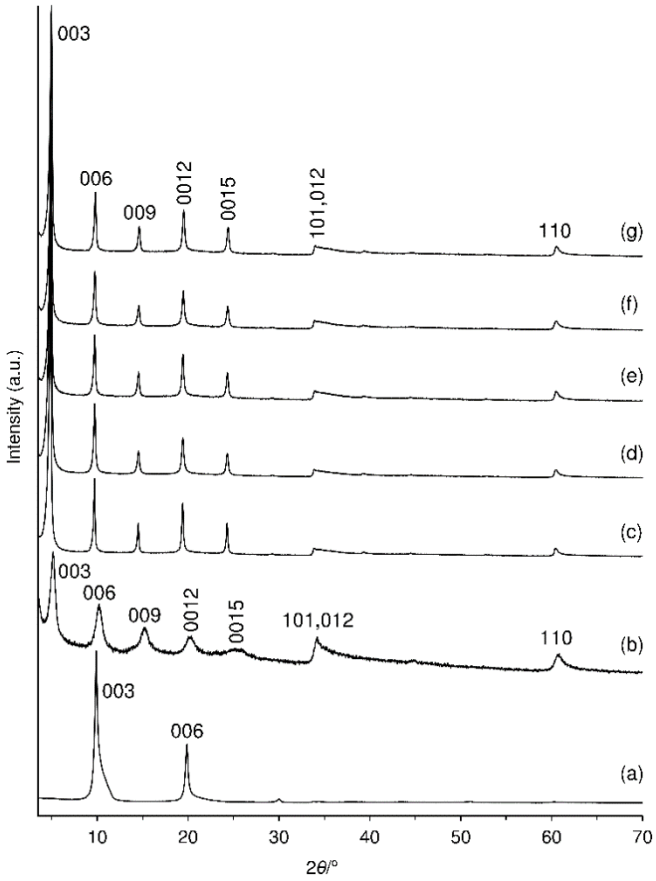

Figure 3.2 - Powder XRD patterns of (a) Zn-Al-NO_3, (b) IC-LDH, (c) HS-LDH, (d) IC(3.9%)/HS-LDH, (e) IC(2.2%)/HS-LDH, (f) IC(1.1%)/HS-LDH, and (g) IC(0.6%)/HS-LDH.

However, a tilted arrangement with the molecules inclined at an angle of *ca*. 45º with respect to the *c* axis seems possible, as shown in Figure 3.3. In this model the chromophore molecules are stacked in a J-type arrangement. This is in line with conclusions drawn from UV-Vis spectroscopy, as will be described in Section 3.4.3. A similar arrangement of guest species was proposed by Bauer *et al.* for composites of the tetra-anion of a perylene bisimide dye and LDHs.[2] The IC-LDH phase obtained in the present work is interesting since it differs from that previously reported. Thus, Kato *et al.*[15] and later Jung and Huh,[16] prepared Mg-Al and Zn-Al LDHs intercalated with indigo carmine by a similar direct synthesis route, but with Mg/Al and Zn/Al molar ratios of 3, and concluded that the IC dianions were arranged with their C=C axes almost perpendicular to the hydroxide layers, resulting in hydrotalcite-type phases with a basal spacing of about 22 Å.

The powder XRD pattern of the HS-LDH sample containing solely HS anions presents six sharp and symmetric 00*l* reflections between 3.5 and 30º 2θ, with a basal spacing (d_{003}) of 18.3 Å (Figure 3.2). The arrangement of HS anions between the layers cannot be unambiguously inferred from the observed basal spacing. However, two extreme possibilities can be proposed in which the HS molecules adopt either a tilted bilayer arrangement with extensive interdigitation (*i.e.*, an antiparallel

interpenetrating style) or a more strongly tilted bilayer arrangement with minimal interdigitation. Figure 3.3 shows a schematic representation of the former configuration for which the calculated basal spacing matches the observed value. Previous experimental and computational studies seem to support this packing mode for alkylsulfonates intercalated in LDHs.[17-19] The powder XRD patterns of the cointercalated LDH samples are all very similar to that displayed by HS-LDH (Figure 3.2). Only one series of (00*l*) reflections is observed and the basal spacing (18.2-18.3 Å) matches that observed for HS-LDH. The (003) reflection for the cointercalated samples is only slightly broader [half-peak width (fwhm) = 0.26-0.29º] than that for HS-LDH (fwhm = 0.23º), and no progressive increase in the fwhm occurs as *x* increases from 0.6 to 3.9%. For comparison, the fwhm of the (003) reflection for IC-LDH is 0.56º. These results suggest that IC and the surfactant HS disperse uniformly in the galleries of the LDH host in the cointercalated samples, forming a single homogeneous phase.

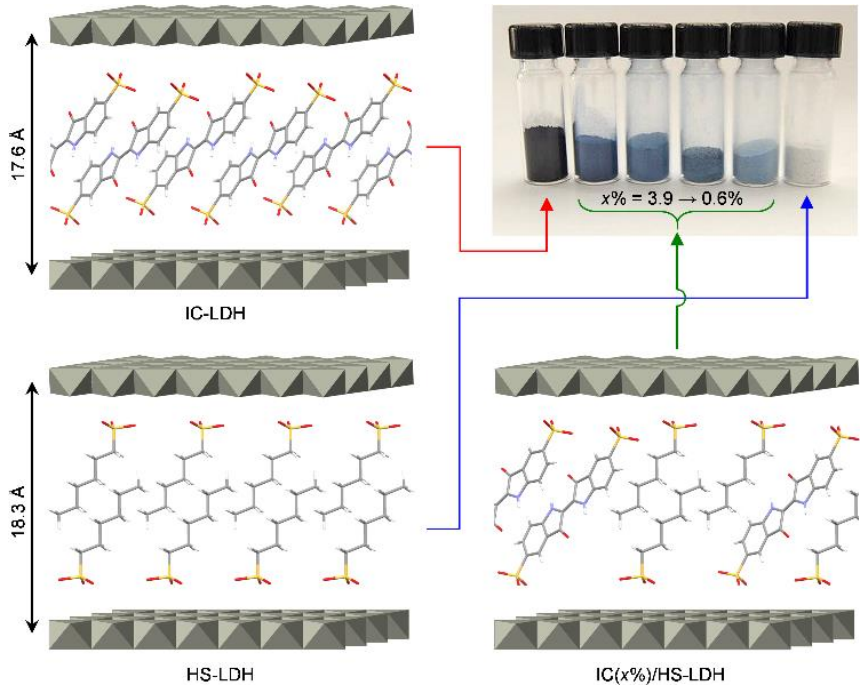

Figure 3.3 - Schematic representation of the possible arrangements of IC and HS anions between the brucite-like layers in the materials IC-LDH, HS-LDH, and IC(*x*%)/HS-LDH.

3.3.2 Fourier Transform Infrared spectroscopy

The FT-IR spectra of the sample IC-LDH confirm the presence of structurally intact indigo carmine anions. In particular, the 300-1800 cm^{-1} region of the IR spectrum of the intercalate is dominated by the bands due to IC, which are generally coincident with those displayed by the IC disodium salt (Figure 3.4). The absorption bands for the asymmetric and symmetric stretching vibrations of the sulfonate group appear at 1192 and 1026/1066 cm^{-1}, respectively, for IC-LDH, which are essentially unshifted compared with those for Na_2IC (1196, 1028/1064 cm^{-1}). Similarly, toward higher frequency, both Na_2IC and IC-LDH exhibit a strong band at 1615 cm^{-1}, which is assigned as a

C=C ring stretching vibration. Whereas the pure dye salt shows a single, sharp band at 1638 cm^{-1} for ν(C=O), IC-LDH shows two overlapping bands at *ca.* 1642 and 1654 cm^{-1}, which could be indicative of a change in the nature of the intramolecular and intermolecular N–H···O hydrogen bonding interactions. The absence of bands at *ca.* 1365 [$\nu_3(CO_3^{2-})$] or 1383 cm^{-1} [$\nu_3(NO_3^-)$] in the IR spectrum of IC-LDH indicates that the sample contains minimal or insignificant amounts of carbonate and nitrate.

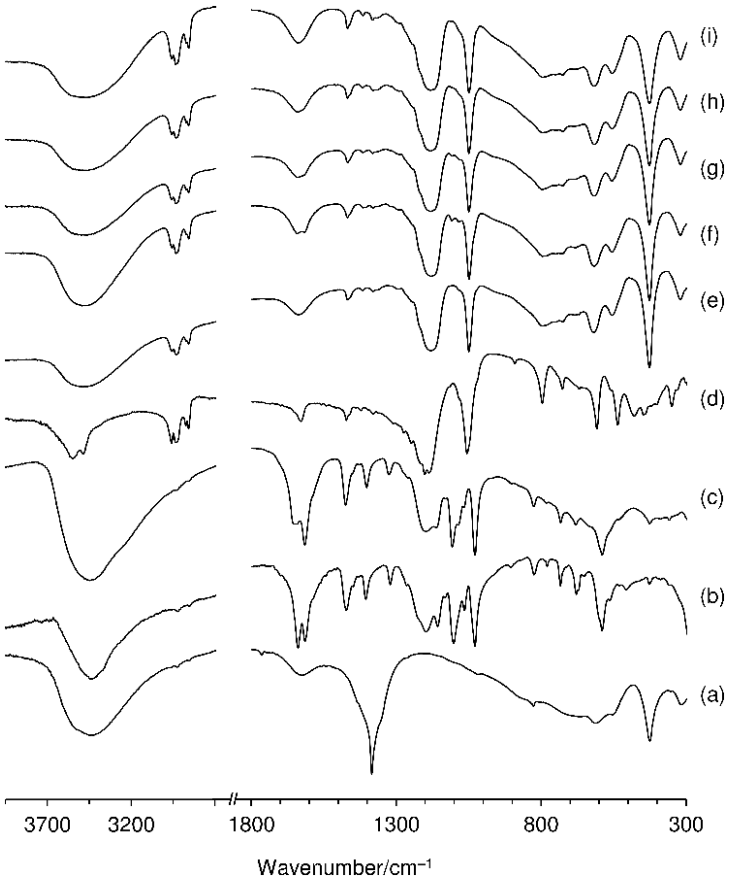

Figure 3.4 - FT-IR spectra in the regions 300-1800 cm^{-1} and 2700-3950 cm^{-1} of (a) NO_3-LDH, (b) Na_2IC, (c) IC-LDH, (d) NaHS, (e) HS-LDH, and the cointercalated samples IC(*x*%)/HS-LDH with *x* = 3.9 (f), 2.2 (g), 1.1 (h) and 0.6 (i).

The FT-IR spectra of the cointercalated samples essentially match that for HS-LDH (see Figure 3.4). The high-frequency region of the vibrational spectrum of HS-LDH (2700-3100 cm^{-1}) reveals the C–H stretching modes while the low-frequency region of 700-1500 cm^{-1} displays the stretching modes of the sulfonate group as well as, e.g., the scissoring and rocking modes of the methylene groups of HS. In general the bands associated with the alkyl chain are coincident with those observed for the pure sodium salt (NaHS). Concerning the headgroup vibrational region, the O=S=O stretching vibrations of the sulfonate group in HS shift from 1055 [$\nu_s(SO_3^-)$] and 1186/1201 cm^{-1} [$\nu_{as}(SO_3^-)$] for NaHS to 1049 and 1181 cm^{-1} for HS-LDH. These small down-shifts in frequency

upon intercalation are attributed to a diminished polarization of the S–O bonds in the SO_3^- groups by the diffusely charged double hydroxide layers, relative to the stronger polarization observed with Na^+ ions.[14] Below 700 cm^{-1}, the IR spectrum of HS-LDH contains several bands due to Zn/Al-OH lattice translation modes that are characteristic of Zn-Al LDHs (426, 555 and 615 cm^{-1}). A weak, broad band at about 1367 cm^{-1} is attributed to the presence of a small amount of carbonate ion. In the IR spectrum of IC(3.9%)/HS-LDH, some weak bands can be attributed to cointercalated IC anions, in particular those at 1617 [ν(C=C)] and 1641 cm^{-1} [ν(C=O)], which are superimposed on the broad water bending vibration. These two bands are also evident in the spectrum of IC(2.2%)/HS-LDH, albeit much weaker, and are not detectable in the spectra of IC(1.1%)/HS-LDH and IC(0.6%)/HS-LDH.

3.3.3 $^{13}C\{^1H\}$ CP MAS NMR spectroscopy

Figure 3.5 shows the $^{13}C\{^1H\}$ CP MAS NMR spectra of Na_2IC, IC-LDH, NaHS, HS-LDH and co-intercalated material with 3.9% of IC. The spectrum for the disodium salt of the dye is quite complex, with some of the carbon atoms displaying two distinct resonances. This may originate from the presence of non-equivalent indigo carmine molecules in the unit cell and/or non-equivalent indoxyl moieties within a single IC molecule. The spectrum of IC-LDH superimposes quite well with that for Na_2IC. On the whole the signals are broader for the intercalated molecules than for those in the sodium salt. Two distinct resonances continue to be observed (at 151.5 ppm and 154.5 ppm) for the benzene ring carbon atom (C^4) that is bonded to the NH group of the pyrrolidone ring.

For the NaHS, single resonances are observed for the carbon atoms in the $(CH_2)_3SO_3^-$ fragment ($C^{1\text{-}3}$), while each of the carbon atoms in the terminal propyl group ($C^{4\text{-}6}$) give rise to two distinct signals, which may be due to conformational heterogeneity in the solid state. In contrast, both LDH samples only present single resonances for all six carbon atoms, which is consistent with an ordered (essentially all-*anti*) conformation of the methylene chains, as schematically represented in Figure 3.3. Due to the low IC loading in IC(3.9%)/HS-LDH, it was not possible to clearly distinguish resonances between 100 and 200 ppm due to the carbon atoms of the intercalated anionic dye.

3.3.4 Scanning Electron Microscopy

SEM studies showed that the morphology of the sample IC-LDH consisted of irregular aggregates of flake-like particles (Figure 3.6). The composition of IC-LDH as deduced from energy dispersive X-ray spectrometry (EDS) analysis (Zn, Al), ICP-OES (Zn, Al), elemental analysis (C, H, N and S) and thermogravimetry (water content) is $[Zn_4Al_2(OH)_{12}][(IC)_{0.9}(CO_3)_{0.1}(H_2O)_6]$. As expected, the final Zn^{2+}/Al^{3+} molar ratio did not differ from the starting ratio of 2. The IC content indicates that the anionic dye in effect balances about 90% of the positive charge of the hydroxide layers. In the proposed composition, carbonate anions counterbalance the remaining 10%. As described above, the presence of measurable amounts of nitrate ions can be excluded on the basis of the FT-IR spectrum. In fact, as described above, FT-IR and $^{13}C\{^1H\}$ CP MAS NMR spectroscopic data for IC-LDH indicate

that the carbonate content may be less than that represented by the above composition. As proposed previously for composites of perylene bisimide dyes and LDHs,[2] it is possible that part of the residual positive charge is counterbalanced by hydroxide anions, *i.e.*, the sample may contain a minor amount of a Zn-Al-OH phase.

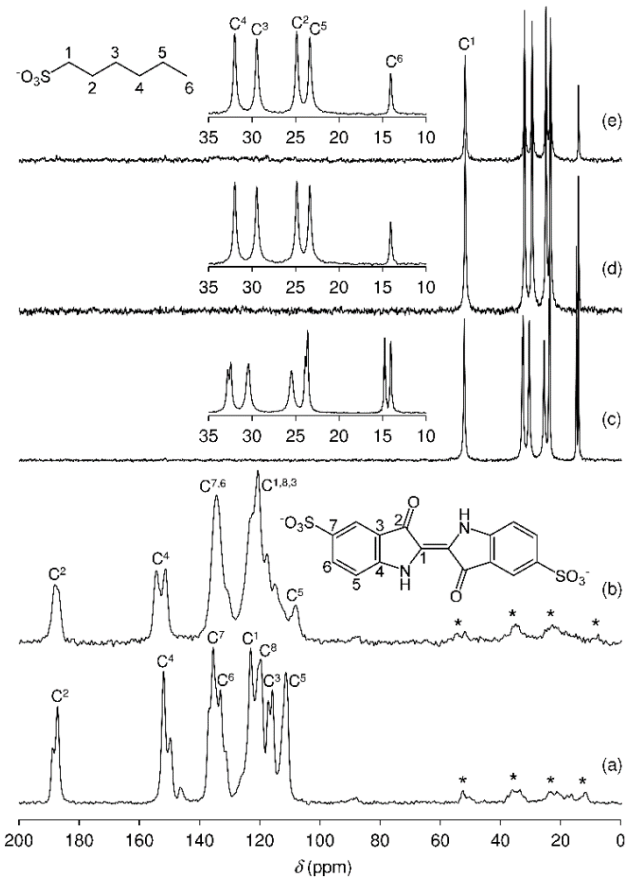

Figure 3.5 - $^{13}C\{^{1}H\}$ CP MAS NMR spectra of (a) Na_2IC, (b) IC-LDH, (c) NaHS, (d) HS-LDH, and the cointercalated sample IC(3.9%)/HS-LDH. Spinning sidebands are indicated by asterisks.

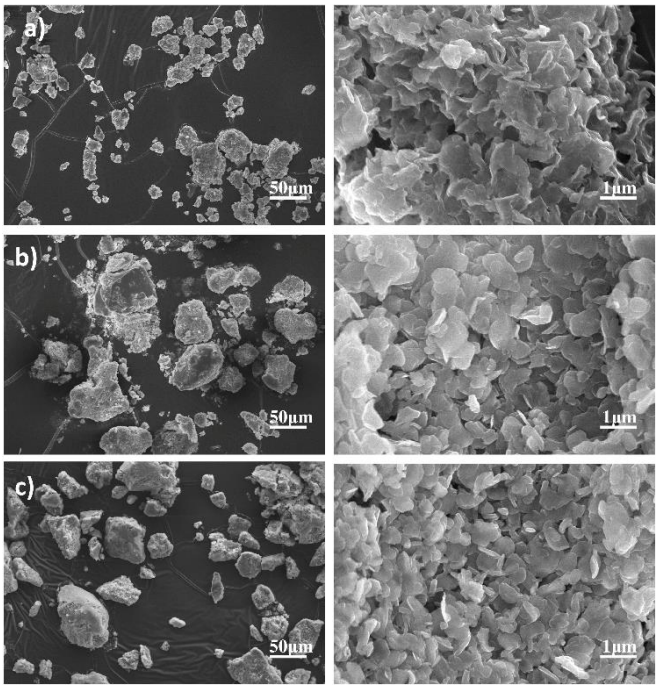

Figure 3.6 - Representative SEM images of a) IC-LDH, b) HS-LDH, and c) IC(3.9%)/HS-LDH.

All four samples in the series IC(x%)/HS-LDH (x = 0-3.9%) display a similar morphology to that observed for IC-LDH, comprising irregular aggregates of flake-like particles (Figure 3.6 and 3.7). EDS, ICP-OES, elemental and thermogravimetric analyses indicated final chemical compositions close to $[Zn_4Al_2(OH)_{12}][(HS)_a(IC)_b(CO_3)_{0.2}(H_2O)_5]$ (a + 2b = 1.6) The data consistently suggested that preferential intercalation of IC anions had occurred to the extent that the final x% values were 3.9, 2.2, 1.1, and 0.6 mol%, *i.e.*, the amount of IC intercalated (relative to that initially present in the starting solution) increased progressively from *ca.* 60% for IC(3.9%)/HS-LDH to 100% for IC(0.6%)/HS-LDH. The combined contents of IC and HS indicate that the organosulfonate anions in effect balance about 80% of the positive charge of the hydroxide layers. In the proposed composition, carbonate anions counterbalance the remaining 20%, although hydroxide anions may also be present, as discussed above for IC-LDH.

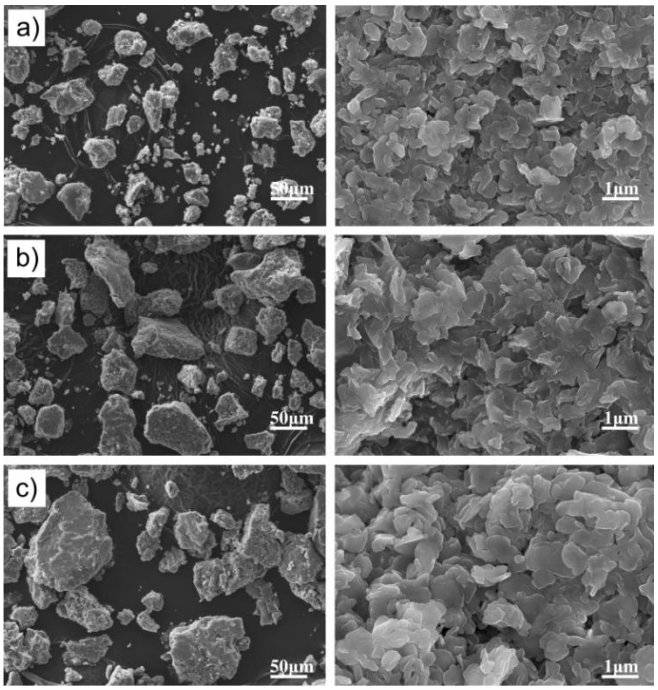

Figure 3.7 - Representative SEM images of (a) IC(2.2%)/HS-LDH, (b) IC(1.1%)/HS-LDH, and (c) IC(0.6%)/HS-LDH.

3.3.5 Thermogravimetric Analysis (TGA)

Thermogravimetric analysis of the sample IC-LDH revealed a 10.8% mass loss from ambient temperature up to 180 ºC, attributed to removal of interlayer water molecules, followed by a further loss of 8.7% up to 300 ºC, attributed to dehydroxylation of the hydroxide layers (Figure 3.8). Decomposition of intercalated IC anions takes place in the interval 350-600 ºC (DTG_{max} = 430 ºC). A final weight loss step of 2.7% takes place between 700 and 800 ºC, leaving a residual mass of 42.4%. If it is assumed that calcination of the LDH leads to a mixture of zinc oxide (zincite) and $ZnAl_2O_4$ (gahnite, spinel) phases (*i.e.*, a solid with the overall composition $Zn_4Al_2O_7$),[14, 20] the expected residual mass (calculated on the basis of the composition referred to above) is 42.2%, which is in excellent agreement with the observed value. For comparison, Figure 3.8 shows also the TGA curve for Na_2IC. The onset of decomposition of the organic dye anions is at 380 ºC, with DTG_{max} = 470 ºC. Hence, IC anions in the intercalate IC-LDH display slightly lower thermal stability than those in the pure sodium salt.

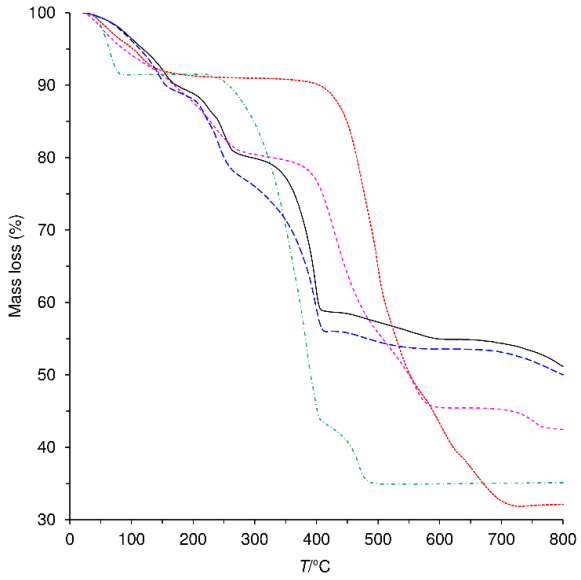

Figure 3.8 - TGA curves for NaHS (– · – ·), Na_2IC (·····), HS-LDH (– – –), IC-LDH (------), and IC(3.9%)/HS-LDH (——).

TGA curves for the samples IC(x%)/HS-LDH (x = 0-3.9%) were quite similar (Figure 3.8 and 3.9). For these surfactant-containing samples, the weight loss processes corresponding to removal of interlayer water molecules (25-165 ºC, 9.5-11.7%) and dehydroxylation of the hydroxide layers (180-280 ºC, 8.1-11.8%) are more clearly separated than those for IC-LDH. The onset of surfactant decomposition for HS-LDH and IC(3.9%)/HS-LDH is at 300-325 ºC, which is significantly higher than that for the pure sodium salt (225 ºC), suggesting that the intercalated HS anions are thermally more stable. Separate weight loss steps corresponding to decomposition of IC anions are not evident in the TGA curves of the cointercalated samples, even for the sample with the highest IC loading (x = 3.9%), presumably because these species decompose in the same temperature interval as that for the HS surfactant.

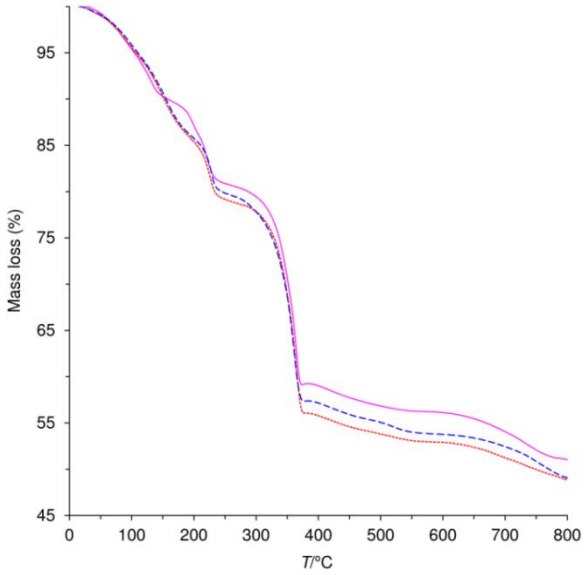

Figure 3.9 - TGA curves for IC(2.2%)/HS-LDH (——), IC(1.1%)/HS-LDH (------) and IC(0.6%)/HS-LDH (– – –).

3.4 Electronic spectra characterization

3.4.1 Singlet-state behavior of Indigo carmine in solution

A study of indigo carmine in solution was performed in order to further understand the behavior of the isolated molecule. Absorption, emission and excitation spectra of Na_2IC in DMF at a higher (3.34×10^{-4} M) and lower (7.43×10^{-6} M) concentrations are depicted in Figure 3.10. Spectra recorded for other concentrations are provided in Figure 3.11. At the highest concentration, the excitation spectrum (Figure 3.10C) shows two bands, which apparently suggests the simultaneous spectra of a mixture of J and H-aggregate type dimers.[2, 21]

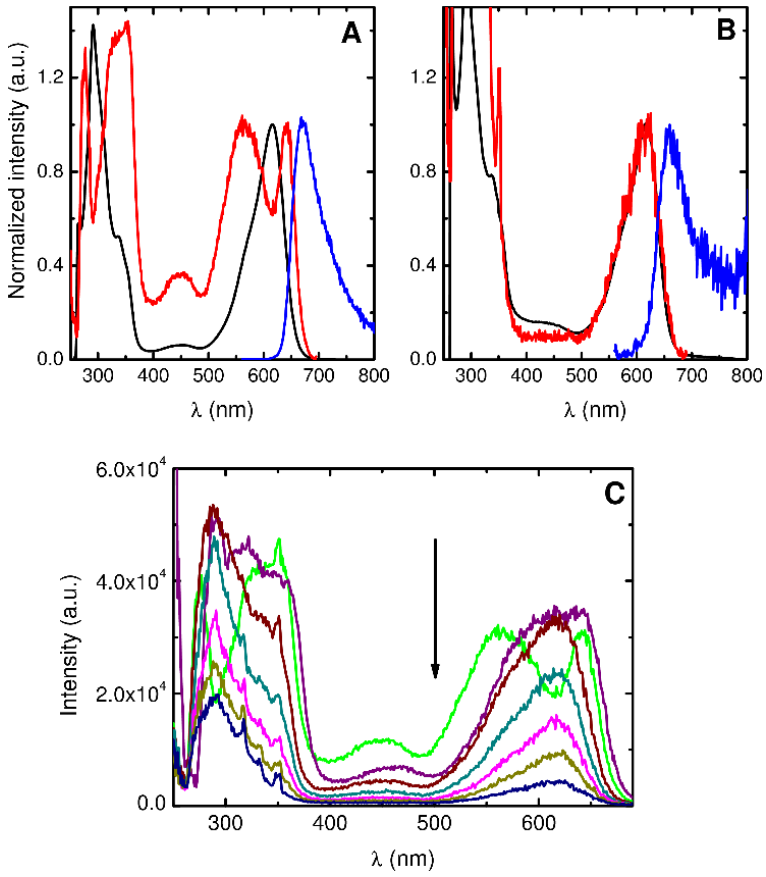

Figure 3.10 - Absorption (black line), fluorescence emission (blue line) and excitation (red line) spectra of Na_2IC in DMF with (**A**) C = 3.34 × 10^{-4} M and (**B**) C = 7.43 × 10^{-6} M. (**C**) Fluorescence excitation spectra of Na_2IC in DMF obtained with λ_{em} = 700 nm and C = 3.34 × 10^{-4} M (green line), C = 1.59 × 10^{-4} M (purple line), C = 1.01 × 10^{-4} M (wine line), C = 5.48 × 10^{-5} M (dark teal line), C = 2.71 × 10^{-5} M (magenta line), C = 1.46 × 10^{-5} M (dark yellow line) and C = 7.43 × 10^{-6} M (dark blue line).

More significantly, two observations can be made upon inspection of the excitation spectra measured for different concentrations and collected along the emission spectra (Figure 3.10C). Firstly, an additional band is observed in the 400-450 nm region when the spectra are collected at λ_{em} = 700 nm. Secondly, the visible ($S_1 \leftarrow S_0$) absorption band matches with the excitation spectra, particularly in the left part (higher wavelength values) of the spectra. This suggests that the emission spectra are reflecting a different level of interactions between the IC chromophores.

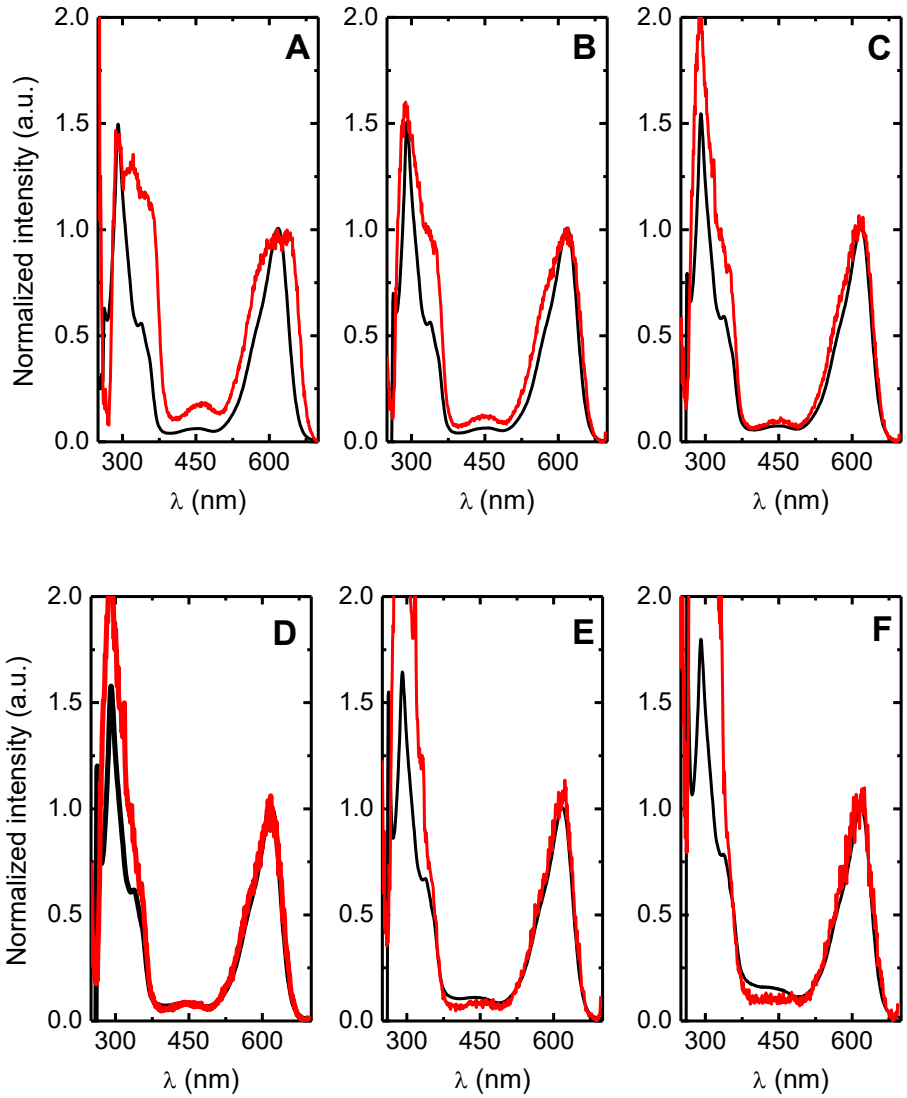

Figure 3.11 - Absorption (black line) and fluorescence excitation spectra (red line) of IC in DMF with (**A**) C = 1.59 × 10^{-4} M, (**B**) C = 1.01 × 10^{-4} M, (**C**) C = 5.48 × 10^{-5} M, (**D**) C = 2.71 × 10^{-5} M, (**E**) C = 1.46 × 10^{-5} M and (**F**) C = 7.43 × 10^{-6} M.

It is known that the main deactivation pathway of indigo excited state essentially occurs through the radiationless internal conversion decay channel and that it is associated with a fast proton transfer involving the excited state intramolecular proton transfer (ESIPT) between the N-H and C=O groups.[22-26] The same is true for IC where, in the case of water, intra and inter (to water) proton transfer may be present opening what can be considered a more efficient radiationless deactivation channel.[27] Time-resolved fluorescence was used to follow proton transfer reactions of indigo and indigo carmine in the excited state.[25, 27-28]

3.4.2 Indigo carmine in solution: Dynamic State Behavior

Time-resolved fluorescence decays of Na_2IC in methanol and DMF solutions, obtained with a picoled at 451 nm and fwhm = 70 ps, were found to be best fitted with single exponential decay times of 20 and 90 ps, respectively (see Figure 3.12).

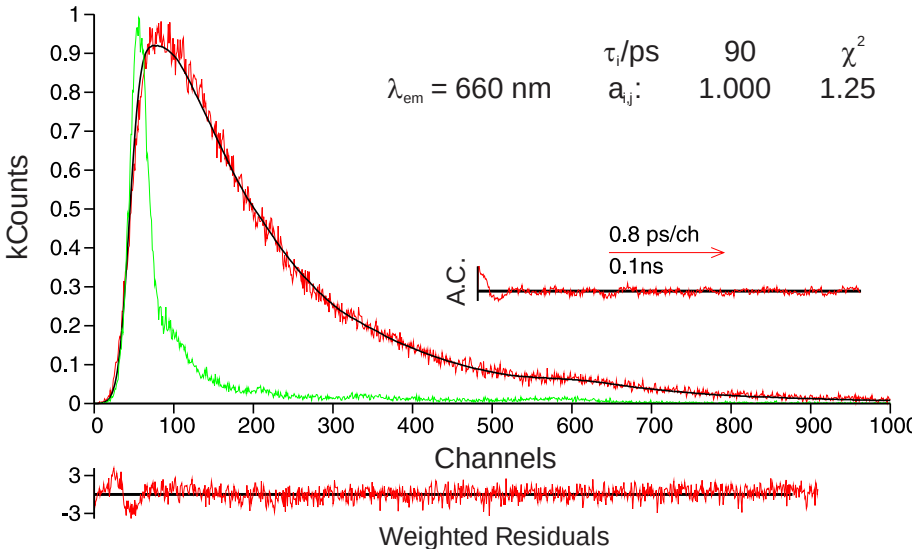

Figure 3.12. Mono-exponential analysis for the fluorescence decay collected at λ_{em} = 660 nm and pulse instrumental response obtained for indigo carmine in DMF at room temperature (λ_{exc} = 451 nm). The experimental conditions and obtained decay times are shown as insets in the figure. Also shown are the weighted residuals, autocorrelation functions (A.C.) and the χ^2 values for a better judgment of the quality of the fit.

However, when the time resolution is increased (fwhm = 22 ps) the decays become bi-exponential, mirroring the decay of the instantaneously formed keto excited form which gives rise to the excited enolic form (Figure 3.13 and Scheme 3.2).[26, 29] For the decays of IC, in DMF and methanol, the single components correspond to the enol form.

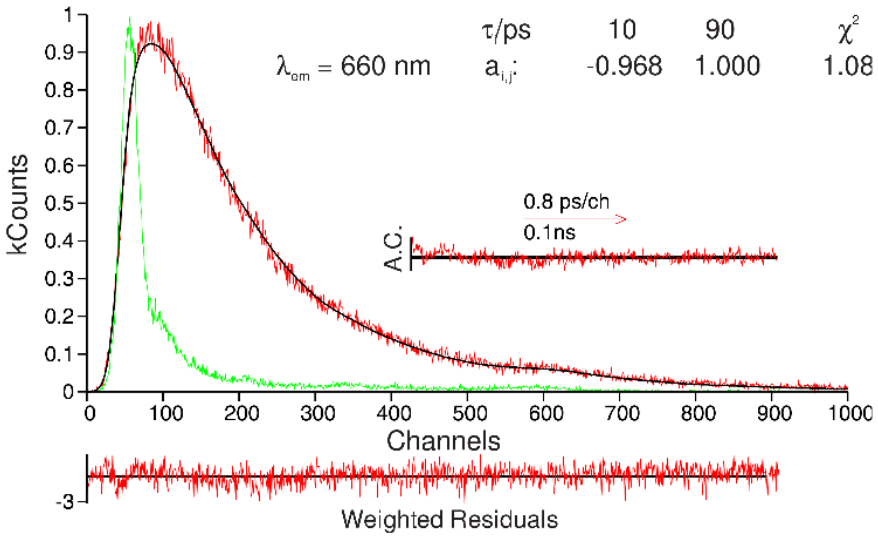

Figure 3.13 - Fluorescence decay collected at λ_{em} = 660 nm and pulse instrumental response obtained for Na_2IC in DMF at room temperature (λ_{exc} = 451 nm). The obtained decay times and pre-exponential factors are shown as insets. Also shown are the weighted residuals, autocorrelation functions (A.C.) and χ^2 values, for a better judgment of the quality of the fit.

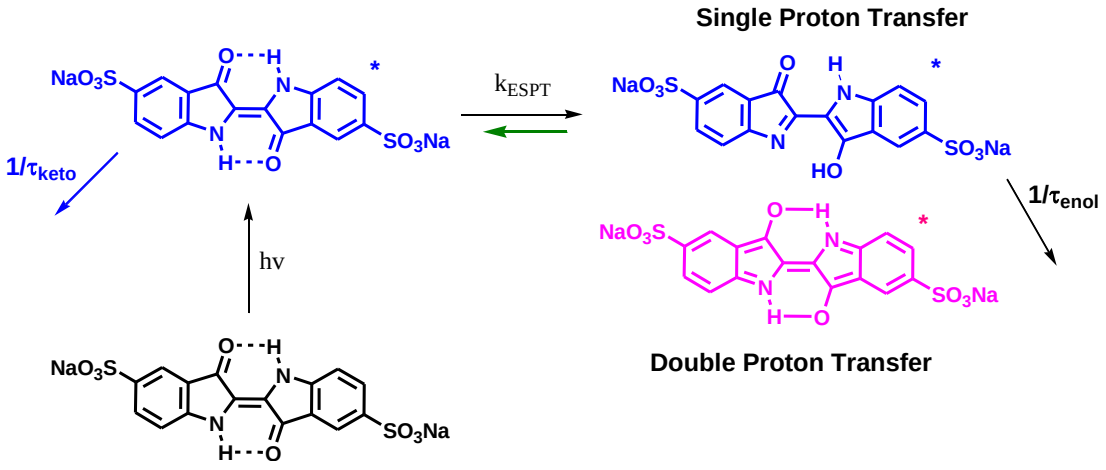

Scheme 3.2 – Schematic representation of the mechanism of kinetic scheme for ESPT for indigo carmine involving two processes: Single proton transfer (SPT) and Double proton transfer (DPT) [based on mechanism of ref[28]].

Although in the literature there is some debate about whether a single or double ESIPT reaction could be involved in the very efficient internal conversion path, with some recent theoretical[22, 30] and experimental studies using femto time resolution[31] on indigo carmine in favor of a single ESIPT process taking place in the subpicosecond-femtosecond time range, in our studies it is clear the ESIPT occurs in the subpicosecond time range.[29, 32] Moreover, and recently a joint experimental and

theoretical study has shown that the ESPT in indigo involves a single proton transfer.[28] Indeed, from the present study the fastest 7.04 ps decay time in DMF suggests that the instantaneously formed keto form of IC transfers its proton to the solvent with an intermolecular rate constant of ~1.4 × 10^{11} s^{-1}, whereas for methanol (with decay times of 8.14 ps and 19.4 ps) the now, likely to be, intramolecular proton transfer is made with a rate constant of ~1.2 × 10^{11} s^{-1}. The decay of the enol (tautomeric) form has a value of 20 ps (in DMF) and 90 ps (in DMSO), in good agreement with the values found by others,[33] where the slowest component of the decay was found to be 22 ps in methanol and 92 ps in DMSO.

3.4.3 LDH-supported indigo carmine

Figure 3.14 compares the absorption spectrum of indigo carmine in DMF with those acquired for LDH-supported IC, with and without cointercalated HS surfactant molecules. In the intercalated IC-LDH, the absorption spectrum of IC is red-shifted relative to the solution spectrum (Figure 3.14A), which is a direct consequence of the different (electrostatic) interactions existing between IC and the positively charged metal hydroxide layers. Comparison of the solid-state spectra for Na_2IC and IC-LDH reveals the appearance of a shoulder at ~ 850 nm for the latter, which likely indicates the formation of the J-aggregate type dimer, although with a different absorption maxima than that for the J-aggregate type dimer found in solution (at ~ 640 nm, see Figure 3.10). This is further enhanced upon introduction of the 1-hexanesulfonate surfactant generating the cointercalated composites IC(*x*%)/HS-LDH. Indeed, the latter present spectra that are clearly similar to that for the concentrated IC solution (Figure 3.10), showing the coexistence of monomer and dimer units.

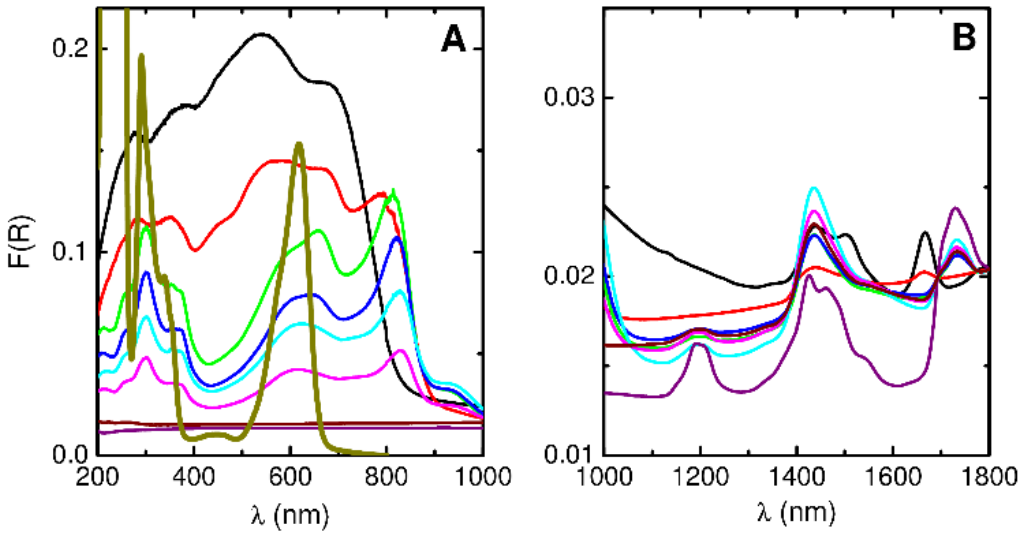

Figure 3.14 - Diffuse reflectance spectra (Kubelka-Munk scale) in the ranges of 200-1000 nm (**A**) and 1000-1800 nm (**B**) for Na_2IC in the solid-state (black line), IC-LDH (red line), the cointercalated samples IC(*x*%)/HS-LDH with HS/IC = 96.1:3.9 (green line), 97.8:2.2 (blue line), 98.9:1.1 (cyan line) and 99.4:0.6 (magenta line), NaHS (purple line), and HS-LDH (wine line). Panel **A** also shows the absorption spectrum of Na_2IC in DMF (dark yellow line; C = 3.34 × 10^{-4} M).

The fingerprint for the addition of HS into the IC-LDH system is the clear differentiation of the broad band observed in the solid (Na_2IC) and IC-LDH absorption spectra which is gradually split into the ~ 600 nm (monomer) and ~ 850 nm (dimer) bands. From this, an additional important consequence is evident, namely the different color mirrored by the different solid samples (Figure 3.1). The surfactant 1-hexanesulfonate plays an important role in preventing the aggregation of the IC dye. Especially noteworthy is the vibronic resolution present in the spectra of all IC(x%)/HS-LDH samples for the absorption band at ~ 300 nm. This band, which only appears in the presence of HS, matches with the band observed for IC in solution, thus showing that the IC molecule is in a more isolated environment when incorporated alongside an excess of HS anions in the LDH.

A more detailed analysis of the spectra in Figure 3.14 shows the absence of electronic transitions within the 200-1000 nm range for both the surfactant (purple line) and the HS-LDH (bordeaux line). However, in the 1000-1800 nm range (Figure 3.14B), additional bands are now observed. Three of these are due C–H stretching second overtone (1193 nm), O–H stretching first overtone (1435 nm), and CH_2, C–H stretching first overtone (1730 nm).[34] These three can be basically considered associated with the hydrated surfactant. In the case of Na_2IC (black line) and IC-LDH (red line), two additional bands are present in this region at 1500 nm (N–H stretching first overtone) and 1665 nm (C–H stretching first overtone in R–CH=CH–R' systems).[34] Both of these bands disappear when IC is cointercalated in the LDH with a large excess of HS anionic surfactant. This strongly suggests that it may be possible to use the N–H stretching band to monitor the IC-HS interaction. In particular, since it is the N-H stretching first overtone that vanishes this may indicate a loss of intermolecular interaction between the IC and remaining water molecules in the LDH cavity – resulting of the HS anionic surfactant intercalation – or between two (or more) IC molecules.

Further information can be obtained from fluorescence data in the solid state. However, due to very low fluorescence displayed by IC and high light dispersion of the samples, the time-resolved studies could not be considered conclusive. From the fluorescence emission spectra in Figure 3.15A it can be seen that an increase in the relative amount of HS leads to a blue-shifted emission band around 660 nm, which matches the emission band of IC in solution. Moreover, the fluorescence excitation spectra (Figure 3.15B) collected at 720 nm for the different IC(x%)/HS-LDH samples clearly show that, with increasing HS/IC molar ratio in the cointercalated systems, the spectra gradually approach that of IC in solution. Specifically, the excitation spectrum for solid Na_2IC shows three peaks at ~ 649 nm, 615 nm and 560 nm. Incorporation of IC into the LDH with increasing amounts of HS gradually leads to a single band with maxima at 615 nm and a band shape similar to that displayed by IC in solution. These observations clearly support the essential role of the alkylsulfonate surfactant in preventing dye aggregation.

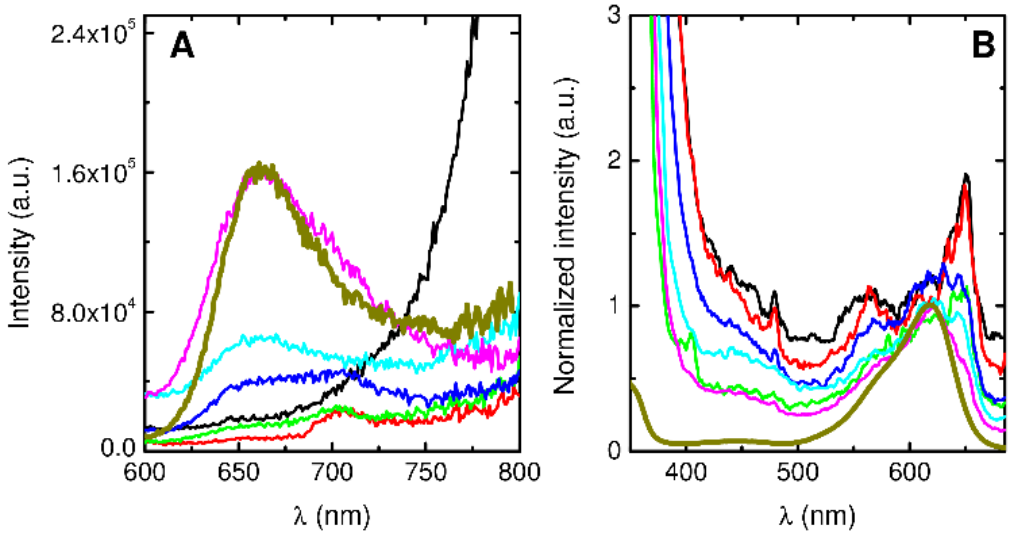

Figure 3.15 - (**A**) Fluorescence emission (λ_{exc} = 550 nm) and (**B**) excitation (λ_{em} = 720 nm) spectra of Na_2IC in the solid-state (black line), IC-LDH (red line), IC(*x*%)/HS-LDH with *x* = 3.9% (green line), 2.2% (blue line), 1.1% (cyan line) and 0.6% (magenta line), and Na_2IC in DMF (dark yellow line).

3.5 Conclusions

In summary, in this chapter it was described the preparation, through a direct coprecipitation route, of an indigo carmine/layered double hydroxide composite material. The intercalated IC molecules adopt a strongly tilted J-type arrangement within the LDH gallery regions. This packing arrangement is fully supported by solid-state UV-Vis absorption data. It was demonstrated that is possible to tune the color and the photophysical properties by varying the HS content – higher surfactant content leads to a better isolation of dye molecules. The photophysical properties of the intercalates shown to be strongly affected by the HS/IC ratio, demonstrating that the surfactant plays a critical role in suppressing the formation of aggregates.

3.6 References

1. Costa, A. L.; Gomes, A. C.; Pillinger, M.; Gonçalves, I. S.; Pina, J.; Seixas de Melo, J. S., Insights into the Photophysics and Supramolecular Organization of Congo Red in Solution and the Solid State. *ChemPhysChem* **2017,** *18* (5), 564.

2. Bauer, J.; Behrens, P.; Speckbacher, M.; Langhals, H., Composites of Perylene Chromophores and Layered Double Hydroxides: Direct Synthesis, Characterization, and Photo- and Chemical Stability. *Advanced Functional Materials* **2003,** *13* (3), 241.

3. Yan, D.; Lu, J.; Ma, J.; Wei, M.; Evans, D. G.; Duan, X., Benzocarbazole anions intercalated layered double hydroxide and its tunable fluorescence. *Physical Chemistry Chemical Physics* **2010,** *12* (45), 15085.

4. Zheng, S.; Lu, J.; Li, W.; Qin, Y.; Yan, D.; Evans, D. G.; Duan, X., The 2-phenylbenzimidazole-5-sulfonate/layered double hydroxide co-intercalation composite and its luminescence response to nucleotides. *Journal of Materials Chemistry C* **2014,** *2* (26), 5161.

5. Yao, M.; Kuratani, K.; Kojima, T.; Takeichi, N.; Senoh, H.; Kiyobayashi, T., Indigo carmine: An organic crystal as a positive-electrode material for rechargeable sodium batteries. *Sci. Rep.* **2014,** *4*.

6. Xu, S.-M.; Zhang, S.-T.; Shi, W.-Y.; Ning, F.-Y.; Fu, Y.; Yan, H., Understanding the thermal motion of the luminescent dyes in the dye-surfactant cointercalated ZnAl-layered double hydroxides: a molecular dynamics study. *RSC Advances* **2014,** *4* (88), 47472.

7. Dang, S.; Yan, D.; Lu, J., 8-Hydroxypyrene-1,3,6-trisulphonate and octanesulphonate co-assembled layered double hydroxide and its controllable solid-state luminescence by hydrothermal synthesis. *Journal of Solid State Chemistry* **2012,** *185* (0), 219.

8. Sun, Z.; Jin, L.; Shi, W.; Wei, M.; Evans, D. G.; Duan, X., Controllable Photoluminescence Properties of an Anion-Dye-Intercalated Layered Double Hydroxide by Adjusting the Confined Environment. *Langmuir* **2011,** *27* (11), 7113.

9. Yan, D.; Lu, J.; Ma, J.; Wei, M.; Qin, S.; Chen, L.; Evans, D. G.; Duan, X., Thin film of coumarin-3-carboxylate and surfactant co-intercalated layered double hydroxide with polarized photoluminescence: a joint experimental and molecular dynamics study. *Journal of Materials Chemistry* **2010,** *20* (24), 5016.

10. Shi, W.; Wei, M.; Evans, D. G.; Duan, X., Tunable photoluminescence properties of fluorescein in a layered double hydroxide matrix and its application in sensors. *Journal of Materials Chemistry* **2010,** *20* (19), 3901.

11. Shi, W.; Sun, Z.; Wei, M.; Evans, D. G.; Duan, X., Tunable Photoluminescence Properties of Fluorescein in a Layered Double Hydroxide Matrix by Changing the Interlayer Microenvironment. *The Journal of Physical Chemistry C* **2010,** *114* (49), 21070.

12. Yan, D.; Lu, J.; Wei, M.; Evans, D. G.; Duan, X., Sulforhodamine B Intercalated Layered Double Hydroxide Thin Film with Polarized Photoluminescence. *The Journal of Physical Chemistry B* **2009,** *113* (5), 1381.

13. Shi, W.; Wei, M.; Lu, J.; Evans, D. G.; Duan, X., Studies on the Orientation and Polarized Photoluminescence of α-Naphthalene Acetate in the Layered Double Hydroxide Matrix. *The Journal of Physical Chemistry C* **2009,** *113* (29), 12888.

14. Gago, S.; Costa, T.; Seixas de Melo, J.; Goncalves, I. S.; Pillinger, M., Preparation and photophysical characterisation of Zn-Al layered double hydroxides intercalated by anionic pyrene derivatives. *Journal of Materials Chemistry* **2008,** *18* (8), 894.

15. Park, I. Y.; Kuroda, K.; Kato, C., Direct synthesis of intercalation compounds between a layered double hydroxide and an anionic dye. *Journal of the Chemical Society, Dalton Transactions* **1990,** (10), 3071.

16. Jung, W. C.; Huh, Y. D., Synthesis of intercalation compounds between a layered double hydroxide and an anionic dye. *Bulletin of the Korean Chemical Society* **1996,** *17* (6), 547.

17. Xu, Z. P.; Braterman, P. S., Synthesis, structure and morphology of organic layered double hydroxide (LDH) hybrids: Comparison between aliphatic anions and their oxygenated analogs. *Applied Clay Science* **2010,** *48* (1–2), 235.

18. Zhang, H.; Xu, Z. P.; Lu, G. Q.; Smith, S. C., Intercalation of Sulfonate into Layered Double Hydroxide: Comparison of Simulation with Experiment. *The Journal of Physical Chemistry C* **2009,** *113* (2), 559.

19. Xu, Z. P.; Braterman, P. S., Competitive Intercalation of Sulfonates into Layered Double Hydroxides (LDHs): the Key Role of Hydrophobic Interactions. *The Journal of Physical Chemistry C* **2007,** *111* (10), 4021.

20. Costantino, U.; Coletti, N.; Nocchetti, M.; Aloisi, G. G.; Elisei, F.; Latterini, L., Surface Uptake and Intercalation of Fluorescein Anions into Zn−Al−Hydrotalcite. Photophysical Characterization of Materials Obtained. *Langmuir* **2000,** *16* (26), 10351.

21. Eisfeld, A.; Briggs, J. S., The J- and H-bands of organic dye aggregates. *Chemical Physics* **2006,** *324* (2-3), 376.

22. Cui, G.; Thiel, W., Nonadiabatic dynamics of a truncated indigo model. *Physical Chemistry Chemical Physics* **2012,** *14* (35), 12378.

23. Yamazaki, S.; Sobolewski, A. L.; Domcke, W., Molecular mechanisms of the photostability of indigo. *Physical Chemistry Chemical Physics* **2011,** *13* (4), 1618.

24. Iwakura, I.; Yabushita, A.; Kobayashi, T., Kinetic isotope effect on the proton-transfer in indigo carmine. *Chemical Physics Letters* **2010,** *484* (4–6), 354.

25. Iwakura, I.; Yabushita, A.; Kobayashi, T., Why is Indigo Photostable over Extremely Long Periods? *Chemistry Letters* **2009,** *38* (11), 1020.

26. Seixas de Melo, J.; Rondão, R.; Burrows, H. D.; Melo, M. J.; Navaratnam, S.; Edge, R.; Voss, G., Photophysics of an Indigo Derivative (Keto and Leuco Structures) with Singular Properties. *The Journal of Physical Chemistry A* **2006,** *110* (51), 13653.

27. Nagasawa, Y.; Taguri, R.; Matsuda, H.; Murakami, M.; Ohama, M.; Okada, T.; Miyasaka, H., The effect of hydrogen-bonding on the ultrafast electronic deactivation dynamics of indigo carmine. *Physical Chemistry Chemical Physics* **2004,** *6* (23), 5370.

28. Pina, J.; Sarmento, D.; Accoto, M.; Gentili, P. L.; Vaccaro, L.; Galvão, A.; Seixas de Melo, J. S., Excited-State Proton Transfer in Indigo. *The Journal of Physical Chemistry B* **2017,** *121* (10), 2308.

29. Seixas de Melo, J. S.; Rondão, R.; Burrows, H. D.; Melo, M. J.; Navaratnam, S.; Edge, R.; Voss, G., Spectral and Photophysical Studies of Substituted Indigo Derivatives in Their Keto Forms. *ChemPhysChem* **2006,** *7* (11), 2303.

30. Moreno, M.; Ortiz-Sanchez, J. M.; Gelabert, R.; Lluch, J. M., A theoretical study of the photochemistry of indigo in its neutral and dianionic (leucoindigo) forms. *Physical Chemistry Chemical Physics* **2013,** *15* (46), 20236.

31. Iwakura, I.; Yabushita, A.; Kobayashi, T., Transition State in a Prevented Proton Transfer Observed in Real Time. *Bulletin of the Chemical Society of Japan* **2011,** *84* (2), 164.

32. Rondao, R.; de Melo, J. S.; Schaberle, F. A.; Voss, G., Excited state characterization of a polymeric indigo. *Physical Chemistry Chemical Physics* **2012,** *14* (5), 1778.

33. Chatterley, A. S.; Horke, D. A.; Verlet, J. R. R., On the intrinsic photophysics of indigo: a time-resolved photoelectron spectroscopy study of the indigo carmine dianion. *Physical Chemistry Chemical Physics* **2012,** *14* (46), 16155.

34. Osborne, B. G.; Fearn, T.; Hindle, P. H., *Practical NIR Spectroscopy : With Applications in Food and Beverage Analysis*. 2nd ed.; Longman Singapore Publishers (Pte) Ltd. : Singapore, **1993**.

3. CONTROLLING THE FLUORESCENCE BEHAVIOR OF A LDH-SUPPORTED 1-PYRENESULFONATE

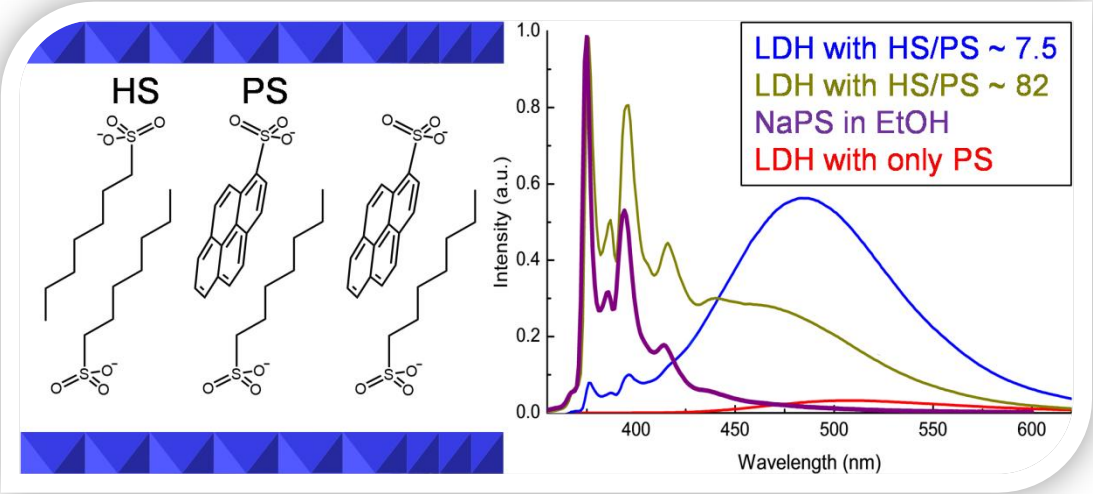

4.1 Introduction

As mentioned in the previous chapter, due to the low fluorescence displayed by IC, it was not possible to obtain a more in depth analysis of the photophysical characterization, in particular from the time-resolved measurements. Taking in consideration the studies done by Seixas de Melo *et al*.[1-9] in the past recent years relative to pyrene derivatives, a high emissive probe, and following on from our previous work[10] on the preparation and photophysical characterization of Zn-Al LDHs intercalated by anionic pyrene derivatives, herein the cointercalation of 1-pyrenesulfonate (PS) and 1-heptanesulfonate (HpS) in a Zn-Al LDH is reported.

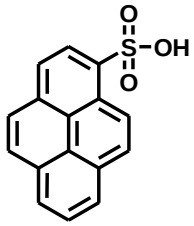

1-Pyrenesulfonate

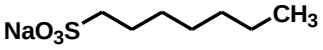

1-Heptanesulfonate (HpS)

Scheme 4.1 – Chemical structures and acronyms of 1-pyrenesulfonic acid and the surfactant 1-heptanesulfonate.

4.2 Synthesis and structural characterization

The direct synthesis method was used to prepare Zn-Al LDHs containing solely 1-pyrenesulfonate anions (denoted as PS-LDH) or an alkylsulfonate surfactant, or a mixture of the two. Previous work by Wei and co-workers showed that the cointercalation of alkylsulfonate surfactants and organic chromophores works best, both in terms of sample homogeneity and fluorescence performance, when the two guest anions are "size-matched".[11-12] Therefore, it was chosen 1-heptanesulfonate (HpS) since its length when fully extended (13.7 Å, which takes into account van der Waals radii for the terminal H and O atoms) is similar to that estimated for PS (12.7 Å).

Moreover, four different samples were prepared by varying the molar percentage of 1-pyrenesulfonate in the starting solutions (4.9, 2.3, 1.06 and 0.5 mol%) obtaining the cointercalated LDH samples PS(x%)/HpS-LDH, in which x% is the final molar percentage of PS present in the isolated solids (calculated *vs*. the total content of PS + HpS). As carried out for PS-LDH and HpS-LDH, the same method was used and the reactions were performed using a 100% excess of organosulfonate anions over that theoretically required for a final LDH with the ideal composition $Zn_2Al(OH)_6(A)\cdot nH_2O$.

4.2.1 Powder XRD

The powder XRD patterns of PS-LDH and HpS-LDH, recorded at ambient temperature in the range of 3.5-70º 2θ, present several reflections that are characteristic of hydrotalcite-like materials (Figure 4.1). Between five and six symmetric, equally spaced basal reflections are found between 3.5 and 30º 2θ, corresponding to basal spacings (d_{003}) of 18.8 Å for PS-LDH and 19.4 Å for HpS-LDH. The powder XRD pattern for PS-LDH is similar to that obtained after intercalation of PS by ion-exchange of a Zn-Al-NO_3 precursor.[10] As discussed previously,[10] the arrangement of PS anions between the layers cannot be unambiguously inferred from the observed basal spacing. However, two extreme possibilities can be proposed in which the PS molecules adopt either an almost perpendicular (or slightly tilted) bilayer arrangement with extensive interdigitation (*i.e.*, an antiparallel interpenetrating style) or a strongly tilted bilayer arrangement with minimal interdigitation. Figure 4.2 shows a schematic representation of the former configuration for which the calculated basal spacing matches the observed value. A similar arrangement of guest anions can be envisaged for HpS-LDH (Figure 4.2).

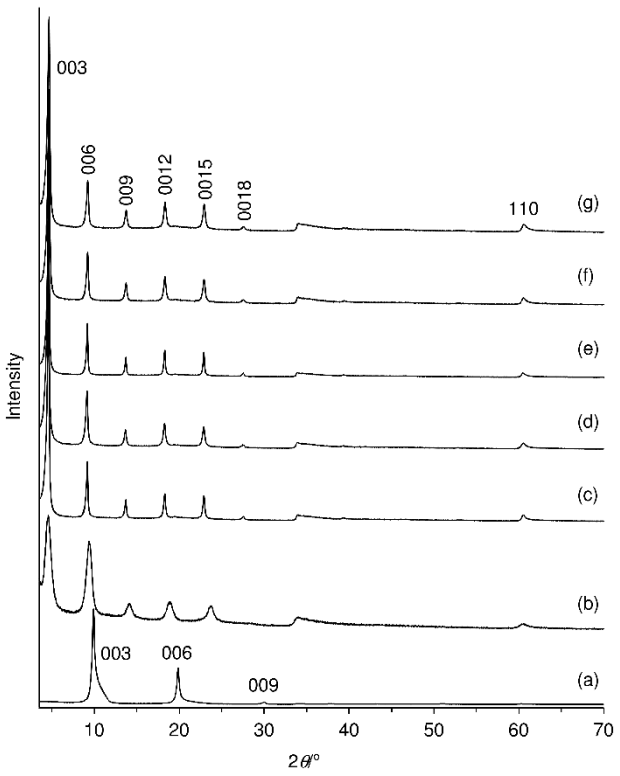

Figure 4.1 - Powder XRD patterns of (a) Zn-Al-NO_3, (b) PS-LDH, (c) HpS-LDH, (d) PS(11.8%)/HpS-LDH, (e) PS(4.7%)/HpS-LDH, (f) PS(2.3%)/HpS-LDH, and (g) PS(1.2%)/HpS-LDH.

The powder XRD patterns of the cointercalated LDH samples are all very similar to that displayed by HpS-LDH (Figure 4.1). Only one series of (00*l*) reflections are observed. Neither the basal spacing (19.2-19.4 Å) nor the half-peak width (fwhm) of the (003) reflection (0.21-0.31º) change significantly for the samples PS(*x*%)/HpS-LDH (*x*% = 0-11.8%). Furthermore, the fwhm of the (003) reflection for all of the cointercalated samples is less than that of PS-LDH (0.86º). This indicates that PS and the surfactant HpS disperse uniformly in the galleries of the LDH host, forming a homogeneous phase. Previous experimental and computational studies seem to support this packing mode for alkylsulfonates intercalated in LDHs.[13-15]

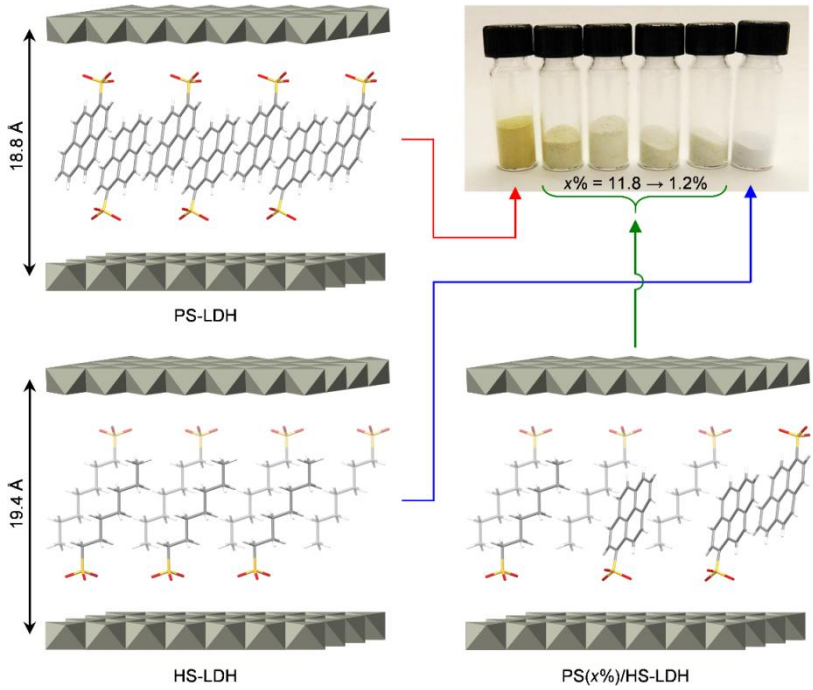

Figure 4.2 - Schematic representation of the possible arrangements of PS and HpS anions between the brucite-like layers in the materials PS-LDH, HpS-LDH, and PS(*x*%)/HpS-LDH. For PS-LDH the PS anions are grouped such that the PS-PS intermolecular distance is ca. 3.2 Å, which is a typical value for a pyrene excimer.

4.2.2 Elemental analysis

Elemental analysis data for PS-LDH and HpS-LDH indicated that both materials had chemical compositions close to $Zn_4Al_2(OH)_{12}(A)_{1.7}(CO_3)_{0.15}{\cdot}nH_2O$ (*n* = 5.5-6.0), where A = PS or HpS. For the co-intercalated samples, elemental analysis indicated final chemical compositions close to $Zn_4Al_2(OH)_{12}(PS+HpS)_{1.7}(CO_3)_{0.15}{\cdot}5.5H_2O$. Surprisingly, the data consistently evidenced that preferential intercalation of PS had occurred to the extent that the final *x*% values were 11.8, 4.7, 2.3, and 1.2 mol%, *i.e.* practically all PS anions initially in solution were intercalated.

4.2.3 Thermogravimetry

TGA data were consistent with the compositions referred above. Thus, PS-LDH and HpS-LDH materials display a weight loss of *ca.* 10.5% up to 175 ºC, attributed to loss of interlayer water molecules (Figure 4.3). Upon increasing temperature, a dehydroxylation step takes place for both materials in the interval 180-280 ºC, followed by decomposition of the organic guest anions between 275 and 410 ºC for HpS-LDH (DTG_{max} = 385 ºC), and 400 and 570 ºC for PS-LDH (DTG_{max} = 490 ºC). Decomposition of HpS anions in HpS-LDH occurs at a slightly higher temperature than that for the pure sodium salt (onset = 210 ºC, DTG_{max} = 350 ºC). Intercalated PS anions in PS-LDH display remarkably higher thermal stability than the corresponding sodium salt (onset = 300 ºC, DTG_{max} = 380 ºC). Residual masses at 800 ºC are 36.1% for PS-LDH and 47.7% for HpS-LDH. If it is assumed that calcination of both LDHs leads to a mixture of zinc oxide (zincite) and $ZnAl_2O_4$ (gahnite, spinel) phases (*i.e.*, a solid with the overall composition $Zn_4Al_2O_7$),[10, 16] the expected residual masses are 38.3% and 45.8%, respectively, which are in reasonable agreement with the observed values.

TGA curves for the samples PS(*x*%)/HpS-LDH (*x*% = 1.2-4.7%) were very similar (Figure 4.3 and Figure 4.4), with DTG_{max} values of 225-230 ºC for the dehydroxylation step and 255-265 ºC for the decomposition step (of intercalated organosulfate anions). No separate weight loss step for decomposition of PS anions could be discerned.

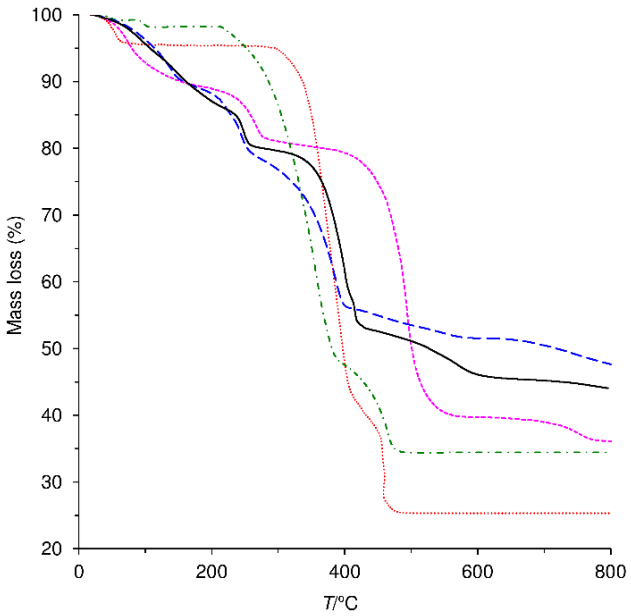

Figure 4.3 - TGA curves for NaHpS (– · – · –), NaPS (·····), HpS-LDH (– – –), PS-LDH (------), and PS(11.8%)/HpS-LDH (——).

Overall the three TGA curves are comparable with that for HpS-LDH, although the dehydroxylation and decomposition steps for the latter are shifted by 15-20 ºC towards higher temperature. The TGA curve for PS(11.8%)/HpS-LDH shows an opposite trend in that the

dehydroxylation and HpS decomposition steps are displaced towards higher temperature (DTG_{max} = 250 and 400 ºC) when compared with those for HpS-LDH. The decomposition of HpS anions in PS(11.8%)/HpS-LDH prompted the early decomposition of PS anions, as evidenced by the additional small step above 400 ºC (DTG_{max} = 416 ºC). Residual masses at 800 ºC for the cointercalated samples are in reasonable agreement with the expected values calculated on the basis of the chemical compositions and the assumption that the residue is a mixture of ZnO and $ZnAl_2O_4$.

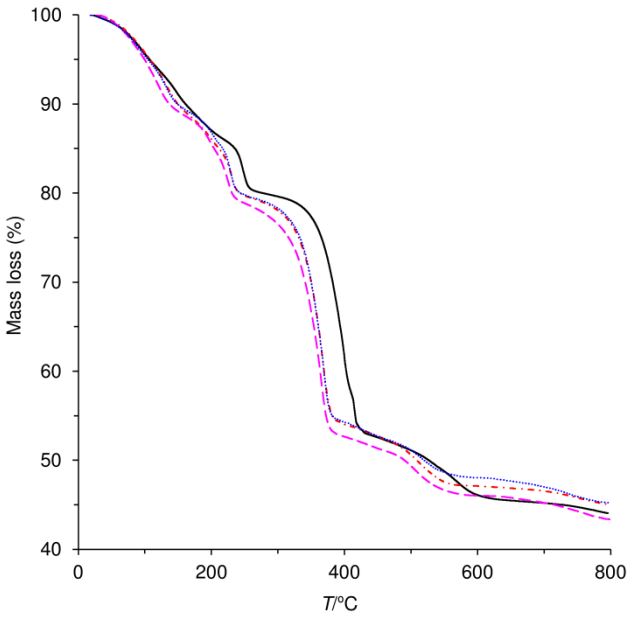

Figure 4.4 - TGA curves for the cointercalated samples PS(*x*%)/HpS-LDH with *x*% = 1.2% (– – –), 2.3% (– · – ·), 4.7% (·····), and 11.8% (——).

4.2.4 Differential Scanning Calorimetry (DSC)

DSC data showed endothermic peaks at 195 and 220 ºC for HpS-LDH and 261 ºC for PS-LDH, which can be attributed to the dehydroxylation steps, and exothermic peaks at 408 ºC for HpS-LDH and 509 ºC for PS-LDH, corresponding to the decomposition of the intercalated organic anions (see Figure 4.5). For the PS(11.8%)/HpS-LDH sample and in accordance with TGA results, the DSC curve showed two exothermic peaks at 410 and 417 ºC.

4.2.5 FTIR and Raman spectroscopies

The FT-IR and FT-Raman spectra confirmed the successful intercalation of the organosulfonate anions. The high-frequency region of the vibrational spectra (2700-3100 cm^{-1}) reveals the C–H stretching modes while the low-frequency region of 700-1750 cm^{-1} displays the stretching modes of the sulfonate group as well as, for example, the scissoring and rocking modes of the methylene groups of HpS, and the ring stretching modes of PS (Figure 4.6; please see the

experimental section for assignments).[17-19] In general the bands associated with either the pyrene group or the alkyl chain are coincident with those observed for the pure sodium salts.

Concerning the headgroup vibrational region, the O=S=O stretching vibrations of the sulfonate group in PS shift (in the IR spectra) from 1062 [$\nu_s(SO_3^-)$] and 1192 cm^{-1} [$\nu_{as}(SO_3^-)$] for the pure dye salt to 1055 and 1176 cm^{-1} for PS-LDH.

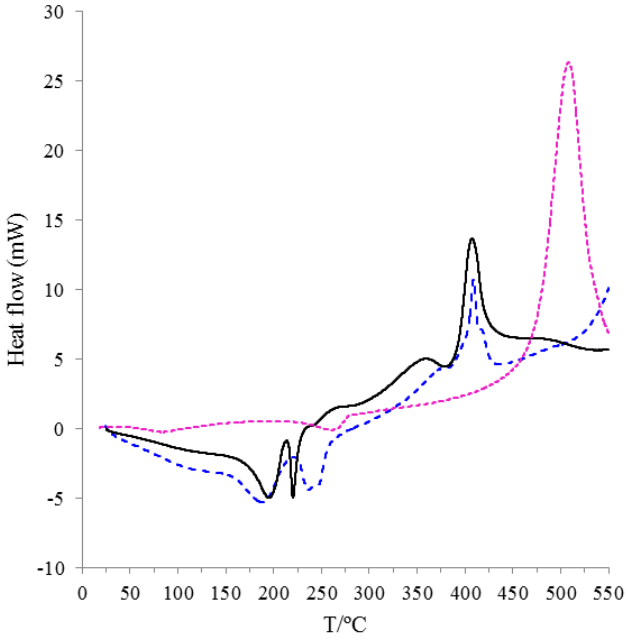

Figure 4.5 – DSC curves for HpS-LDH (– – –), PS-LDH (------) and PS(11.8%)/Hps-LDH (——).

Small frequency shifts were also evident for the respective HpS compounds (1049 and 1188 cm^{-1} for HpS-LDH *vs*. 1055 and 1193 cm^{-1} for NaHpS). The down-shifts in frequency upon intercalation are attributed to a diminished polarization of the S–O bonds in the SO_3^- groups by the diffusely charged double hydroxide layers, relative to the stronger polarization observed with Na^+ ions.[10, 20-21] The interaction with the LDH surface probably involves an electrostatic binding through a hydrogen bond of the type S=O···H–O–M (M = Zn, Al).

A comparison of the Raman spectra of NaHpS and HS-LDH (Figure 4.7) reveals that the down-shift in frequency for the $\nu_s(SO_3^-)$ mode upon intercalation is larger (17 cm^{-1}) than that observed in the IR spectra (6 cm^{-1}). An identical shift of 17 cm^{-1} was observed for the same (but much weaker) band in the Raman spectra of NaPS and PS-LDH. The larger shift observed in the Raman spectra can be attributed to correlation coupling effects.[20] Thus, for NaHpS, the wavenumber of $\nu_s(SO_3^-)$ is higher (1067 cm^{-1}) in the Raman than in the IR spectrum (1055 cm^{-1}). In contrast, the wavenumbers for this mode are coincident in the IR and Raman spectra of HpS-LDH. The decrease in $\Delta\nu_s(SO_3^-)$ (i.e., the difference between the IR and Raman spectra for the $\nu_s(SO_3^-)$ wavenumber) on going from NaHpS to

HpS-LDH is likely due to an increase in the separation of adjacent SO_3^- groups, preventing correlation coupling.

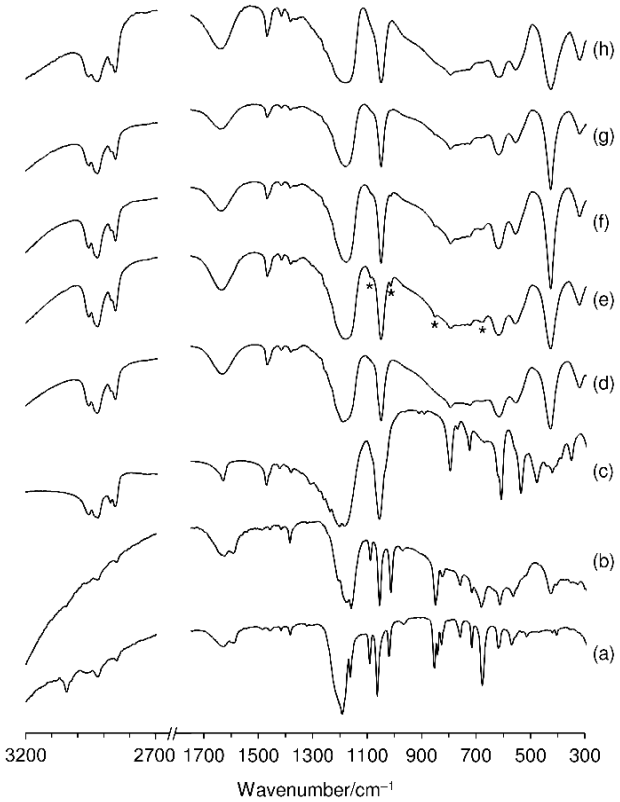

Figure 4.6 - FT-IR spectra in the regions 300-1750 cm^{-1} and 2700-3200 cm^{-1} of (a) NaPS, (b) PS-LDH, (c) NaHpS, (d) HpS-LDH, and the cointercalated samples PS(*x*%)/HpS-LDH with *x* = 11.8 (e), 4.7 (f), 2.3 (g) and 1.2 (h). The asterisks highlight bands assigned to cointercalated PS anions.

These observations therefore seem to support the packing model represented in Figure 4.2. The same effect has been observed for metal salts of bis(2-ethylhexyl)sulfosuccinate, in which $\Delta\nu_s(SO_3^-)$ decreases with increasing counterion radius.[20] Below 700 cm^{-1}, the FT-IR spectra of PS-LDH and HpS-LDH contain several bands due to the guest species in addition to Zn/Al-OH lattice translation modes that are characteristic of Zn-Al LDHs (426, 553 and 615 cm^{-1}). Both of the intercalated LDHs exhibit a very weak, broad band at about 1367 cm^{-1}, which can be attributed to the presence of a small amount of carbonate ion.

For cointercalated samples (PS(*x*%)/HpS-LDH), the FT-IR and Raman spectra further confirmed the presence of both PS and HpS anions. Thus, the IR spectra essentially match that displayed by HpS-LDH (Figure 4.6). However, some additional peaks are due to PS anions, e.g. the peak at 1013 cm^{-1}, which weakens on going from PS(11.8%)/HpS-LDH to PS(1.2%)/HpS-LDH. The Raman spectrum of PS(11.8%)/HpS-LDH shows numerous bands that are coincident with those displayed by either PS-LDH or HpS-LDH (Figure 4.7).

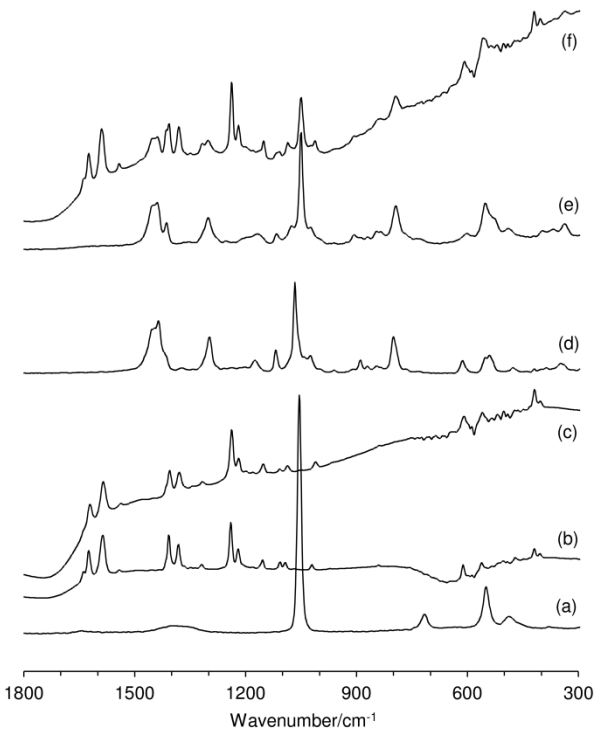

Figure 4.7 - FT-Raman spectra in the region 300-1800 cm^{-1} of (a) NO_3-LDH, (b) NaPS, (c) PS-LDH, (d) NaHpS, (e) HpS-LDH, and (f) the cointercalated sample PS(11.8%)/HpS-LDH.

4.2.6 $^{13}C\{^1H\}$ CP MAS NMR spectroscopy

The $^{13}C\{^1H\}$ CP MAS NMR spectra of NaPS and PS-LDH are quite similar and display several overlapping signals in the region of aromatic carbon atoms (115-140 ppm; Figure 4.8).

Both the sodium salt NaHpS and the intercalate HpS-LDH display only a single resonance for the methyl carbon atoms. In contrast, whereas the sodium salt NaHpS displays multiple sharp resonances for each type of methylene carbon atom (possibly due to conformational heterogeneity in the solid state), the material HpS-LDH only displays five fairly broad single peaks (C^3 and C^4 are not resolved as separate resonances). The spectrum of HpS-LDH is therefore consistent with an ordered (essentially all-*trans*) conformation of the methylene chains, as schematically represented in Figure 4.2.

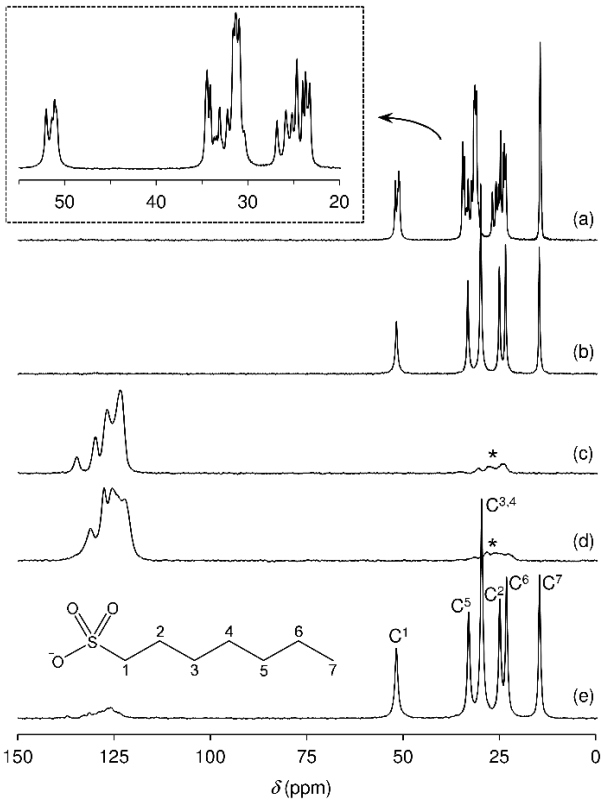

Figure 4.8 - $^{13}C\{^{1}H\}$ CP MAS NMR spectra of (a) NaHpS, (b) HpS-LDH, (c) NaPS, (d) PS-LDH, and (e) PS(11.8%)/HpS-LDH. The asterisks denote spinning sidebands in spectra (c) and (d).

Similarly, the $^{13}C\{^{1}H\}$ CP MAS NMR spectrum of PS(11.8%)/HpS-LDH exhibits several weak overlapping signals in the region of aromatic carbon atoms (115-140 ppm) together with six peaks in the region of aliphatic carbon atoms (10-55 ppm), which are all coincident with the corresponding resonances observed for PS-LDH and HpS-LDH. The CH_2 and CH_3 resonances for the cointercalated sample are noticeably broader than those for HpS-LDH.

4.2.7 SEM images

SEM studies showed that all of the cointercalated samples PS(*x*%)/HpS-LDH exhibited a similar morphology comprising irregular aggregates of platelike particles (Figure 4.9).

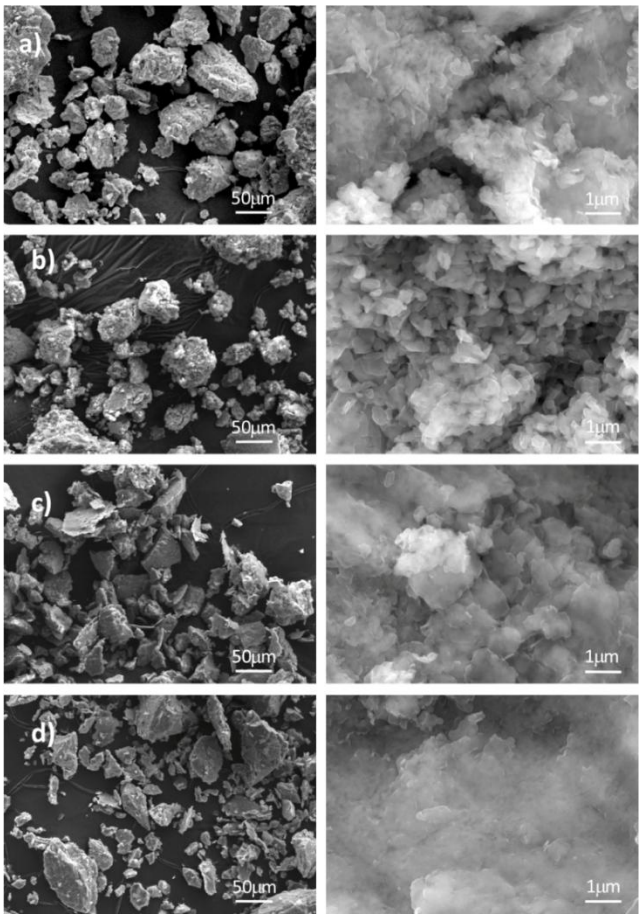

Figure 4.9 - SEM images for the cointercalated samples PS(*x*%)/HpS-LDH with *x*% = 11.8% (a), 4.7% (b), 2.3% (c) and 1.2% (d).

4.3 Photophysical characterization

The spectral and photophysical behaviors of all the intercalates with different loadings of PS and HpS were investigated by using UV-Vis absorption, steady-state and time-resolved fluorescence techniques.

4.3.1 UV-Vis absorption and emission spectra and time resolved fluorescence: solution behavior

Prior to the solid state study of PS intercalated in the Zn-Al LDH in the presence (or absence) of the HpS surfactant, the solution behavior of this probe was investigated in solvents of different polarity (measured by the dielectric constant of the solvent; see Table 4.1). The absorption and fluorescence spectra and lifetimes were measured in ethanol, methanol, dimethylformamide, dimethylsulfoxide and water in aerated and degassed solutions (Table 4.1). The absorption and fluorescence spectra display a single (monomer) band with wavelength maxima that are solvent

independent. This solvent independence does not apply to the intensity ratio of the first and third vibronic peaks of PS (I_1/I_3), which is found to change with the solvent and can, by analogy with pyrene itself, constitute a useful way of measuring the polarity of the media probed by PS. In the case of pyrene this ratio varies from 1.8 in water to 0.6 in nonpolar solvents such as hexane.[22-23] From the PS data in Table 4.1 it can be seen that, in contrast to pyrene,[24] this probe does not display a gradual (I_1/I_3 vibronic) dependence with polarity. However, it looks clear that the more polar solvent water with the higher dielectric constant value (ϵ) displays the highest I_1/I_3 value. Moreover, from Table 4.1 it can be seen that for the hydroxylic solvents (EtOH, MeOH and H_2O) the I_1/I_3 vibronic ratio increases with the dielectric constant, and a similar trend is evident for the nonprotic solvents (DMF and DMSO).

Table 4.1 - Lifetimes of 1-pyrenesulfonate in different solvents in aerated and degassed solutions, together with the dielectric constants of the solvents and I_1/I_3 vibronic ratio.

Solvent	τ (ns)	τ (ns) in degassed solution	Dielectric constant (ϵ)[a]	I_1/I_3
EtOH	22.3	127.6	24.55	3.14
MeOH	19.4	129	32.66	4.02
DMF	41.6	185.6	36.71	1.55
DMSO	90.1	159.7	46.45	2.17
H_2O	57.3	65.7	80.16	4.44

[a] Values taken from ref[25].

Lifetimes values in ethanol and methanol were previously reported[26] and are in good agreement with those presented in Table 4.1. From Table 4.1, it is also worth noting the (i) dependence of the lifetime values on the dielectric constants, and (ii) almost insignificant change in the τ value in water in the presence and absence (degassed solution) of oxygen. Also water with the highest dielectric constant value displays, in degassed solution, the lowest lifetime value.

4.3.2 UV-Vis absorption and emission spectra: solid state behavior

The absorption and fluorescence emission spectra are shown in Figure 4.10. Two bands are observed in the emission spectra (right side of the Figure 4.10) for PS(*x*%)/HpS-LDH (*x*% = 1.2-11.8%): a structured band at 376 nm corresponding to the pyrene monomer, and an additional nonstructured band shifted to longer wavelengths (with maxima at 495 nm) characteristic of excimer emission.[27-28] For the material PS-LDH, only the nonstructured band at 495 nm is observed. Upon decrease of PS and increase of the surfactant (higher HpS/PS ratio) the intensity of the monomer band (376 nm) gradually increases, reflecting the fact that a higher level (concentration) of PS in its

monomer (isolated) form becomes present, thus showing that the surfactant prevents PS aggregation inside the LDH gallery regions.

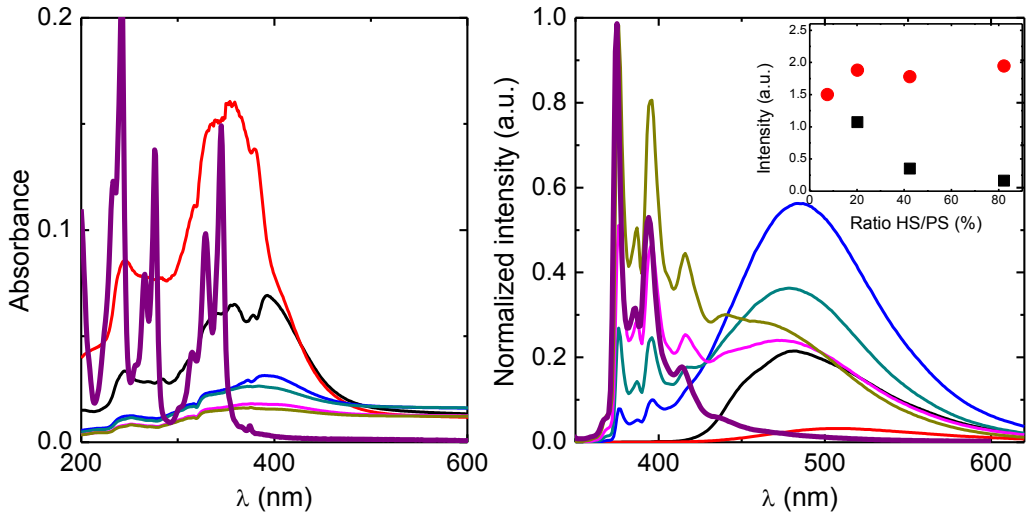

Figure 4.10 - Absorption (*left*) and emission (*right*) spectra of sodium 1-pyrenesulfonate powder (black line), PS-LDH (red line), PS(*x*%)/HpS-LDH with *x*% = 11.8% (blue line), 4.7% (dark teal line), 2.3% (magenta line) and 1.2% (dark yellow line), and PS in ethanol (purple line). The inset in the right graph shows the I_E/I_M (black filled squares) and I_1/I_3 (red filled circles) intensities as a function of the HpS/PS ratio in the Zn-Al LDH.

As indicated in Figure 4.10 (inset) the I_E/I_M and the I_1/I_3 vibronic ratios provide a powerful tool to quantitatively follow the spectral and photophysical properties of these hybrid systems upon a gradual addition of HpS. The PS(*x*%)/HpS-LDH with *x*% = 11.8% leads to a HpS/PS ratio of 7.5, the 4.7% to HpS/PS = 20.3, the 2.3% to HpS/PS = 42.5 and finally the 1.2% to HpS/PS = 82.3. It can be seen that the I_E/I_M ratio decreases with the increase in the HpS/PS ratio, thus showing that more isolated PS molecules are gradually present at the expense of a decrease of dimer (or other order aggregates) contribution. From the data it can be seen that upon introduction of the HpS surfactant (to the already present PS) the I_1/I_3 ratio changes from 1.5 (for HpS/PS ~ 7.5, *i.e.* HpS:PS = 88.2:11.8) to ~ 1.78-1.95 for the other loadings. These values are markedly different from those listed in Table 4.1 for water and protic solvents, and are very close to those observed for pyrene in micellar solutions of tetraalkylammonium perfluorooctanoate surfactants (I_1/I_3 varying from 1.55 to 1.96).[29] This shows that in the PS/HpS-LDH systems, upon gradual addition of HpS, particularly from the ratio HpS/PS = 20.3 to 82.3, the aggregation of the PS probe gradually decreases its importance relative to the more isolated PS (surrounded by the surfactant). Moreover, the fact that the I_1/I_3 increases (from the lower to the highest HpS content) in the PS/HpS-LDH system strongly suggests that the medium probed by the average molecules of PS contributing to this ratio is becoming more hydrophilic. This shows that the system is close to a situation where there is more PS found "isolated" from other PS molecules, in

coexistence, however, with dimer structures as attested by the strong contribution of the 495 nm band. This will be discussed in detail in section 4.3.4.

4.3.3 Fluorescence quantum yields in solid state

The fluorescence quantum yields of all LDH samples were obtained in the solid state using Quantaurus-QY equipment and the results are presented in Table 4.2. The values obtained (with λ_{exc} = 315 nm in the monomer region and λ_{exc} = 395 nm in the excimer) are in agreement with the qualitative fluorescence spectra obtained in the Spex fluorimeter. As the HpS content increases, there is an increase in fluorescence quantum yield too. These data are in great agreement with absorption and fluorescence results showing even more that more isolated molecules of PS increase as the dimer (or order aggregates) species decreases leading to an increase in fluorescence quantum yield.

Table 4.2 - Fluorescence quantum yields of LDH systems in the solid state at room temperature (λ_{exc} = 315 nm and 395 nm).

Compound	Φ_F (λ_{exc} = 315 nm)	Φ_F (λ_{exc} = 395 nm)
PS powder	0.078	0.033
PS-LDH	0.024	0.022
PS(11.8%)/HpS-LDH	0.313	0.185
PS(4.7%)/HpS-LDH	0.387	0.266
PS(2.3%)/HpS-LDH	0.379	0.352
PS(1.2%)/HpS-LDH	0.410	0.467

4.3.4 Time-resolved fluorescence: solid state behavior

Due to the complexity of the fluorescence decays of solid materials, and in particular of LDH systems, in the literature it is often usual to see that the interpretation of these is made through the concept of average lifetime(s).[11, 30-32] However, this frequently rises several questions one of which is a correct description of the molecular behaviour observed. Fluorescence decay times were obtained for all samples in the solid state with different excitation wavelengths (282, 311 and 339 nm) and collected at 375, 480 and 520 nm. The decay time values and pre-exponential factors are, within the experimental error, independent of the excitation wavelength (see Figure 4.11 for data obtained with λ_{exc} = 311 nm and Figure 4.12 for data obtained with λ_{exc} = 282 and 339 nm).

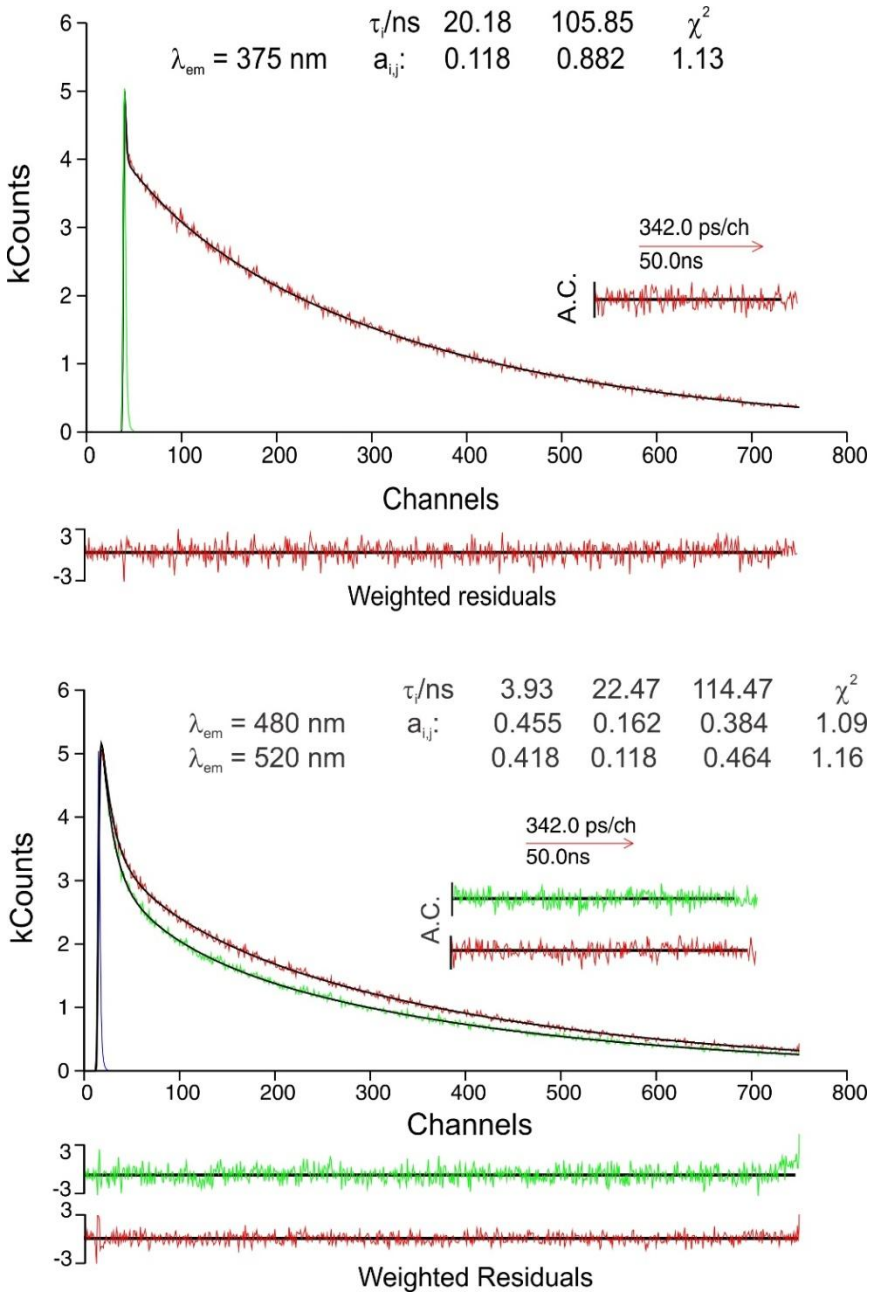

Figure 4.11 - Fluorescence decays collected at the monomer (*top panel* with λ_{em} = 375 nm) and excimer (*bottom panel* with λ_{em} = 480 and 520 nm) emission wavelengths for PS(1.2%)/HpS-LDH (HpS/PS = 82.3) in the solid state at room temperature (λ_{exc} = 311 nm). Independent analysis at 375 nm (*top panel*) and global analysis at 480 and 520 nm (*bottom panel*) of the decays. For a better judgment of the quality of the fits, autocorrelation (A.C.) functions, weighted residuals and χ^2 values are provided as insets.

At the monomer emission wavelength (375 nm) the fluorescence decays can only be properly fitted with two components: a shorter one with a lifetime of ~ 20 ns and a longer one with ~ 106 ns. This indicates that PS can be found in different microenvironments which are, at this emission

wavelength where only the monomer species are emitting, associated with a distribution of PS in two situations: (i) one where PS likely probes an oxygen-free microenvironment (associated with the longer decay time) surrounded by HS surfactant molecules, and (ii) a second one where a PS molecule is found, although in its monomer form, with other nearby PS (but not at the ~ 3.2-3.5 Å intermolecular interaction distance for excimer/dimer formation), which leads to quenching of these by energy transfer; this second situation could be further explored with alternative decays laws, particularly based on non-exponential (or stretched) laws, which are made when the identification of the different kinetic species is frequently not evident.[33]

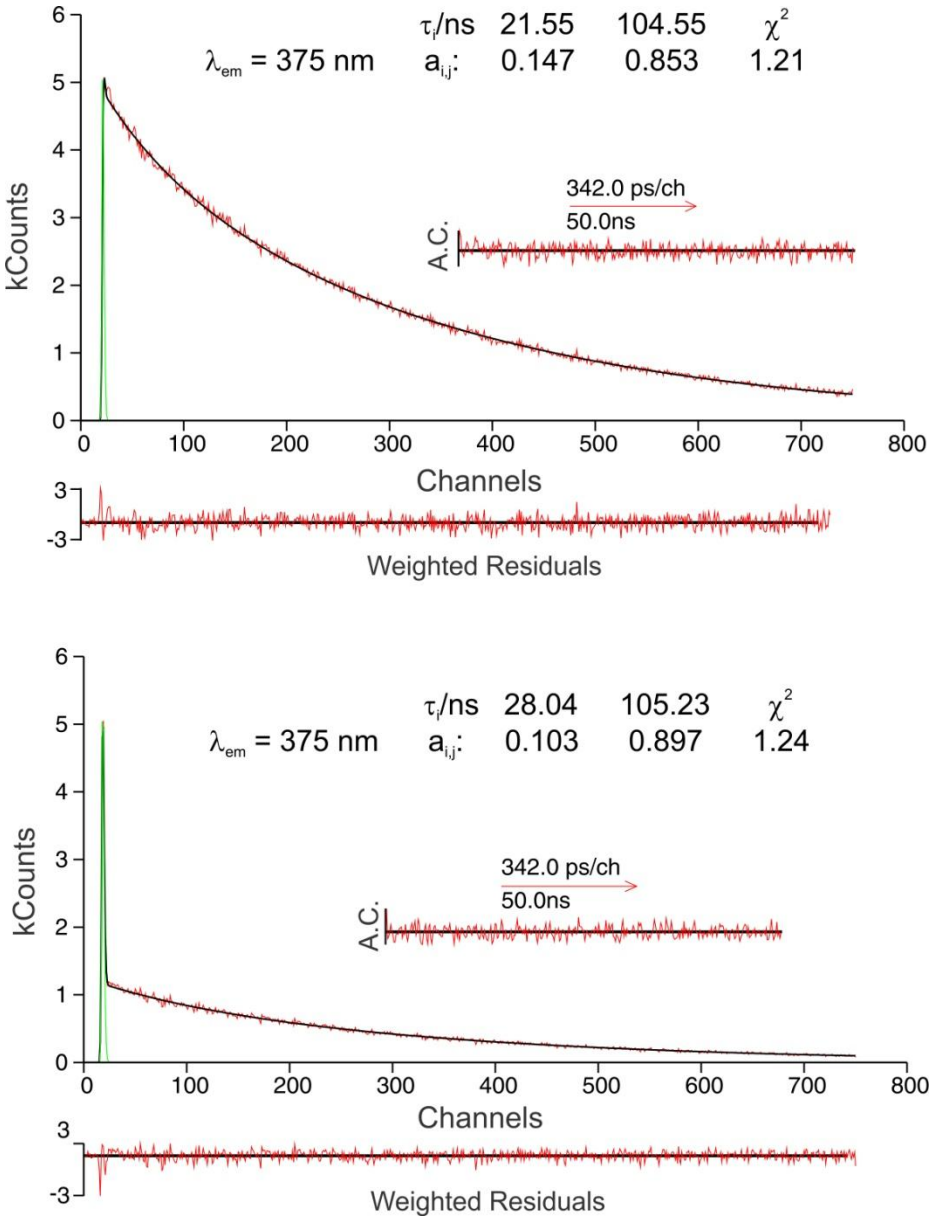

Figure 4.12 - Fluorescence decays collected at the monomer (λ_{em} = 375 nm) emission wavelength for the sample PS(1.2%)/HpS-LDH (HpS/PS = 82.3) in the solid state at room temperature. (*Top panel*) λ_{exc} = 282 nm; (*Bottom panel*) λ_{exc} = 339 nm. For a better judgment of the quality of the fits, autocorrelation functions (A.C.), weighted residuals and χ^2 values are presented.

Indeed, this biexponential analysis can be compared with that made using a dispersive kinetic analysis of the decays according to Equation 4.1.

$$I(t) = I_0(t)e^{-(kt)^{\beta}} \quad \textbf{(4.1)}$$

where $I(t)$ is the fluorescence intensity dependence with time, $I_0(t)$ the fluorescence intensity at time zero, and β a parameter that varies between 0 and 1.[32-33]

With the present fluorescence decays, the fittings are found good with sums of two and three exponentials, but never with a single-exponential decay, as can be seen in Figures 4.13 and 4.14. Indeed, attempts to fit the decays with other decay laws including dispersive kinetics (eq 4.1)[32] were found to be inadequate in achieving a correct fit of the decays (see below and data in Table 4.3 and Figures 4.13 and 4.14). Additional analysis with dispersive kinetics (eq 4.1) and first order (single exponential, eq 4.2) are presented in Table 4.3 and Figures 4.14 and 4.15 covering the whole range of samples with different HpS/PS ratios, the PS (powder) and for PS-LDH.

$$I(t) = A_1 e^{(-t/t_1)} + y_0 \quad \textbf{(4.2)}$$

Table 4.3 – Lifetimes and β values recovered from a dispersive kinetic analysis and a single exponential analysis (with no deconvolution) of the decays for the different PS(x%)/HpS-LDH samples obtained with λ_{exc} = 311 nm and λ_{em} = 375 nm and 480 nm.

	Dispersive kinetics		**Single exponential**
λ_{em} = 375 nm	**β**	**τ (ns)**	**τ (ns)**
PS(1.2%)/HpS-LDH	0.848	88.5	86.4
λ_{em} = 480 nm			
PS(1.2%)/HpS-LDH	0.471	28.74	50.40
PS(2.3%)/HpS-LDH	0.529	28.36	43.70
PS(4.7%)/HpS-LDH	0.643	38.54	46.50
PS(11.8%)/HpS-LDH	0.525	18.64	31.07
PS-LDH	0.364	0.59	4.30
PS powder	0.992	2.45	2.44

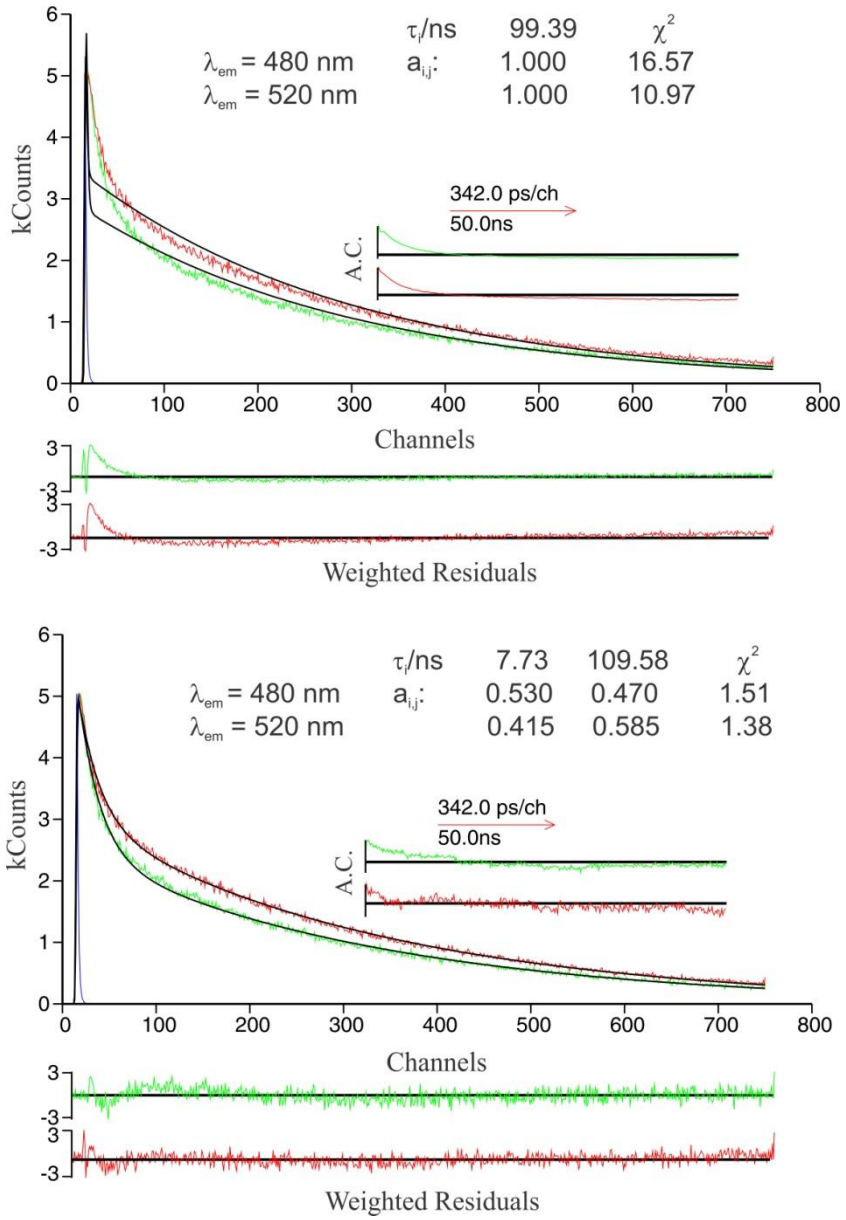

Figure 4.13 - Fluorescence decays collected at λ_{em} = 480 and 520 nm for the sample PS(11.8%)/HpS-LDH analyzed with a single exponential (*top panel*) and double exponential fit (*bottom panel*).

In the case of single exponential analysis in Figure 4.14, the poor adjustment of the overall decay is clear, whereas in the case of dispersive kinetic analysis only in the first part of the decay (~10 ns) can the fit be considered reasonable.

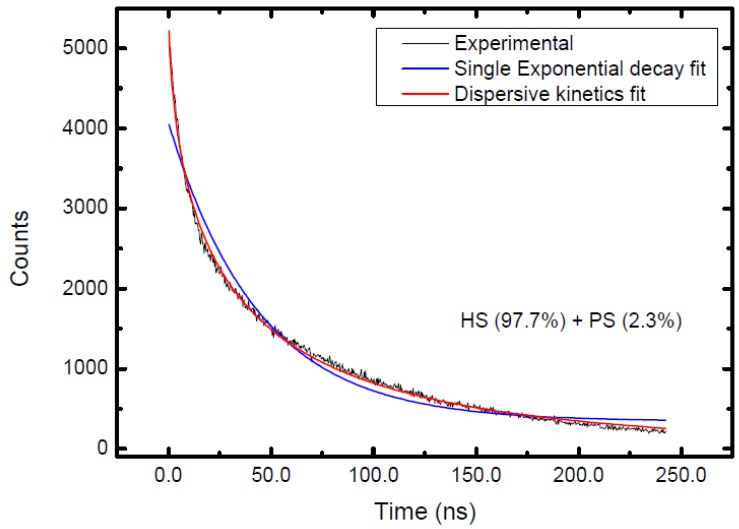

Figure 4.14 – Fluorescence decays and analysis resulting from a dispersive kinetic analysis (red line) and single exponential analysis (blue line) for the PS(2.3%)/HpS-LDH sample obtained with λ_{exc} = 311 nm and λ_{em} = 480 nm.

The single exponential analysis in Table 4.3 (made with the fittings of the decays after time zero – that is without deconvolution of the decays) leads to significant differences of the major component of the decays when compared with the sum of exponentials. For example, in the PS(11.8%)/HpS-LDH mixture the 36 ns component only represents 37% of the decay, whereas in Table 4.3 the 31.07 ns component is the major one in the single exponential fit.

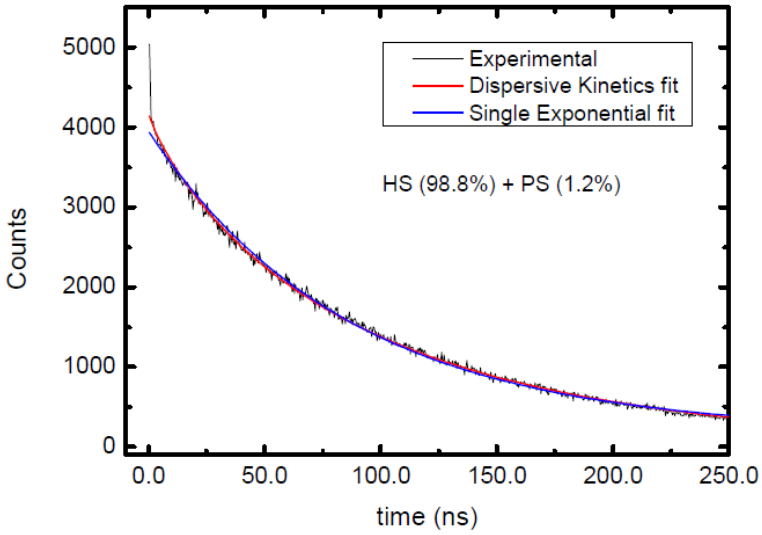

Figure 4.15 - Fluorescence decays and analysis resulting from a dispersive kinetic analysis (red line) and single exponential analysis (blue line) for the PS(1.2%)/HpS-LDH sample obtained with λ_{exc} = 311 nm and λ_{em} = 375 nm.

However, as can be seen in Table 4.3 and Figures 4.13-4.15, the fits to decay laws other than sums of exponentials are nor acceptable. Moreover, the analysis at 375 nm (Figure 4.15) leads to a β value 0.85, but the lack of a good fit is evident, particularly in the first part of the decay (shorter times). In this analysis the decay time values obtained from the single exponential (86.4 ns) and discrete kinetic (88.5 ns) analysis are close to each other but do not recover either of the two components resulting from the sum of exponentials (20 and 106 ns in Figure 4.11), in which a good fit is clearly obtained in the entire decay.

From the double exponential decays at 375 nm obtained for different HpS/PS ratios, it can be seen that upon increase of HpS (and therefore increase in the HpS/PS ratio) both lifetime values increase, but with a levelling-off of the τ_2 decay time at a HpS/PS ratio of 20.3 (Figure 4.16). In addition, the pre-exponential factors associated with each of these two components change in a reciprocal manner (Figure 4.16), i.e., as the ratio HpS/PS increases, there is an increase in the contribution from the longer component (τ_1, A_{11}) together with a concomitant decrease of the shorter component (τ_2, A_{12}). Moreover, since there is a simultaneous change both in the pre-exponential factor and lifetimes values, it is better to observe the fractional contribution (C_i) of each species, given by the following equation (Eq. 4.3)

$$C_i\ (\%) = \frac{a_i\ \tau_i}{\sum_{i=1}^{n} a_i \tau_i} \times 100 \qquad \textbf{(4.3)}$$

where n stands for the number of exponential terms, a_i represents the contribution of each exponential term at $t = 0$, and τ_i are the associated decay times.

The second component (associated with the shorter decay time, τ_2) decreases its relative contribution (% C) with the HpS/PS ratio (from 54% to 2.5%, Figure 4.16). The longer decay component, whose importance (seen by the C_1 value) increases with the HpS/PS ratio, is related to isolated PS monomer units in the LDH interlayer region. As a consequence, the second decay time (τ_2) should be associated with a monomer with a neighbouring pyrene; with the decrease of the HpS/PS ratio, the contribution of these monomers with a neighbouring pyrene increases along with a decrease in the decay time value since they constitute, very likely, closely lying pyrene units.

Upon going to 480 and 520 nm emission wavelengths, the decays are now tri-exponential. For the higher HpS/PS ratio (with a value of *ca*. 82), although two of the components have similar lifetime values (22.5 ns and 114 ns) to those obtained with emission at 375 nm (20 and 106 ns), a different physical meaning should be attributed to these components. One of the decay times, whose component is always the dominant one (seen by the C_1) at these wavelengths, is attributed to the decay of the excimer (similar values have been reported for pyrene in the presence of dodecyl sulphate in LDH matrices).[20] Moreover, the fact that this value is higher than the solution decay time for the excimer decay can be explained by the fact that fluorescence lifetimes of the dyes in LDH

systems are longer than that in solution,[31, 34-35] which is associated with the dominance of the radiative over the radiationless decay channel when PS is found between the rigid LDH layers.

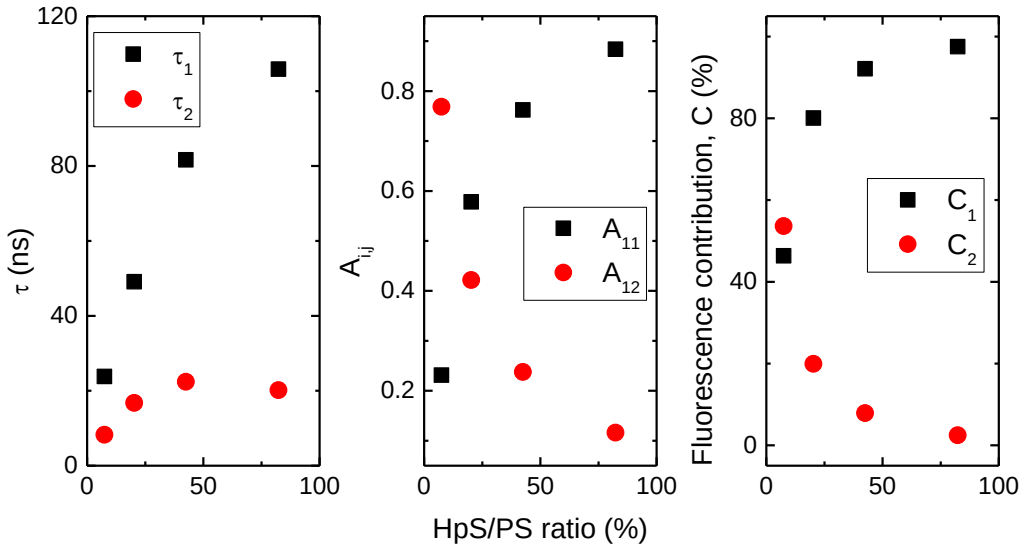

Figure 4.16 - *(From left to the right)* Decay times τ_1 and τ_2, pre-exponential A_{11} and A_{12} factors, and fluorescence contribution obtained with λ_{exc} = 311 nm and emission at 375 nm for different HpS/PS ratios in the cointercalated samples PS(*x*%)/HpS-LDH in the solid state.

The two other shorter components should be associated with dimers in the ground state (or possibly higher order aggregates). The shorter component (which at the higher HpS/PS ratio of 82.3 displays a lifetime of 3.9 ns) should be clearly identified with a ground-state dimer; indeed, similar values have been reported for dimers existing in other pyrene systems.[4, 36-37] This decay time is always associated with the component with the minor contribution (as seen by the C_3 contribution). Despite the similarity of the lifetime value for the middle decay component at 480 and 520 nm (22 ns for HpS/PS = 82.3) with the value of 20 ns obtained at 375 nm, these have a different physical meaning. Indeed, the fact that (i) this value is dependent on the amount of PS in the LDH gallery, and (ii) it emits at 480/520 nm with a contribution (C_2) of the total fluorescence ranging from 4 to 40%, indicates that this component should be physically linked to pyrene aggregates in a different microenvironment.

4.4 Conclusions

In summary, the cointercalation of 1-pyrenesulfonate and the surfactant 1-heptanesulfonate in Zn-Al LDHs has been achieved through a direct synthesis route. The photophysical properties of the intercalates can be tuned by changing the HS/PS ratio, demonstrating that the surfactant plays an important role in preventing the aggregation of the substituted pyrene, acting as a regulator of the microenvironment within the LDH gallery. The work shows that it was possible to perform a fine-tuning of the spectral and photophysical properties of the hybrid LDH (PS-LDH) by varying the amount of the HS surfactant (PS/HS-LDH), thus regulating the microenvironment in the inorganic galleries.

4.5 References

1. de Castro, C. S.; Cova, T. F. G. G.; Pais, A. C. C.; Pinheiro, D.; Nuñez, C.; Lodeiro, C.; Seixas de Melo, J. S., Probing metal cations with two new Schiff base bischromophoric pyrene based chemosensors: Synthesis, photophysics and interactions patterns. *Dyes and Pigments* **2016,** *134*, 601.

2. Pinheiro, D.; de Castro, C. S.; Seixas de Melo, J. S.; Oliveira, E.; Nuñez, C.; Fernández-Lodeiro, A.; Capelo, J. L.; Lodeiro, C., From yellow to pink using a fluorimetric and colorimetric pyrene derivative and mercury (II) ions. *Dyes and Pigments* **2014,** *110*, 152.

3. Fernández-Lodeiro, J.; Núñez, C.; de Castro, C. S.; Bértolo, E.; Seixas de Melo, J. S.; Capelo, J. L.; Lodeiro, C., Steady-State and Time-Resolved Investigations on Pyrene-Based Chemosensors. *Inorganic Chemistry* **2013,** *52* (1), 121.

4. Costa, T.; Sérgio Seixas de Melo, J.; Castro, C. S.; Gago, S.; Pillinger, M.; Gonçalves, I. S., Picosecond Dynamics of Dimer Formation in a Pyrene Labeled Polymer. *The Journal of Physical Chemistry B* **2010,** *114* (39), 12439.

5. Costa, T.; Seixas de Melo, J.; Burrows, H. D., Fluorescence Behavior of a Pyrene-End-Capped Poly(ethylene oxide) in Organic Solvents and in Dioxane−Water Mixtures. *The Journal of Physical Chemistry B* **2009,** *113* (3), 618.

6. Costa, T.; Seixas de Melo, J. S., The effect of γ-cyclodextrin addition in the self-assembly behavior of pyrene labeled poly(acrylic) acid with different chain sizes. *Journal of Polymer Science Part A: Polymer Chemistry* **2008,** *46* (4), 1402.

7. Seixas de Melo, J.; Costa, T.; Francisco, A.; Macanita, A. L.; Gago, S.; Goncalves, I. S., Dynamics of short as compared with long poly(acrylic acid) chains hydrophobically modified with pyrene, as followed by fluorescence techniques. *Physical Chemistry Chemical Physics* **2007,** *9* (11), 1370.

8. de Melo, J. S. S.; Costa, T.; Oliveira, N.; Schillén, K., Fluorescence studies on the interaction between pyrene-labelled poly(acrylic acid) and cyclodextrins. *Polymer International* **2007,** *56* (7), 882.

9. Seixas de Melo, J.; Costa, T.; Miguel, M. d. G.; Lindman, B.; Schillén, K., Time-Resolved and Steady-State Fluorescence Studies of Hydrophobically Modified Water-Soluble Polymers. *The Journal of Physical Chemistry B* **2003,** *107* (46), 12605.

10. Gago, S.; Costa, T.; Seixas de Melo, J.; Goncalves, I. S.; Pillinger, M., Preparation and photophysical characterisation of Zn-Al layered double hydroxides intercalated by anionic pyrene derivatives. *Journal of Materials Chemistry* **2008,** *18* (8), 894.

11. Sun, Z.; Jin, L.; Shi, W.; Wei, M.; Evans, D. G.; Duan, X., Controllable Photoluminescence Properties of an Anion-Dye-Intercalated Layered Double Hydroxide by Adjusting the Confined Environment. *Langmuir* **2011,** *27* (11), 7113.

12. Shi, W.; Sun, Z.; Wei, M.; Evans, D. G.; Duan, X., Tunable Photoluminescence Properties of Fluorescein in a Layered Double Hydroxide Matrix by Changing the Interlayer Microenvironment. *The Journal of Physical Chemistry C* **2010,** *114* (49), 21070.

13. Xu, Z. P.; Braterman, P. S., Synthesis, structure and morphology of organic layered double hydroxide (LDH) hybrids: Comparison between aliphatic anions and their oxygenated analogs. *Applied Clay Science* **2010,** *48* (1–2), 235.

14. Zhang, H.; Xu, Z. P.; Lu, G. Q.; Smith, S. C., Intercalation of Sulfonate into Layered Double Hydroxide: Comparison of Simulation with Experiment. *The Journal of Physical Chemistry C* **2009,** *113* (2), 559.

15. Venkataraman, N. V.; Bhagyalakshmi, S.; Vasudevan, S.; Seshadri, R., Conformation and orientation of alkyl chains in the layered organic-inorganic hybrids: (CnH2n+1NH3)2PbI4 (n = 12,16,18). *Physical Chemistry Chemical Physics* **2002,** *4* (18), 4533.

16. Costantino, U.; Coletti, N.; Nocchetti, M.; Aloisi, G. G.; Elisei, F.; Latterini, L., Surface Uptake and Intercalation of Fluorescein Anions into Zn−Al−Hydrotalcite. Photophysical Characterization of Materials Obtained. *Langmuir* **2000,** *16* (26), 10351.

17. Viana, R. B.; da Silva, A. B. F.; Pimentel, A. S., Infrared Spectroscopy of Anionic, Cationic, and Zwitterionic Surfactants. *Advances in Physical Chemistry* **2012,** *2012*, 14.

18. Park, S.-H.; Lee, C. E., Layered Copper Hydroxide n-Alkylsulfonate Salts: Synthesis, Characterization, and Magnetic Behaviors in Relation to the Basal Spacing. *The Journal of Physical Chemistry B* **2005,** *109* (3), 1118.

19. Feng, Y.; Schmidt, A.; Weiss, R. A., Compatibilization of Polymer Blends by Complexation. 1. Spectroscopic Characterization of Ion−Amide Interactions in Ionomer/Polyamide Blends. *Macromolecules* **1996,** *29* (11), 3909.

20. Mohanambe, L.; Vasudevan, S., Aromatic Molecules in Restricted Geometries: Pyrene Excimer Formation in an Anchored Bilayer. *The Journal of Physical Chemistry B* **2006,** *110* (29), 14345.

21. Moran, P. D.; Bowmaker, G. A.; Cooney, R. P.; Bartlett, J. R.; Woolfrey, J. L., Vibrational spectra of metal salts of bis(2-ethylhexyl)sulfosuccinate (AOT). *Journal of Materials Chemistry* **1995,** *5* (2), 295.

22. Karpovich, D. S.; Blanchard, G. J., Relating the polarity-dependent fluorescence response of pyrene to vibronic coupling. Achieving a fundamental understanding of the py polarity scale. *The Journal of Physical Chemistry* **1995,** *99* (12), 3951.

23. Dong, D. C.; Winnik, M. A., The Py scale of solvent polarities. *Canadian Journal of Chemistry* **1984,** *62* (11), 2560.

24. Montalti, M.; Credi, A.; Prodi, L.; Gandolfi, M. T., *Handbook of Photochemistry*. 3rd ed.; CRC Press: Boca Raton, FL: **2006**.

25. Shakhverdov, T. A.; Kalinin, V. N.; Érgashev, R., Quenching of excited states of pyrene sulfonate solutions and their metal complexes by molecular oxygen. *Theor Exp Chem* **1987,** *23* (3), 281.

26. Menger, F. M.; Whitesell, L. G., Binding properties of 1-pyrenesulfonic acid in water. *The Journal of Organic Chemistry* **1987,** *52* (17), 3793.

27. Xing, H.; Yan, P.; Xiao, J.-X., Unusual location of the pyrene probe solubilized in the micellar solutions of tetraalkylammonium perfluorooctanoates. *Soft Matter* **2013,** *9* (4), 1164.

28. Nakatani, K.; Ishizaki, S.; Kitamura, N., "Time-Resolved Total Internal-Reflection Fluorometry of 1-Pyrene Sulfonate Anion at a Liquid/Liquid Interface". *Analytical Sciences* **1996,** *12* (5), 701.

29. Li, S.; Lu, J.; Ma, H.; Xu, J.; Yan, D.; Wei, M.; Evans, D. G.; Duan, X., Ordered Blue Luminescent Ultrathin Films by the Effective Coassembly of Tris(8-hydroxyquinolate-5-sulfonate)aluminum and Polyanions with Layered Double Hydroxides. *Langmuir* **2011,** *27* (18), 11501.

30. Dang, S.; Yan, D.; Lu, J., 8-Hydroxypyrene-1,3,6-trisulphonate and octanesulphonate co-assembled layered double hydroxide and its controllable solid-state luminescence by hydrothermal synthesis. *Journal of Solid State Chemistry* **2012,** *185* (0), 219.

31. Yan, D.; Lu, J.; Ma, J.; Wei, M.; Qin, S.; Chen, L.; Evans, D. G.; Duan, X., Thin film of coumarin-3-carboxylate and surfactant co-intercalated layered double hydroxide with polarized photoluminescence: a joint experimental and molecular dynamics study. *Journal of Materials Chemistry* **2010,** *20* (24), 5016.

32. Siebrand, W.; Wildman, T. A., Dispersive kinetics: a structural approach to nonexponential processes in disordered media. *Accounts of Chemical Research* **1986,** *19* (8), 238.

33. Seixas de Melo, J.; Pina, J.; Dias, F. B.; Maçanita, A. L., Experimental Techniques for excited state characterization. In *Applied Photochemistry*, Evans, R. C.; Douglas, P.; Burrows, H. D., Eds. Springer: **2013**; pp 533.

34. Yan, D.; Lu, J.; Wei, M.; Evans, D. G.; Duan, X., Recent advances in photofunctional guest/layered double hydroxide host composite systems and their applications: experimental and theoretical perspectives. *Journal of Materials Chemistry* **2011,** *21* (35), 13128.

35. Li, S.; Lu, J.; Xu, J.; Dang, S.; Evans, D. G.; Duan, X., Bis(8-hydroxyquinolate-5-sulfonate)zinc intercalated layered double hydroxide and its controllable luminescent properties. *Journal of Materials Chemistry* **2010,** *20* (43), 9718.

36. de Melo, J. S. S.; Costa, T.; de Castro, C. S.; Macanita, A. L., Photophysics of fluorescently labeled oligomers and polymers. In *Photochemistry: Volume 41*, The Royal Society of Chemistry: **2013**; Vol. 41, pp 59.

37. Ilharco, L. M.; Martinho, J. M. G., Hybrid and Nonhybrid Silica Sol−Gel Systems Doped with 1,12-Bis(1-pyrenyl)dodecane. *Langmuir* **1999,** *15* (22), 7490.

5. COINTERCALATION OF TWO INDIGO DERIVATIVES INTO LDH AND LHS

5.1 Introduction

The concept of cointercalation is fairly unexplored as far as hybrid pigments containing layered inorganic hosts are concerned. Most of the research performed to date has centered around dye-surfactant cointercalations similar to the one mentioned before for IC and LDHs.[1-5] Only a few papers have reported on the cointercalation of two different dye molecules. Dianqing and co-workers described the synthesis of multicolour hybrid pigments by the cointercalation of either C.I. Acid Yellow and C.I. Acid blue or Acid Green 25 and Acid Yellow 25 in a Zn-Al LDH.[6-7] Duan and co-workers successfully cointercalated 4,4-diaminostilbene-2,2-disulfonate and 4,4-dinitro-stilbene-2,2-disulfonate anions into Zn-Al LDHs to produce composite materials with electron donor-acceptor character for photoelectrochemical water splitting.[8]

Motivated by recent research on MB-related materials and the potential of organic dye cointercalation for the synthesis of hybrids with tunable colours and photophysical properties, the present work describes a comparative study of LDH and LHS materials containing either solely IC or thioindigo-5,5'-disulfonate anions (TIS), or a mixture of the two dyes in different molar ratios (Scheme 5.1). As-synthesised and thermally treated materials have been comprehensively characterized with a view to confirming genuine cointercalation and getting insights into the nature of the host-guest and guest-guest interactions.

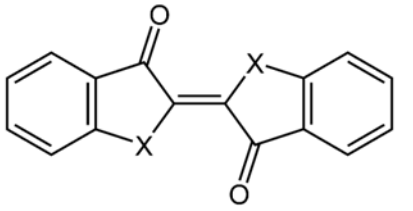

X = NH: Indigo; X = S: Thioindigo

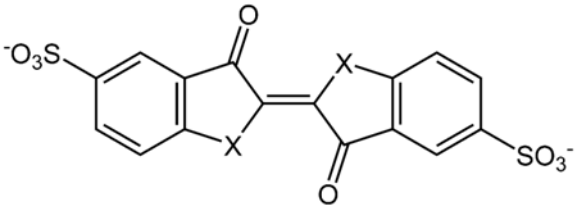

X = NH: Indigo carmine (IC)
X = S: Thioindigo-5,5'-disulfonate (TIS)

Scheme 5.1 - Chemical structures of indigo, thioindigo, and sulfonated derivatives.

5.2 Synthesis of cointercalated indigo derivatives

At a constant pH value, the (co)precipitation method was used to prepare Zn_2Al-LDHs and Zn-LHSs containing solely IC (IC-LDH, IC-LHS) or TIS (TIS-LDH, TIS-LHS) anions, or a mixture of the two indigo derivatives (IC(*n*%)/TIS-LDH or IC(*n*%)/TIS-LHS, where *n*% is the initial molar percentage of IC anions in the reaction mixture). The procedures used are slightly modified versions of those reported recently for the synthesis of IC-LDH[9] and IC-LHS[10] materials. During (co)precipitation the pH of the reaction mixtures was maintained between 7.5 and 8.0. For the LDH materials, the coprecipitation step was followed by ageing of the gel-like slurry at 65 °C for 18 h. In the case of the LHS materials, the solid products were immediately filtered following complete addition of the NaOH solution since it was found that ageing of the gel, even at room temperature, led to the formation of an unidentified impurity phase. The synthesis of pure LHS phases was also promoted by fixing the net OH/Zn molar ratio at 0.5, in agreement with observations reported by Newman and Jones (higher ratios favour the formation of ZnO and/or $Zn(OH)_2$ impurity phases).[11] The colours of the isolated solids were very dark blue for the LDH intercalates with *n* = 50-100, dark blue for IC-LHS (*n* = 100), and ruby/wine for TIS-LDH and TIS-LHS (*n* = 0). The colours of the samples IC(80%)/TIS-LHS (purplish blue) and IC(50%)/TIS-LHS (dark lilac) were consistent with the expected IC and TIS contents.

5.3 Structural characterization of the materials

5.3.1 Powder X-Ray Diffraction

The PXRD patterns of the LDH and LHS materials are shown in Figure 5.1. The patterns for the LDH intercalates are typical of hydrotalcite-type materials with an expanded interlayer spacing, displaying up to seven equally spaced 00*l* basal reflections between 3.5 and 30° 2θ. The basal spacings for the end-members of the series are 21.90 Å for IC-LDH and 21.05 Å for TIS-LDH. The former distance is slightly lower than the 22.2-22.4 Å distances previously reported for IC-intercalated (Zn/Mg)-Al LDHs with a metal cation molar ratio of 3:1 prepared by the coprecipitation method.[12-13] Our group previously reported a basal spacing of 17.6 Å for an IC-LDH prepared using the same procedure as used in the present work. The difference between this distance and the current value of 21.9 Å may be because the previous material had a final Zn/Al molar ratio slightly lower than 2. For samples containing both IC and TIS, the basal spacing lie between those for IC-LDH and TIS-LDH, and decrease with increasing TIS content: 21.80 Å for IC(98%)/TIS-LDH, 21.55 Å for IC(90%)/TIS-LDH, and 21.20 Å for IC(50%)/TIS-LDH. This trend is consistent with genuine cointercalation of the two indigo derivatives rather than the presence of a mixture of IC-LDH and TIS-LDH phases.

The experimental powder XRD pattern of NO_3-LHS was found in agreement with a simulated pattern calculated using the crystal structure data reported by Stählin and Oswald for $Zn_5(OH)_8(NO_3)_2{\cdot}2H_2O$ (Figure 5.2).[14] In agreement with results reported by Newman and Jones for a

synthetic zinc hydroxide nitrate,[11] the CHN analyses and TGA data for NO_3-LHS indicate the presence of a small number of impurity CO_3^{2-} anions in the product (see spectroscopic characterization in Chapter 7).

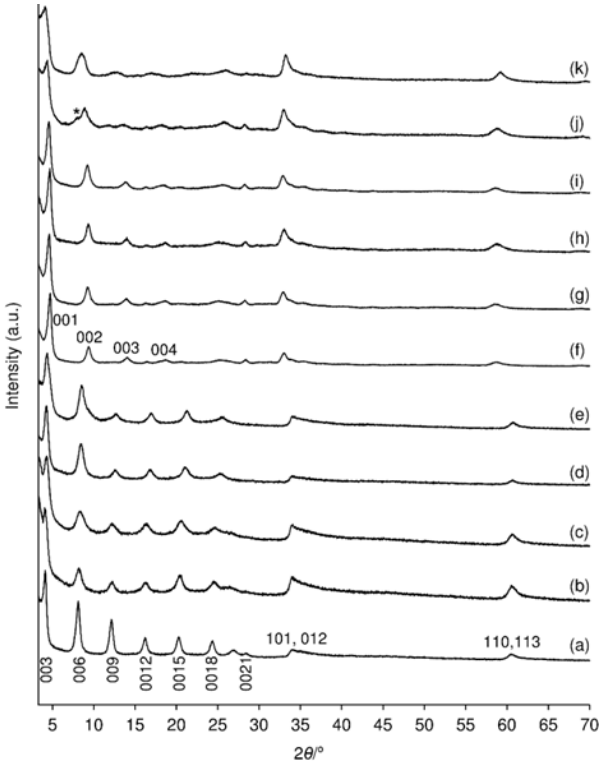

Figure 5.1 - PXRD patterns of (a) IC-LDH, (b) IC(98%)/TIS-LDH, (c) IC(90%)/TIS-LDH, (d) IC(50%)/TIS-LDH, (e) TIS-LDH, (f) IC-LHS, (g) IC(98%)/TIS-LHS, (h) IC(90%)/TIS-LHS, (i) IC(80%)/TIS-LHS, (j) IC(50%)/TIS-LHS, and (k) TIS-LHS. Basal (00*l*) reflections are indicated for IC-LDH and IC-LHS. The asterisk in pattern (j) indicates a shoulder that is attributed to the 002 reflection for a TIS-LHS phase.

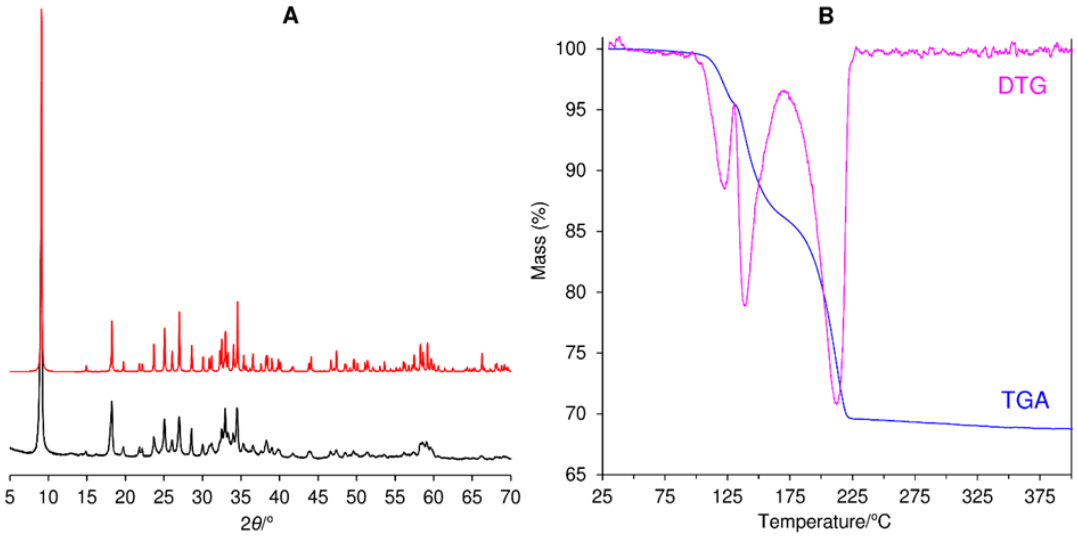

Figure 5.2 - Powder XRD pattern (**A**) and TGA data (**B**) for NO_3-LHS. The red pattern in **A** is a simulated diffractogram calculated using published crystal structure data for $Zn_5(OH)_8(NO_3)_2{\cdot}2H_2O$.[14] In **B** the differential thermogravimetric (DTG) profile is also shown.

The crystal structure of a polymorphic form of Na_2IC was recently described.[15] In the structure, layers composed of sodium ions and IC molecules are alternately stacked. Figure 5.3 depicts one IC molecule in the structure viewed along the 010 direction. The vertical distance *a* shown in Figure 5.3 is a good estimate of the longest dimension of the molecule (that includes van der Waals radii for the S-bound oxygens). Based on the unit cell parameters, the value of *a* is 17.6 Å, which is in good agreement with previously reported DFT calculations that yielded a value of 17.5 Å for the longest dimension of the molecule.[10] It may also be assumed that 17.6 Å is also a good estimate of the longest dimension of the TIS anion. If the thickness of a brucite-type layer is taken as 4.8 Å, the interlayer spacings for the LDH materials fall in the range of 16.25-17.10 Å, which suggests that the indigo derivatives adopt a near-vertical orientation with an angle of 65-80º with respect to the host layers. Figure 5.4 illustrates an idealized model for intercalated TIS anions that reproduce the observed basal spacing of 21.05 Å. Similar arrangements can be envisaged for the other LDH intercalates. In the model, the aromatic rings of adjacent TIS anions are in a slipped face-to-face π-π stacking arrangement, which is the type of molecular packing observed in the crystal structures of indigo,[16-17] monothioindigo[18] and thioindigo.[19] For indigo and monothioindigo, molecules are also linked by strong intermolecular hydrogen bonds involving the NH and carbonyl groups. In the structure of thioindigo, the molecules exhibit only van der Waals interactions and molecular stacking. While N–H···O interactions are present in the crystal structure of Na_2IC, the π-stacked columnar structure is absent, as illustrated in Figure 5.3b.[15] Hence, referring to the idealized model presented in Figure 5.4, other types of packing arrangements (i.e., different from face-to-face alignment) may be present in the LDH intercalates, and these may vary according to the IC/TIS contents, being influenced to some degree by the nature of intermolecular hydrogen-bonding interactions.

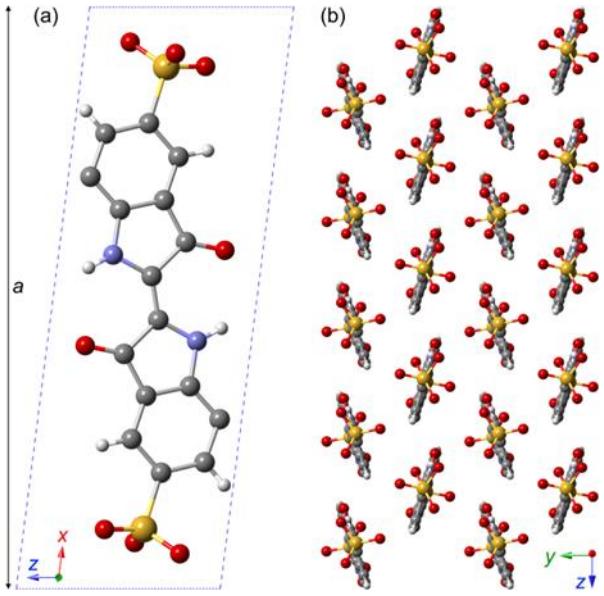

Figure 5.3 - Crystal structure of Na_2IC[15]: (a) View of one IC molecule along the *b* axis. (b) Two-dimensional packing of the IC molecules in the *bc*-plane.

In proposing interlayer arrangements in LDHs and related materials, the area available to each anion must be considered. For LDHs with layers of the type $[M^{2+}_{1-x}M^{3+}_{x}(OH)_2]^{x+}$, the area per unit charge is $(1/x)a_0^2\sin60$, where a_0 is the unit cell parameter. Zn_2Al-LDHs have unit layer charge areas of about 25 $Å^2$ ($a_0 \approx 3.07$ Å, $x = 0.33$). In the structure of Na_2IC, the IC anions are quite efficiently close-packed in the *bc* plane (Figure 5.3b), and the average cross-sectional area occupied by each IC anion is 24.7 Å, which corresponds to an area per unit negative charge of 12.35 $Å^2$. Hence, a Zn_2Al-LDH should be able to comfortably accommodate a monolayer of intercalated IC or TIS anions, even if the anions adopt a non-vertical orientation with respect to the host layers and/or are spaced further apart.

For the LHS materials, the diffractograms are not dissimilar to those for the LDH intercalates, displaying four basal reflections up to about 20° 2θ and some non-basal peaks towards higher angles. The pattern and basal spacing of 18.95 Å for IC-LHS are in agreement with those reported by Wypych and co-workers.[10] Curiously, the basal spacing tends to follow the opposite trend to that observed for the LDH materials, i.e. it increases with increasing TIS content: 19.10 Å for IC(98%)/TIS-LHS and IC(90%)/TIS-LHS, 19.25 Å for IC(80%)/TIS-LHS, 19.80 Å for IC(50%)/TIS-LHS, and 21.00 Å for TIS-LHS. For the 002 reflection in the pattern of IC(50%)/TIS-LHS, a distinct shoulder on the low-angle side may be due to a pure TIS-LHS phase, suggesting that genuine cointercalation of the two indigo derivatives to give a single intercalated phase is only possible for an IC content higher than 50%.

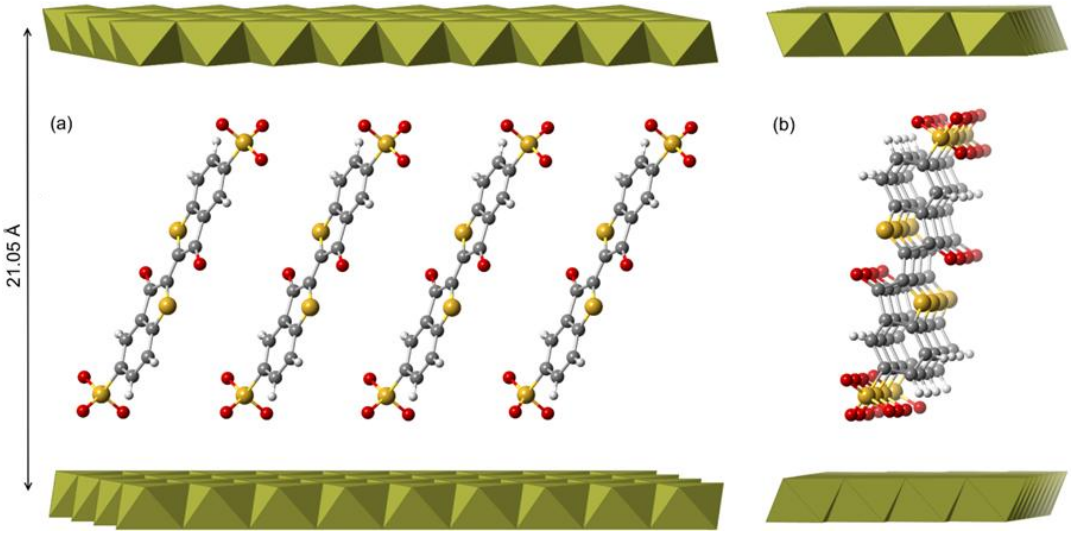

Figure 5.4 - Idealized model of one of the possible guest packing modes in TIS-LDH featuring face-to-face alignment of TIS molecules. A side-on view of (a) is shown in (b).

Wypych and co-workers performed DFT simulations in order to model the anion arrangement in their LHS material intercalated by IC molecules.[10] The calculations were performed by considering that the structure of the positively charged zinc hydroxide layer was similar to that for the known compound $Zn_5(OH)_8(NO_3)_2\cdot2H_2O$ (NO_3^- as the interlayer anion),[14] and that IC anions would interact

with the LHS layers through electrostatic attractions and hydrogen bonds to zinc-bonded water molecules. The predicted basal spacing of 19.30 Å was similar to the experimental value of 19.07 Å. The structural model presented by Wypych and co-workers was used in the present work as a starting point to model the anion arrangement in TIS-LHS. Figure 5.5 shows a possible arrangement of TIS molecules that gives rise to a basal spacing equal to the observed value of 21.0 Å. There is reasonable agreement between the experimental PXRD pattern for TIS-LHS and a simulated pattern for the model, especially concerning the basal reflections (Figure 5.6). The TIS molecules in the model are inclined at an angle of about 59° with respect to the host layers, which is slightly higher than the value of 54° for the reported IC-LHS model.[10]

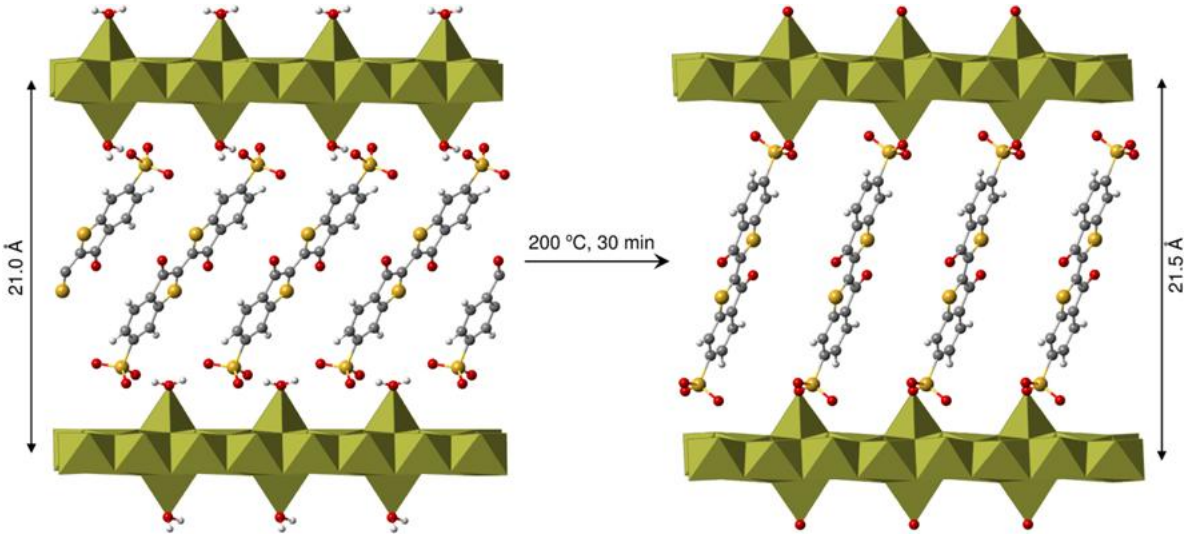

Figure 5.5 - Possible arrangement of intercalated TIS anions in TIS-LHS and TIS-LHS$_{ht}$. The model for TIS-LHS corresponds to the stoichiometric composition of $Zn_5(OH)_8(TIS)(H_2O)_2$ (see discussion).

The structural model for TIS-LHS (and IC-LHS reported by Wypych and co-workers[10]) corresponds to the idealized stoichiometric composition of $Zn_5(OH)_8(TIS)(H_2O)_2$. Visualization of this model in space-filling mode (van der Waals radii) shows that the guest molecules are quite tightly close-packed. LHSs have higher layer charge densities than LDHs. Referring to the structure of $Zn_5(OH)_8(NO_3)_2(H_2O)_2$,[14] the unit layer charge area is about 17.2 Å^2. The minimum area per unit negative charge for IC anions, estimated above as 12.35 Å^2 from the cross-sectional area, is lower than this unit layer charge area. However, the net area per unit negative charge will be higher for a monolayer of intercalated guest anions that are inclined at angles less than 90° with respect to the host layers as is the case in the structural models. Hence, the structural models feature a high packing density in the interlayer region.

The samples TIS-LHS and IC-LHS were thermally treated at 200 °C under air in a manner similar to that described previously for IC-LHS.[10] The PXRD patterns of the resultant materials (Figure 5.6), denoted as TIS-LHS$_{ht}$ and IC-LHS$_{ht}$, indicate the retention of a layered structure, albeit with reduced crystallinity, and the basal spacings are estimated as 21.5 Å for TIS-LHS$_{ht}$ and 19.3 Å for IC-

LHS_{ht}, which represent slight expansions (0.35-0.50 Å) with respect to the initial spacings. Wypych and co-workers obtained similar results upon thermal treatment of IC-LHS and, with the help of DFT calculations and FT-IR spectroscopy, concluded that the intercalated IC anions became grafted to the host structure via covalent bonds between Zn^{tetra} atoms and sulfonate oxygen atoms.

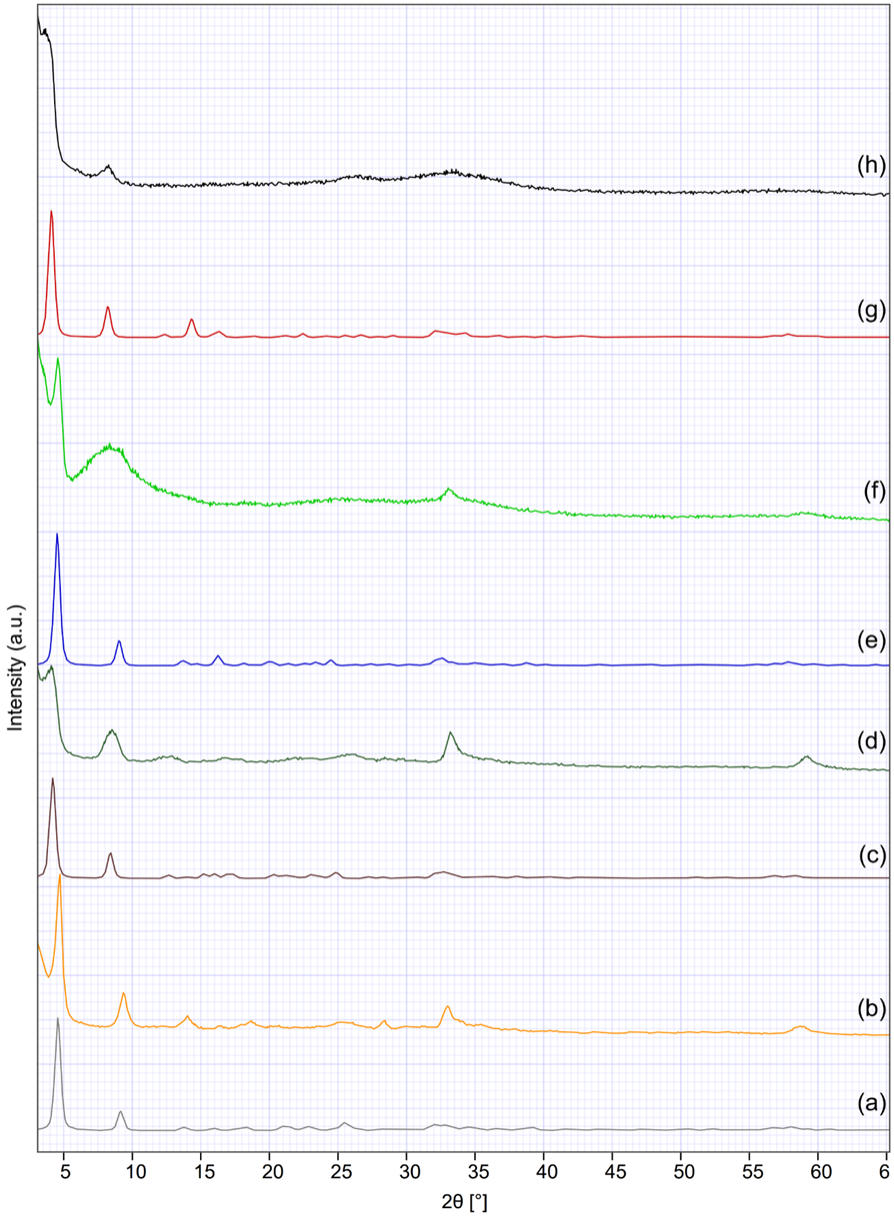

Figure 5.6 - Simulated (a,c,e,g) and experimental (b,d,f,h) powder XRD patterns of (a,b) IC-LHS, (c,d) TIS-LHS, (e,f) $IC\text{-}LHS_{ht}$, and (g,h) $TIS\text{-}LHS_{ht}$. The simulated patterns for IC-LHS and $IC\text{-}LHS_{ht}$ were calculated using previously reported structural models (without any further modification).[9] The simulated patterns for TIS-LHS and $TIS\text{-}LHS_{ht}$ were calculated using the modified structural models with basal spacings of 21.0 Å and 21.5 Å, respectively, as described above.

The structural model presented by Wypych and co-workers was used as a starting point to model the anion arrangement in TIS-LHS$_{ht}$. Figure 5.5 shows a possible arrangement of grafted TIS molecules that reproduces the observed basal spacing of 21.5 Å. In Figure 5.6, the experimental PXRD patterns for TIS-LHS$_{ht}$ and IC-LHS$_{ht}$ are compared with the simulated patterns calculated for the corresponding structural models.

5.3.2 FTIR spectroscopy

Regarding the cointercalated samples, clear FT-IR evidence for the presence of both IC and TIS anions was only obtained for the samples with n = 50%. For the samples obtained using higher values of n (lower TIS contents), the infrared spectra in the 300-1800 cm^{-1} range were dominated by the bands due to IC, and no bands due to TIS could be discerned. In particular, the 350–1800 cm^{-1} region of the IR spectra of the intercalates with n = 0 or 100 is dominated by the bands due to IC (n = 100) or TIS (n = 0), which are generally coincident (to within 8 cm^{-1}) with those displayed by Na_2IC or H_2TIS (Figure 5.7). The absorption bands for the asymmetric and symmetric stretching vibrations of the sulfonate group appear at 1199 and 1028/1065 cm^{-1}, respectively, for IC-LDH and IC-LHS, which are unshifted compared with those for Na_2IC (1196, 1028/1065 cm^{-1}). Slightly more pronounced shifts were observed for the TIS samples: 1033/1085 cm^{-1} for TIS-LDH and TIS-LHS vs. 1031/1090 cm^{-1} for H_2TIS. Towards higher frequency, Na_2IC, IC-LDH and IC-LHS exhibit a strong band at 1615±1 cm^{-1}, which is assigned as a C=C ring stretching vibration. The corresponding band for H_2TIS, TIS-LDH and TIS-LHS appears at 1592±1 cm^{-1}. The pure dyes Na_2IC and H_2TIS display a single band at 1638 and 1657 cm^{-1}, respectively, for ν(C=O). Whereas single ν(C=O) bands are observed for IC-LHS (1641 cm^{-1}), TIS-LDH (1654 cm^{-1}) and TIS-LHS (1649 cm^{-1}), IC-LDH shows two overlapping bands with peak maxima at *ca.* 1642 and 1655 cm^{-1}, exactly as found previously for an IC-LDH sample with the shorter basal spacing of 17.6 Å.[9] The modification of the ν(C=O) absorption band for the IC-LDH samples is presumably related with the nature of the hydrogen bonding interactions involving the carbonyl groups and either N-H groups (intramolecular or intermolecular) or interlayer water molecules. Inspection of the 1350-1550 cm^{-1} spectral region for all LDH and LHS samples showed the absence of bands that could be ascribed to asymmetric ν_3 stretching modes of nitrate (expected at 1385±5 cm^{-1}) or carbonate (expected at 1385±5 and 1510±10 cm^{-1} for phases related to hydrozincite, or 1365±5 cm^{-1} for “free” uncoordinated interlayer anions) species.

Differences observed between the FT-IR spectra of IC-LHS and IC-LHS$_{ht}$, most notably in the 1100-1250 cm^{-1} region, match those reported previously,[10] and support thermally-induced guest-to-host grafting via the sulfonate oxygens (Figure 5.7). On the other hand, no significant differences were observed between the FT-IR spectra for TIS-LHS and TIS-LHS$_{ht}$, and therefore some caution is required in drawing conclusions about any changes in the nature of the host-guest interaction.

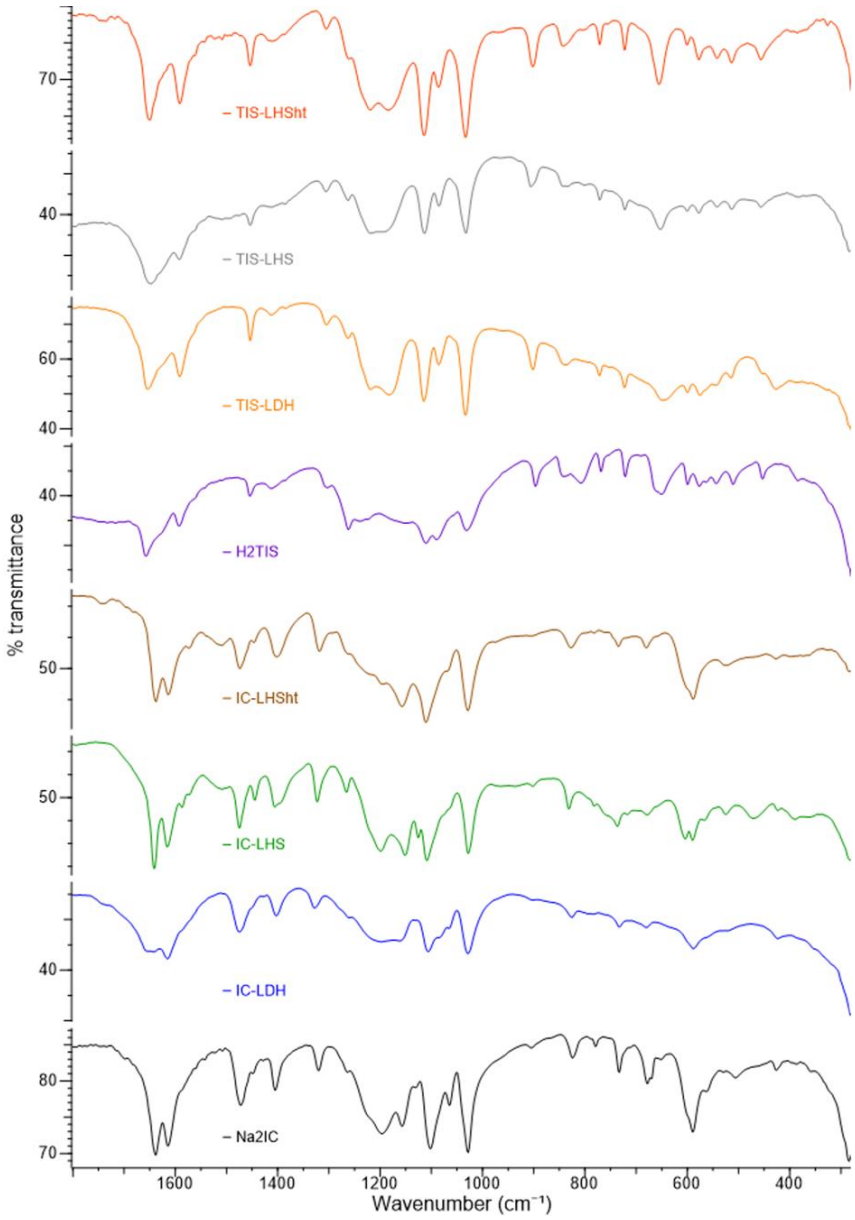

Figure 5.7 - FT-IR spectra in the 300-1800 cm^{-1} region of Na_2IC, IC-LDH, IC-LHS, IC-LHS_{ht}, H_2TIS, TIS-LDH, TIS-LHS and TIS-LHS_{ht}.

Figures 5.8 and 5.9 compare the FT-IR spectra of IC-LDH, TIS-LDH, IC-LHS and TIS-LHS with those for the cointercalated samples. Only the spectra for IC(50%)/TIS-LDH and IC(50%)/TIS-LHS display bands for both anionic indigo derivatives, which can be readily identified by reference to the spectra for the samples containing only IC or TIS.

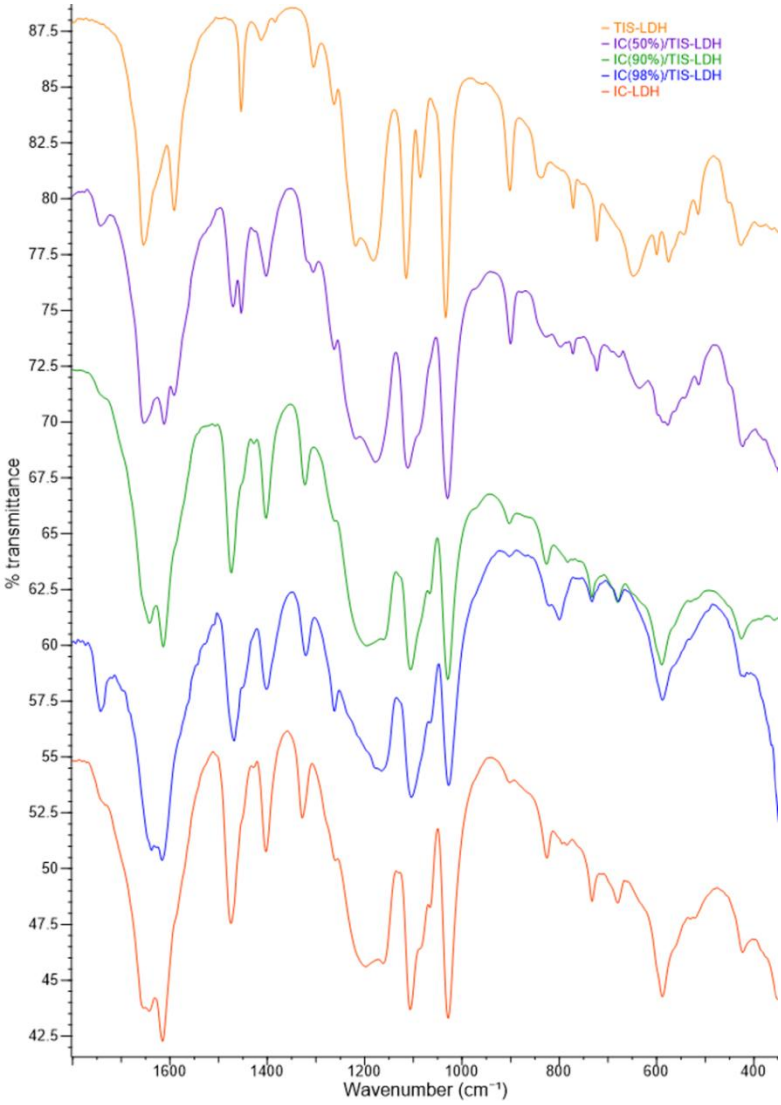

Figure 5.8 - FT-IR spectra in the 350-1800 cm^{-1} region of IC-LDH, TIS-LDH, and the cointercalated samples.

However, the cointercalation of TIS anions in the samples IC(90%)/TIS-LDH and IC(98%)/TIS-LDH may be responsible for changes observed in the ν(C=O) bands around 1650 cm^{-1}. Thus, the characteristic spectral profile for IC-LDH consisting of two overlapping bands with peak maxima at 1642 and 1655 cm^{-1} is not observed for the cointercalated samples, which show only one resolved band with a maximum at ca. 1640 cm^{-1}. The introduction of only a small quantity of TIS anions within the IC-dominated interlayer region may be sufficient to have an effect on hydrogen-bonding interactions involving carbonyl groups, thereby affecting the ν(C=O) absorption bands for IC anions.

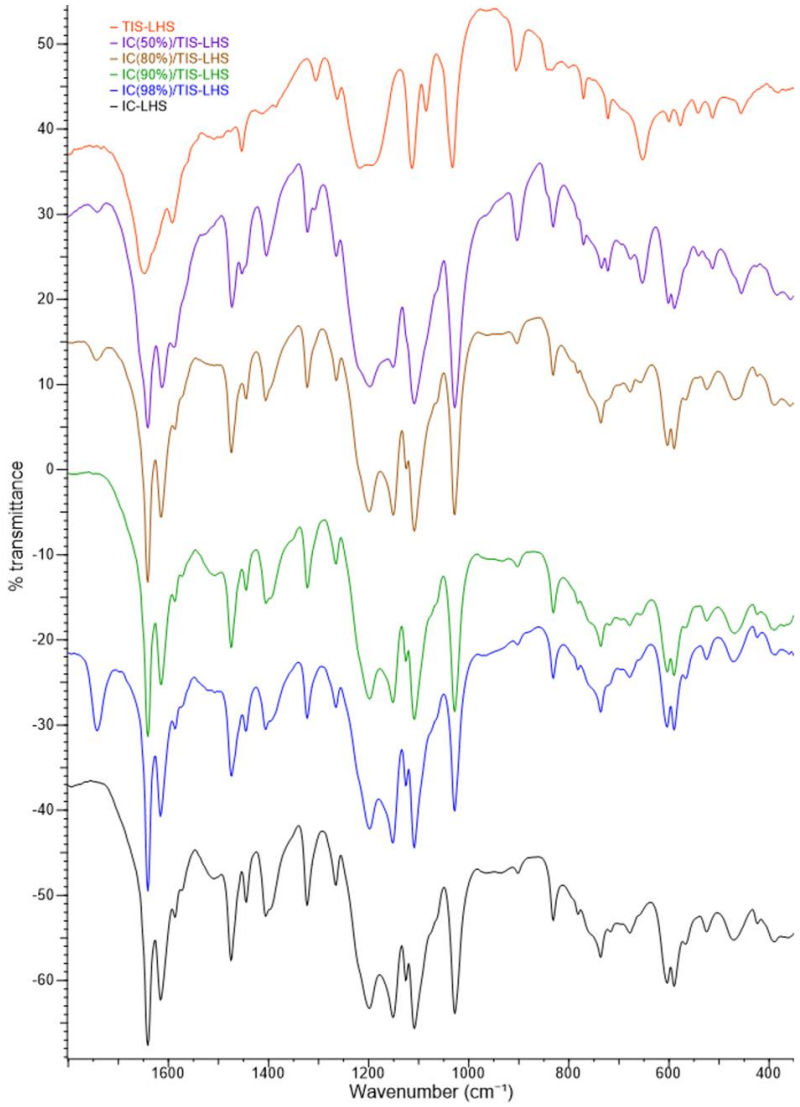

Figure 5.9 - FT-IR spectra in the 350-1800 cm^{-1} region of IC-LHS, TIS-LHS, and the cointercalated samples.

5.3.3 Raman spectroscopy

Figure 5.10 shows the Raman spectra for Na_2IC, IC-LDH, H_2TIS, TIS-LDH, TIS-LHS and TIS-LHS_{ht}; good quality spectra could not be obtained for IC-LHS and IC-LHS_{ht}. The spectral data supplement the FT-IR spectra and point to the presence of structurally intact IC or TIS anions. For the salt Na_2IC, the very strong band at 1580 cm^{-1} is assigned to ν(C=C) and the weak band at 1296 cm^{-1} probably has a sulfonate symmetric stretching contribution.[20] The former mode is unshifted in the spectrum of IC-LDH, while the latter band shifts by 5 cm^{-1} towards lower frequency. For H_2TIS and all the TIS-intercalated samples, the corresponding absorption bands are found at 1520±2 cm^{-1} and 1302±2 cm^{-1}, and an additional weak band at 1674-1675 cm^{-1} may be assigned to the ν(C=O) stretching vibration.

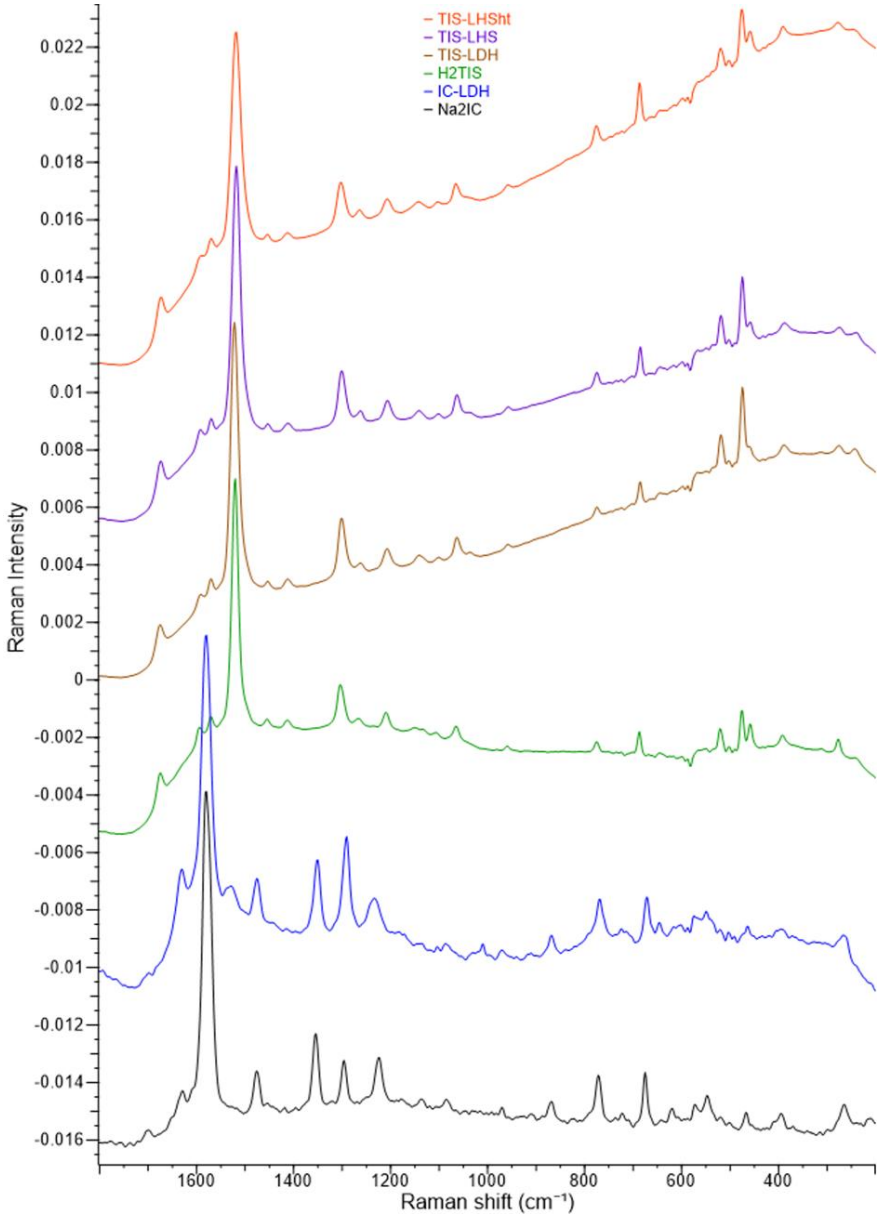

Figure 5.10 - Raman spectra in the 200-1800 cm^{-1} region of Na_2IC, IC-LDH, H_2TIS, TIS-LDH, TIS-LHS and $TIS\text{-}LHS_{ht}$.

5.3.4 $^{13}C\{^1H\}$ CP MAS NMR spectroscopy

Figure 5.11 shows the $^{13}C\{^1H\}$ CP MAS NMR spectra of Na_2IC, IC-LDH, IC-LHS, H_2TIS, TIS-LDH and TIS-LHS. As reported previously,[9] the spectrum for Na_2IC is quite complex, with some of the chemically equivalent carbon atoms displaying two distinct resonances. This may originate from the presence of non-equivalent indigo carmine molecules in the unit cell and/or non-equivalent indoxyl moieties within a single IC molecule. Peaks are observed in similar chemical shift ranges for IC-LDH. However, the spectrum for the intercalated indigo derivative is simplified in that single peaks are

observed for each chemically equivalent carbon atom, e.g. one resonance at 187.7 ppm for the carbonyl group (2,2'-C).

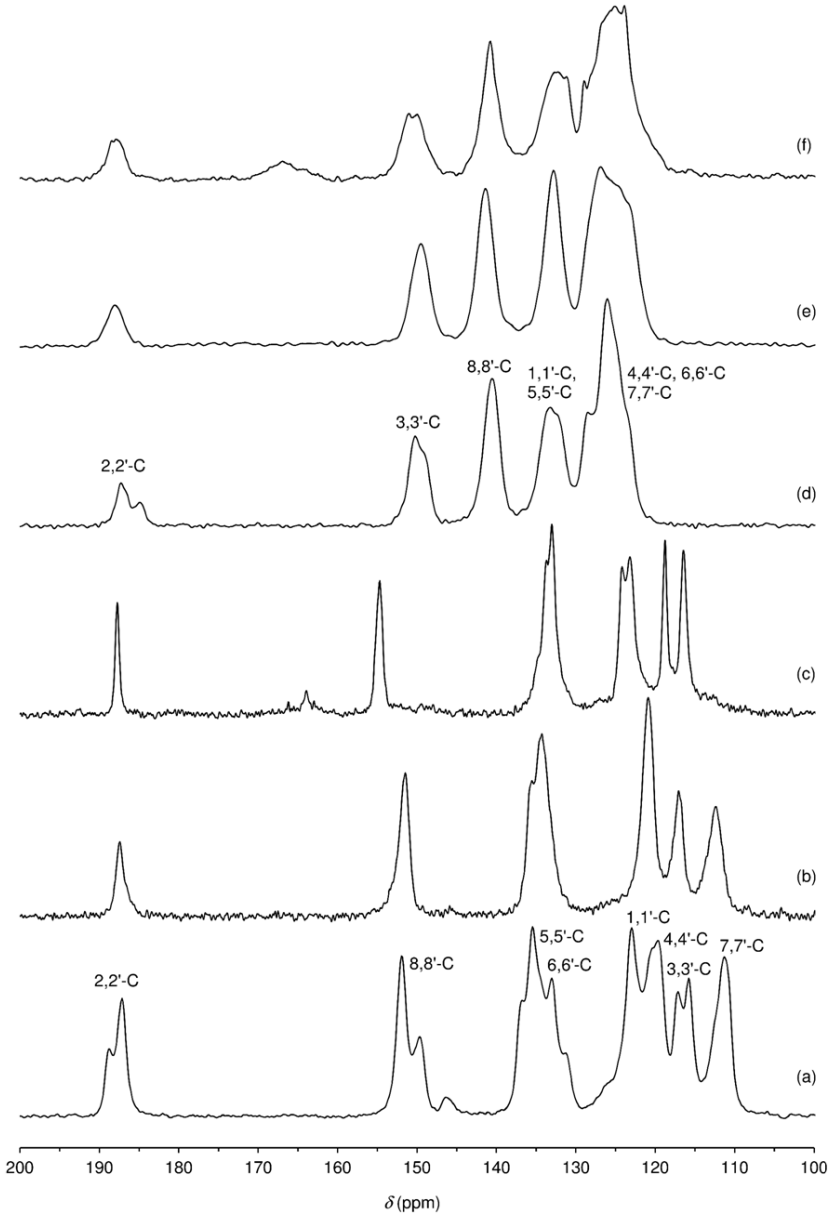

Figure 5.11 - $^{13}C\{^{1}H\}$ CP MAS NMR spectra of (a) Na_2IC, (b) IC-LDH, (c) IC-LHS, (d) H_2TIS, (e) TIS-LDH and (f) TIS-LHS. The atom numbering scheme is given in experimental section (Chapter 7).

The same effect is evident for IC-LHS, which gives rise to quite sharp peaks indicative of a high degree of structural order for the intercalated molecules. However, the spectra of IC-LDH and IC-LHS are quite different concerning the chemical shift values of some resonances, with signals for IC-LHS (e.g. 8,8'-C) being downfield-shifted with respect to the corresponding signals for IC-LDH. Such variations are not apparent for the TIS samples where the spectra of TIS-LDH and TIS-LHS are very similar and superimpose quite well with that for H_2TIS.

5.3.5 Elemental analysis

Chemical compositions for the intercalated samples were estimated by elemental (CHNS) and thermogravimetric analyses (Table 5.1). For the LDH samples, the experimental data consistently indicated that (i) the combined IC and TIS contents were slightly lower than the ideal stoichiometric value for an LDH with Zn/Al = 2, and (ii) the final bulk IC:TIS molar ratios for the cointercalated samples were, to within experimental error, consistent with the expected values based on the initial molar ratios used in the syntheses. The combined IC and TIS contents indicated that the anionic dyes balanced 91-95% of the positive charge of the hydroxide layers. The remaining 5-9% may be balanced by (co)intercalated carbonate, nitrate and/or hydroxide anions. As found previously for IC-LDH,[9] FT-IR and CP MAS NMR data indicated that the samples contained minimal or insignificant amounts of carbonate or nitrate. It was therefore propose that the major fraction of the residual positive charge may be counterbalanced by hydroxide anions, as suggested previously for composites of perylene bisimide dyes and LDHs.[21] The general composition for the LDH composites is therefore written as $Zn_4Al_2(OH)_{12}(IC_{n/100}TIS_{(100-n)/100})_z(OH)_{2(1-z)}(H_2O)_m$, where z = 0.91-0.95 and m = 4.5-5.5.

While elemental analyses for the cointercalated LHS samples indicated that the final bulk IC:TIS molar ratios were close to the starting values, the combined IC and TIS contents for these samples and also IC-LHS and TIS-LHS were significantly lower than those expected for the stoichiometric composition of $Zn_5(OH)_8(IC_{n/100}TIS_{(100-n)/100})(H_2O)_m$. The presence of significant amounts of interfering carbonate and/or chloride ions in the composites was not supported by FT-IR spectroscopy and energy dispersive X-ray spectrometry analyses for chlorine, respectively. In analogy with that suggested above for the LDH samples, one possibility is that the LHS samples contain cointercalated hydroxide ions, which could be coordinated (instead of water molecules) to the tetrahedrally coordinated zinc atoms. Another possibility is that the layer charge densities of the LHS composites are lower than the ideal value due to the fraction of tetrahedrally coordinated Zn^{2+} ions being lower than the expected value. In other words, upon completion of the coprecipitation and self-assembly process, not all empty octahedral sites in the resultant brucite-type layers are capped above and below by tetrahedrally coordinated zinc atoms. For such materials, the layer composition may be more generally expressed as $[Zn^{octa}{}_3Zn^{tetra}{}_{(2-y)}(OH)_8(H_2O)_{(2-y)}]^{(2y)+}$, where octa/tetra indicate octahedrally/tetrahedrally coordinated zinc atoms, and y gives the number of missing Zn^{tetra}. Lang and co-workers uncovered a similar phenomenon for layered zinc hydroxide salts intercalated with dodecyl sulfate anions and suggested that LHS materials may have a general propensity to exhibit this kind of variability of the zinc ion distribution within the hydroxide layers.[22] When the lower than expected IC+TIS contents for the LHS composites are associated exclusively with missing Zn^{tetra}, the general composition is $Zn_{5-y}(OH)_8(IC_{n/100}TIS_{(100-n)/100})_{1-y}(H_2O)_m$, where y = 0.32-0.50 and m = 2.5-3.5 (Table 5.1). This would mean a Zn^{tetra} removal of 16-25% (consistent with a reduction of the layer charge by 32-50%).

5.3.6 Thermogravimetric analysis

The thermal stability of TIS-LHS was investigated by TGA to determine whether thermally-induced guest-to-host covalent grafting would be possible as reported previously for a zinc hydroxide salt intercalated by IC.[10] Heat treatment of TIS-LHS results in a gradual mass loss of 9.4% up to 150 °C, attributed to removal of physisorbed/intercalated water (Figure 5.12). This is followed by a more abrupt loss of 5.4% up to 190 °C (DTG_{max} = 177 °C), which may be due to partial decomposition of the LHS structure. Decomposition of intercalated TIS anions manifests itself as a single step between 430 and 570 °C (DTG_{max} = 540 °C), leaving a residual mass of 47.2%, which is good agreement with the expected value of 46.8% calculated on the basis of the proposed chemical composition (Table 5.1) and the assumption that the residue is ZnO. It is noteworthy that the thermal stability of intercalated TIS anions is enhanced in relation to that for H_2TIS, which displays the onset of decomposition at about 325 °C (DTG_{max} = 370 °C). The TGA curve for IC-LHS was also measured and found to be similar to that for TIS-LHS (up to 350 °C) and to the curve reported by Wypych and co-workers for their IC-LHS material (Figure 5.13).[10] In contrast to that observed for the thioindigo derivative, intercalated IC anions display lower thermal stability (onset = 360 °C, DTG_{max} = 430 °C) than those in the sodium salt Na_2IC (onset = 400 °C, DTG_{max} = 470 °C).

The covalent grafting of TIS molecules in TIS-LHS_{ht} is nevertheless supported by the similarity of the TGA curves (up to 350 °C) for TIS-LHS_{ht} and IC-LHS_{ht} (Figures 5.12 and 5.13). Decomposition of the organic molecules in the heat-treated samples occurred over the same temperature ranges (identical DTG_{max}) as those for TIS-LHS and IC-LHS.

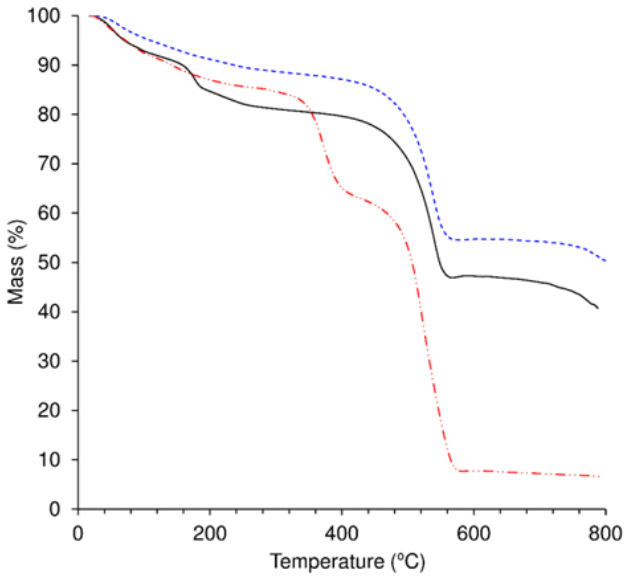

Figure 5.12 - TGA curves of H_2TIS (– · · – · ·), TIS-LHS (———), and TIS-LHS_{ht} (– – – –).

Table 5.1 - Chemical compositions of IC(*n*%)/TIS-LDH and IC(*n*%)/TIS-LHS samples.

Material code	Chemical composition	Calcd (found)					
		C	H	N	S	H_2O[a]	RM_{TGA}[b]
IC-LDH	$Zn_4Al_2(OH)_{12}(C_{16}H_8N_2O_8S_2)_{0.95}(OH)_{0.1}(H_2O)_5$	18.06 (18.09)	2.96 (2.87)	2.63 (2.69)	6.03 (5.90)	8.9 (11.2)	42.3 (34.5)
TIS-LDH	$Zn_4Al_2(OH)_{12}(C_{16}H_6O_8S_4)_{0.92}(OH)_{0.16}(H_2O)_{4.5}$	17.31 (17.51)	2.63 (2.72)	- -	11.55 (11.35)	7.9 (8.1)	41.9 (43.4)
IC(98%)/TIS-LDH	$Zn_4Al_2(OH)_{12}((C_{16}H_8N_2O_8S_2)_{0.98}(C_{16}H_6O_8S_4)_{0.02})_{0.92}(OH)_{0.16}(H_2O)_5$	17.68 (17.58)	2.97 (2.95)	2.53 (2.60)	6.02 (6.18)	9.0 -	42.8 -
IC(90%)/TIS-LDH	$Zn_4Al_2(OH)_{12}((C_{16}H_8N_2O_8S_2)_{0.90}(C_{16}H_6O_8S_4)_{0.10})_{0.91}(OH)_{0.18}(H_2O)_{5.5}$	17.36 (17.0)	3.03 (3.05)	2.28 (2.28)	6.37 (6.50)	9.8 -	42.4 -
IC(50%)/Ti-LDH	$Zn_4Al_2(OH)_{12}((C_{16}H_8N_2O_8S_2)_{0.50}(C_{16}H_6O_8S_4)_{0.50})_{0.92}(OH)_{0.16}(H_2O)_5$	17.42 (17.37)	2.84 (2.9)	1.27 (1.01)	8.72 (8.79)	8.9 (9.1)	42.1 (42.7)
IC-LHS	$Zn_{4.59}(OH)_8(C_{16}H_8N_2O_8S_2)_{0.59}(H_2O)_{3.2}$	15.28 (15.10)	2.60 (2.45)	2.23 (2.21)	5.10 (5.11)	7.8 (8.0)	50.4 (50.3)
TIS-LHS	$Zn_{4.68}(OH)_8(C_{16}H_6O_8S_4)_{0.68}(H_2O)_{3.5}$	16.05 (15.96)	2.36 (2.10)	- -	10.71 (10.3)	7.7 (9.4)	46.8 (47.2)
IC(98%)/TIS-LHS	$Zn_{4.6}(OH)_8((C_{16}H_8N_2O_8S_2)_{0.98}(C_{16}H_6O_8S_4)_{0.02})_{0.6}(H_2O)_{3.5}$	15.32 (15.30)	2.65 (2.35)	2.19 (2.20)	5.21 (5.01)	8.4 -	49.8 -
IC(90%)/TIS-LHS	$Zn_{4.5}(OH)_8((C_{16}H_8N_2O_8S_2)_{0.9}(C_{16}H_6O_8S_4)_{0.1})_{0.5}(H_2O)_{3.5}$	13.62 (13.63)	2.70 (2.15)	1.79 (1.81)	5.00 (4.53)	8.9 -	51.9 -
IC(80%)/TIS-LHS	$Zn_{4.63}(OH)_8((C_{16}H_8N_2O_8S_2)_{0.8}(C_{16}H_6O_8S_4)_{0.2})_{0.63}(H_2O)_{2.8}$	15.96 (16.15)	2.44 (2.35)	1.86 (1.86)	6.39 (6.41)	6.6 (7.0)	49.7 (50.6)
IC(50%)/TIS-LHS	$Zn_{4.5}(OH)_8((C_{16}H_8N_2O_8S_2)_{0.5}(C_{16}H_6O_8S_4)_{0.5})_{0.5}(H_2O)_{2.5}$	13.84 (13.78)	2.40 (2.08)	1.01 (0.97)	6.93 (7.09)	6.5 -	52.8 -

[a] Found values in parentheses are based on the observed TGA weight loss at 150 ºC.

[b] Residual TGA masses at 650 ºC (LDHs) or 600 ºC (LHSs) in parentheses are compared with the weight percent of $Zn_4Al_2O_7$ (LDHs) or ZnO (LHSs) calculated for the proposed chemical composition.

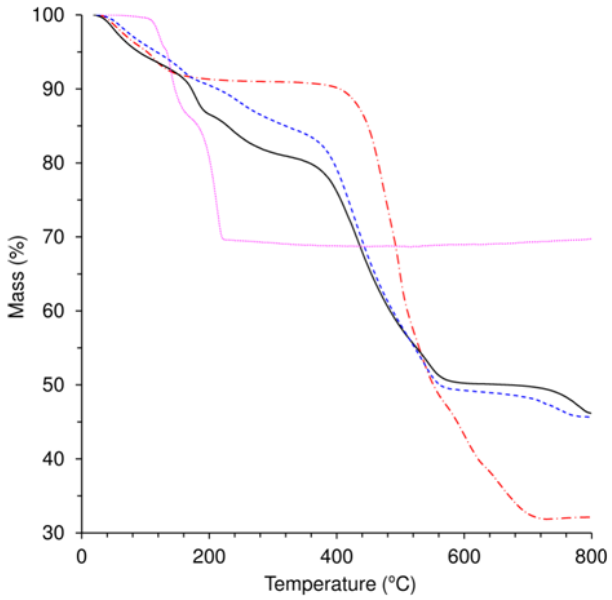

Figure 5.13 - TGA curves of Na_2IC (– · · – · ·), NO_3-LHS (·····), IC-LHS (———), and IC-LHS_{ht} (– – –).

5.3.7 Scanning Electron Microscopy

Figure 5.14 shows representative SEM images of NO_3-LHS. High magnification images of IC-LDH revealed a sheet-like morphology with regular stacking, in agreement with the lamellar character of the structure (Figure 5.15). Individual platelets have irregular forms and sizes, with no well-defined corners. This type of morphology is generally present for IC(90%)/TIS-LDH, IC(50%)/TIS-LDH and TIS-LDH, although the latter clearly presents a slightly different morphology consisting of finer, smaller-sized crystallites. The sample IC(50%)/TIS-LDH seems to present a morphology that is intermediate between that for IC-LDH and TIS-LDH, which is consistent with the formation of a single cointercalated phase. High magnification SEM images of IC-LHS showed a flake-like structure with irregular plates of various sizes (Figure 5.15). A similar morphology was found for IC(80%)/TIS-LHS. Somewhat in parallel with that observed for the LDH samples, the sample TIS-LHS comprises finer, smaller-sized crystallites, while IC(50%)/TIS-LHS seems to exhibit an intermediate morphology. SEM images for the thermally treated samples IC-LHS_{ht} and TIS-LHS_{ht} do not reveal a substantially different morphology from that observed for IC-LHS and TIS-LHS, respectively.

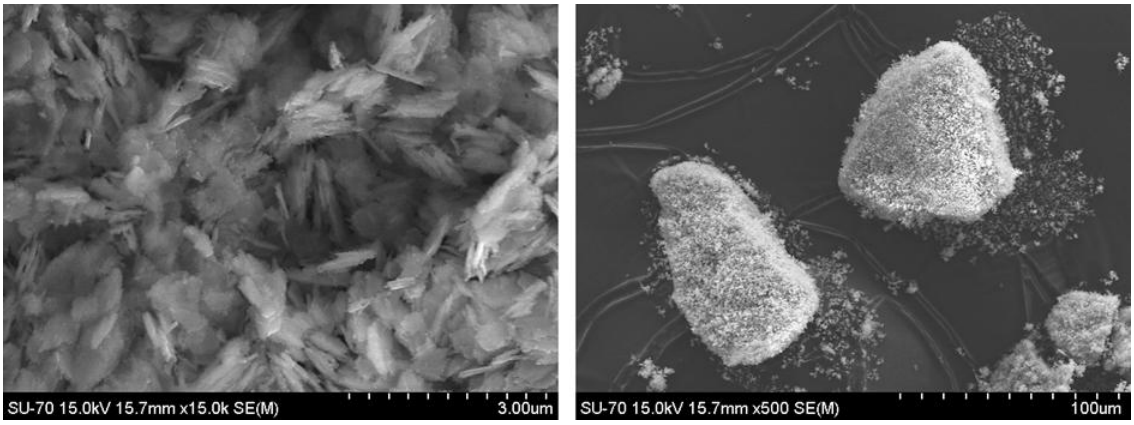

Figure 5.14 - Representative SEM images of NO_3-LHS.

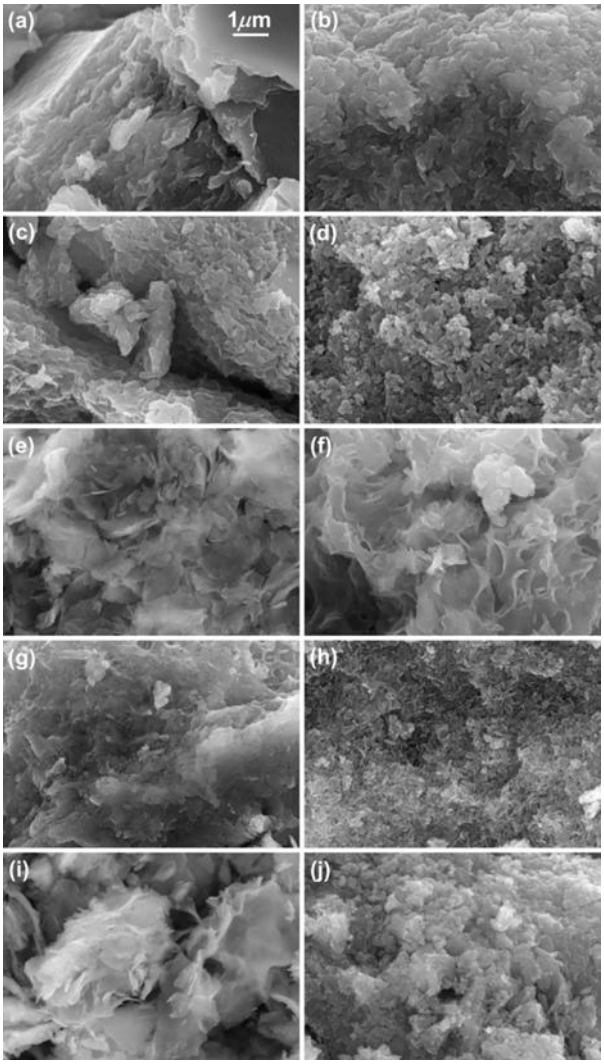

Figure 5.15 - Representative SEM images (15000× magnification) of (a) IC-LDH, (b) IC(90%)/TIS-LDH, (c) IC(50%)/TIS-LDH, (d) TIS-LDH, (e) IC-LHS, (f) IC(80%)/TIS-LHS, (g) IC(50%)/TIS-LHS, (h) TIS-LHS, (i) IC-LHS_{ht}, and (j) TIS-LHS_{ht}. The scale bar shown in (a) applies to all images.

5.4 Photophysical characterization

5.4.1 Steady-state measurements in the solid state

The absorption spectra of a mixture of IC and TIS with that of the individual IC and TIS intercalated in LDH and LHS as well thermally treated samples IC-LHS$_{ht}$ and TIS-LHS$_{ht}$ are shown in Figure 5.16.

The first observation in the NO_3-LDH and NO_3-LHS spectra is a complete absence of bands in the visible region with, however, a clear band in the UV region, at 300 nm for NO_3-LDH and 296 nm for NO_3-LHS, corresponding to the presence of NO_3^- ions in interlayer matrixes (see Figure 5.16).[23] A new band at 265 nm is formed and is present in intercalated and co-intercalated samples due to SO_3^- group of intercalated indigo derivatives.[24]

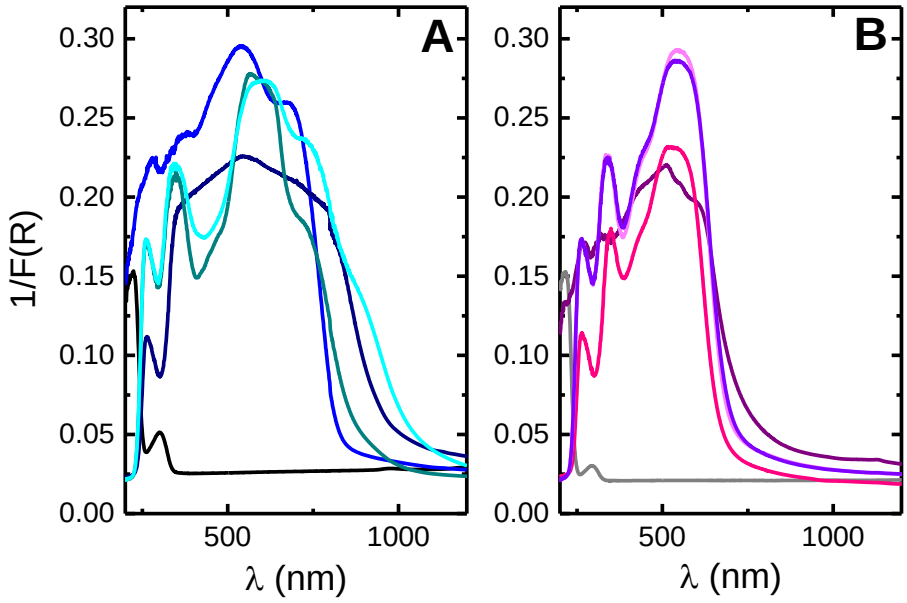

Figure 5.16 – Diffuse reflectance spectra (Kubelka-Munk scale) in the range of 200-1200 nm of (**A**) NO_3-LDH (black line), Na_2IC (blue line), IC-LDH (navy line), IC-LHS (dark cyan line) and IC-LHS$_{ht}$ (cyan line); (**B**) NO_3-LHS (grey line), H_2TIS (purple line), TIS-LDH (pink line), TIS-LHS (light magenta) and TIS-LHS$_{ht}$ (violet line).

Comparing the absorption spectra of Na_2IC and IC-LDH (Figure 5.16A), the wavelength absorption maxima of the two samples is identical (538 nm) but in the case of IC-LDH the spectrum becomes broader in comparison with dye itself. This suggests that in the LDH galleries the orientation of IC molecules favours J-type aggregates which are present together with the monomer units., which is in agreement with our previous study reported in literature.[9] For IC-LHS, the absorption spectrum seems to be better resolved than Na_2IC and even more than IC-LDH, with a wavelength maximum at

565 nm and a shoulder around 730 nm. Comparison of the spectra of H_2TIS (powder) with that of TIS-LDH (Figure 5.16B) shows that the first displays a wavelength maximum at 507 nm whereas in the hybrid the value is red-shifted (538 nm). However, the main difference lies in the fact that the bandwidth in TIS-LDH decreases relative to the observed with the spectra of the powder. This indicates that in the powder (H-type) aggregates are present whereas in TIS-LDH the dye is more close to the isolated (in comparison for example with the solution behavior) situation. This is also compatible with the observation of emission from TIS-LDH (Figure 5.17C), that is strongly quenched in the solid (powder) state; a characteristic of aggregates (and particularly of H-type) that are known to be poorly emissive. The TIS-LHS absorption spectrum is quite similar to that of TIS-LDH. The charge density calculations described above (in the synthesis and characterization section) seem to be supportive of this fact since they suggest that the IC/TIS molecules can be spaced quite far apart and still balance the host layer charge. It can be also emphasised the presence of intercalated water molecules between TIS molecules and the impossibility of intermolecular C=O···H-N interactions involving TIS.

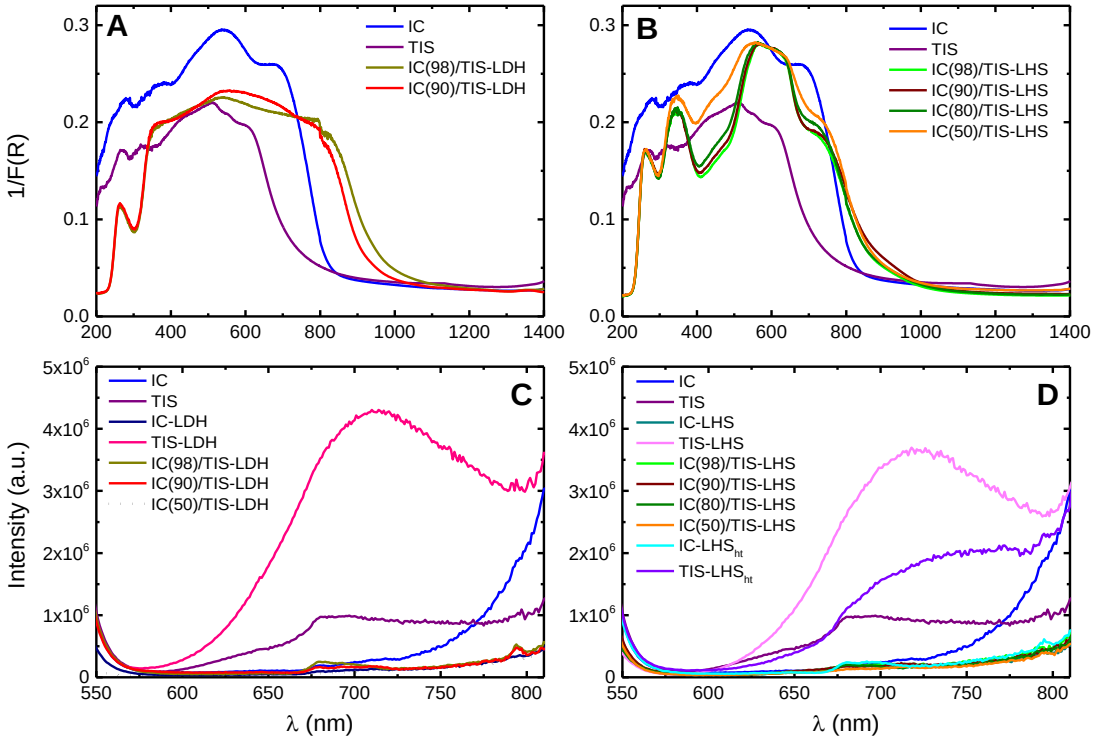

Figure 5.17 – (**A**, **B**) Diffuse reflectance spectra (Kubelka-Munk scale) and (**C**, **D**) fluorescence emission spectra of LDH and LHS samples in solid state with excitation wavelength at 530 nm.

For IC(*n*%)/TIS-LDHs materials (Figure 5.17A) some observations can be made: (i) a broader band close to the spectra of IC-LDH in the case of the lower amount of TIS (IC(*98*%)/TIS-LDH); (ii) for IC(*90*%)/TIS-LDH the spectra, although close in shape to IC(*98*%)/TIS-LDH, shows an additional

shoulder, visible between 540 and 750 nm. This may indicate that further increment of TIS in the mixture leads to either the formation of a new dimer (involving the interaction between TIS and IC) or the promotion of J-type aggregates of IC (since now the new band is red-shifted relative to that of IC-LDH). Good quality spectrum could not be obtained for IC(*50*%)/TIS-LDH. From Figure 5.17B), it can be seen that all mixtures of IC(*n*%)/TIS-LHSs materials showed similar spectra with an increase in vibronic resolution compared with cointercalated LDH systems and a red-shift of the wavelength maxima (560 nm) when compared to Na_2IC. The spectrum of IC(*50*%)/TIS-LHS (the sample with higher amount of TIS), shows a broad band at about 450 nm, more intense than the observed for the other samples, which is a direct consequence of the TIS dye content in the hybrid.

Fluorescence emission. Although it was not unable to obtain absolute fluorescence quantum yield values, the fluorescence spectra provide additional relevant information on the studied systems particularly in the case of TIS-LDH and TIS-LHS. Figure 5.17 (C, D) shows the emission spectra of the studied samples with excitation at 530 nm (TIS emission wavelength maxima). The most interesting feature, which is in line with the above observation of more individualized TIS monomer molecules in TIS-LDH is the fact that the emission is augmented by a factor of ~10 (although as said before no absolute quantum yields could be obtained, it can be observed an increment in the emission by ~ one order of magnitude on going from the solid (H_2TIS – purple line) to the TIS-LDH hybrid (pink line in Figure 5.17C)). In the case of all IC(*n*%)/TIS-LDHs samples the presence of IC strongly quenches the emission of TIS, mirroring an efficient energy transfer process similar to what was observed by Zheng and co-authors[8] with the co-intercalation of 4,4-diaminostilbene-2,2-disulfonate and 4,4-dinitro-stilbene-2,2-disulfonate in LDH hybrids.

Figure 5.17D shows the emission spectra of all LHS samples with excitation at the same wavelength referred above (530 nm). An increase of the fluorescence intensity of TIS when incorporated into the LHS *vs*. in the solid/powder is observed. This constitutes, once more and as seen with IC, an indication that the dye becomes more isolated when intercalated into the LHS cavity. The simultaneous presence of IC and TIS co-intercalated in the LHS, leads to an efficient energy transfer (from TIS to IC) which is mirrored by the strong decrease in the (or even absence) fluorescence, as was also observed for the IC(*n*%)/TIS-LDHs samples.

Investigation of the dehydration effect of LHS samples on photophysical properties. Figure 5.16 shows the absorption (A, B) spectra of hydrated and non-hydrated samples. From this figure, two observations can be made: (i) in the case of TIS-LHS_{ht} (violet line in Figure 5.16), there is no change in the absorption spectra and (ii) the opposite was observed for IC-LHS; the absorption spectrum of IC-LHS_{ht} material (cyan line) is different from the hydrated one (IC-LHS) with the appearance of a new band to longer wavelengths which suggests an increase in the level of aggregation, i.e., less water in the system leads to an increase in aggregation. In other words, for IC-LHS (hydrated state), the molecules are more isolated, with H-bonding (C=O···H-N) interactions being mainly intramolecular

(water prevents intermolecular interactions). After heat treatment (IC-LHS_{ht} sample), the loss of water promotes further aggregation via intermolecular C=O···H-N interactions; this cannot occur with TIS due to lack of NH group, and so the molecules remain "isolated" even after thermal treatment. This batochromic shift observed here was also seen by others with IC-LHS[10] and for methyl orange in a LDH.[25]

With the emission spectra of TIS-LHS samples, both materials were excited at 610 nm (spectra not shown) with same absorbance and a quenching in the fluorescence is observed when the hybrid is dehydrated. In IC-LHS samples, no apparent change is observed in the fluorescence spectra (and intensity).

5.4.2 Time-Resolved measurements

LDH- and TIS-LHS hybrids. Figure 5.18 shows the fluorescence decay of TIS-LDH best fitted with a double exponential decay law. This bi-exponential decay mirrors, as previously mentioned, the simultaneous presence of monomer and dimer structures. Indeed, the shorter decay time (81 ps) is close to the value obtained in water for TIS (130 ps). This is the major species in the ground-state (with excitation at 451 nm and therefore direct excitation of TIS) and with a pre-exponential factor of 0.74. The second (and dominant emissive species with ~ 60% of the emission at 700 nm) is associated to the emission of the dimer within the galleries of the TIS-LDH hybrid. The fluorescence decay of TIS-LHS shows a similar decay law, also fitted with a double exponential. The shorter component has again a value (95 ps) comparable to that found in solution. The lifetime value of the second component is basically equal to that found in TIS-LDH. The relative amount of the dimer and monomer species (as seen by the pre-exponential factors) is similar to that found for the TIS-LDH system. These results seem to be fully consistent with estimates of the TIS densities (molecule/A^2) for TIS-LDH and TIS-LHS mentioned above.

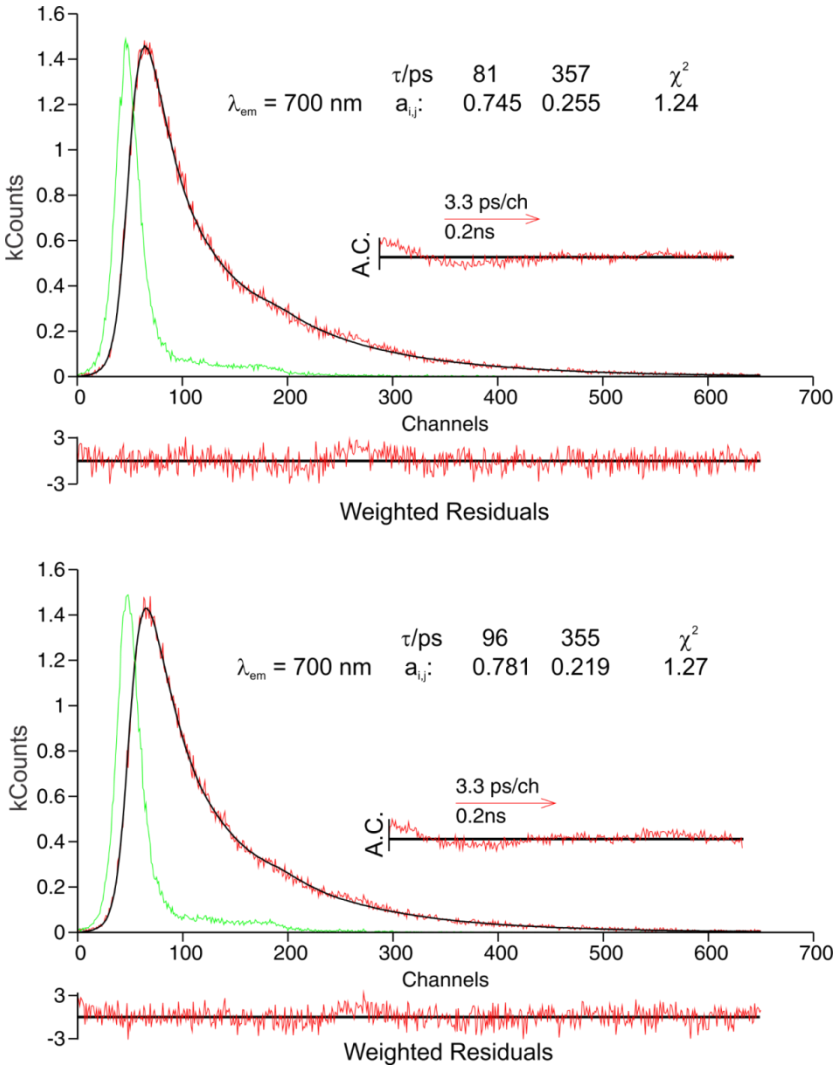

Figure 5.18 – Fluorescence decays collected at 700 nm for TIS-LDH (*top panel*) and TIS-LHS (*bottom panel*) in the solid state at room temperature (λ_{exc} = 451 nm). For a better judgment of the quality of the fits, autocorrelation (A. C.) functions, weighted residuals, and χ^2 values are provided as insets.

5.5 Conclusions

In summary, cointercalation of thioindigo disulfonate (TIS) and indigo carmine (IC) in Zn,Al-LDHs and Zn,Al-LHSs were achieved successfully through a coprecipitation synthesis. From the photophysical characterization of the intercalates it was observed an efficient process of energy transfer from TIS to IC molecule. In the hydrated state, IC molecules showed to be more isolated in LHSs than TIS species which indicate that water prevents intermolecular interactions. The same doesn't happen for TIS due to the lack of NH group in the molecule skeleton.

5.6 References

1. Costa, A. L.; Gomes, A. C.; Pillinger, M.; Gonçalves, I. S.; Seixas de Melo, J. S., Controlling the Fluorescence Behavior of 1-Pyrenesulfonate by Cointercalation with a Surfactant in a Layered Double Hydroxide. *Langmuir* **2015,** *31* (16), 4769.
2. Zheng, S.; Lu, J.; Li, W.; Qin, Y.; Yan, D.; Evans, D. G.; Duan, X., The 2-phenylbenzimidazole-5-sulfonate/layered double hydroxide co-intercalation composite and its luminescence response to nucleotides. *Journal of Materials Chemistry C* **2014,** *2* (26), 5161.
3. Sun, Z.; Jin, L.; Shi, W.; Wei, M.; Evans, D. G.; Duan, X., Controllable Photoluminescence Properties of an Anion-Dye-Intercalated Layered Double Hydroxide by Adjusting the Confined Environment. *Langmuir* **2011,** *27* (11), 7113.
4. Shi, W.; Wei, M.; Evans, D. G.; Duan, X., Tunable photoluminescence properties of fluorescein in a layered double hydroxide matrix and its application in sensors. *Journal of Materials Chemistry* **2010,** *20* (19), 3901.
5. Shi, W.; Sun, Z.; Wei, M.; Evans, D. G.; Duan, X., Tunable Photoluminescence Properties of Fluorescein in a Layered Double Hydroxide Matrix by Changing the Interlayer Microenvironment. *The Journal of Physical Chemistry C* **2010,** *114* (49), 21070.
6. Chen, T.; Tang, P.; Feng, Y.; Li, D., Facile Color Tuning, Characterization, and Application of Acid Green 25 and Acid Yellow 25 Co-intercalated Layered Double Hydroxides. *Industrial & Engineering Chemistry Research* **2017,** *56* (19), 5495.
7. Tang, P.; Feng, Y.; Li, D., Facile synthesis of multicolor organic–inorganic hybrid pigments based on layered double hydroxides. *Dyes and Pigments* **2014,** *104*, 131.
8. Zheng, S.; Lu, J.; Yan, D.; Qin, Y.; Li, H.; Evans, D. G.; Duan, X., An Inexpensive Co-Intercalated Layered Double Hydroxide Composite with Electron Donor-Acceptor Character for Photoelectrochemical Water Splitting. **2015,** *5*, 12170.
9. Costa, A. L.; Gomes, A. C.; Pillinger, M.; Gonçalves, I. S.; de Melo, J. S. S., An Indigo Carmine-Based Hybrid Nanocomposite with Supramolecular Control of Dye Aggregation and Photobehavior. *Chemistry – A European Journal* **2015,** *21* (34), 12069.
10. Maruyama, S. A.; Tavares, S. R.; Leitão, A. A.; Wypych, F., Intercalation of indigo carmine anions into zinc hydroxide salt: A novel alternative blue pigment. *Dyes and Pigments* **2016,** *128*, 158.
11. Newman, S. P.; Jones, W., Comparative study of some layered hydroxide salts containing exchangeable interlayer anions. *J Solid State Chem* **1999,** *148*.
12. Jung, W. C.; Huh, Y. D., Synthesis of intercalation compounds between a layered double hydroxide and an anionic dye. *Bulletin of the Korean Chemical Society* **1996,** *17* (6), 547.
13. Park, I. Y.; Kuroda, K.; Kato, C., Direct synthesis of intercalation compounds between a layered double hydroxide and an anionic dye. *Journal of the Chemical Society, Dalton Transactions* **1990,** (10), 3071.
14. Stahlin, W.; Oswald, H. R., The crystal structure of zinc hydroxide nitrate, Zn5(OH)8(NO3)2.2H2O. *Acta Crystallographica Section B* **1970,** *26* (6), 860.

15. Yao, M.; Kuratani, K.; Kojima, T.; Takeichi, N.; Senoh, H.; Kiyobayashi, T., Indigo carmine: An organic crystal as a positive-electrode material for rechargeable sodium batteries. *Sci. Rep.* **2014,** *4*.

16. Kettner, F.; Hüter, L.; Schäfer, J.; Röder, K.; Purgahn, U.; Krautscheid, H., Selective crystallization of indigo B by a modified sublimation method and its redetermined structure. *Acta Crystallographica Section E: Structure Reports Online* **2011,** *67* (Pt 11), o2867.

17. Süsse, P.; Steins, M.; Kupcik, V., Indigo: Crystal structure refinement based on synchrotron data. In *Zeitschrift für Kristallographie*, **1988**; Vol. 184, p 269.

18. Bruning, J.; Heintz, D.; Meents, A.; Bolte, M.; Schmidt, M. U., Monothioindigo, determined by microcrystal structure analysis. *Acta Crystallographica Section C* **2010,** *66* (9), o459.

19. Haase-Wessel, W.; Ohmasa, M.; Süsse, P., Thioindigo: Crystal structural data for modification II. *Naturwissenschaften* **1977,** *64* (8), 435.

20. Shadi, I. T.; Chowdhry, B. Z.; Snowden, M. J.; Withnall, R., Analysis of the conversion of indigo into indigo carmine dye using SERRS. *Chemical Communications* **2004,** (12), 1436.

21. Bauer, J.; Behrens, P.; Speckbacher, M.; Langhals, H., Composites of perylene chromophores and layered double hydroxides: Direct synthesis, characterization; and photo- and chemical stability. *Advanced Functional Materials* **2003,** *13* (3), 241.

22. Demel, J.; Hynek, J.; Kovář, P.; Dai, Y.; Taviot-Guého, C.; Demel, O.; Pospíšil, M.; Lang, K., Insight into the Structure of Layered Zinc Hydroxide Salts Intercalated with Dodecyl Sulfate Anions. *The Journal of Physical Chemistry C* **2014,** *118* (46), 27131.

23. Ahmed, A. A. A.; Talib, Z. A.; Hussein, M. Z.; Zakaria, A., Zn–Al layered double hydroxide prepared at different molar ratios: Preparation, characterization, optical and dielectric properties. *J Solid State Chem* **2012,** *191*.

24. Babakhani, S.; Talib, Z. A.; Hussein, M. Z.; Ahmed, A. A. A., Optical and Thermal Properties of Zn/Al-Layered Double Hydroxide Nanocomposite Intercalated with Sodium Dodecyl Sulfate. *Journal of Spectroscopy* **2014,** *2014*, 10.

25. Costantino, U.; Coletti, N.; Nocchetti, M.; Aloisi, G. G.; Elisei, F., Anion Exchange of Methyl Orange into Zn−Al Synthetic Hydrotalcite and Photophysical Characterization of the Intercalates Obtained. *Langmuir* **1999,** *15* (13), 4454.

6. Final Remarks and Future Perspectives

The work developed in this thesis led to the creation of new organic/inorganic hybrid materials with interesting structural and photophysical properties.

New insights into the photophysical properties of Congo Red in solution were provided and have successfully demonstrated that the anionic dye can be incorporated into a layered double hydroxide by the direct coprecipitation method. From the photophysical studies it was shown that the solution behavior of CR is consistent with the formation of an excited species that decays with ~ 7 ps mainly through the radiationless internal conversion channel. With the CR-LDH hybrid slipped cofacial J-type aggregate of the dye is assembled within the interlayer region, giving rise to a large basal spacing of 26.2 Å. This arrangement is different from the rod-like or ribbon-like supramolecular dye structures proposed in the literature for CR in aqueous solutions, which are built up from the face-to-face stacking (with zero or very small offset) of CR molecules. In the present case, we found a different binding force, namely the host-guest electrostatic interaction which is operative in addition to the water-dye and dye-dye interactions.

The extraordinary durability of Maya Blue has motivated researchers to reproduce this technology on MB-related materials. In this thesis, an indigo carmine/layered double hydroxide composite material was also prepared by a coprecipitation route, aiming to mimetic a MB hybrid with new constituents. The basal spacing of 17.6 Å for the resultant hydrotalcite-type phase is about 5 Å shorter than what previously reported for other IC/LDH composites. This can be attributed to the formation of a distinct phase in which the intercalated IC molecules adopt a strongly tilted J-type arrangement within the gallery regions. The synthetic method used for IC-LDH was successfully used for the cointercalation of IC and 1-hexanesulfonate anions, leading to well-ordered materials in which the HS/IC molar ratio ranges from *ca.* 25 to 165. Higher surfactant content leads to a photophysical behavior that increasingly mirrors that observed in concentrated IC solutions. It was shown that the level of IC-HS interaction in the composite materials can be followed by monitoring changes in overtone bands found in the near-IR region of the absorption spectra.

The cointercalation of 1-pyrenesulfonate and the surfactant 1-heptanesulfonate in Zn-Al LDHs has been achieved through the same coprecipitation method. Upon increasing the relative amount of HS in the LDH, the monomer becomes more isolated as can be seen in the fluorescence emission spectra with the presence of a vibrational band at 375 nm. The fluorescence lifetimes reveal the presence of two types of monomers (subject to different microenvironments) at 375 nm, and at 480 and 520 nm, the three lifetimes are attributed to an excimer and dimers (or higher order aggregates) in different microenvironments. The decays collected at 375 nm are bi-exponentials with a major component of 105 ns for the highest HS/PS ratio, which further loses importance with an increase in the PS content. When the decays are collected at 480 and 520 nm, the fits are tri-exponentials with a major component varying from 108 to 124 ns, attributed to an excimer.

Thioindigo is an indigo derivative with significant differences in the electronic spectral and photophysical properties, namely displaying high fluorescence quantum yields and longer fluorescence lifetimes. Incorporation of thioindigo disulfonate (TIS) and indigo carmine (IC) in Zn,Al-LDHs and Zn,Al-LHSs and the simultaneous loading of the two dyes intercalated in different

proportions were achieved successfully through the same coprecipitation method. The PXRD showed that IC molecules adopt a near-vertical orientation with an angle of 65-80º with respect to the host layers while the TIS molecules are in a slipped face-to-face π-π stacking arrangement. The photophysical properties of intercalates can be tuned by changing the IC/TIS loadings, showing that are an efficient process of energy transfer from IC to TIS molecule decreasing a lot the fluorescence emission of TIS.

In this thesis, the synthesis of LDH and LHS hosts with different type of guests (CR, IC, PS and TIS) was investigated. In particular, the possibility to tune not only color but mainly the photophysical properties of the hybrid materials by changing the dye content amount constitutes an advantage for specific applications of these composites. From a photochemistry point of view, the shielding effect provided by the host is of an extreme importance to photochemistry applications. Beside the photochemistry field, these kind of hosts have also promising and interesting properties when applied in the biological area as drug delivery and medicine. Due to the infinite capacity to undergo exchange reactions with a huge diversity of guests possessing different characteristics and the easy way of preparation make of these systems even more interesting. Moreover, the possibility to create multifunctional materials with enhanced properties when compared with the individual components bring some highlights to the host-guest chemistry world.

The next directions of this work will involve the encapsulation of these types of guests into to curcubiturils (CBs). These organic hosts, similar to cyclodextrins, are water-soluble macrocyclic compounds composed of glyceryl units and depending on the number of these units, they can have smaller or bigger cavity size which makes them an interesting hosts because they can accommodate different type of molecules.

7. Experimental Section

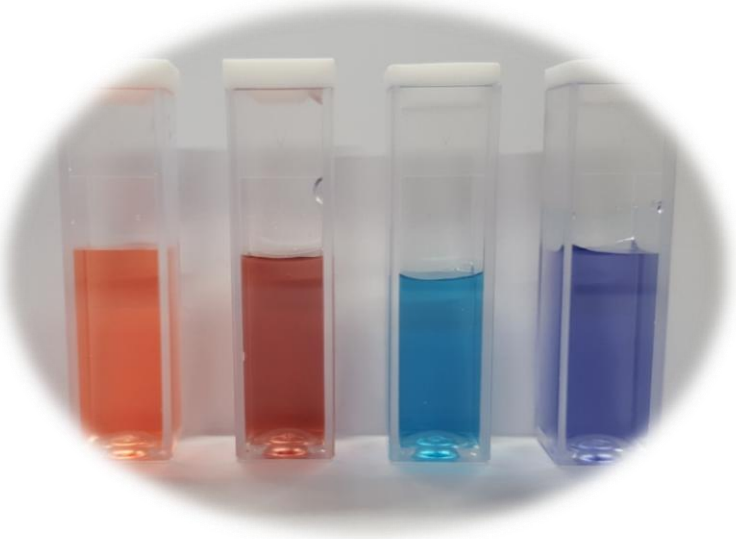

7.1. Materials

Congo Red (CR) [sodium salt of 3,3'-([1,1'-biphenyl]-4,4'-diyl)bis(4-aminonaphthalene-1-sulfonic acid)] was obtained from BDH Chemicals and recrystallized from water-ethanol (1:1) before use as described below (Section 7.2.1) by Ana L. Costa at University of Aveiro. Indigo carmine (Na_2IC, Sigma-Aldrich), sodium 1-hexanesulfonate monohydrate (NaHS, 98%, Sigma-Aldrich), 1-heptanesulfonic acid sodium salt (NaHpS, 98%, Sigma-Aldrich), 1-pyrenesulfonic acid sodium salt (NaPS, Fluka), thioindigo (TCI chemicals), chrolosulfonic acid (99%, Sigma-Aldrich), sodium bicarbonate (99.5%, JMGS), $Zn(NO_3)_2{\cdot}6H_2O$ (98%, Fluka), $Al(NO_3)_3{\cdot}9H_2O$ (98.5%, Riedel-de-Haën), 1 M NaOH (Fluka) and acetone (99.5%, Sigma-Aldrich) were obtained from commercial sources and were used as received. Thioindigo disulfonic acid [(*E*)-3,3'-dioxo-3*H*,3'*H*-[2,2'-bibenzo[*b*]thiophenylidene]-5,5'-disulfonic acid (H_2TIS)] and respective precursor (thioindigo disulfonyl dichloride) were synthesized by Ricardo C. Pereira at University of Coimbra (described in Section 7.2.10 and 7.2.11). All LDH preparations were performed under nitrogen using deionized and decarbonated (DD) water. The water was Milli-Q grade.

Dimethylsulfoxide (DMSO, for CR solutions), dimethylformamide (DMF, for IC solutions), ethanol and methanol (for PS solutions) for photophysical characterization, dichloromethane (for thioindigo disulfonyl dichloride synthesis)and acetone (for washing LDH and LHS materials) were of spectroscopic or equivalent grade and were used as received.

7.2 Synthesis and spectroscopic data of materials

7.2.1 Recristallization of Congo Red

7.2.2 NO_3-LDH

For reference, a nitrate-form Zn-Al LDH was prepared by using the standard method of coprecipitation of the Zn^{2+} and Al^{3+} hydroxides (initial Zn^{2+}/Al^{3+} molar ratio in solution = 2) in the presence of nitrate ions at constant pH (7.5–8) under nitrogen, followed by aging of the gel at 80 °C for 20 h.[1] Anal. Calcd for $[Zn_4Al_2(OH)_{12}][(NO_3)_2(H_2O)_{2.5}]$ (688.7): H, 2.49; N, 4.07. Found: H, 2.26; N, 4.12%. TGA showed a mass loss of 7.0% up to 150 ºC (calcd, for loss of $2.5H_2O$: 6.5%), and a residual mass of 64.6% at 700 ºC (calcd, for $Zn_4Al_2O_7$: 62.1%). FT-IR (KBr, cm^{-1}): ν = 3448 (br), 2925 (w), 1624 (br), 1385 (vs), 1018 (w), 825 (w), 613 (m), 555 (sh), 426 (vs), 314 (m). Raman (cm^{-1}): ν = 3420, 1389, 1055, 716, 550, 489, 114.

7.2.3 CR-LDH

A solution of $Zn(NO_3)_2{\cdot}6H_2O$ (1.49 g, 5 mmol) and $Al(NO_3)_3{\cdot}9H_2O$ (0.94 g, 2.5 mmol) in DD water (30 mL) was added dropwise to a solution of CR (1.74 g, 2.5 mmol) in DD water (150 mL) with efficient mixing. The pH of the reaction mixture was maintained at 7.5-8 by simultaneous addition of 0.5 M NaOH. Once addition of the Zn^{2+}/Al^{3+} solution was complete, the resultant red gel-like slurry (pH 7.5-8) was stirred for 18 h at 65 °C. The dark red solid was isolated by filtration, washed several times with DD water and acetone (4 × 50 mL), and finally dried at room temperature under reduced pressure in a vacuum desiccator. Anal. Calcd for $[Zn_4Al_2(OH)_{12}][(C_{32}H_{22}N_6O_6S_2)_{0.86}(CO_3)_{0.14}(H_2O)_7]$ (1213.7): C, 27.37; H, 3.73; N, 5.95; S, 4.54. Found: C, 27.54; H, 3.61; N, 5.86; S, 4.40%. TGA showed a mass loss of 10.2% up to 200 ºC (calcd, for loss $7H_2O$: 10.4%), and a residual mass of 35.8% at 800 ºC (calcd, for $Zn_4Al_2O_7$: 35.2%). FT-IR (KBr, cm^{-1}): ν = 3426 (br), 2964 (w), 2923 (w), 2854 (w), 1612 (s), 1508 (w), 1448 (w), 1431 (w), 1375 (m), 1261 (m), 1225 (w), 1174 [s, $\nu_{as}(SO_3^-)$], 1105 (m), 1043 [s, $\nu_s(SO_3^-)$], 947 (w), 914 (w), 858 (w), 802 (s), 831 (m), 756 (m), 721 (w), 696 (m), 669 (m), 624 (m), 596 (m), 536 (w), 462 (w), 424 (m). Raman (cm^{-1}): ν = 3394 (br), 1590 (vs), 1451 (m), 1433 (m), 1373 (vs), 1325 (m), 1281 (m), 1248 (w), 1211, 1151 (vs), 1040 (w), 942 (w), 408 (w), 359 (w). $^{13}C\{^1H\}$ CP MAS NMR: δ = 149.9 (C^1), 138.8 (C^{10}), 137.0 (C^4), 126.5 ($C^{14,13,8,7,5,3}$), 124.3 ($C^{12,11,9,2}$), 115.0 (C^6) (see Scheme 7.1 for the atom numbering scheme).

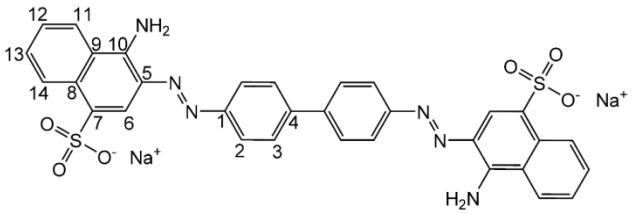

Scheme 7.1 - Atom numbering scheme for NMR assignments of CR.

7.2.4 IC-LDH (a)

A solution of $Zn(NO_3)_2{\cdot}6H_2O$ (2.98 g, 10 mmol) and $Al(NO_3)_3{\cdot}9H_2O$ (1.88 g, 5 mmol) in DD water (60 mL) was added dropwise to a solution of Na_2IC (2.33 g, 5 mmol) in DD water (250 mL) with efficient mixing. The pH of the reaction mixture was maintained at 7.5-8 by simultaneous addition of 0.5 M NaOH. Once addition of the Zn^{2+}/Al^{3+} solution was complete, the resultant blue gel-like slurry (pH 7.5-8) was stirred for 18 h at 65 °C. The dark blue solid was isolated by filtration, washed several times with DD water and acetone (3 × 50 mL), and finally dried at room temperature under reduced pressure in a vacuum desiccator. Anal. Calcd for $[Zn_4Al_2(OH)_{12}][(C_{16}H_8N_2O_8S_2)_{0.9}(CO_3)_{0.1}(H_2O)_6]$ (1012.0): C, 17.21; H, 3.11; N, 2.49; S, 5.70; Zn, 25.84; Al, 5.33. Found: C, 17.02; H, 3.09; N, 2.53; S,

5.68; Zn, 25.7; Al, 5.2. TGA showed a mass loss of 10.8% up to 180 ºC (calcd, for loss of $6H_2O$: 10.7%), and a residual mass of 42.4% at 800 ºC (calcd, for $Zn_4Al_2O_7$: 42.2%). FT-IR (KBr, cm^{-1}): $\tilde{\nu}$ = 3445 (br), 1653/1643 (s), 1615 (vs), 1474 (s), 1402 (m), 1325 (m), 1263 (w), 1198 (s, bd), 1163 (s), 1105 (vs), 1085 (sh), 1066 (w), 1028 (vs), 825 (m), 783 (w), 733 (m), 681 (m), 590 (s), 424 (m), 388 (w), 359 (w). $^{13}C\{^1H\}$ CP MAS NMR: δ = 187.9 (C^2), 154.5 (C^4), 151.5 (C^4), 134.8 ($C^{6,7}$), 120.9 (C^1), 117.1 (C^8), 114.2 (C^3), 107.8 (C^5).

7.2.5 HS-LDH (f)

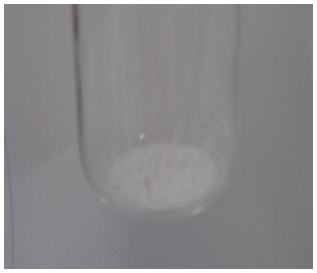

A solution of $Zn(NO_3)_2{\cdot}6H_2O$ (2.98 g, 10 mmol) and $Al(NO_3)_3{\cdot}9H_2O$ (1.88 g, 5 mmol) in DD water (60 mL) was added dropwise to a solution of NaHS (2.06 g, 10 mmol) in DD water (100 mL) with efficient mixing. The pH of the reaction mixture was maintained at 7.5-8 by simultaneous addition of 0.5 M NaOH. Once addition was complete, the resultant gel-like slurry (pH 7.5-8) was stirred for 18 h at 65 °C. The colorless solid was isolated by filtration, washed several times with DD water and acetone (3 × 50 mL), and finally dried at room temperature under reduced pressure. Anal. Calcd for $[Zn_4Al_2(OH)_{12}][(C_6H_{13}O_3S)_{1.57}(CO_3)_{0.215}(H_2O)_5]$ (882.0): C, 13.12; H, 4.85; S, 5.71; Zn, 29.66; Al, 6.12. Found: C, 13.1; H, 4.81; S, 5.70; Zn, 30.3; Al, 6.3. TGA showed a mass loss of 10.5% up to 165 ºC (calcd, for loss of $5H_2O$: 10.2%), and a residual mass of 50.0% at 800 ºC (calcd, for $Zn_4Al_2O_7$: 48.5%). FT-IR (KBr, cm^{-1}): $\tilde{\nu}$ = 3473 (br), 2958 (m) [$\nu_{as}(CH_3)$], 2933 (m) [$\nu_{as}(CH_2)$], 2873 (w) [$\nu_s(CH_3)$], 2856 (m) [$\nu_s(CH_2)$], 1635 (br), 1468 (m) [$\delta(CH_2)$], 1415 (w), 1380 (w), 1365 (w), 1181 (vs) [$\nu_{as}(SO_3^-)$], 1049 (vs) [$\nu_s(SO_3^-)$], 796 (m), 725 (w), 615 (s), 555 (m), 426 (vs), 320 (m). $^{13}C\{^1H\}$ CP MAS NMR: δ = 14.1 (C^6), 23.2 (C^5), 24.6 (C^2), 29.6 (C^3), 32.2 (C^4), 51.8 (C^1).

7.2.6 Synthesis of IC(*x*%)/HS-LDH composites

A solution of $Zn(NO_3)_2{\cdot}6H_2O$ (2.98 g, 10 mmol) and $Al(NO_3)_3{\cdot}9H_2O$ (1.88 g, 5 mmol) in DD water (60 mL) was added dropwise to a solution of NaHS (*a* mmol) and Na_2IC (*b* mmol; $a + 2b = 10$ mmol; b = 0.245, 0.115, 0.053 or 0.025 mmol) in DD water (80 mL) with efficient mixing. The pH of the reaction mixture was maintained at 7.5-8 by simultaneous addition of 0.5 M NaOH. Once addition of the Zn^{2+}/Al^{3+} solution was complete, the resultant gel-like slurry (pH 7.5-8) was stirred for 18 h at 65 °C. The solid was isolated by filtration, washed several times with DD water and acetone (3 × 50 mL), and finally dried at room temperature under reduced pressure. The samples are denoted IC(*x*%)/HS-LDH, where *x* is the final mol% content of IC calculated (*vs*. the total content of IC + HS) for the compositions given below.

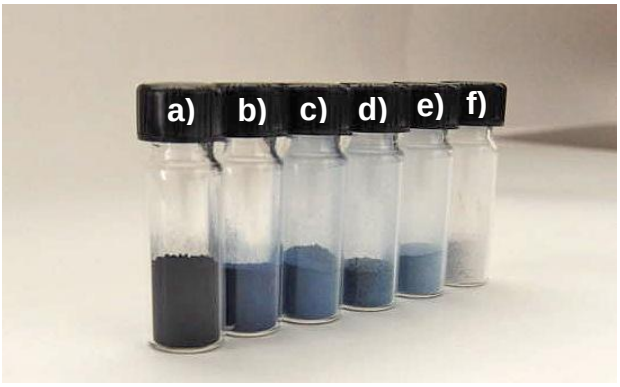

Figure 7.1 – Picture of the obtained LDH materials: a) IC-LDH, b) IC(3.9%)/HS-LDH, c) IC(2.2%)/HS-LDH, d) IC(1.1%)/HS-LDH, e) IC(0.6%)/HS-LDH and f) HS-LDH.

IC(3.9%)/HS-LDH (b): Anal. Calcd for $[Zn_4Al_2(OH)_{12}][(C_6H_{13}O_3S)_{1.48}(C_{16}H_8N_2O_8S_2)_{0.06}(CO_3)_{0.2}(H_2O)_{4.5}]$ (882.4): C, 13.67; H, 4.65; N, 0.19; S, 5.81; Zn, 29.64; Al, 6.12. Found: C, 13.43; H, 4.71; N, 0.20; S, 5.82; Zn, 29.4; Al, 6.3. FT-IR (KBr, cm^{-1}): $\tilde{\nu}$ = 3473 (br), 2958 (m), 2933 (m), 2873 (w), 2856 (m), 1641 (w), 1617 (w), 1468 (m), 1415 (w), 1403 (sh), 1381 (w), 1180 (vs), 1107 (w), 1049 (vs), 796 (m), 725 (sh), 617 (s), 555 (m), 426 (vs), 320 (m). $^{13}C\{^1H\}$ CP MAS NMR: δ = 14.1 (HS-C^6), 23.2 (HS-C^5), 24.9 (HS-C^2), 29.4 (HS-C^3), 31.9 (HS-C^4), 51.7 (HS-C^1). TGA showed a mass loss of 9.5% up to 165 ºC (calcd, for loss of $4.5H_2O$: 9.2%), and a residual mass of 51.2% at 800 ºC (calcd, for $Zn_4Al_2O_7$: 48.4%).

IC(2.2%)/HS-LDH (c): Anal. Calcd for $[Zn_4Al_2(OH)_{12}][(C_6H_{13}O_3S)_{1.54}(C_{16}H_8N_2O_8S_2)_{0.035}(CO_3)_{0.195}(H_2O)_5]$ (890.6): C, 13.48; H, 4.79; N, 0.11; S, 5.80. Found: C, 13.52; H, 4.72; N, 0.11; S, 5.79%. TGA showed a mass loss of 10.3% up to 165 ºC (calcd, for loss of $5H_2O$: 10.1%), and a residual mass of 51.0% at 800 ºC (calcd, for $Zn_4Al_2O_7$: 48.0%).

IC(1.1%)/HS-LDH (d): Anal. Calcd for $[Zn_4Al_2(OH)_{12}][(C_6H_{13}O_3S)_{1.56}(C_{16}H_8N_2O_8S_2)_{0.017}(CO_3)_{0.203}(H_2O)_5]$ (886.8): C, 13.32; H, 4.82; N, 0.05; S, 5.76. Found: C, 13.40; H, 4.80; N, 0.05; S, 5.72. TGA showed a mass loss of 11.7% up to 165 ºC (calcd, for loss of $5H_2O$: 10.2%), and a residual mass of 48.9% at 800 ºC (calcd, for $Zn_4Al_2O_7$: 48.2%).

IC(0.6%)/HS-LDH (e): Anal. Calcd for $[Zn_4Al_2(OH)_{12}][(C_6H_{13}O_3S)_{1.56}(C_{16}H_8N_2O_8S_2)_{0.01}(CO_3)_{0.21}(H_2O)_5]$ (884.2): C, 13.22; H, 4.83; N, 0.03; S, 5.73. Found: C, 13.23; H, 4.77; N, 0.04; S, 5.69. TGA showed a mass loss of 11.2% up to 165 ºC (calcd, for loss of $5H_2O$: 10.2%), and a residual mass of 49.1% at 800 ºC (calcd, for $Zn_4Al_2O_7$: 48.3%).

7.2.7 PS-LDH (1)

A solution of $Zn(NO_3)_2{\cdot}6H_2O$ (1.49 g, 5 mmol) and $Al(NO_3)_3{\cdot}9H_2O$ (0.94 g, 2.5 mmol) in DD water (30 mL) was added dropwise to a solution of NaPS (1.52 g, 5 mmol) in DD water (100 mL) with efficient mixing. The pH of the reaction mixture was maintained at 7.5-8 by simultaneous addition of 0.5 M NaOH. Once addition of the Zn^{2+}/Al^{3+} solution was complete, the resultant yellow gel-like slurry (pH 7.5-8) was stirred for 18 h at 65 °C. The pale yellow solid was isolated by filtration, washed several times with DD water and acetone (4 × 50 mL), and finally dried at room temperature under reduced pressure in a vacuum desiccator. Anal. Calcd for $Zn_4Al_2(OH)_{12}(C_{16}H_9O_3S)_{1.7}(CO_3)_{0.15}{\cdot}6H_2O$ (1114.9): C, 29.46; H, 3.55; S, 4.89; Zn 23.46; Al, 4.84. Found: C, 29.26; H, 3.58; S, 5.06; Zn, 23.4; Al, 5.0. TGA showed a mass loss of 10.5% up to 175 ºC (calcd, for loss of $6H_2O$: 9.7%), and a residual mass of 36.1% at 800 ºC (calcd, for $Zn_4Al_2O_7$: 38.3%). FT-IR (KBr, cm^{-1}): ν = 3462 (br), 3046 (w) [ν(C-H)], 1626 (m), 1591 (m), 1543 (w), 1487 (w), 1456 (w), 1417 (w), 1385 (m), 1205 (sh), 1176 (m) [$\nu_{as}(SO_3^-)$], 1159 (s), 1088 (m), 1055 (s) [$\nu_s(SO_3^-)$], 1012 (s), 970 (w), 849 (s), 825 (w), 758 (m), 715 (w), 681 (m), 613 (m), 563 (m), 426 (m), 405 (w), 351 (w), 326 (w). Raman (cm^{-1}): ν = 3049, 1621, 1585, 1405, 1379, 1238, 1219, 1152, 1086, 1011, 609, 560, 519, 419. $^{13}C\{^1H\}$ CP MAS NMR: δ = 122.5, 123.9, 125.3, 127.8, 131.6.

7.2.8 HpS-LDH (6)

A solution of $Zn(NO_3)_2{\cdot}6H_2O$ (2.98 g, 10 mmol) and $Al(NO_3)_3{\cdot}9H_2O$ (1.88 g, 5 mmol) in DD water (60 mL) was added dropwise to a solution of NaHS (2.02 g, 10 mmol) in DD water (80 mL) with efficient mixing. The pH of the reaction mixture was maintained at 7.5-8 by simultaneous addition of 0.5 M NaOH. Once addition of the Zn^{2+}/Al^{3+} solution was complete, the resultant gel-like slurry (pH 7.5-8) was stirred for 18 h at 65 °C. The colorless solid was isolated by filtration, washed several times with DD water and acetone (2 × 50 mL), and finally dried at room temperature under reduced pressure in a vacuum desiccator. Anal. Calcd for $Zn_4Al_2(OH)_{12}(C_7H_{15}O_3S)_{1.7}(CO_3)_{0.15}{\cdot}5.5H_2O$ (932.4): C, 15.52; H, 5.24; S, 5.84; Zn, 28.05; Al, 5.79. Found: C, 15.58; H, 5.26; S, 6.11; Zn, 28.8; Al, 5.7. TGA showed a mass loss of 10.7% up to 175 ºC (calcd, for loss of $5.5H_2O$: 10.6%), and a residual mass of 47.7% at 800 ºC (calcd, for $Zn_4Al_2O_7$: 45.8%). FT-IR (KBr, cm^{-1}): ν = 3473 (br), 2957 (m) [$\nu_{as}(CH_3)$], 2924 (m) [$\nu_{as}(CH_2)$], 2872 (sh) [$\nu_s(CH_3)$], 2855 (m) [$\nu_s(CH_2)$], 1631 (m), 1467 (m) [$\delta(CH_2)$], 1415 (w), 1379 (m), 1188 (s) [$\nu_{as}(SO_3^-)$], 1049 (s) [$\nu_s(SO_3^-)$], 795 (w), 723 (w) , 615 (m), 553 (m), 426 (s), 320 (m). Raman (cm^{-1}): ν = 3417, 2963, 2926, 2876, 2854, 2732, 1439, 1414, 1301, 1254, 1168, 1116, 1075, 1050, 907, 870, 846, 794, 602, 552, 490, 368, 338, 262, 224, 206. $^{13}C\{^1H\}$ CP MAS NMR: δ = 14.7 (C^7), 23.4 (C^6), 25.1 (C^2), 29.9 ($C^{3,4}$), 33.2 (C^5), 51.9 (C^1).

7.2.9 Synthesis of PS(*x*%)/HpS-LDH composites

A solution of $Zn(NO_3)_2 \cdot 6H_2O$ (2.98 g, 10 mmol) and $Al(NO_3)_3 \cdot 9H_2O$ (1.88 g, 5 mmol) in DD water (60 mL) was added dropwise to a solution of NaHpS (*a* mmol) and NaPS (*b* mmol; *a* + *b* = 10 mmol; *b* = 0.490, 0.230, 0.106 or 0.050 mmol) in DD water (80 mL) with efficient mixing. The pH of the reaction mixture was maintained at 7.5-8 by simultaneous addition of 0.5 M NaOH. Once addition of the Zn^{2+}/Al^{3+} solution was complete, the resultant gel-like slurry (pH 7.5-8) was stirred for 18 h at 65 °C. The solid was isolated by filtration, washed several times with DD water and acetone (3 × 50 mL), and finally dried at room temperature under reduced pressure in a vacuum desiccator. The samples are denoted PS(*x*%)/HpS-LDH, where *x* is the final mol% content of PS calculated (vs. the total content of PS + HpS) for the compositions given below.

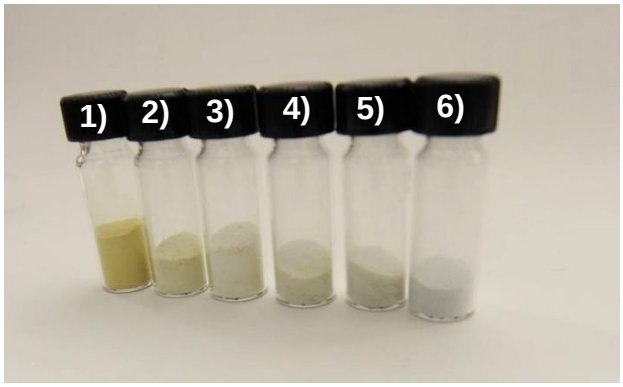

Figure 7.2 – Picture of the obtained LDH materials: 1) PS-LDH, 2) PS(11.8%)/HpS-LDH, 3) PS(4.7%)/HpS-LDH, 4) PS(2.3%)/HpS-LDH, 5) PS(1.2%)/HpS-LDH and 6) HpS-LDH.

PS(11.8%)/HpS-LDH (2). Anal. Calcd for $Zn_4Al_2(OH)_{12}(C_7H_{15}O_3S)_{1.5}(C_{16}H_9O_3S)_{0.2}(CO_3)_{0.15} \cdot 5.5H_2O$ (952.8): C, 17.46; H, 5.00; S, 5.72; Zn, 27.45; Al, 5.66. Found: C, 17.62; H, 5.15; S, 5.68; Zn, 27.5; Al, 5.7. TGA showed a mass loss of 11.1% up to 175 ºC (calcd, for loss of $5.5H_2O$: 10.4%), and a residual mass of 44.0% at 800 ºC (calcd, for $Zn_4Al_2O_7$: 44.9%).

PS(4.7%)/HpS-LDH (3). Anal. Calcd for $Zn_4Al_2(OH)_{12}(C_7H_{15}O_3S)_{1.62}(C_{16}H_9O_3S)_{0.08}(CO_3)_{0.15} \cdot 5.5H_2O$ (940.6): C, 16.31; H, 5.15; S, 5.80. Found: C, 16.29; H, 5.26; S, 5.82. TGA showed a mass loss of 11.3% up to 175 ºC (calcd, for loss of $5.5H_2O$: 10.5%), and a residual mass of 45.2% at 800 ºC (calcd, for $Zn_4Al_2O_7$: 45.4%).

PS(2.3%)/HpS-LDH (4). Anal. Calcd for $Zn_4Al_2(OH)_{12}(C_7H_{15}O_3S)_{1.7}(C_{16}H_9O_3S)_{0.04}(CO_3)_{0.13} \cdot 5.5H_2O$ (942.5): C, 16.15; H, 5.23; S, 5.92. Found: C, 16.15; H, 5.46; S, 5.84. TGA showed a mass loss of 11.8% up to 175 ºC (calcd, for loss of $5.5H_2O$: 10.5%), and a residual mass of 45.0% at 800 ºC (calcd, for $Zn_4Al_2O_7$: 45.3%).

PS(1.2%)/HpS-LDH (5). Anal. Calcd for $Zn_4Al_2(OH)_{12}(C_7H_{15}O_3S)_{1.68}(C_{16}H_9O_3S)_{0.02}(CO_3)_{0.15}\cdot 5.5H_2O$ (934.5): C, 15.72; H, 5.22; S, 5.83; Zn, 27.99; Al, 5.77. Found: C, 15.96; H, 5.16; S, 5.84; Zn, 28.3; Al, 5.9. TGA showed a mass loss of 12.0% up to 175 ºC (calcd, for loss of $5.5H_2O$: 10.6%), and a residual mass of 43.4% at 800 ºC (calcd, for $Zn_4Al_2O_7$: 45.7%).

7.2.10 (*E*)-3,3'-dioxo-3*H*,3'*H*-[2,2'-bibenzo[*b*]thiophenylidene]-5,5'-disulfonyl dichloride, denoted as thioindigo disulfonyl dichloride

Chlorosulfonic acid (20 mL, 0.3 mol) was added to thioindigo (1.20 g, 4 mmol) and the mixture was kept at 60 ºC for 24 h under N_2 atmosphere. The solution was cooled to room temperature and 50 mL of a saturated solution of $NaHCO_3$ in water was added. The resultant garnet-coloured solid was filtered and washed with saturated aq. $NaHCO_3$ (50 mL) and H_2O (50 mL). The solid was dried at 40 ºC overnight and purified by flash chromatography with silica gel using dichloromethane as eluent to obtain a bright orange solution that after evaporation of the solvent yielded thioindigo disulfonyl dichloride as a reddish solid (1.83 g, 93%).

7.2.11 (*E*)-3,3'-dioxo-3*H*,3'*H*-[2,2'-bibenzo[*b*]thiophenylidene]-5,5'-disulfonic acid, denoted as thioindigo disulfonic acid (H_2TIS)

A suspension of thioindigo disulfonyl dichloride (1.83 g) in 500 mL of water was heated at 110 ºC for 48 h to obtain a purple solution. After water evaporation under reduced pressure a purple solid was obtained and dried at 100 ºC for 12 h to give thioindigo disulfonic acid in quantitative yield. FT-IR (KBr, cm^{-1}): 1657 (s), 1593 (m, 1454 (m), 1412 (m), 1303 (m), 1261 (s), 1150 (bd), 1111 (s), 1089 (m), 1032 (s), 897 (m), 841 (w), 808 (m), 769 (w), 721 (w), 650 (m), 600 (w), 577 (w), 563 (w), 543 (w), 511 (w), 453 (w). ^{1}H NMR (400 MHz, DMSO-d_6, r.t., ppm): δ = 8.02 (d, J = 1.5 Hz, 2H, 4,4'-H), 7.96 (dd, J = 8.1, 1.5 Hz, 2H, 6,6'-H), 7.81 (d, J = 8.1 Hz, 2H, 7,7'-H). ^{13}C NMR (101 MHz, DMSO-d_6, r.t., ppm): δ = 189.1 (2,2'-C), 147.4, 147.1 (3,3'-C, 8,8'-C), 133.6, 132.8 (1,1'-C, 5,5'-C), 127.6 (6,6'-C), 124.5 (7,7'-C), 122.8 (4,4'-C). HR-ESI for $C_{16}H_6NaO_8S_4^-$: m/z = 476.8830 M^-.

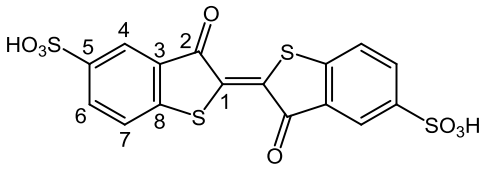

Scheme 7.2 - Atom numbering scheme for NMR assignments of H_2TIS.

7.2.12 General synthesis of intercalated LDHs (IC(*n*%)/TIS-LDH)

A solution of $Zn(NO_3)_2 \cdot 6H_2O$ (*x* mmol) and $Al(NO_3)_3 \cdot 9H_2O$ (*x*/2 mmol) in DD water (30 mL) was added dropwise to a solution containing Na_2IC (*a* mmol) and/or Na_2TIS (*b* mmol) in DD water (*z* mL) with vigorous stirring ($a + b = x/2$; $n\% = 100 \times a/(a + b)$; $n = 100, 98, 90, 50, 0$). The value of *x* was 3.33 for $n = 100$, and 2.50 for the remaining materials; the value of *z* was 30 for $n = 0$, and 80 for the remaining materials. Solutions containing the disodium salt Na_2TIS were prepared using H_2TIS and 2 equiv. of NaOH. During addition of the Zn^{2+}/Al^{3+} solution the pH of the reaction mixture was maintained at 7.5-8.0 through dropwise addition of 0.25 M (*n*% = 0-98) or 0.5 M (*n*% = 100) NaOH. Once addition of the Zn^{2+}/Al^{3+} solution was complete, the resultant gel-like slurry was stirred for 18 h at 65 °C. The solid product was isolated by filtration, washed several times with DD water and acetone, and finally dried at room temperature under reduced pressure in a vacuum desiccator. For simplicity, the materials containing solely IC or TIS are denoted as IC-LDH and TIS-LDH.

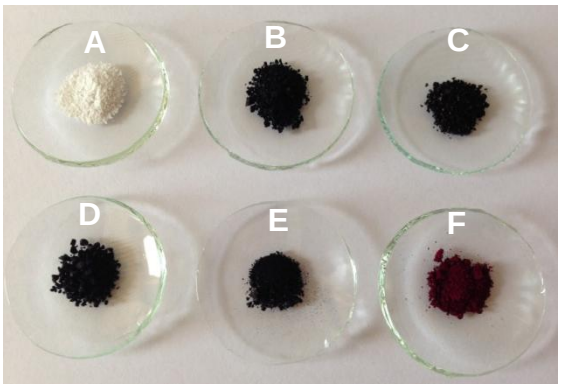

Figure 7.3 – Picture of the obtained LDH materials: A) NO_3-LDH, B) IC-LDH, C) IC(98%)/TIS-LDH, D) IC(90%)/TIS-LDH, E) IC(50%)/TIS-LDH and F) TIS-LDH.

IC-LDH (B). FTIR (KBr, cm^{-1}): ν = 3465 (br), 1655/1642 (s), 1616 (vs), 1475 (s), 1402 (m), 1329 (m), 1260 (w), 1199 (s), 1163 (s), 1107 (vs), 1065 (w), 1028 (vs), 825 (m), 785 (w), 733 (m), 681 (m), 588 (s), 424 (m). Raman (cm^{-1}): ν = 3207, 3087, 1630, 1580, 1529, 1475, 1351, 1291, 1233, 869, 769, 672, 549, 464, 395, 267. $^{13}C\{^1H\}$ CP MAS NMR: δ = 187.7 (2,2'-C), 151.7 (8,8'-C), 135.8, 134.7 (5,5'-C, 6,6'-C), 121.2 (1,1'-C, 4,4'-C), 117.2 (3,3'-C), 112.7 (7,7'-C).

TIS-LDH (F). FTIR (KBr, cm^{-1}): ν = 3477 (br), 1654 (vs), 1591 (vs), 1454 (s), 1413 (w), 1385 (w), 1305 (m), 1263 (m), 1219 (m), 1182 (vs), 1115 (vs), 1086 (m), 1033 (vs), 902 (m), 837 (m), 771 (w), 723 (m), 647 (m), 600 (m), 577 (m), 543 (m), 514 (m), 426 (m). Raman (cm^{-1}): ν = 3066, 1675, 1570, 1522 (vs), 1454, 1412, 1301 (m), 1207, 1140, 1063, 775, 685, 519, 475, 388, 276. $^{13}C\{^1H\}$ CP MAS NMR: δ = 189.0 (2,2'-C), 150.1 (3,3'-C), 141.8 (8,8'-C), 133.3 (1,1'-C, 5,5'-C), 127.5 (4,4'-C, 6,6'-C, 7,7'-C).

IC(98%)/TIS-LDH (C). FTIR (KBr, cm^{-1}): ν = 3445 (br), 1641 (s), 1614 (vs), 1471 (s), 1402 (m), 1320 (m), 1260 (w), 1198 (s), 1163 (s), 1105 (vs), 1065 (w), 1028 (vs), 822 (w), 800 (w), 733 (w), 681 (w), 588 (m), 424 (m).

IC(90%)/TIS-LDH (D). FTIR (KBr, cm^{-1}): ν = 3450 (br), 1641 (s), 1614 (vs), 1473 (s), 1402 (m), 1323 (m), 1260 (w), 1196 (s), 1163 (s), 1105 (vs), 1066 (w), 1030 (vs), 903 (w), 825 (m), 783 (w), 733 (m), 681 (m), 590 (s), 426 (m).

IC(50%)/TIS-LDH (E). FTIR (KBr, cm^{-1}): ν = 3450 (br), 1655 (s), 1640 (sh), 1612 (vs), 1589 (s), 1470 (m), 1453 (m), 1402 (m), 1318 (sh), 1305 (m), 1262 (m), 1218 (sh), 1180 (s), 1112 (s), 1030 (vs), 900 (m), 828 (m), 799 (m), 772 (m), 732 (sh), 723 (m), 678 (w), 649 (m), 513 (m).

7.2.13 NO_3-LHS (G)

The zinc hydroxide nitrate NO_3-LHS was prepared by co-precipitation from a 0.5 M solution of $Zn(NO_3)_2$ with a 0.5 M solution of NaOH (OH/Zn molar ratio of 0.5). The NaOH solution (25 mL, 12.5 mmol) was added dropwise to 0.5 M $Zn(NO_3)_2$ (50 mL, 25 mmol) at room temperature with vigorous stirring. The white solid product was immediately filtered following complete addition of the NaOH solution, washed with cold decarbonated and deionised water, and finally vacuum-dried. Anal. Calcd for $Zn_5(OH)_8(NO_3)_{1.6}(CO_3)_{0.2}\cdot 1.5H_2O$ (601.2): C, 0.40; H, 1.84; N, 3.73. Found: C, 0.40; H, 1.81; N, 3.70%. TGA revealed a mass loss of 4.45% at 130 ºC (calcd for loss of $1.5H_2O$: 4.49%). The residual mass at 400 ºC was 68.8% (calcd for ZnO: 67.7%). FT-IR (KBr, cm^{-1}): 3575 (m), 3477 (br), 1639 (m), 1383 (vs), 1010 (w), 887 (m), 838 (m), 765 (m), 637 (s), 520 (sh), 466 (m), 436 (w), 384 (m). Raman (cm^{-1}): 3573 (vw), 3489 (w), 1054 (vs), 729 (w), 709 (w), 436 (w), 401 (m), 291 (w), 212 (w).

7.2.14 General synthesis of intercalated LHSs (IC(*n*%)/TIS-LHS)

The procedure used is similar to that reported by Maruyama *et al.* for the preparation of an LHS material intercalated by IC.[22] A solution of $ZnCl_2$ (0.57 g, 4.18 mmol) in DD water (50 mL) was added dropwise to a solution containing Na_2IC (*a* mmol) and/or Na_2TIS (*b* mmol) in DD water (50 mL) with vigorous stirring ($a + b = 1$; $n\% = 100 \times a/(a + b)$; n = 100, 98, 90, 80, 50, 0). Solutions containing the disodium salt Na_2TIS were prepared using H_2TIS and 2 equiv. of NaOH. During addition of the $ZnCl_2$ solution the pH of the reaction mixture was maintained at 7.5-8.0 through dropwise addition of 0.17 M NaOH. Once addition of the $ZnCl_2$ solution was complete, the resultant gel-like slurry was immediately filtered and the solid product washed several times (5×50 mL) with DD water, and finally dried at room temperature under reduced pressure. For simplicity, the materials containing solely IC or TIS are denoted as IC-LHS and TIS-LHS.

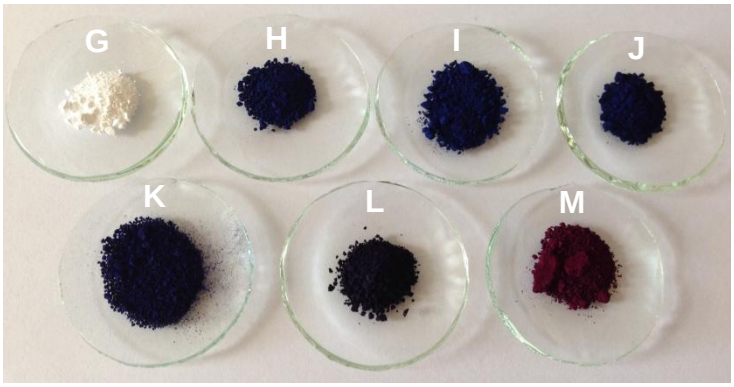

Figure 7.4 – Picture of the obtained LHS materials: G) NO_3-LHS, H) IC-LHS, I) IC(98%)/TIS-LHS, J) IC(90%)/TIS-LHS, K) IC(80%)/TIS-LHS L) IC(50%)/TIS-LHS and F) TIS-LHS.

IC-LHS (H). FTIR (KBr, cm^{-1}): ν = 3440 (s), 1641 (vs), 1615 (s), 1587 (w), 1475 (s), 1444 (m), 1402 (m), 1325 (m), 1265 (m), 1199 (s, bd), 1151 (vs), 1126 (m), 1109 (vs), 1028 (vs), 903 (w), 831 (m), 783 (w), 736 (m), 717 (w), 678 (m), 603 (s), 590 (s), 567 (m), 524 (m), 470 (m), 424 (m), 388 (w), 363 (w). $^{13}C\{^1H\}$ CP MAS NMR: δ = 187.7 (2,2'-C), 154.7 (8,8'-C), 133.1, 133.0 (5,5'-C, 6,6'-C), 121.1 (1,1'-C, 4,4'-C), 118.3 (3,3'-C), 116.4(7,7'-C).

TIS-LHS (M). FTIR (KBr, cm^{-1}): ν = 3490 (br), 1649 (vs), 1592 (m), 1454 (m), 1306 (w), 1263 (w), 1219 (m), 1193 (m), 1113 (s), 1085 (m), 1033 (s), 906 (w), 843 (w), 771 (m), 721 (m), 652 (s), 600 (w), 577 (m), 542 (w), 513 (m), 457 (w). Raman (cm^{-1}): ν = 3064, 1674, 1592, 1569, 1518 (vs), 1452, 1411, 1300 (m), 1301, 1262, 1206, 1141, 1102, 1063, 775, 685 (m), 519 (m), 475 (m), 388. $^{13}C\{^1H\}$ CP MAS NMR: δ = 187.8 (2,2'-C), 150.7 (3,3'-C), 140.4 (8,8'-C), 132.0 (1,1'-C, 5,5'-C), 125 (4,4'-C, 6,6'-C, 7,7'-C).

IC(98%)/TIS-LHS (I). FTIR (KBr, cm^{-1}): ν = 3342 (s), 1641 (vs), 1615 (s), 1587 (w), 1508 (sh), 1475 (s), 1444 (m), 1405 (m), 1323 (m), 1265 (m), 1200 (s, bd), 1151 (vs), 1126 (m), 1109 (vs), 1028 (vs), 903 (w), 831 (m), 783 (w), 736 (m), 717 (w), 678 (m), 603 (s), 590 (s), 567 (m), 524 (m), 470 (m), 424 (m), 390 (w), 363 (w).

IC(90%)/TIS-LHS (J). FTIR (KBr, cm^{-1}): ν = 3342 (s), 1641 (vs), 1614 (s), 1587 (w), 1508 (sh), 1475 (s), 1444 (m), 1406 (m), 1323 (m), 1265 (m), 1198 (s, bd), 1151 (vs), 1126 (m), 1109 (vs), 1028 (vs), 903 (w), 831 (m), 783 (w), 736 (m), 719 (w), 678 (m), 603 (s), 590 (s), 567 (m), 524 (m), 469 (m), 424 (m), 390 (w), 370 (w).

IC(80%)/TIS-LHS (K). FTIR (KBr, cm^{-1}): ν = 3342 (s), 1641 (vs), 1614 (s), 1587 (w), 1508 (sh), 1475 (s), 1444 (m), 1406 (m), 1323 (m), 1265 (m), 1198 (s, bd), 1151 (vs), 1126 (m), 1109 (vs), 1028 (vs), 903 (w), 831 (m), 783 (w), 736 (m), 719 (w), 678 (m), 603 (s), 590 (s), 567 (m), 524 (m), 469 (m), 424 (m), 390 (w), 370 (w).

IC(50%)/TIS-LHS (L). FTIR (KBr, cm^{-1}): ν = 3342 (s), 1641 (vs), 1614 (s), 1589 (m), 1508 (sh), 1473 (m), 1454 (m), 1445 (sh), 1404 (m), 1323 (m), 1308 (sh), 1265 (m), 1198 (s, bd), 1151 (vs), 1109 (vs), 1028 (vs), 904 (m), 831 (m), 771 (w), 735 (m), 721 (m), 676 (w), 654 (m), 602 (m), 590 (m), 514 (m), 512 (m), 455 (m), 384 (w), 370 (w).

7.2.15 Heat treatment of LHS samples

The samples IC-LHS and TIS-LHS (ca. 200 mg of each sample) were placed in a Petri dish and heated at 200 ºC for 30 min in an oven under static air atmosphere. The resultant heat-treated samples ($IC\text{-}LHS_{ht}$ and $TIS\text{-}LHS_{ht}$) were stored under nitrogen while awaiting their respective characterisation.

7.3 Cleaning procedures

After filtration, the filters were cleaned using a concentrated solution of chloridric acid (HCl) or nitric acid (HNO_3) and washed several times with water, due to intense color of dye that was impregnated during the filtration process.

7.4 Structural characterization techniques

7.4.1 Powder X-Ray Diffraction

PXRD patterns were recorded in transmission mode using a Philips Analytical Empyrean (θ/2θ) diffractometer equipped with a PIXcel1D detector, with automatic data acquisition (X'Pert Data Collector v4.2 software) and monochromatized Cu-K_α radiation (λ = 1.5406 Å). Each sample was mounted between two Mylar foils and then placed in the sample holder. The samples were step-scanned with 0.02º 2θ steps and a counting time of 50 s per step.

Simulated PXRD patterns, structural models and representations were generated using CrystalMaker® and CrystalDiffract® software.[2-3]

7.4.2 Scanning Electron Microscopy

Scanning electron microscopy (SEM) images were collected using a Hitachi SU-70 microscope operating at 15 kV. Samples were prepared by deposition on aluminium sample holders followed by carbon coating using an Emitech K 950 carbon evaporator.

EDS analyses were performed on the same instrument equipped with a Bruker Quantax 400 spectrometer.

7.4.3 Thermogravimetric Analysis and Differential Scanning Calorimetry

TGA and DSC were performed using a Shimadzu TGA-50 and DSC-50 systems at a heating rate of 5 ºC min^{-1} under air by Celeste Azevedo.

7.4.4 Fourier Transform Infrared spectroscopy

FT-IR spectra were obtained as KBr pellets using a FTIR Mattson-7000 spectrophotometer and recorded in transmission mode from 4000 to 300 cm^{-1} with a resolution of 4 cm^{-1}.

7.4.5 Raman spectroscopy

Raman spectra were recorded on a Bruker RFS100/S FT instrument (Nd:YAG laser, 1064 nm excitation, InGaAs detector).

7.4.6 $^{13}C\{^{1}H\}$ cross-polarization (CP) magic-angle spinning (MAS) NMR

Solid-state $^{13}C\{^{1}H\}$ cross-polarization magic-angle spinning NMR spectra were recorded at 100.62 MHz on a Bruker Avance 400 spectrometer using 3.5 µs ^{1}H 90º pulses, a 2 ms contact time, a spinning rate of 10 kHz, and 5 s recycle delays. Chemicals shifts are quoted in ppm relative to TMS.

7.4.7 Elemental Analysis

Elemental analysis for C, H, N and S was performed at the University of Aveiro by Manuela Marques with a Leco TruSpec 630-200-200 analyzer. Zn and Al contents were determined by ICP-OES at C.A.C.T.I., the University of Vigo, Spain.

7.5 Photophysical Instrumentation and Methods

7.5.1 Absorption

The absorption spectra, either in solution or in solid state, were recorded with Cary 5000 UV-Vis-NIR spectrophotometer. The molar extinction coefficient (ε) was obtained from the slope of the absorption with (at least) five solutions of different concentrations versus the concentration (correlation values > 0.999). For titration of CR, a solution of the dye in water (pH 6.3) was prepared with an absorbance below 0.2 at 497 nm. The pH was adjusted by addition of HCl and NaOH solutions (0.1 and 1 M).

The solid state spectra were recorded by diffuse reflectance using the referred equipment equipped with an integrated sphere. A baseline with NO_3-LDH and NO_3-LHS was made before

measuring solid state spectra of LDH and LHS samples, respectively. The diffuse reflectance was then corrected for the Kubelka-Munk factor defined by equation:

$$F(R) = \frac{(1 - \%R)^2}{(2 \times \%R)}$$

7.5.2 Steady-State Fluorescence

The solution and solid-state spectra were recorded with a Horiba-Jobin-Ivon SPEX Fluorolog 3-22 spectrometer and were corrected for the instrumental response. The solid-state fluorescence spectra were obtained using triangular quartz cuvettes.

7.5.2.1 Fluorescence Quantum Yields in Solution at Room Temperature

Fluorescence quantum yields (ϕ_F) were determined by comparison with references of known quantum yield. The fluorescence standards (references) used were α-oligothiophene α6 (ϕ_F = 0.41 in dioxane[4]) for CR in water, and cresyl violet (ϕ_F = 0.54 in ethanol[5]) for CR in DMSO. The emission quantum yields of these standards should be independent of the excitation wavelength, so the standards can be used in their full absorption range. In practice, the quantum yields are determined by comparison of the integrated area under the emission spectra of optically matched solutions of the sample compound (*cp*) and that of the suitable reference (*ref*) compound. The absorption and emission range of the sample and reference compounds should match as close as possible. The absorbance values should be kept as low as possible to avoid inner filter effects (usually with A < 0.2). Under these conditions, using the same excitation wavelength, the unknown fluorescence quantum yield (Φ_F^{cp}) is calculated using the following equation:[6]

$$\Phi_F^{cp} = \frac{\int I(\lambda)^{cp} d\lambda}{\int I(\lambda)^{ref} d\lambda} \frac{OD_{ref}}{OD^{cp}} \cdot \frac{n_{cp}^2}{n_{ref}^2} \cdot \Phi_F^{ref}$$

where, n_x ids the refractive index of the solvent in which the sample compound and reference were dissolved, and OD_x is the optical density of the reference and sample compound at the excitation wavelength.

7.5.2.2 Fluorescence Quantum Yields in Solid-State at Room Temperature

The absolute fluorescence quantum yields for the materials described in Chapter 4 were obtained in powder form using a Quantaurus-QY Absolute PL quantum yield spectrometer from Hamamatsu equipped with an integrating sphere. This system does not require the use of known reference standards. The principle of quantum yield measurement is the comparison of the reference spectrum (only the empty quartz cells or quartz cells with solvent, in case of solutions samples) with sample spectrum giving immediately the fluorescence quantum yield value, as illustrated in Figure 7.5.

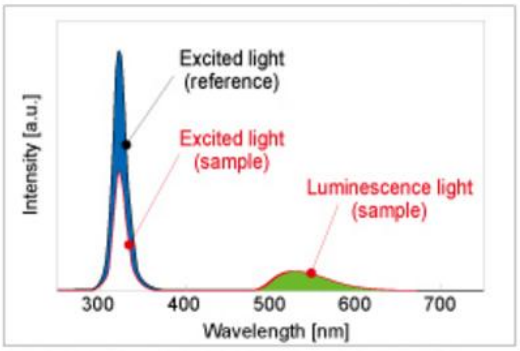

Figure 7.5 – Excitation at the same wavelength in reference and sample generating the fluorescence emission spectrum of sample (taken from http://www.hamamatsu.com/jp/en/C11347-11).

7.5.3 Time-Resolved Fluorescence

7.5.3.1 Fluorescence decays with nanosecond time-resolution

The fluorescence decays were measured using a home-built time-correlated single photon counting (TCSPC) apparatus with an IBH NanoLED (with excitation at 282, 311 and 339 nm) as excitation source. Triangular quartz cuvettes were used and the emission, collected at the surface front at right angle (90º) geometry and at magic angle polarization, was detected through a double subtractive Oriel Cornerstone 260 monochromator by a Hamamatsu microchannel plate photomultiplier (R3809U-50). The signal acquisition and data processing were performed employing a Becker & Hickl SPC-630 TCSPC module. The fluorescence decays and the instrumental response function (IRF) were collected using 1024 channels in a 342 ps/channel scale, until 5000 counts at maximum were reached. The full width at half-maximum (fwhm) of the IRF was 0.95-1.10 ns for the nanoled with λ_{exc} = 311 nm, 0.89 ns with λ_{exc} = 282 ns and 0.93-1.0 ns with λ_{exc} = 339 nm, and found to be highly reproducible with identical system parameters. Deconvolution of the fluorescence decay curves was performed using the modulating function method as implemented by Striker *et al.* in the SAND program.[7]

7.5.3.2 Fluorescence decays with picosecond time-resolution

In this case, fluorescence decays were measured using home-built picosecond time correlated single photon counting (TCSPC) equipment. The excitation source consisted of a picosecond Spectra Physics mode-lock Tsunami Laser (Ti:Sapphire) Model 3950 (repetition rate of about 82 MHz, tuning range 700-1000 nm), pumped by a Millenia Pro-10s, frequency-doubled continuous wave (CW), diode pumped, solid-state laser (λ_{em} = 532 nm). A harmonic generator model GWU-23PS (Spectra Physics) was used to produce the second and third harmonic from the Ti:Sapphire laser exciting beam frequency output. The excitation was 444 nm (for IC-based LDH) and the horizontally polarized output beam from the GWU (second harmonic) was first passed through a ThorLabs depolarizer (WDPOL-A)

followed by a Glan-Thompson polarizer (Newport 10GT04) with vertical polarization. Fluorescence decays and the IRF were collected using 4096 channels in a 0.8 ps per channel scale, until 1-3 kilo counts (kCounts) at maximum were reached. The fwhm of the IRF (measured using a LUDOX scattering solution in water) was about 21 ps and was highly reproducible with identical system parameters. After deconvolution of the experimental signal, the time resolution of the apparatus was ca. 2 ps.[8]

Alternatively, the fluorescence decays were obtained using a PicoQuant PicoLED (model LDH-P-C450b, λ_{exc} = 450 nm) as the excitation source; in this case the fwhm of the IRF was about 70 ps. Deconvolution of the fluorescence decay curves was performed by using the same program referred above. As discussed in the Chapter 3, the rising component associated with the ESIPT in IC can only be observed with excitation with the Ti:Sapphire laser, whereas the decay of IC is reproduced with both excitation sources.

7.5.4 Femtosecond Time-Resolved Transient Absorption (fs-TA) spectroscopy

The experimental setup for ultrafast spectroscopic and kinetic measurements was described previously.[9] Probe light in the VIS range was generated by passing a small portion of the 795 nm light from a Solstice-100F laser through a computerized optical delay (with a time window of up to 8 ns) and focusing in a sapphire plate to generate white-light continuum in the 450-800 nm range. All measurements, for CR in solutions, were obtained in a 2 mm quartz cuvette with absorptions ≤ 0.3 at the pump excitation wavelength, and to avoid multiphoton absorption the laser pump power was kept at ≤ 0.5 μJ. The IRF of the system was assumed to be equal to that of the pump-probe cross correlation determined from the measurement of the instantaneous stimulated Raman signal from the pure solvent (in a 2 mm cuvette). Typical values for the IRF of the system were found to be better than 250 fs. To avoid photodegradation, the solutions were stirred during the experiments or in movement using a motorized translating sample holder. Transient absorption data were analyzed using the Surface Xplorer PRO program from Ultrafast Systems and the global analysis of the data (from which the lifetimes and decay associated spectra, DAS, of the observed transients were obtained) was performed using Glotaran software.[10] For further details about the global analysis of the data (including singular value decomposition) and the interpretation of the resulting outputs (DAS and concentration profiles), the reader is advised to see reference.[10]

7.6 References

1. Gomes, A. C.; Bruno, S. M.; Gamelas, C. A.; Valente, A. A.; Abrantes, M.; Goncalves, I. S.; Romao, C. C.; Pillinger, M., Intercalation of a molybdenum [small eta]3-allyl dicarbonyl complex in a layered double hydroxide and catalytic performance in olefin epoxidation. *Dalton Transactions* **2013,** *42* (23), 8231.

2. *CrystalMaker®: A crystal and molecular structures modelling program for Mac and Windows*, version 9; CrystalMaker Software Ltd, Oxford, UK.

3. *CrystalDiffract®*, version 6; CrystalMaker Software Ltd, Oxford, UK.

4. Becker, R. S.; deMelo, J. S.; Macanita, A. L.; Elisei, F., Comprehensive evaluation of the absorption, photophysical, energy transfer, structural, and theoretical properties of alpha-oligothiophenes with one to seven rings. *Journal of Physical Chemistry* **1996,** *100* (48), 18683.

5. Montalti, M.; Credi, A.; Prodi, L.; Gandolfi, M. T., *Handbook of Photochemistry*. 3rd ed.; CRC Press: Boca Raton, FL: **2006**.

6. Murov, S.; Carmichael, I.; Hug, G., *Handbook of Photochemistry*. 2nd ed.; Marcel Dekker, Inc., New York: **1993**.

7. Striker, G.; Subramaniam, V.; Seidel, C. A. M.; Volkmer, A., Photochromicity and fluorescence lifetimes of green fluorescent protein. *Journal of Physical Chemistry B* **1999,** *103* (40), 8612.

8. Pina, J.; Seixas de Melo, J.; Burrows, H. D.; Maçanita, A. L.; Galbrecht, F.; Bunnagel, T.; Scherf, U., Alternating Binaphthyl-Thiophene Copolymers: Synthesis, Spectroscopy, and Photophysics and Their Relevance to the Question of Energy Migration versus Conformational Relaxation. *Macromolecules* **2009,** *42* (5), 1710.

9. Pina, J.; Seixas de Melo, J. S.; Eckert, A.; Scherf, U., Unusual photophysical properties of conjugated, alternating indigo-fluorene copolymers. *Journal of Materials Chemistry A* **2015,** *3* (12), 6373.

10. Snellenburg, J. J.; Laptenok, S.; Seger, R.; Mullen, K. M.; van Stokkum, I. H. M., Glotaran: A Java-Based Graphical User Interface for the R Package TIMP **2012,** *49* (3), 22.